Astronomy and Astrophysics Library

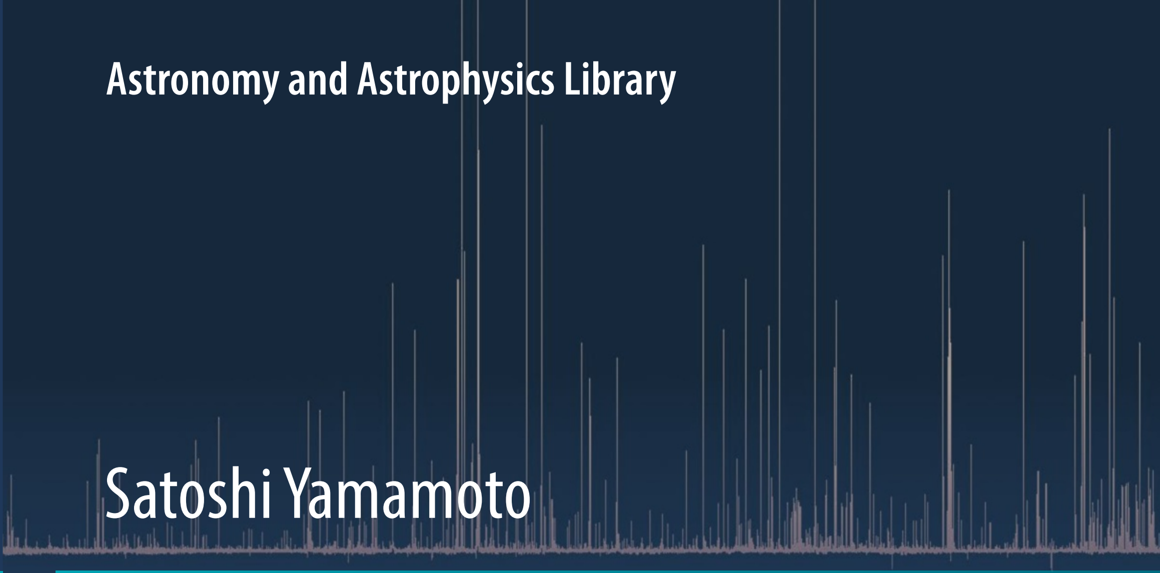

Satoshi Yamamoto

Introduction to Astrochemistry

Chemical Evolution from Interstellar Clouds to Star and Planet Formation

A&A LIBRARY

Springer

Astronomy and Astrophysics Library

More information about this series at http://www.springer.com/series/848

Satoshi Yamamoto

Introduction to Astrochemistry

Chemical Evolution from Interstellar Clouds to Star and Planet Formation

Springer

Satoshi Yamamoto
Department of Physics
The University of Tokyo
Tokyo, Japan

ISSN 0941-7834 ISSN 2196-9698 (electronic)
Astronomy and Astrophysics Library
ISBN 978-4-431-54170-7 ISBN 978-4-431-54171-4 (eBook)
DOI 10.1007/978-4-431-54171-4

Library of Congress Control Number: 2016962456

© Springer Japan 2017
This work is subject to copyright. All rights are reserved by the Publisher, whether the whole or part of the material is concerned, specifically the rights of translation, reprinting, reuse of illustrations, recitation, broadcasting, reproduction on microfilms or in any other physical way, and transmission or information storage and retrieval, electronic adaptation, computer software, or by similar or dissimilar methodology now known or hereafter developed.
The use of general descriptive names, registered names, trademarks, service marks, etc. in this publication does not imply, even in the absence of a specific statement, that such names are exempt from the relevant protective laws and regulations and therefore free for general use.
The publisher, the authors and the editors are safe to assume that the advice and information in this book are believed to be true and accurate at the date of publication. Neither the publisher nor the authors or the editors give a warranty, express or implied, with respect to the material contained herein or for any errors or omissions that may have been made. The publisher remains neutral with regard to jurisdictional claims in published maps and institutional affiliations.

Cover illustration: Satoshi Yamamoto

Printed on acid-free paper

This Springer imprint is published by Springer Nature
The registered company is Springer Japan KK
The registered company address is: Chiyoda First Bldg. East, 3-8-1 Nishi-Kanda, Chiyoda-ku, Tokyo 101-0065, Japan

Preface

In modern astronomy and astrophysics, chemistry is becoming increasingly important. Molecules are found everywhere in the universe owing to rapid progress of spectroscopic observations particularly in the radio, infrared, and optical regimes. Exploring chemical compositions of astronomical sources itself is of fundamental importance in understanding evolution of matter in the history of the universe. Moreover, chemical compositions are widely used as a powerful tool for investigating physical conditions and formation processes of astronomical sources. Such a chemical approach will rapidly be expanded to various areas of astronomical and astrophysical studies in the near future. Astrochemistry is now one of the fundamental subfields of astronomy and astrophysics.

Astrochemistry is becoming more and more complicated as it progresses rapidly. Hence, it is not easy even for experts to understand its whole scope in detail. When researchers working in astronomy and astrophysics employ astrochemistry to cope with actual problems, they may sometimes utilize a small, particular part of astrochemistry for their studies without careful consideration of assumptions and limitations hidden in the background. In order to make full use of the power of astrochemistry, a deep understanding of its fundamental astrochemical concepts based on physics and chemistry is essential.

On the other hand, astrochemistry is deeply related to molecular science, which includes molecular physics, molecular spectroscopy, chemical dynamics, and theoretical chemistry. Because chemical processes in the universe are generally ongoing under extreme physical conditions of low density and low temperature in comparison with terrestrial conditions, astrochemistry has been posing new and interesting research subjects in molecular science. In order for researchers in molecular science to discover new chemical and physical phenomena in astronomical studies, a deep understanding of the fundamental concepts of astrochemistry will be very useful.

This book is organized to describe those fundamental concepts for researchers and students in the broad fields of astronomy, astrophysics, and molecular science. For this reason, recent topics are not always included, although some of them are introduced as examples. Furthermore, this book does not cover the entire field of astrochemistry but puts a particular emphasis on outlining chemical evolution from molecular clouds to star and planet formation. For other subfields of astrochemistry (e.g., external galaxies and late-type stars), readers should refer to available review articles, although the basic part of the astrochemical concept in this book will still be useful for understanding their contents.

Twenty-five years ago, I moved from the spectroscopic field to the astrochemistry field, triggered by fortuitous discoveries of some new interstellar molecules. Since then, I have been studying the chemical evolution of molecular clouds toward star and planet formation with my colleagues and graduate students. Because of my limited experience and knowledge of this field, I am afraid that some important issues might be missing or poorly presented. However, I was encouraged by the younger generation desiring an introductory book on astrochemistry, and I have made up my mind to publish this work. I welcome any suggestions and criticisms from readers.

Finally, I express my sincere gratitude to all my colleagues and collaborators, particularly to Nami Sakai, Tomoya Hirota, Takeshi Sakai, Yoshimasa Watanabe, Shuji Saito, Masatoshi Ohishi, Norio Kaifu, and the late Hiroko Suzuki. I also thank the members of my group for their valuable comments.

I dedicate this book to my wife, Keiko.

Tokyo, Japan Satoshi Yamamoto
November 17, 2014

Contents

Chapter 1
Introduction

1.1 Matter in Space

According to recent cosmological observations (Hinshaw et al. 2013; Planck Collaboration 2014), 95.4 % of the total mass of the Universe is composed of dark energy and dark matter, and the contribution of baryons (comprising atoms and molecules, familiar to all) is only 4.6 %. Nevertheless, the existence of this small baryonic fraction enables structures such as galaxies, stars, and planets to form. Likewise, it is well known that 98 % of the total mass of baryons is composed of hydrogen (H) and helium (He), whereas the total contribution of heavy elements such as carbon (C), nitrogen (N), and oxygen (O) is only about 2 %. However, the presence of this smaller fraction of heavy elements makes possible the enormous variety of compounds creating the rich chemical world of materials around us.

In astronomy, exploring structure formation and physical evolution processes is a fundamental task in understanding the history of the Universe. For instance, the formation of the first stars, the formation of galaxies, and the formation of stars and planets in galaxies are all currently outstanding topics, and a significant amount of research is being conducted to understand the detailed processes involved during formation and evolution. At the same time, exploring the chemical evolution of matter in the Universe is also a fundamental goal of astronomy. One important aspect of this evolution is nucleosynthesis in stars. Although only H, deuterium (D), He, and a small amount of lithium (Li) were produced in the Big Bang, heavy elements have been produced in stars little by little over the long history of the Universe (1.38×10^{10} yr). Synthesized heavy elements in stars are distributed into the interstellar medium in supernova explosions and mass-loss processes of late-type stars. Increasing abundances of heavy elements significantly affect the physical process of star formation by increasing the cooling rate of interstellar gas. A more important and interesting aspect of the evolution of matter is molecular evolution, which is particularly important in relation to understanding star and planet formation and eventually the origin of the Solar System. How are various

S. Yamamoto, *Introduction to Astrochemistry*, Astronomy and Astrophysics Library 7, DOI 10.1007/978-4-431-54171-4_1

molecules formed in interstellar clouds? How large can molecules grow in these clouds? How are molecules incorporated into stars and planets? These questions represent current frontiers in astronomy. Studies of structure formation processes and chemical evolution processes of matter are apparently two halves of a whole toward a comprehensive understanding of the history of the Universe.

1.2 Interstellar Matter and Its Circulation

In our Galaxy (the Milky Way), about 90 % of the baryon mass resides in stars, and the remaining is in interstellar matter. Because the total mass of the Galaxy is of the order of $10^{11}\,M_{\odot}$, the total mass of interstellar matter is about $10^{10}\,M_{\odot}$. Interstellar matter consists of gas and dust particles; the latter are composed of silicate and carbonaceous compounds, with sizes typically about 0.1 μm in diameter. Gas dominates by mass, and the dust-to-gas mass ratio is about 0.01 in the solar neighborhood. Because this ratio depends on metallicity—the abundance of heavy elements—it varies among galaxies and even within our Galaxy.

Elemental abundances in interstellar matter near the solar neighborhood are listed in Table 1.1 as number ratios relative to hydrogen nuclei. Hydrogen is the most abundant element in the Universe, and helium is the second most abundant. Second raw elements such as C, N, and O have abundances of 10^{-3}–10^{-4} relative to H. Heavier elements generally show lower abundances, and abundance significantly varies within the same raw elements, reflecting the nucleosynthetic processes occurring in stars. In particular, iron (Fe), being the element with the highest binding energy per nucleon, is relatively abundant despite its high mass. The elemental abundances given here do not correspond to abundances in the gas phase. Because heavier elements tend to exist in dust grains, their gas-phase abundances are generally lower.

Interstellar matter is not uniformly distributed over the galaxy, but is rather concentrated in clumps and filaments of various scales, called "clouds." Figure 1.1 shows the density and temperature for some representative classes of clouds. The density and temperature of extended clouds such as diffuse clouds, intercloud gas, coronal gas, and some molecular clouds lie almost on a straight line with constant pressure, indicating that these clouds are in pressure equilibrium. In contrast, the densest parts of molecular clouds are gravitationally contracting and hence deviate from the line of constant pressure. Moreover, H II regions around high-mass stars, where hydrogen mostly exists as H^+, are not on the line.

The coronal and intercloud components of the interstellar medium are both diffuse and ionized and are often referred to as hot ionized medium (HIM) and warm ionized medium (WIM), respectively (McKee and Ostriker 1977). Such media will form diffuse clouds after their protons recombine with electrons. In diffuse clouds, atomic hydrogen and molecular hydrogen coexist. As the temperature decreases and the density increases, the diffuse clouds gradually become opaque to interstellar ultraviolet (UV) radiation, and hydrogen molecules become

Table 1.1 Cosmic abundance of elements[a]

Element	Relative abundance
H	1.00E 0
He	8.51E-02
Li	1.12E-11
Be	2.40E-11
B	5.01E-10
C	2.69E-03
N	6.76E-05
O	4.90E-04
F	3.63E-08
Ne	8.51E-05
Na	1.74E-06
Mg	3.98E-05
Al	2.82E-06
Si	3.24E-05
P	2.57E-07
S	1.32E-05
Cl	3.16E-07
Ar	2.51E-06
K	1.07E-07
Ca	2.19E-06
Sc	1.41E-09
Ti	8.91E-08
V	8.51E-09
Cr	4.37E-07
Mn	2.69E-07
Fe	3.16E-05

[a] Asplund et al. (2009)

the dominant form of hydrogen. Such clouds are called molecular clouds. Molecular clouds are the formation sites of new stars. Protostars are formed by the gravitational contraction of molecular cloud cores. In general, molecular clouds harbor rich molecules formed in the gas phase and on dust grains. Protostars further evolve into main-sequence stars, during which time planetary systems are formed.

Main-sequence stars are stable for relatively long times during hydrogen burning. The lifetime of a 1 $M_\odot$ main-sequence star is 10^{10} yr. After hydrogen burning is completed, main-sequence stars evolve into late-type star stages. Some late-type stars show considerable mass loss, which supplies gas and dust to the interstellar medium. Massive stars ($>8\ M_\odot$) finally end their lives via supernova explosions, which are the most energetic events in the Universe. Through supernova explosions, heavy elements formed during nucleosynthesis in stars revert to interstellar medium. Thus, interstellar matter circulates throughout the galaxy over the entire life cycle of stars.

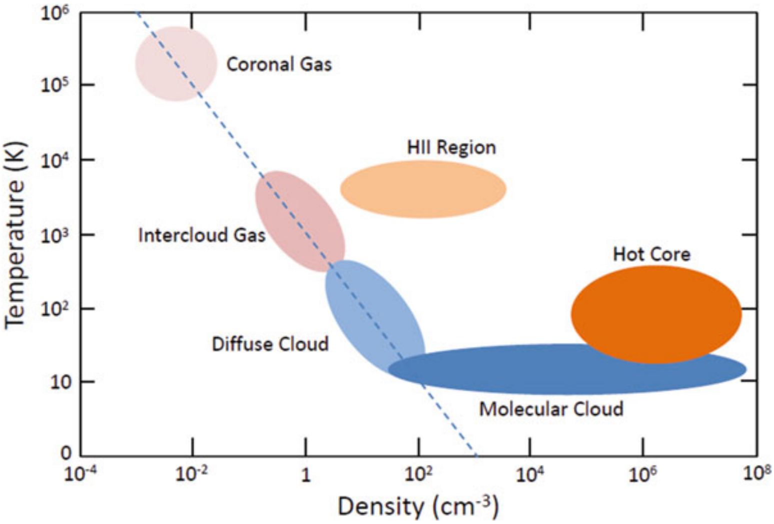

Fig. 1.1 Temperature-density diagram of interstellar clouds. The dashed line indicates the constant-pressure line. The diffuse interstellar medium is in pressure equilibrium

In the large-scale circulation of interstellar matter, the richest phase of molecules occurs from the diffuse cloud stage to the star- and planet-formation stage. In this book, we concentrate on chemical processes in this phase. Envelopes of evolved stars are important places for the formation of dust grains and also exhibit rich molecular chemistry. Because excellent reviews and books are dedicated to these processes (e.g., Glassgold 1996; Ziurys 2006; Agundez et al. 2008), we do not repeat these discussions in this book.

1.3 Interstellar Molecules

It is more than 75 years since the existence of molecules in interstellar clouds was first established. In 1940, McKellar identified sharp optical absorption lines (387.46 nm and 430.03 nm) in spectra toward bright stars detected using the Mount Wilson 100-inch telescope as the electronic transitions of CN (*B*-*X*) and CH (*A*-*X*), respectively. Subsequently, Douglas and Herzberg (1941) found CH^+ in interstellar clouds. Although these discoveries were just the tip of the iceberg of molecular astronomy, they did not receive much attention from astronomers; these molecules were thought to be fragments of large molecules or grains.

In the interim, rapid advances in microwave technology in the 1940s enhanced the sensitivity of radio astronomy. Muller and Oort (1951) and Ewen and Purcell (1951) discovered emissions from atomic hydrogen (H I) at 1.42 GHz (21 cm) in interstellar clouds. This finding established the existence of cold atomic clouds in interstellar space. Because radio waves penetrate through our Galaxy, the rotation of our Galaxy was studied in detail by observations of the H I 21-cm line (e.g., Oort et al. 1958; Van de Hulst et al. 1954; Kalberla et al. 2005; McClure-Griffiths et al. 2009; Peek et al. 2011). In 1955, Townes presented thorough discussions of the possibilities of detecting atoms and molecules using radio observations (Townes 1957). Townes pointed out the importance of rotational spectral lines of molecules. However, this proposal also did not receive much attention from astronomers.

In 1963, Weinreb et al. detected the Λ-type doubling transition (1.67 GHz) of OH in absorption spectra toward the bright radio continuum source Cassiopeia A. OH was the first interstellar molecule detected by radio astronomical observations. The radio emissions from OH often show anomalous features, including maser action. Strong OH masers have been the subject of astrophysical studies of interstellar clouds, as well as late-type stars (Robinson and McGee 1967; Elitzur 1992). Above all, the importance of molecules was first recognized with the detection of NH_3. In 1968, Cheung et al. detected the inversion transition of NH_3 at 23.6 GHz in emission spectra toward the center of our Galaxy. The existence of a familiar molecule such as NH_3 in interstellar clouds clearly demonstrated the existence of a new world of molecular astronomy. Cheung et al. (1969) also detected extremely bright rotational emission from H_2O at 22.2 GHz toward the Orion Nebula and W49, which was later found to be due to maser action. Additionally, Snyder et al. (1969) detected the first organic interstellar molecule, H_2CO. Following these discoveries, HCN and CO were successively reported in interstellar clouds (Snyder and Buhl 1971; Wilson et al. 1970). The original papers reporting the discoveries of these molecules clearly convey the vivid surprise and excitement of their authors.

To date, we know of about 170 interstellar molecules; see Table 1.2. Molecules containing up to 13 atoms have so far been found in interstellar media. Most of these molecules have been detected by radio observations of their rotational spectral lines; some have been identified by optical or infrared observations of their electronic or vibration-rotation spectra. A few characteristic features of interstellar molecules can be deduced from Table 1.2. First, many chemically reactive species such as free radicals and molecular ions are listed. This fact reflects the very low density and very low temperature conditions of interstellar clouds compared with laboratory conditions. Given the extreme conditions, chemically reactive species can survive for a long time. Second, the existence of ionic species such as HCO^+, H_3^+, and C_6H^- means that interstellar clouds are weakly ionized plasmas. As will be discussed in later chapters, these ions play central roles in the formation of various molecules in interstellar clouds. Third, a number of highly unsaturated hydrocarbon molecules such as carbon-chain molecules and their geometrical isomers exist despite the hydrogen-dominated conditions of interstellar clouds. The presence of unsaturated hydrocarbon molecules in interstellar clouds is the most characteristic feature of interstellar chemistry and is one of the important subjects of this book. Finally, saturated complex organic molecules such as $HCOOCH_3$ and $(CH_3)_2O$ can be found in some sources, meaning that chemical evolution in interstellar clouds produces fairly complex molecules even under

Table 1.2 Molecules found in interstellar clouds

Simple neutral molecules
H_2, CH, CN, CO, HCl, NH, NO, NS, OH, PN, SO, SiO, SiS, CS, HF, O_2, SH, CH_2, HCN, HCO, H_2O, H_2S, HNC, HNO, N_2O, OCS, SO_2, CO_2, NH_2, HO_2, NH_3, H_2CO, H_2CS, CH_3, H_2O_2, CH_4
Ionic species
(Cation)
CH^+, CO^+, SO^+, CF^+, OH^+, SH^+, HCl^+, ArH^+, HCO^+, HCS^+, HOC^+, N_2H^+, H_3^+, H_2O^+, H_2Cl^+, OH_3^+, $HCNH^+$, HCO_2^+, C_3H^+, H_2COH^+, NH_4^+, H_2NCO^+, HC_3NH^+
(Anion)
C_4H^-, C_6H^-, C_8H
Carbon-chain molecules and their isomers
C_2, C_3, C_2H, C_2O, C_2S, c-C_3H, l-C_3H, C_3N, C_3O, C_3S, C_2H_2, C_5, C_4H, l-C_3H_2, c-C_3H_2, HC_3N, HCCNC, HNC_3, C_5H, l-C_4H_2, C_5N, C_6H, CH_3CCH, HC_5N, CH_3C_3N, C_6H_2, CH_2CCHCN, CH_3C_4H, HC_7N, CH_3C_5N, HC_9N, CH_3C_6H, $HC_{11}N$
Complex organic molecules
HCOOH, CH_2CO, CH_3CN, CH_3NC, CH_3OH, CH_3SH, HC_2CHO, c-C_3H_2O, CH_2CNH, HNCHCN, CH_2CHCN, CH_3CHO, CH_3NH_2, c-C_2H_4O, H_2CCHOH, $HCOOCH_3$, CH_3COOH, CH_2OHCHO, CH_2CHCHO, NH_2CH_2CN, CH_3CHNH, CH_3CH_2CN, $(CH_3)_2O$, CH_3CH_2OH, CH_3CONH_2, C_3H_6, CH_3CH_2SH, $(CH_3)_2CO$, $(CH_2OH)_2$, CH_3CH_2CHO, C_2H_5OCHO, CH_3OCOCH_3, $C_2H_5OCH_3$, n-C_3H_7CN
Other molecules
FeO, HNCO, HNCS, H_2CN, HCNO, HOCN, HSCN, CH_2CN, H_2CNH, NH_2CN, HCOCN, HNCNH, CH_3O, NH_2CHO

Note: Based on the Cologne Database for Molecular Spectroscopy (CDMS) (Muller et al. 2001, 2008). The classification of molecules is arbitrary

extreme conditions. These saturated organic molecules are thought to be produced mainly by grain-surface reactions.

In addition to gas-phase molecules, some molecules are found on dust grains as solid molecules by infrared observations. Although water ice (H_2O) is a dominant species on dust grains, other species such as CO, CO_2, CH_4, NH_3, and CH_3OH are known to be contained in H_2O ice. The interplay between the gas-phase species and solid-phase species is a central issue in current astrochemical studies.

1.4 Importance of Chemistry

After the discoveries of various molecules in interstellar clouds, the important and interesting goal became the understanding of the chemical processes that produce these species. Molecular synthesis through gas-phase ion–molecule reactions was proposed and successfully explained the basic molecular abundances observed in interstellar clouds (e.g., Klemperer 1970; Herbst and Klemperer 1973; Watson 1974). This mechanism of molecular formation was verified via the identification of molecular ions such as HCO^+ and HN_2^+ (Woods et al. 1975; Saykalley et al. 1976). Later, the importance of neutral–neutral reactions was recognized, even in low-temperature conditions (Herbst et al. 1994). The rate coefficients of the gas-phase reactions are often available from laboratory experiments. Even if the rate coefficients are not measured, they can be estimated based on theoretical considerations and/or quantum chemical calculations. Hence, a reaction network considering a number of reactions can be developed quite readily, and numerical simulations using the network are applied to interpret the observational data (e.g., Herbst and Leung 1989; Prasad and Huntress 1980; Millar and Nejad 1985; Graedel et al. 1982; Lee et al. 1996).

In addition to the gas-phase processes, molecular synthesis through grain-surface reactions was also considered just after the discovery of interstellar molecules (Watson and Salpeter 1972a, b; Watson 1976; Iguchi 1975; Allen and Robinson 1977; Tielens and Hagen 1982). A reaction network similar to the gas-phase network was also constructed, and numerical calculations were performed to simulate the observed abundances. However, reaction probabilities on grain surfaces are much more uncertain, mainly because the grain surface itself is an inhomogeneous system. Laboratory experiments are more difficult, and theoretical estimates are less certain than for gas-phase processes. Hence, many assumptions have to be made in deriving the reaction probabilities when constructing a reaction network. For this reason, grain-surface models received less attention than the gas-phase models for comparison with observations in the 1970s and 1980s.

Although the gas-phase chemical model succeeded in explaining the observed abundances in cold quiescent molecular clouds, it failed to reproduce the abundances of saturated complex organic molecules found in high-mass, star-forming regions. Furthermore, the depletion of molecules onto dust grains was observationally established (e.g., Caselli et al. 1999). Under these circumstances, the importance of gas-grain interactions was recognized as critical. Large chemical models considering gas-grain interactions were developed to simulate chemical compositions (e.g., Hasegawa et al. 1992; Garrod et al. 2007; Aikawa et al. 2005). Surface reactions were studied in the laboratory, proffering better assumptions in the chemical models. The gas-grain chemical model is now a standard model for studying the chemical compositions of molecular clouds.

Detections of various interstellar molecules and relevant studies pertaining to their production mechanisms stimulated molecular science researchers and gave rise to various new investigations of molecular spectroscopy, molecular dynamics, surface science, and quantum chemical calculations. Many new interstellar molecules, mostly free radicals, were identified with the aid of laboratory molecular spectroscopy. Above all, it should be remembered that an experiment aimed at understanding the formation processes of carbon-chain molecules eventually led to the discovery of fullerene C_{60} (Kroto et al. 1985). C_{60} itself was also discovered in space many years later (Cami et al. 2010). Even now, astrochemical studies are continually posing many interesting problems in the field of molecular science.

Given the steady progress of observational studies, source-to-source variations of chemical compositions were recognized as an interesting line of research. Exploring the origin of the chemical diversity in dense molecular cloud cores led scientists to establish the concept of chemical evolution (e.g., Suzuki et al. 1992).

Because chemical compositions systematically vary as clouds evolve, chemical compositions can be used as an age tracer of dense cores. On the other hand, some molecules preferentially exist in special physical conditions such as shocked regions, photodissociation regions, and hot molecular cores around protostars. Thus, chemical compositions are now being used to diagnose the physical conditions and evolutionary stages of various astronomical sources. A chemical approach is indispensable in modern astrophysics, and it will only become more so in the future.

1.5 Principal Aim of This Book

This book describes the basic aspects of astrochemistry for researchers and graduate students who are investigating molecules in interstellar media or who are purely interested in the subject. This book is also for researchers in fields of molecular science and planetary science. The main aim of this book is to provide the fundamental physical and chemical concepts that astrochemical concepts are entirely based on. Astrochemistry is a rapidly growing field that is constantly pushing its frontiers. Researchers in this field need to remain abreast of rapid developments and also have to produce new ideas and concepts from new observational results. Furthermore, chemical models are becoming more and more complex, which makes it difficult for nonexperts to understand their applicability and limitations. To handle such situations, basic concepts of astrochemistry are essential and hence are covered in this book. Nevertheless, current frontiers and topics of astrochemistry that are still controversial are not expanded on, although some recent works are introduced as examples of applications. The reader is encouraged to seek out the excellent review articles on these topical issues. Radio astronomy is the most important observational technique of astrochemistry; its basic principles are briefly introduced in the Appendix. Additional details of radio astronomy are comprehensively presented in other books, and we hope that the reader will refer to these resources.

1.6 Units Used in Astronomy

Because astrochemistry is an interdisciplinary field, the participation of researchers outside of astronomy is essential for the development of the field. Hence, some readers may not be familiar with the units used in astronomy. Before proceeding, we briefly summarize here several of these important units:

1. Astronomical unit (au): One au corresponds to the average distance between the Sun and the Earth, 1.496×10^{11} m.

2. Parsec (pc): One pc corresponds to the distance to an object whose annual parallax is 2 arc seconds, the object being on the line perpendicular to the orbital plane of the Earth. One pc is 3.086 × 10^{16} m, and hence an apparent source size of 1 arc second at a distance of 100 pc corresponds to a size of 100 au.
3. Visual extinction (A_v): Visual extinction describes the loss in magnitude of visible light with a wavelength of 550 nm attenuated because of absorption and scattering (extinction) by interstellar dust. Extinction is represented in units of magnitudes; an extinction of 1 magnitude means that the intensity is reduced by a factor of $10^{0.4}$ (~2.512). Visual extinction is approximately proportional to the column density of the hydrogen atom. For our local galactic neighborhood:

$$N(\mathrm{H}) = 2 \times 10^{21} A_v \ \ \mathrm{cm}^{-2}. \tag{1.1}$$

   Alternatively, it is related to the column density of H_2 in molecular clouds:

$$N(\mathrm{H}_2) = 1 \times 10^{21} A_v \ \ \mathrm{cm}^{-2}. \tag{1.2}$$

   Note that the coefficient of proportionality may be different for galaxies of different metallicity.
4. Solar mass ($M_\odot$): A mass unit, where 1 $M_\odot$ corresponds to 1.988 × 10^{30} kg.
5. Solar luminosity ($L_\odot$): A luminosity unit, where 1 $L_\odot$ corresponds to 3.845 × 10^{26} W.

1.7 Reaction Rates

Coefficients of reaction rates are often essential in discussing chemical processes in interstellar clouds. The values of such coefficients used in this book are mostly taken from the University of Manchester Institute of Science and Technology (UMIST) Database for Astrochemistry (McElroy et al. 2013).

References

W.S. Adams, Annual Report of the Director of the Mount Wilson Observatory 1938–1939, pp. 23

M. Agundez, J. Cernicharo, J.R. Pardo, J.P. Fonfria Exposito, M. Guelin, E.D. Tenenbaum, L.M. Ziurys, A.J. Apponi, Astrophys. Space Sci. **313**, 229 (2008)

Y. Aikawa, E. Herbst, H. Roberts, P. Caselli, Astrophys. J. **620**, 330 (2005)

M. Allen, G.W. Robinson, Astrophys. J. **212**, 396 (1977)

M. Asplund, N. Grevesse, A.J. Sauval, P. Scott, Ann. Rev. Astron. Astrophys. **47**, 481 (2009)

J. Cami, J. Bernard-Salas, E. Peeters, S. Malek, Science **329**, 1180 (2010)

P. Caselli, C.M. Walmsley, M. Tafalla, L. Dore, P.C. Myers, Astrophys. J. **523**, L165 (1999)

A.C. Cheung, D.M. Rank, C.H. Townes, D.D. Thornton, W.J. Welch, Phys. Rev. Lett. **21**, 1701 (1968)

A.C. Cheung, D.M. Rank, C.H. Townes, D.D. Thornton, W.J. Welch, Nature **221**, 626 (1969)
A.E. Douglas, G. Herzberg, Astrophys. J. **94**, 381 (1941)
M. Elitzur, Ann. Rev. Astron. Astrophys. **30**, 75 (1992)
H.I. Ewen, E.M. Purcell, Nature **168**, 356 (1951)
R.T. Garrod, V. Wakelam, E. Herbst, Astron. Astrophys. **467**, 1103 (2007)
A.E. Glassgold, Ann. Rev. Astron. Astrophys. **34**, 241 (1996)
T.E. Graedel, W.D. Langer, M.A. Frerking, Astrophys. J. Suppl. **48**, 321 (1982)
T.I. Hasegawa, E. Herbst, C.M. Leung, Astrophys. J. Suppl. **82**, 167 (1992)
E. Herbst, W. Klemperer, Astrophys. J. **185**, 505 (1973)
E. Herbst, C.M. Leung, Astrophys. J. Suppl. **69**, 271 (1989)
E. Herbst, H.-H. Lee, D.A. Howe, T.J. Millar, Mon. Not. R. Astr. Soc. **268**, 335 (1994)
G. Hinshaw, D. Larson, E. Komatsu, et al., Astrophys. J. Suppl. **208**, 19 (2013)
T. Iguchi, Publ. Astron. Soc. Japan **27**, 515 (1975)
P.M.W. Kalberla, W.B. Burton, D. Hartmann, E.M. Arnal, E. Bajaja, R. Morras, W.G.L. Roppel, Astron. Astrophys. **440**, 775 (2005)
W. Klemperer, Nature **227**, 1230 (1970)
H.W. Kroto, J.R. Heath, S.C. O'Brien, R.F. Curl, R.E. Smalley, Nature **318**, 162 (1985)
H.-H. Lee, R.P.A. Bettens, E. Herbst, Astron. Astrophys. Suppl. **119**, 111 (1996)
N.M. McClure-Griffiths et al., Astrophys. J. Suppl. **181**, 398 (2009)
C.F. McKee, J.P. Ostriker, Astrophys. J. **218**, 148 (1977)
D. McElroy, C. Walsh, A.J. Markwick, M.A. Cordiner, K. Smith, T.J. Millar, Astron. Astrophys. 550, A36 (2013). http://udfa.ajmarkwick.net/
A. McKellar, Publ. Astron. Soc. Pac. **52**, 187 (1940)
T.J. Millar, L.A.M. Nejad, Mon. Not. R. Astr. Soc. **217**, 507 (1985)
C.A. Muller, J.H. Oort, Nature **168**, 357 (1951)
H.S.P. Muller, S. Therwirth, D.A. Roth, G. Winnewisser, Astron. Astrophys. **370**, L49 (2001)
H.S.P. Muller, F. Schloder, J. Stutzki, G. Winnewisser, J. Mol. Struct. **742**, 215 (2008)
J.H. Oort, F.J. Kerr, G. Westerhout, Mon. Not. R. Astr. Soc. **118**, 379 (1958)
J.E.G. Peek et al., Astrophys. J. Suppl. **194**, 20 (2011)
Planck Collaboration, Astron. Astrophys. **571**, A16 (2014)
S.S. Prasad, W.T. Huntress Jr., Astrophys. J. Suppl. **43**, 1 (1980)
B.J. Robinson, R.X. McGee, Ann. Rev. Astron. Astrophys. **5**, 183 (1967)
R.J. Saykalley, T.A. Dixson, T.G. Anderson, P.C. Szanto, R.C. Woods, Astrophys. J. **205**, L101 (1976)
L.E. Snyder, D. Buhl, Astrophys. J. **163**, L47 (1971)
L.E. Snyder, D. Buhl, B. Zuckerman, P. Palmer, Phys. Rev. Lett. **22**, 679 (1969)
H. Suzuki, S. Yamamoto, M. Ohishi, N. Kaifu, S. Ishikawa, Y. Hirahara, S. Takano, Astrophys. J. **392**, 551 (1992)
A.G.G.M. Tielens, W. Hagen, Astron. Astrophys. **114**, 245 (1982)
C.H. Townes, in *The Fourth International Astronomical Union Symposium, Manchester 1955*, ed. by H.C. Van de Hulst, (Cambridge University Press, Cambridge 1957), paper 16
Van de Hulst, C.A. Muller, J.H. Oort, Bull., Astron. Inst. Netherlands **452**, 117 (1954)
W.D. Watson, Astrophys. J. **188**, 35 (1974)
W.D. Watson, Rev. Mod. Phys. **48**, 513 (1976)
W.D. Watson, E.E. Salpeter, Astrophys. J. **174**, 321 (1972a)
W.D. Watson, E.E. Salpeter, Astrophys. J. **175**, 659 (1972b)
S. Weinreb, A.H. Barrett, M.L. Meeks, J.C. Henry, Nature **200**, 829 (1963)
R.W. Wilson, K.B. Jefferts, A.A. Penzias, Astrophys. J. **161**, L43 (1970)
R.C. Woods, T.A. Dixon, R.J. Saykalley, P.C. Szanto, Phys. Rev. Lett. **35**, 1269 (1975)
L.M. Ziurys, Proc. Nat. Acad. Sci. **103**, 12274 (2006)

Chapter 2
Derivation of Molecular Abundances

2.1 Thermal Emission

Here, we consider the relation between radiation emitted by matter and the temperature of matter. Imagine a gas burner heating a brick. The brick appears first tinged with red; later, as it continues to be heated, it shines as white light. This experiment indicates that a brick emits visible light at high temperature and that its color depends on its temperature. Then, what about a brick at room temperature? When a room-temperature brick is set in a closed room and the light in the room is turned off, we cannot see the brick. That is, the brick at room temperature does not emit visible light detectable by human eyes. We usually recognize a brick at room temperature by the light that it reflects from sunlight or lights in the room. Nevertheless, a room-temperature brick emits electromagnetic radiation in the infrared part of the spectrum. Even without any illumination, we can indeed detect such bricks using an infrared camera. Matter at different temperatures emits electromagnetic waves of different wavelengths. For lower-temperature objects, the emitted wavelengths become longer. Interstellar matter, whose temperature is as low as 10 K, does not emit even infrared radiation but instead emits radio waves. Cold interstellar matter can accordingly be traced by radio observations.

Radiation from matter at a nonzero temperature is called *thermal emission*. In general, its intensity depends on the composition of material as well as its temperature, to be described below. However, we can suppose as an extreme case that matter is completely opaque and absorbs all radiation at any wavelength without reflection. Such matter is called a *blackbody*. Among all matter, a blackbody gives the maximum thermal emission at a given temperature. The above condition defining a blackbody is too idealized, however, and it is rarely fulfilled in reality. Most blackbodies can be regarded as blackbodies in a particular range of wavelengths. For instance, let us consider a brick and an iron block of similar shape. At room temperature, these two objects can be readily distinguished in terms of how they reflect visible light. Hence, they cannot be regarded as blackbodies. At high

S. Yamamoto, *Introduction to Astrochemistry*, Astronomy and Astrophysics Library 7, DOI 10.1007/978-4-431-54171-4_2

temperatures, both the brick and iron block similarly radiate white light; hence, we cannot distinguish them. In this situation, radiation from the environment is absorbed, and emissions from the two objects are seen. Hence, both the brick and iron block can be regarded as blackbodies in this instance. It should be noted that the emission from blackbodies does not depend on its composition, but only on its temperature. The importance of this characteristic was first noted by Gustav Kirchhoff (Kirchhoff 1860). Based on his findings, Max Planck later established the theory of blackbody radiation and introduced the Planck constant (Planck 1901). This theory was one of the important milestones in the development of quantum theory.

Energy emitted from the blackbody per area dS, time dt, frequency $d\nu$, and solid angle $d\Omega$ is written as:

$$dE = B_\nu(T) dS dt d\nu d\Omega, \tag{2.1}$$

where $B_\nu(T)$ is the intensity of the blackbody radiation at temperature T. The intensity is represented by the Planck function as:

$$B_\nu(T) = \frac{2h\nu^3}{c^2} \frac{1}{\exp(h\nu/k_B T) - 1}, \tag{2.2}$$

where h denotes the Planck constant, c the speed of light, v the frequency of radiation, and k_B the Boltzmann constant. The units of $B_\nu(T)$ are erg s^{-1} cm^{-2} Hz $^{-1}$ sr^{-1}. It should be noted that, for a given frequency, $B_\nu(T)$ only depends on temperature, irrespective of composition and structure of the blackbody. Figure 2.1 shows a plot of $B_\nu(T)$ as a function of frequency for various temperatures. The frequency corresponding to the peak intensity rises at higher temperatures, the relationship being known as Wien's displacement law. For instance, the surface temperature of the Sun is 6000 K, and hence the Sun can be regarded as a blackbody with that temperature. Its radiation has an intensity peak in the visible wavelengths. In contrast, the cosmic microwave background radiation can be well approximated as a blackbody with a temperature of 2.73 K, whose intensity peak appears in the microwave regime.

If $h\nu/k_B T \ll 1$, then by expanding the exponential part of Eq. (2.2), the following approximate relation known as the Rayleigh–Jeans law is derived:

$$B_\nu(T) \cong \frac{2v^2}{c^2} k_B T. \tag{2.3}$$

In this case, the intensity is proportional to temperature. Note that this equation does not involve the Planck constant and is regarded as the classical limit of blackbody radiation. In contrast, for $h\nu/k_B T \gg 1$, Wien's law holds:

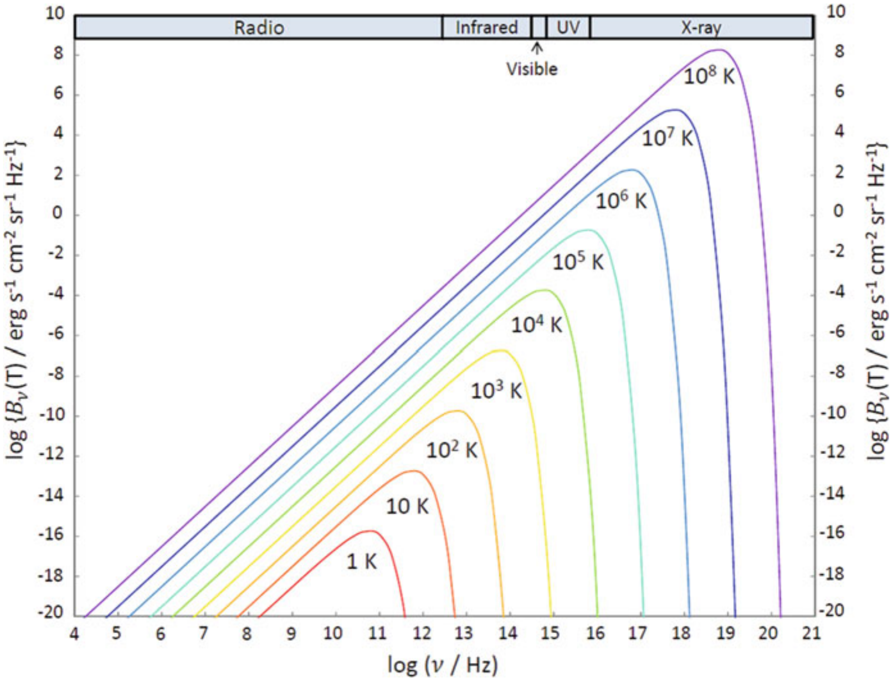

Fig. 2.1 Spectral lines for blackbody radiation at various temperatures (Note the log–log scale of the plot)

$$B_\nu(T) \cong \frac{2h\nu^3}{c^2}\exp\left(-\frac{h\nu}{k_B T}\right). \tag{2.4}$$

In this case, the intensity exponentially decreases with increasing frequency.

As noted, blackbody radiation only depends on the temperature of the emitting source. Nevertheless, thermal radiation generally contains rich information about the nature of matter (e.g., atoms and molecules). For instance, we can determine the abundance of atoms and molecules in interstellar clouds from the intensities of their spectral lines. In the following sections, we describe the thermal radiation from atoms and molecules.

2.2 Information Derived from Spectral Line Observations

2.2.1 Radiative Transfer

Consider the propagation of an electromagnetic wave with a frequency ν in interstellar clouds. Here, we assume that radiation travels in straight lines. This assumption is justified when the beam diameter is much larger than the wavelength ($\lambda = c/\nu$). Similar to Eq. (2.1), the intensity I_ν of the wave is defined from:

$$dE = I_\nu dSdtd\nu d\Omega. \tag{2.5}$$

The unit of intensity is erg s^{-1} cm^{-2} sr^{-1} Hz^{-1}. Although intensity is conserved in the vacuum of space (Problem 2.1), it varies due to absorption and emission by atoms and molecules in the intervening clouds. We define the x axis as the direction of propagation. A change in intensity, dI_ν, for an infinitesimal propagation of dx is represented as:

$$dI_\nu = -\alpha_\nu I_\nu dx + j_\nu dx, \tag{2.6}$$

where α_ν is an absorption coefficient and j_ν stands for emissivity. Hence, the following radiation transfer equation holds:

$$\frac{dI_\nu}{dx} = -\alpha_\nu I_\nu + j_\nu. \tag{2.7}$$

In general, α_ν and j_ν vary from position to position and hence are functions of x. Dividing both sides of this equation by α_ν and defining a new variable τ_ν:

$$d\tau_\nu = \alpha_\nu dx, \tag{2.8}$$

the equation simplifies:

$$\frac{dI_\nu}{d\tau} = -I_\nu + S_\nu, \tag{2.9}$$

where,

$$S_\nu = j_\nu / \alpha_\nu. \tag{2.10}$$

Here, S_ν is called the source function, whose meaning is described below. By solving the differential equation, the intensity at any position can be obtained, if S_ν is known. As a boundary condition, the intensity at $x = 0$ ($\tau_\nu = 0$) is set as $B_\nu(T_b)$, meaning that the source radiation is blackbody radiation at T_b. If the cloud only exists for $x \geq 0$, the background radiation should be the cosmic microwave background radiation ($T_b = 2.73$ K). For simplicity, we assume that the cloud is physically and chemically homogeneous. Then, S_ν is constant over all positions $x \geq 0$, and we obtain the intensity at $x = L$ as follows:

$$I_\nu = S_\nu + \exp(-\tau_\nu)[B_\nu(T_b) - S_\nu], \tag{2.11}$$

where,

$$\tau_\nu = \alpha_\nu L. \tag{2.12}$$

Here, τ_ν is a dimensionless quantity referred to as the optical depth or optical thickness. This quantity is related to the physical thickness of the cloud, L, by the above relation. Even for large physical thicknesses, the optical depth can be very small if the absorption coefficient is small.

We consider here a source function, S_ν. Suppose that the above cloud is completely enclosed with a blackbody at a temperature of T. After sufficient time, the cloud will be in thermal equilibrium at this temperature. If we make an infinitesimally small hole to look at the cloud inside, the intensity that we observe is $B_\nu(T)$, which is because the system (the cloud enclosed by the blackbody) remains a blackbody. Furthermore, we can set $T_b = T$. Hence, Eq. (2.11) is written as:

$$B_\nu(T) = S_\nu + \exp(-\tau_\nu)[B_\nu(T) - S_\nu]. \tag{2.13}$$

This relation must hold for any value of τ_ν, because blackbody radiation is independent of the internal structure of the emitting body. To satisfy this condition, the source function must be the Planck function. Specifically, we obtain:

$$S_\nu = B_\nu(T). \tag{2.14}$$

This result means that the absorption coefficient and the emissivity are not independent, but their ratio (the source function) is constrained by the temperature through the Planck function. This relation is known as Kirchhoff's law of thermal radiation and is based on the physical requirement that emission and absorption have to be balanced in thermal equilibrium.

By substituting S_ν with $B_\nu(T)$ in Eq. (2.11), we obtain:

$$I_\nu = B_\nu(T) + \exp(-\tau_\nu)[B_\nu(T_b) - B_\nu(T)]. \tag{2.15}$$

In actual observations, the target position and a nearby position without any cloud emission and absorption are alternatively observed, and their difference is taken to reduce the effects of gain variation of the telescope system and changes in atmospheric conditions. Because the intensity toward the off-source position is given as

$$I_\nu = B_\nu(T_b), \tag{2.16}$$

the difference is written as:

$$\Delta I_\nu = [B_\nu(T) - B_\nu(T_b)]\{1 - \exp(-\tau_\nu)\}. \tag{2.17}$$

This value represents the intensity actually observed by radio telescopes.

In radio astronomy, the intensity is typically represented by a temperature scale. As recognized by differentiating the Planck function by T, the intensity of a blackbody monotonically increases with increasing temperature at a given frequency (Problem 2.2). Hence, the intensity can be represented by the temperature at which a blackbody emits the same intensity. In particular, the intensity is proportional to the temperature in the Rayleigh–Jeans law ($h\nu/k_BT \ll 1$). Hence, the temperature scale of the intensity, ΔT, is defined using the Rayleigh–Jeans law, regardless of its validity. Then, we obtain:

$$\Delta T = \frac{h\nu}{k_B}\left\{\frac{1}{\exp(h\nu/k_BT)-1} - \frac{1}{\exp(h\nu/k_BT_b)-1}\right\}\{1-\exp(-\tau_\nu)\}. \tag{2.18}$$

If $h\nu/k_BT \ll 1$, the equation can be further simplified as:

$$\Delta T = (T - T_b)\{1-\exp(-\tau_\nu)\}. \tag{2.19}$$

This temperature scale for intensity is very useful because we can avoid the rather complex units of erg $\mathrm{s^{-1}\ cm^{-2}\ Hz^{-1}\ sr^{-1}}$ and can readily imagine a physical temperature of an emitter. Furthermore, this scale is convenient for intensity calibrations from blackbody radiation, as explained in Chap. 11.

2.2.2 Absorption Coefficient

As described above, the observed intensity depends on the temperature of the cloud, the background temperature, and the optical depth. The optical depth is related to the absorption coefficient, which reflects all electromagnetic properties of an emitter. Here, we formulate the absorption coefficient in terms of the properties of atoms or molecules. For simplicity, we first consider a two-level system, of lower level l and upper level u specified by the energy levels of a molecule or an atom (Fig. 2.2), and consider the absorption coefficient for the transition from level l to level u. The absorption probability per unit time is represented by $B_{\ell u}J_\nu$, where B_{ij} is

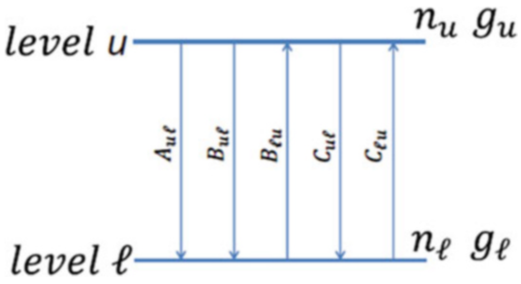

Fig. 2.2 Two-level system: Populations for the upper and lower levels are denoted by n_u and n_ℓ, respectively; degeneracies by g_u and g_ℓ, respectively. Spontaneous emission, stimulated emission, and absorption are indicated by the corresponding Einstein coefficients; collisional excitation and de-excitation are also indicated

the Einstein B coefficient for the transition from level i to level j, and J_ν represents the mean intensity for the molecule:

$$J_\nu = \frac{1}{4\pi} \int I_\nu d\Omega. \tag{2.20}$$

A similar relation holds for a stimulated emission from level u to level l. Hence, the energy extracted from an electromagnetic-wave beam in a frequency range $d\nu$, solid angle $d\Omega$, time dt, and volume dV is given by:

$$-dI_\nu d\nu d\Omega dt dS = \frac{h\nu}{4\pi}\phi(\nu)(n_\ell B_{\ell u} - n_u B_{u\ell}) I_\nu d\nu d\Omega dt dV, \tag{2.21}$$

where n_i stands for a number of molecules populating level i. Here, $\phi(v)$ is a line profile function satisfying the following normalization relation:

$$\int \phi(v)dv = 1. \tag{2.22}$$

Because $dV = dSdx$, the absorption coefficient is written as:

$$\alpha_\nu = \frac{h\nu}{4\pi}\phi(\nu)(n_\ell B_{\ell u} - n_u B_{u\ell}), \tag{2.23}$$

by comparing Eq. (2.21) with its definition:

$$dI_\nu = -\alpha_\nu I_\nu dx. \tag{2.24}$$

The Einstein B coefficients, $B_{\ell \mathrm{u}}$ and $B_{u\ell}$, are related to each other and are proportional to the Einstein A coefficient, $A_{u\ell}$, as:

$$g_\ell B_{\ell u} = g_u B_{u\ell}, \tag{2.25}$$

and

$$B_{u\ell} = \frac{c^2}{2h\nu_{u\ell}^3} A_{u\ell}. \tag{2.26}$$

Here, g_i represents the degeneracy of level i, and $\nu_{u\ell}$ is the resonance frequency for the two-level system. Using these relations, the absorption coefficient becomes:

$$\alpha_{u\ell} = \frac{c^2 n_u}{8\pi\nu_{u\ell}^2 \Delta\nu} \left\{ \exp\left(\frac{h\nu_{u\ell}}{k_B T}\right) - 1 \right\} A_{u\ell} \ , \tag{2.27}$$

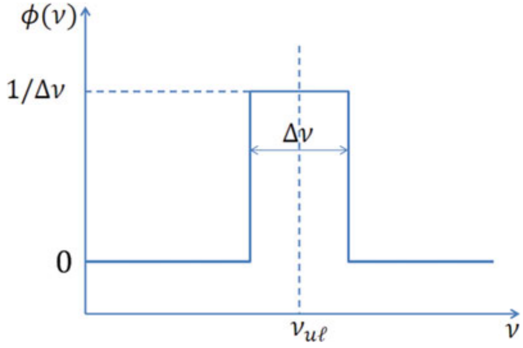

Fig. 2.3 Line profile function employed for simplicity. The line center frequency is $\nu_{u\ell}$, and the line width is $\Delta\nu$

where the Boltzmann distribution at a temperature T is assumed for the populations of level l and level u according to:

$$\frac{n_u}{n_\ell} = \frac{g_u}{g_\ell}\exp\left(-\frac{h\nu_{u\ell}}{k_B T}\right). \tag{2.28}$$

Here, the line profile function is approximated, as shown in Fig. 2.3:

$$\phi(\nu) = \frac{1}{\Delta\nu}, \tag{2.29}$$

where the line width, $\Delta\nu$, is assumed to be much smaller than $\nu_{u\ell}$. The Einstein A coefficient is written as:

$$A_{u\ell} = \frac{64\pi^4\nu_{u\ell}^3 S_{u\ell}\mu^2}{3hc^3 g_u}. \tag{2.30}$$

Here, $S_{u\ell}$ is the line strength, which is the square of the matrix elements for the direction cosines (Sect. 2.4.3), and μ is the dipole moment responsible for the transition. In the case of a linear (or diatomic) molecule, $S_{u\ell}$ equals $J+1$ for the transition $J+1 \leftrightarrow J$. These values are tabulated in spectral line databases for many molecules.

If a Boltzmann distribution at temperature T is assumed for the level population, the number of molecules in level u per unit volume can be written in terms of the total number of molecules, n:

$$n_u = \frac{g_u}{U(T)}n\exp\left(-\frac{E_u}{k_B T}\right), \tag{2.31}$$

where $U(T)$ is the partition function at temperature T, and E_u the upper-state energy. By combining Eqs. (2.27), (2.30), and (2.31), we obtain:

$$\alpha_{u\ell} = \frac{8\pi^3 \nu_{u\ell} S_{u\ell} \mu^2}{3hc\Delta\nu U(T)} n \left\{ \exp\left(\frac{h\nu_{u\ell}}{k_B T}\right) - 1 \right\} \exp\left(-\frac{E_u}{k_B T}\right). \tag{2.32}$$

The line width is usually represented in terms of a velocity width, rather than a frequency width, because the line width largely depends on the Doppler effect. The velocity width is defined as:

$$\Delta v = \frac{\Delta\nu}{\nu_{u\ell}} c. \tag{2.33}$$

Considering this relation, we finally obtain an expression for the optical depth as:

$$\tau_{u\ell} = \frac{8\pi^3 S_{u\ell} \mu^2}{3h\Delta v U(T)} \left\{ \exp\left(\frac{h\nu_{u\ell}}{k_B T}\right) - 1 \right\} \exp\left(-\frac{E_u}{k_B T}\right) N, \tag{2.34}$$

where N is the column density, $N = nL$. Apparently, the optical depth is proportional to the column density, the line strength, and the square of the dipole moment. Unless the depth of the cloud (L) along the line of sight is known, only the column density can be derived from observations.

In derivation of Eq. (2.34), the level population is assumed to be represented by the Boltzmann distribution at a temperature T to relate the population of the upper level to the total number of molecules. If this assumption is satisfied, the system is said to be in *local thermodynamic equilibrium* (LTE). For a rotational energy-level system, this temperature is called the rotation temperature.

The excitation temperature, T_{ex}, for the transition $u \rightarrow \ell$ can be determined by the populations of level l and level u using the following relation:

$$\frac{n_u g_\ell}{n_\ell g_u} = \exp\left(-\frac{h\nu}{k_B T_{ex}}\right), \tag{2.35}$$

In LTE conditions, the excitation temperature is the same as the rotation temperature. In interstellar clouds, molecules are excited and de-excited in collisions with H_2 molecules, although collisions with H atoms and electrons are also important in some cases. That is, the H_2 molecules form a heat bath. If the collisions are sufficiently frequent when compared with radiation probabilities, the rotation temperature is close to the kinetic temperature of H_2, and the LTE condition is satisfied. If the collisions are less frequent, cooling by radiation processes becomes more important. The level population then diverges from LTE and cannot be represented by a single Boltzmann distribution. In this case, the excitation temperature differs from transition to transition and is usually lower than the gas kinetic temperature. We describe this situation in Sect. 2.3.

2.2.3 Optically Thin Case: Rotation Diagram Analysis

When the optical depth of a spectral line is much lower than unity, we term the line as being optically thin. Because the optical depth is proportional to the column density and the line strength, optically thin generally refers to a low column density or low line strength. In this case, the intensity can be approximated by expanding the exponential function as:

$$\Delta T = \frac{h\nu_{u\ell}}{k_B}\left\{\frac{1}{\exp(h\nu_{u\ell}/k_BT)-1}-\frac{1}{\exp(h\nu_{u\ell}/k_BT_b)-1}\right\}\tau_{u\ell}. \tag{2.36}$$

Specifically, the intensity is proportional to the optical depth, and consequentially to the column density. The photons emitted in the cloud all escape without being absorbed in the cloud.

If we assume that $h\nu/k_BT \ll 1$ and $T \gg T_b$, we obtain at LTE:

$$\Delta T\Delta v = \frac{8\pi^3\nu_{u\ell}S_{u\ell}\mu^2}{3k_BU(T)}\exp\left(-\frac{E_u}{k_BT}\right)N. \tag{2.37}$$

This expression can be modified giving:

$$\ln\frac{3k_BW}{8\pi^3\nu_{u\ell}S_{u\ell}\mu^2} = \ln\frac{N}{U(T)}-\frac{E_u}{k_BT}, \tag{2.38}$$

where W is the integrated intensity. For the idealized box-shaped line profile function shown in Fig. 2.3, $W = \Delta T\Delta v$. If multiple transitions are observed for the same species, the observed values for the left-hand side can be plotted against the upper-state energy E_u. The relation should be linear if the LTE condition is satisfied. In this case, $1/\ k_BT$ is obtained from the slope, whereas $N/U(T)$ can be derived from the intercept. The column density is then evaluated by calculating the partition function at the derived temperature. This method is called the rotation diagram method and can be applied to derive the column density and rotation temperature for molecules in warm and dense clouds such as star-forming cores, where the assumptions required for this method are reasonably fulfilled. An example toward the low-mass protostar R CrA IRS7B is shown in Fig. 2.4 (Watanabe et al. 2012). In actual cases, the fit is sometimes not successful, because the observed cloud consists of multiple components with different physical conditions, and/or LTE does not apply. We stress that the rotation diagram method is not appropriate for cold clouds as LTE does not always hold. The non-LTE effect on the rotation diagram is discussed in detail by Goldsmith and Langer (1999).

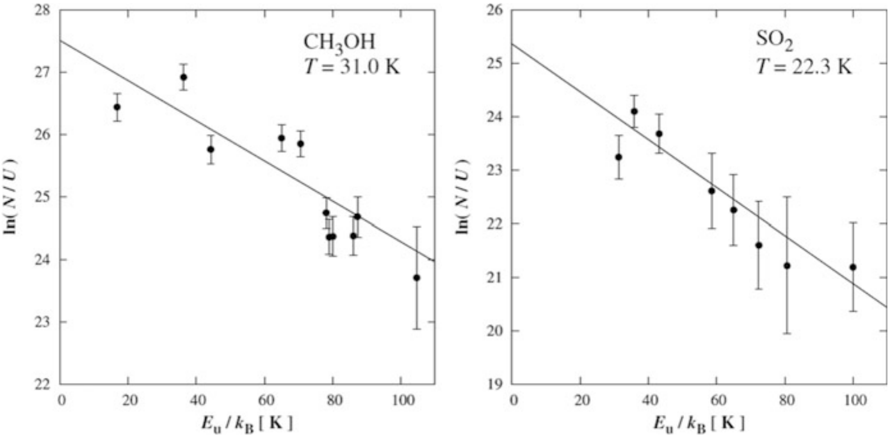

Fig. 2.4 Examples of rotation diagrams for the CH_3OH and SO_2 lines observed toward the low-mass protostar R CrA IRS7B (Reprinted with permission from Watanabe et al. (2012). Copyright 2012 American Astronomical Society)

2.2.4 *Optically Thick Case*

In contrast, the optical depth can often be much higher than unity for abundant species such as CO, HCN, and HCO^+. In this case, the line is said to be optically thick. Because the exponential part of Eq. (2.19) can be ignored for $\tau_\nu \gg 1$, the intensity is simply:

$$\Delta T = T, \tag{2.39}$$

assuming that $h\nu/k_B T \ll 1$ and $T \gg T_b$. That is, the observed temperature equals the excitation temperature. In the optically thick case, the photons emitted in the interior of the cloud are completely reabsorbed within the cloud, and the intensity is determined by the surface temperature. That is, within the line profile, the cloud behaves as a blackbody at the excitation temperature of the molecule, and the cloud surface can be regarded as a "photosphere." Hence, the column density cannot be derived from the optically thick line.

In this case, lines of rare isotopic species are observed in determining the column density of normal species. For instance, the abundances of ^{13}CO and $C^{18}O$ are lower than those of the normal species by factors of 1/59 and 1/560 in the local interstellar medium, respectively (Wilson and Rood 1994; Lucas and Liszt 1998). Hence, the optical depths of the ^{13}CO and $C^{18}O$ lines are lower than those of the normal species by 1/59 and 1/560, respectively. If the ^{13}CO line is optically thin, the column density of ^{13}CO can be obtained from the intensity of the ^{13}CO line. In this calculation, the excitation temperature obtained from the optically thick ^{12}CO line can be used. Then, the column density of the normal species is determined by multiplying by factor 59. However, the ^{13}CO line can often be optically thick in cold dense clouds. To determine the optical depth of the ^{13}CO line (τ_{13}), the C^{18}O line is employed. If the excitation temperatures of both species are assumed to be the same, we obtain the following relation for the integrated intensity ratio of the ^{13}CO and C^{18}O lines:

$$\frac{W(^{13}\mathrm{CO})}{W(\mathrm{C}^{18}\mathrm{O})} = \frac{1 - \exp(-\tau_{13})}{1 - \exp(-59\tau_{13}/560)}. \tag{2.40}$$

The τ_{13} value can be obtained by solving this equation, unless both the ^{13}CO and C^{18}O lines are optically thin. The excitation temperature is then derived from τ_{13} using Eq. (2.18). If the C^{18}O line is optically thick, rarer isotopic species such as C^{17}O and ^{13}C^{18}O are used. It should be noted that the same excitation temperature for different isotopic species is just an assumption. This condition may not be fulfilled for very high optical depths. To take into account such an effect, an excitation calculation for rotational levels is necessary (Sect. 2.3).

Note that the isotope ratio may depend on sources. It is known that the ratios depend on the distance from the center of our Galaxy (e.g., Millam et al. 2005). The isotope ratios can be different in the envelopes of evolved stars. An effect of isotope selective photodissociation (van Dishoeck and Black 1988; Warin et al. 1996; van Dishoeck and Visser 2015) would also change the ratios in translucent clouds (Sect. 3.7).

A similar technique is applicable to lines with hyperfine structure (Chap. 10). A good example is CCH. The lowest transition ($N = 1 - 0$) of this molecule is split into six fine and hyperfine components due to magnetic interactions of the electron spin ($S = 1/2$) and the nuclear spin of the hydrogen nucleus ($I = 1/2$). The line strengths of the components are listed in Table 2.1. Because the optical depth is proportional to the line strength, the intensities of hyperfine components should be proportional to their line strengths for the optically thin case, as long as a common excitation temperature can be applied. Figure 2.5 shows the CCH line observed in spectra toward low-mass star-forming regions (Sakai et al. 2009). The observed patterns differ significantly from those expected based on line strengths. Although the line strength ratio of the strongest component relative to the weakest component is 10, the corresponding intensity ratio (R) is apparently smaller than 10 for some sources, indicating that the strongest component is not optically thin. As in the case of the ^{13}CO and C^{18}O lines, the intensity ratio (R) is expressed in terms of the optical depth of the strongest component (τ_s):

Table 2.1 Frequencies of hyperfine components of CCH ($N = 1–0$)

Transition	Frequency (GHz)	Line strength
$J = 3/2–1/2, F = 1–1$	87.284156	0.17
$J = 3/2–1/2, F = 2–1$	87.316925	1.67
$J = 3/2–1/2, F = 1–0$	87.328624	0.83
$J = 1/2–1/2, F = 1–1$	87.402004	0.83
$J = 1/2–1/2, F = 0–1$	87.407165	0.33
$J = 1/2–1/2, F = 1–0$	87.446512	0.17

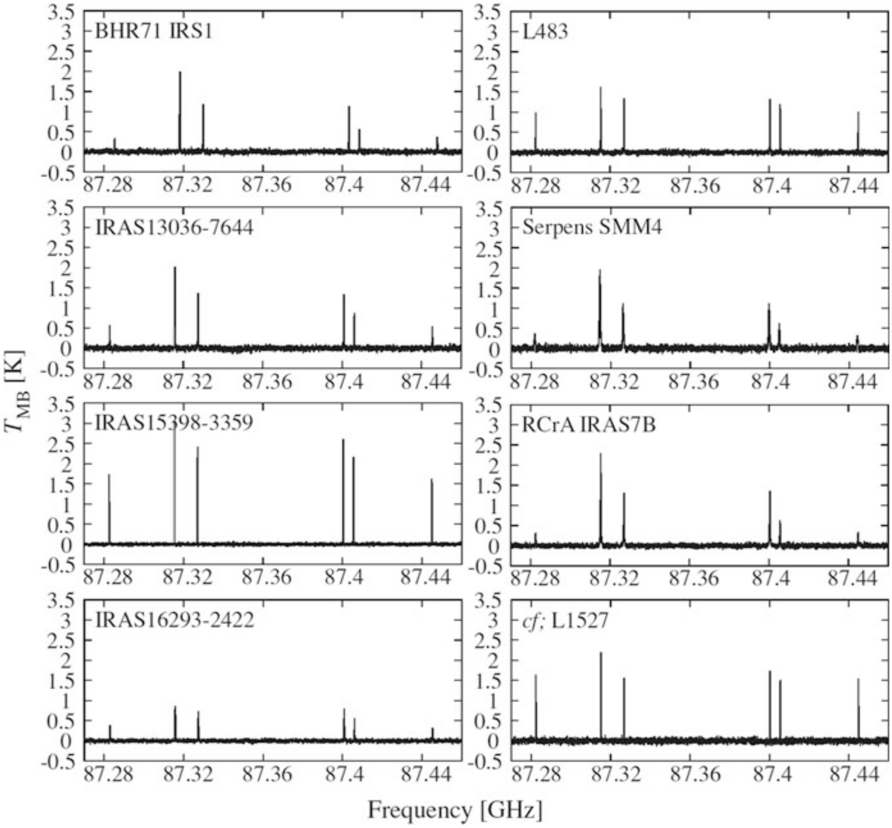

Fig. 2.5 The $N = 1{-}0$ transition of CCH toward various low-mass protostellar sources. The transition is split into six fine and hyperfine components by the magnetic interaction between the electron spin ($S = 1/2$) and the nuclear spin of the hydrogen nucleus ($I = 1/2$) as well as the electron-spin rotation interaction (Chap. 10). Line strengths of the components are given in Table 2.1. Spectral patterns differ from the pattern of the line strengths in some sources because of the optical depth effect (Reprinted with permission from Sakai et al. (2009). Copyright 2009 American Astronomical Society)

$$R = \frac{1 - \exp(-\tau_s)}{1 - \exp(-\tau_s/10)}, \tag{2.41}$$

where the same excitation temperature is assumed for both components. The optical depth τ_s is evaluated by solving this equation. Alternatively, it can be determined more accurately by fitting all of the hyperfine components simultaneously. Note that the same excitation temperature for all of the hyperfine components is just an assumption. Several authors have noted that excitation temperatures can vary among the hyperfine components. Such a "hyperfine anomaly" is indeed reported for HN_2^+ and DCO^+ (e.g., Caselli et al. 1995; van der Tak et al. 2009), although its effect on intensity is minimal.

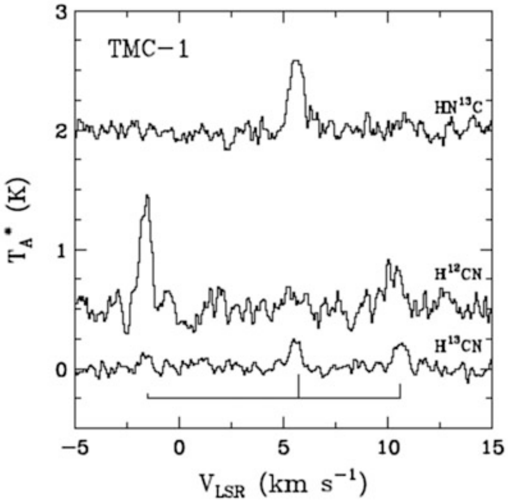

Fig. 2.6 Observed spectra of the $J = 1{-}0$ transition for HCN, $H^{13}CN$, and $HN^{13}C$ toward TMC-1 (CP). The HCN and $H^{13}CN$ lines are split into three hyperfine components due to the nuclear quadrupole interaction by the N nucleus ($I = 1$). The schematic appearing below the spectra indicate the line strengths of the hyperfine components. The strongest hyperfine component is missing for HCN, and the second strongest hyperfine component is observed only weakly, indicating significant self-absorption by foreground gas (Reprinted with permission from Hirota et al. (1998). Copyright 1998 American Astronomical Society)

An additional important issue for an optically thick line is absorption by foreground gas. In the above formulation, we simply assumed a homogeneous (isolated) cloud for simplicity. However, clouds often exist within structures, such as a dense cloud surrounded by a diffuse envelope. In this case, molecules in the diffuse envelope do not contribute to emission lines because of the low H_2 density (Sect. 2.3), but they absorb emission lines of the same species from a dense cloud. This situation occurs when molecules are also very abundant in a diffuse envelope. A good example is the $J = 1 - 0$ transition of HCN observed in the cold dense core of TMC-1 (cyanopolyyne peak; CP), as shown in Fig. 2.6 (Hirota et al. 1998). The $J = 1 - 0$ transition consists of three hyperfine components arising from the nuclear quadrupole interaction of the N nucleus ($I = 1$). The line strengths of the three components are also shown in Fig. 2.6. In TMC-1 (CP), the hyperfine component with the strongest line strength almost disappears, and the hyperfine component with the weakest line strength is the brightest. This observation cannot be explained by optical depth discussed above but is ascribed to absorption due to foreground gas. The hyperfine component with the weakest line strength also suffers from this effect to some extent but is smaller because of its weak line strength. For this reason, the HCN abundance in TMC-1 (CP) is derived from observations of $H^{13}CN$ (Hirota et al. 1998).

2.3 Mechanism Determining Excitation Temperature

The population of rotational levels is determined by a balance of excitation and de-excitation by collision with H_2 and absorption and emission of photons. For simplicity, we refer to the two-level system (Fig. 2.2) to consider the effect of these processes. A time derivative of the number of molecules in level *l* in a unit volume is represented as:

$$\frac{dn_\ell}{dt} = -B_{\ell u}B_\nu(T_b)n_\ell + B_{u\ell}B_\nu(T_b)n_u + A_{u\ell}n_u - C_{\ell u}n_\ell + C_{u\ell}n_u, \tag{2.42}$$

where $C_{\ell u}$ and $C_{u\ell}$ are the rate coefficients for collisional excitation and de-excitation processes. Although a similar equation describes level u, it is trivial because $n_\ell + n_\mathrm{u} = \mathrm{const}$. From the microbalance principle, $C_{\ell u}$ and $C_{u\ell}$ must satisfy:

$$g_\ell C_{\ell u} = g_u C_{u\ell}\exp\left(-\frac{h\nu}{k_B T_k}\right), \tag{2.43}$$

where T_k is the kinetic temperature of H_2. Using the relations between the Einstein coefficients (Eqs. (2.25) and (2.26)), Eq. (2.42) can be modified to give:

$$\frac{dn_\ell}{dt} = -\frac{A_{u\ell}\left(\frac{g_u}{g_\ell}n_\ell - n_u\right)}{\exp\left(\frac{h\nu}{k_B T_b}\right) - 1} + A_{u\ell}n_u + C_{u\ell}\left\{n_u - \frac{g_u}{g_\ell}n_\ell\exp\left(-\frac{h\nu}{k_B T_k}\right)\right\}. \tag{2.44}$$

In the steady state, the right-hand side is set to zero. Hence, we obtain:

$$\frac{n_u g_\ell}{n_\ell g_u} = \frac{A_{u\ell}\left\{\exp\left(\frac{h\nu}{k_B T_b}\right) - 1\right\}^{-1} + C_{u\ell}\exp\left(-\frac{h\nu}{k_B T_k}\right)}{A_{u\ell}\exp\left(\frac{h\nu}{k_B T_b}\right)\left\{\exp\left(\frac{h\nu}{k_B T_b}\right) - 1\right\}^{-1} + C_{u\ell}}. \tag{2.45}$$

Here, $C_{u\ell}$ is related to the H_2 density:

$$C_{u\ell} = n(\mathrm{H}_2)\sigma < v >, \tag{2.46}$$

where $<\nu>$ is the mean relative velocity between the molecule and the H_2 molecule and σ is the cross section for collisional de-excitation. Physical backgrounds for $<\nu>$ and σ are described in Sect. 3.1. The excitation temperature can be obtained by using Eqs. (2.35) and (2.45).

If the H_2 density is very high, the terms including $C_{u\ell}$ become dominant in comparison with the terms including $A_{u\ell}$. In this limit, the above relation can be approximated to give:

$$\frac{n_u g_\ell}{n_\ell g_u} \cong \exp\left(-\frac{h\nu}{k_B T_k}\right). \tag{2.47}$$

Hence, the excitation temperature equals the kinetic temperature of H_2, T_k. In contrast, the terms including $A_{u\ell}$ become dominant for the low H_2 density limit. In this case, Eq. (2.45) can be approximated as:

$$\frac{n_u g_\ell}{n_\ell g_u} \cong \exp\left(-\frac{h\nu}{k_B T_b}\right). \tag{2.48}$$

Then, the excitation temperature equals the cosmic background temperature. That is, the level population is thermalized through collisions with H_2 for the high-density case; the level population is thermalized by the cosmic microwave background radiation for the low H_2 density case. For intermediate H_2 densities, the level population is determined by the balance between collisional and radiation processes. Figure 2.7 schematically shows the excitation temperature as a function of H_2 density.

As shown in Eq. (2.17), the excitation temperature needs to be much higher than the cosmic microwave background temperature for a strong emission to be observed. Specifically, the upper level has to be well populated from frequent collisions with H_2 against de-excitation by radiation. The H_2 density necessary for a significant population in the upper level can roughly be estimated by equilibrating the emission rate and the collision rate:

$$A_{u\ell} = C_{u\ell}. \tag{2.49}$$

Hence, the required H_2 density, $n_{\rm cr}$, is given as:

Fig. 2.7 Schematic of the H_2 density dependence of the excitation temperature calculated using Eqs. (2.45) and (2.35). At low H_2 densities, the excitation temperature is the same as the cosmic microwave background temperature. In the high-density limit, the excitation temperature approaches the kinetic temperature of H_2. $n_{\rm cr}$ indicates the critical density

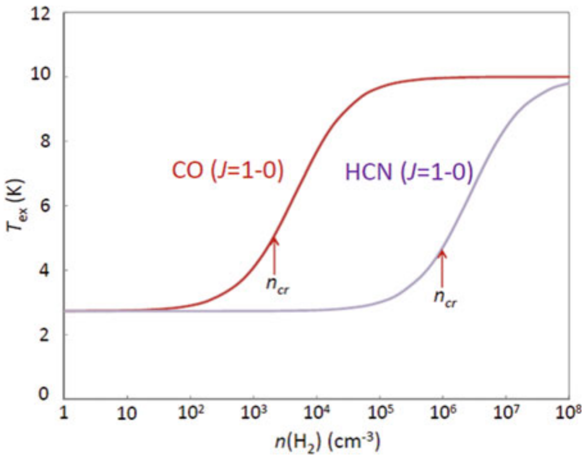

$$n_{\mathrm{cr}} = \frac{A_{u\ell}}{\sigma < v >}. \tag{2.50}$$

This H_2 density is called the critical density for the transition. Note that it is just an order-of-magnitude estimate of the H_2 density required for producing an emission line for the two-level system. The collisional rate coefficient defined as $\sigma < v>$ is typically of the order of 10^{-11} cm^3 s^{-1} (see Chap. 3). The Einstein A coefficient is proportional to the cube of the frequency and the square of the transition dipole moment (Eq. (2.30)). For example, the dipole moments of CO and HCN are 0.110 D and 2.99 D, respectively, and hence the Einstein A coefficients of their $J = 1 - 0$ transitions at 115.27 GHz and 88.63 GHz are 7.19×10^{-8} s^{-1} and 2.41×10^{-5} s^{-1}, respectively. Using these values, the critical densities for the CO ($J = 1 - 0$) and HCN ($J = 1 - 0$) transitions are evaluated to be 2×10^3 cm^{-3} and 1×10^6 cm^{-3}, respectively, where the collisional rate coefficients of 3.3×10^{-11} cm^3 s^{-1} and 2.4×10^{-11} cm^3 s^{-1} at 10 K are employed, respectively (see the databases for collisional cross sections: Leiden Atomic and Molecular Database (LAMDA), Schoier et al. 2005: Ro-vibrational Collisional Excitation Database and Utilities (BASECOL), Dubernet et al. 2013). As a result, CO ($J = 1 - 0$) emission can arise even from less-dense regions; such emission is useful for delineating the large-scale structure of molecular clouds. In contrast, the HCN ($J = 1 - 0$) line preferentially traces dense parts of molecular clouds, called dense cores. As seen in the strong frequency dependence of the Einstein A coefficient, submillimeter-wave lines, which usually have higher critical densities than millimeter-wave lines, are employed to trace the densest parts of molecular clouds such as star-forming cores.

The above discussion for the two-level system can be extended to multilevel systems. In this case, a set of rate equations similar to Eq. (2.42) is solved to determine level populations, from which the excitation temperature and the optical depth for each transition are evaluated. The line intensity can then be calculated using Eq. (2.18). The excitation temperatures can be different for different transitions in the intermediate H_2 density case, which corresponds to the non-LTE condition.

For such excitation calculations, state-to-state collisional rate coefficients are necessary. These coefficients are evaluated using the intermolecular potential function between the molecule and the H_2 molecule evaluated from quantum chemical calculations. It should be noted that they are sometimes derived by using the potential function between the molecule and the He atom for simplicity (i.e., no anisotoropy for He). For simple molecules, these coefficients have been tabulated in the database shown above. However, the coefficients are not always available for less common molecules and molecules with fine and hyperfine splitting. In this case, the collisional rate coefficients for a similar-sized molecule are often employed. It should be noted, however, that the collisional rate coefficients are significantly different even for HCN and HNC (Dumonchel et al. 2010). More data are apparently necessary to compile databases of collisional cross sections of various molecules.

Sometimes the level population of a certain two-level system is inverted, that is, the left-hand side of Eq. (2.45) is larger than unity. In this case, both the optical depth and the excitation temperature become negative, and hence the background radiation is exponentially amplified in a cloud due to stimulated emission, resulting in very bright line emission. This phenomenon caused by population inversion is known as a microwave amplification of stimulated emission of radiation (MASER), which is the microwave version of a light amplification of stimulated emission of radiation (LASER). Such population inversion typically occurs in a limited range of physical conditions, and hence maser emission originates from a small region. Nevertheless, maser emission is generally bright because of its exponential amplification. Interstellar maser emission has been observed for particular lines of OH, H_2CO, CH_3OH, SiO (vibrationally excited states), H_2O, and others (Elitzur 1992a, b).

For abundant molecules, the optical depth of the line in a certain volume of a cloud becomes higher than unity. In this case, a photon emitted from that volume is reabsorbed within the same volume. This process results in a smaller effective Einstein A coefficient. This effect is called radiation trapping. The level population has to be calculated by considering this effect. If the radiation emitted from that volume is not absorbed in other regions of the cloud, the effect of radiation trapping can readily be calculated. This situation is realized, for instance, if a cloud has a large velocity gradient (LVG) due to infall (or expansion). In such a case, the radiation is not absorbed in the other regions of the cloud because of velocity differences. This situation is referred to as the LVG model (Goldreich and Kwan 1974; Castor 1970). In this case, the modified Einstein A coefficient for a spherical cloud is given as:

$$A'_{u\ell} = \frac{1 - \exp(-\tau_{u\ell})}{\tau_{u\ell}} A_{u\ell}, \tag{2.51}$$

Although the assumption for the LVG model does not always hold true in actual clouds, it is frequently employed as the simplest model to derive the excitation temperature and the optical depth of emission lines. More sophisticated treatments are given in the literature (de Jong et al. 1975; de Jong et al. 1980; Guilloteau et al. 1981).

2.4 Practical Issues for Deriving Molecular Abundances

2.4.1 Source Structure

The above formulation contains various assumptions. First of all, the cloud is assumed to be homogeneous in physical and chemical conditions along a line of sight. In reality, physical conditions and molecular abundances vary within a cloud. For instance, H_2 density will be lower at the periphery of the cloud. Furthermore, molecular abundances will also vary within a cloud because of different chemical processes in different cloud regions. For example, some molecules are abundant in dense regions; other molecules are abundant in the periphery. Observations trace the emission integrated over these effects along a line of sight.

This situation is further complicated by the limited spatial resolution of telescopes. If the source size is smaller than the telescope resolution (beam size), the observed emission is significantly diluted. For instance, we consider a circular source with a diameter of θ_s with a uniform surface brightness on the celestial sphere. If this source is observed with a Gaussian beam with a full-width at half maximum (FWHM) beam size of θ_b, the observed intensity becomes weaker by a factor of:

$$1 - \exp\left(-\frac{1.44\theta_s^2}{\theta_b^2}\right). \tag{2.52}$$

If the surface brightness distribution is represented by a Gaussian function with an FWHM width of θ_s, the intensity becomes weaker by a factor of:

$$\frac{\theta_s^2}{\theta_s^2 + \theta_b^2}. \tag{2.53}$$

The decrease in the intensity is called the beam dilution effect. The limited resolution causes an additional problem when we employ the intensity data observed with different beam sizes. The beam size of a telescope depends on the observed frequency (Chap. 11). Hence, we have to be careful when the intensities of two or more lines observed at different frequencies are used to derive the column densities and excitation temperatures. If the source size is comparable to or smaller than the beam size, the correction for the beam dilution effect is very important so as not to introduce systematic error into the interpretation of the data.

Moreover, the source structure can be different for different lines of sight. If the cloud has an internal structure whose size is smaller than the telescope resolution (beam size), the observing emission is "beam averaged." If the molecular abundances vary among small-scale structures, the derived column density is also "beam averaged."

Fractional abundances are typically derived relative to the H_2 molecule for comparison with chemical models. In this case, the observed column density has to be divided by the H_2 column density observed with the same beam size. Because we cannot directly observe the H_2 molecule in interstellar clouds as it lacks electric dipole-allowed transitions in the radio and infrared regimes, the H_2 column density is derived from observations of rare isotopic species lines of CO such as $C^{18}O$ by assuming a relative abundance. However, it is known that CO is depleted onto dust grains in cold and dense parts of clouds, as described in Chap. 6. Hence, the H_2 column density derived from the rare isotopic species lines of CO would be underestimated. Furthermore, the critical densities of the CO lines are lower than those of other molecular lines, and hence CO emission tends to trace longer distances along the line of sight than the other molecular lines.

Instead of CO, the millimeter-wave and submillimeter-wave continuum emission of dust grains is often used to derive the H_2 column density. In this case, we need to assume the emissivity of dust grains and the gas-to-dust ratio (about 100). In any case, we have to consider that the H_2 column density and temperature are again beam averaged. Hence, the derived fractional abundances are also beam-averaged values. If the source is expected to have internal structure unresolved with the telescope beam, we have to be careful in interpreting the abundances.

2.4.2 Forward and Backward Approaches

The above method deriving the column density (or the fractional abundance relative to H_2) from the observed intensity is regarded as a backward approach, tracing back from the observational result to the origin of emission. Then, the observed column densities or the abundances are compared with those of other sources and chemical model calculations. This method is a conventional technique used in astrochemistry, and also in radio astronomy. As discussed in the previous section, various assumptions are used in this approach. However, observations with higher spatial resolution would improve the situation by tracing a particular region of the cloud with higher uniformity.

An alternative approach is possible if the physical and chemical structures of a source are well established or can be reasonably assumed. Protostellar cores, protoplanetary disks, and late-type stars are typical examples for which the physical structure is relatively well known. In these cases, the expected emission, including the velocity structure convolved with the telescope beam size, can be calculated based on the source model by numerically integrating the radiative transfer equation, where the excitation temperature and optical depth are evaluated from position to position by solving a set of rate equations. A Monte Carlo method is sometimes employed for more precise calculations. Such a method can be regarded as a forward approach, in contrast to the conventional backward approach. The forward approach has gradually become popular in astrochemical studies (e.g., Maret et al. 2005; Shoier et al. 2002; Zernickel et al. 2012). By comparing results of the radiative transfer calculation with observed intensities, the initial model parameters can be optimized. A reasonable physical and chemical model and an appropriate choice of model parameters are essential for success using this forward approach. That is, observations with higher spatial resolution will be very useful for constraining the model and its parameters.

2.4.3 Molecular Parameters

In deriving molecular abundances, we use various molecular parameters such as rest frequencies, dipole moments, line strengths, upper-state (or lower-state) energies, Einstein coefficients, partition functions, and state-to-state collisional rate coefficients. These parameters are usually tabulated in databases (e.g., CDMS, LAMDA, BACECOL) and/or in the literature. In using these parameters, it is necessary to pay attention to the following points.

1. *Consistency between line strengths and partition functions*

The rotational transition is allowed in molecules with a permanent electric dipole moment. The space-fixed component of the dipole moment interacts with the electric field of the electromagnetic wave and can be written in terms of the direction cosines between molecular-fixed components of the dipole moment and the electric field. Provided that the electric field is along the z axis, which is perpendicular to the line of sight, the space-fixed component of the dipole moment is:

$$\mu_Z = \mu_a \Phi_{aZ} + \mu_b \Phi_{bZ} + \mu_c \Phi_{cZ}, \tag{2.54}$$

where μ_k ($k = a, b, c$) represents the k axis component of the dipole moment with respect to the molecule-fixed axes and Φ_{kZ} ($k = a, b, c$) the direction cosine between the k axis and the z axis. We refer the reader to Chap. 10 for a definition of the molecule-fixed axes. Similar relations hold for μ_X and μ_Y. The line strength is defined as:

$$S_{ij} = \sum_{g=X,Y,Z} \sum_{MM'} \left\{ \int \psi^*_{iM'} \Phi_{kg} \psi_{jM} d\tau \right\}^2 \tag{2.55}$$

(Gordy and Cook 1984). Here, k depends on which component (a, b or c) of the dipole moment is responsible for the transition. ψ_{iM} and ψ_{jM} are the rotational eigenfunctions associated with the levels i and j that are involved in the transition, respectively. The subscript M denotes the magnetic quantum number along the z axis for the total angular momentum J. In the absence of external electric and magnetic fields, the $(2J+1)$ magnetic sublevels are degenerate. The $\Delta M=0$ selection rule holds for the transition for μ_Z, whereas the $\Delta M = \pm 1$ selection rule holds for the transition for $\mu_X \pm i\mu_Y$. After summing up these contributions, S_{ij} is obtained.

As seen in the above definition, S_{ij} depends on the wave functions that are considered. For example, we consider the HCN molecule and its $J = 1-0$ rotational transition. This transition is split into the three hyperfine components $F = 2-1$, $1-1$, and $0-1$ arising from the nuclear quadrupole interaction of the N nucleus ($I = 1$), where F is the quantum number of the total angular momentum (Chap. 10). Their line strengths S_{ij} are 1.667, 1.000, and 0.333, respectively, where the wave functions considering the hyperfine interaction are used. When these line intensities are employed for Eqs. (2.34, 2.37, and 2.38), the partition function has to be calculated by considering the hyperfine levels and their degeneracy $(2F+1)$ using its fundamental definition:

$$U(T) = \sum_m g_m \exp\left(-\frac{E_m}{k_B T}\right), \tag{2.56}$$

where E_m and g_m are the energy and the degeneracy of the m state, respectively. However, these hyperfine components are sometimes blended with one another because of large line broadening due to turbulent motions of a celestial source. In this case, it is not necessary to consider the hyperfine components. The line intensity of the $J = 1{-}0$ transition of 1.000 can be used, which is based on the rotational wave functions without considering the hyperfine interaction. The partition function then has to be calculated without taking into account the hyperfine splitting. Above all, consistent use of S_{ij} and the partition function is mandatory. For S_{ij} values listed in the literature or databases, it is necessary to be careful with their definitions, in particular, the level of degeneracy that is considered. For instance, the line strengths for the K structure lines of a symmetric-top molecule (CH_3CN, CH_3CCH, NH_3, etc.) sometimes include the $\pm K$ degeneracy giving a factor of 2. In these cases, the partition function has to be calculated accordingly.

2. *Treatment of the ortho and para species*

If a molecule has two or more equivalent nuclei with nonzero nuclear spins, particular nuclear-spin functions couple to particular rotational levels. Consider the H_2 molecule, as the simplest case. Four nuclear-spin functions are classified into the following two groups according to 180° rotation about the rotation axis. The symmetric functions are:

$$\alpha\alpha,\ \ \beta\beta,\ \ \frac{1}{\sqrt{2}}(\alpha\beta + \beta\alpha), \tag{2.57}$$

and the asymmetric function is:

$$\frac{1}{\sqrt{2}}(\alpha\beta - \beta\alpha). \tag{2.58}$$

Here, α and β are two nuclear spin states for the hydrogen nucleus ($I = 1/2$). However, the rotational wave function for the even J state is symmetric with respect to 180°rotation about the rotation axis, which for the odd J state is asymmetric. Because the hydrogen nucleus is a fermion, the total wave function, which is the product of the nuclear spin function and the rotational wave function, must change sign when subject to a 180° rotation about the rotation axis (i.e., an exchange of the two hydrogen nuclei). Hence, the odd J state is coupled to the symmetric nuclear-spin function, and the even J state is coupled to the asymmetric nuclear-spin functions. The nuclear spin degeneracy is thus 3 and 1 for odd and even J, respectively. The higher degeneracy state is referred to as ortho; the lower degeneracy state as para. Hence, the odd and even J states are called the ortho and para species, respectively. Because the interconversion between the ortho and para

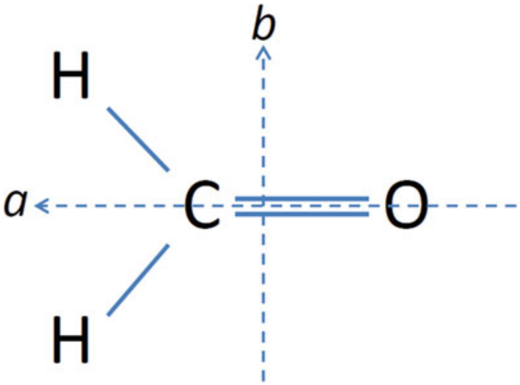

Fig. 2.8 Formaldehyde (H_2CO) molecule. The rotational wave function is represented in the form $\psi = \varphi(\theta,\chi)e^{iK_a\phi}$, where θ, ϕ, and χ are Euler angles. The rotation angle about the *a* axis is represented by ϕ. Hence, the rotation symmetry about the *a* axis only depends on the projected quantum number K_a

species via radiation and collision processes is generally very slow, these species behave as different molecules in interstellar conditions.

Similarly, the H_2CO molecule (Fig. 2.8) consists of ortho and para species because this molecule has two identical hydrogen nuclei ($I = 1/2$), just as for the H_2 molecule. The symmetric and asymmetric nuclear-spin functions couple to the rotational levels with $K_a =$ odd and even, respectively, to satisfy Fermi statistics. Here, K_a is a projected quantum number on the *a* axis (along the CO bond). Hence, the $K_a =$ odd and even states are ortho and para species with different nuclear spin degeneracies of 3 and 1, respectively. If these nuclear degeneracies are applied to the line strengths of the ortho and para states, the partition function has to be calculated based on the same assumption, as discussed in the previous subsection. Another practical method is to treat the ortho and para species as different molecules and to derive their column densities separately. The total column density is obtained as the sum of these two column densities; the ortho-to-para ratio can be obtained by their ratio. It is known that the ortho-to-para ratio is sometimes different from the statistical values in interstellar clouds (e.g. Kahane et al. 1984; Jorgensen et al. 2005; Mangum and Wootten 1993; Hogerheijde et al. 2011). Some conversion mechanisms between the ortho and para species have been proposed, such as conversion on dust grains, reactions with H or H^+, and mixing of the ortho and para species by nuclear spin–rotation interactions or electron spin–rotation interactions, but how these conversion mechanisms are effective is still controversial.

3. *Calculation of partition function*

The partition function should be calculated using Eq. (2.56). The summation can be terminated appropriately by looking at convergence. The classical expressions of the partition functions are known as:

$$U(T) = \frac{k_B T}{hB} \tag{2.59}$$

for diatomic or linear molecules, and

$$U(T) = \sqrt{\pi}\left(\frac{k_B T}{hA}\right)^{1/2}\left(\frac{k_B T}{hB}\right)^{1/2}\left(\frac{k_B T}{hC}\right)^{1/2} \tag{2.60}$$

for nonlinear molecules, where A, B, and C are the rotational constants about the a, b, and c axes of the molecule (Chap. 10). However, Eqs. (2.59) and (2.60) may be used only for high-temperature sources, where $hB/k_B T \ll 1$; they are not appropriate for cold clouds.

In calculating the partition function, the energies and degeneracy of the discrete levels are required. Sometimes, the lowest level does not have zero energy in databases of molecular energy levels. Even in this case, the partition function can be calculated using these energy levels. Then, the upper state energy used for Eqs. (2.34), (2.37), and (2.38) has to be taken from the same database. As seen in Eqs. (2.32) and (2.34), an energy offset of the lowest level is compensated for in the partition function and upper-state energies. For instance, the lowest level of the ortho species of H_2CO (the 1_{11} level) is above that of the para species (the 0_{00} level). When the ortho and para species are treated separately, the partition function for the ortho H_2CO molecule can be calculated without considering this nonzero lowest energy, as long as the upper-state energies are taken accordingly.

Problems

2.1 Consider an electromagnetic wave (rays) traveling in free space. Assume two small areas, dS_1 and dS_2, normal to the beam, which are separated by a distance R. By using the definition of intensity given in Eq. (2.5), show that the intensity at dS_1 is equal to the intensity at dS_2.

2.2 Show that the Planck function monotonically increases as a function of temperature for a given frequency, meaning that any two curves of the Planck function with different temperatures do not cross. If such a crossing occurred, what contradiction in thermodynamics would be expected?

2.3 The peak intensities of the ^{13}CO ($J = 1-0$) and $C^{18}O$ ($J = 1-0$) lines toward a certain source are observed to be 3.0 K and 1.0 K, respectively, with no difference in line widths. Evaluate the optical depth of the both lines as well as the common excitation temperature.

2.4 Consider the effect of the line profile function.

(a) Show that Eq. (2.38) holds for any line profile function.

(b) For a Gaussian profile with a FWHM line width of Δv_G and a peak intensity of ΔT_G, show that the integrated intensity W is given as $W = 1.064\Delta v_G \Delta T_G$. Note that

$$\int_{-\infty}^{\infty} \exp(-x^2)\,dx = \sqrt{\pi}.$$

2.5 H_2O has ortho and para states, because it has two identical H nuclei ($I = 1/2$). The lowest ortho transition is 1_{10}-1_{01} at 556.94 GHz, where the rotational state is designated by $J_{K_aK_c}$ (Chap. 10). For this transition, the line strength and the upper-state degeneracy without nuclear-spin degeneracy are 1.5 and 3, respectively. The dipole moment is 1.94 D. Based on these data, calculate the Einstein A coefficient for the 1_{10}-1_{01} transition. Using this result with the downward collisional cross section for this transition of 4.8×10^{-11} cm^3 s^{-1} at 100 K, evaluate the critical density of this transition at 100 K.

2.6 Show that the optical depth and the excitation temperature are both negative when population inversion occurs, namely,

$$\frac{n_u g_\ell}{n_\ell g_u} > 1.$$

2.7 Derive the classical expression of the partition function for a diatomic (or a linear) molecule, whose rotational energy is given as:

$$E_J = hBJ(J+1).$$

(a) Write down the partition function for a diatomic molecule using Eq. (2.56).
(b) Approximate the summation in the partition function by an integral, and show that the partition function is Eq. (2.59).
(c) Under what circumstances does the approximation used in (b) work well?

2.8 Consider a D_2CO molecule. This molecule has two identical deuterium nuclei ($I = 1$). Hence, 9 (=3 × 3) spin states are available.

(a) Classify these 9 spin states according to the symmetry of the 180° rotation about the *a* axis (along the CO bond). (Hint: refer to Eqs. (2.57) and (2.58).)
(b) The deuterium nucleus is a boson, and hence the total wave function has to be symmetric with respect to the exchange of two deuterium nuclei. Considering that the K_a = even and odd levels are symmetric and asymmetric with respect to 180° rotation about the *a* axis, derive the nuclear-spin degeneracy for the K_a = even and odd levels. Which is the ortho state?

References

P. Caselli, P.C. Myers, P. Thaddeus, Astrophys. J. **455**, L77 (1995)
J.I. Castor, Mon. Not. R. Astr. Soc. **149**, 111 (1970)
T. de Jong, S.-I. Chu, D. A., Astrophys. J. **199**, 69 (1975)
T. de Jong, A. Dalgarno, W. Boland, Astron. Astrophys. **91**, 68 (1980)
M.-L. Dubernet et al., Astron. Astrophys. **553**, A50 (2013)
F. Dumonchel, A. Faure, F. Lique, Mon. Not. R. Astron. Soc. **406**, 2488 (2010)
M. Elitzur, *Astronomical Masers* (Springer, Dordrecht, 1992a)
M. Elitzur, Ann. Rev. Astron. Astrophys. **30**, 75 (1992b)

P. Goldreich, J. Kwan, Astrophys. J. **189**, 441 (1974)

P.F. Goldsmith, W.D. Langer, Astroophys. J. **517**, 209 (1999)

W. Gordy, R.L. Cook, *Microwave Molecular Spectra* (Wiley, New York, 1984)

S. Guilloteau, R. Lucas, A. Omont, Astron. Astrophys. **97**, 347 (1981)

T. Hirota, S. Yamamoto, H. Mikami, M. Ohishi, Astrophys. J. **503**, 717 (1998)

M.R. Hogerheijde et al., Science **334**, 338 (2011)

J.K. Jorgensen, F.L. Schoier, E.F. van Dishoeck, Astron. Astrophys. **437**, 501 (2005)

C. Kahane, M.A. Frerking, W.D. Langer, P. Encrenaz, R. Lucas, Astron. Astrophys. **137**, 211 (1984)

G. Kirchhoff, Phil. Mag. **20**, 1 (1860)

R. Lucas, H. Liszt, Astron. Astrophys. **337**, 246 (1998)

J.G. Mangum, A. Wootten, Astrophys. J. Suppl. **89**, 123 (1993)

S. Maret, C. Ceccarelli, A.G.G.M. Tielens, E. Caux, B. Lefloch, A. Faure, A. Castets, D.R. Flower, Astron. Astrophys. **442**, 527 (2005)

S.N. Millam, C. Savage, M.A. Brewster, L.M. Ziurys, Astrophys. J. **634**, 1126 (2005)

M. Planck, Ann. d. Phys. **4**, 553 (1901)

N. Sakai, T. Sakai, T. Hirota, M. Burton, S. Yamamoto, Astrophys. J. **697**, 769 (2009)

F.L. Schoier, F.F.S. van der Tak, E.F. van Dishoeck, J.H. Black, Astron. Astrophys. **432**, 369 (2005)

F.L. Shoier, J.K. Jorgensen, E.F. van Dishoeck, G.A. Blake, Astron. Astrophys. **390**, 1001 (2002)

F.F.S. van der Tak, H.S.P. Muller, M.E. Harding, J. Gauss, Astron. Astrophys. **507**, 347 (2009)

E.F. van Dishoeck, J.H. Black, Astrophys. J. **334**, 771 (1988)

E.F. van Dishoeck, R. Visser, in *Laboratory Astrochemistry: From Molecules through Nanoparticles to Grains*, ed by S. Schlemmer, T. Giesen, H. Mutschke, C. Jager. (Willy-VCH, Weinheim, 2015)

S. Warin, J.J. Benayoun, Y.P. Viala, Astron. Astrophys. **308**, 535 (1996)

Y. Watanabe, N. Sakai, J.E. Lindberg, J.K. Jorgensen, S.E. Bisschop, S. Yamamoto, Astrophys. J. **745**, 126 (2012)

T.L. Wilson, R. Rood, Ann. Rev. Astron. Astrophys. **32**, 191 (1994)

A. Zernickel, P. Schilke, A. Schmiedeke, D.C. Lis, C.L. Brogan, C. Ceccarelli, C. Comito, M. Emprechtinger, T.R. Hunter, T. Moller, Astron. Astrophys. **546**, A87 (2012)

Chapter 3
Basic Concepts for Gas-Phase Chemical Reactions

3.1 Chemical Reactions: Macroscopic and Microscopic Viewpoints

This section defines the rate equation for a chemical reaction, which will be used throughout this book. For a binary reaction,

$$\mathrm{A} + \mathrm{B} \rightarrow \mathrm{C} + \mathrm{D}, \tag{3.1}$$

there are two different possible viewpoints, macroscopic and microscopic. In the former, we say that a certain number of "A" molecules react with the same number of "B" molecules to yield the same numbers of "C" and "D" molecules. To characterize the rate of this chemical reaction quantitatively, we define the number density of molecule X in a unit volume (cm^{-3}) as [X], which is called the abundance of X. If the above chemical reaction proceeds in a closed system, the abundances of A and B will decrease. The decrease in [A] in a time *dt*, which is the same as the decrease in [B] in a time *dt*, should be proportional to their product at that time. Hence, the rate equation

$$\frac{d[\mathrm{A}]}{dt} = \frac{d[\mathrm{B}]}{dt} = -k[\mathrm{A}][\mathrm{B}] \tag{3.2}$$

holds, where the proportionality coefficient k is a constant called the reaction rate coefficient. This constant is typically measured in cubic centimeters per second ($\mathrm{cm}^3\ \mathrm{s}^{-1}$). The abundances of the product molecules, C and D, increase as the chemical reaction proceeds:

$$\frac{d[\mathrm{C}]}{dt} = \frac{d[\mathrm{D}]}{dt} = k[\mathrm{A}][\mathrm{B}], \tag{3.3}$$

S. Yamamoto, *Introduction to Astrochemistry*, Astronomy and Astrophysics Library 7, DOI 10.1007/978-4-431-54171-4_3

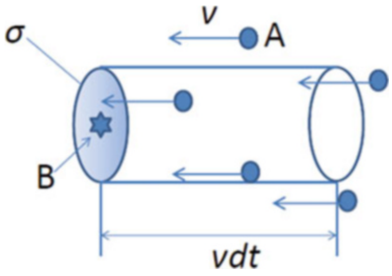

Fig. 3.1 Molecule A collides with target molecule B (*star*) with cross-section σ

where the reaction rate coefficient is the same as that for Eq. (3.2). For a larger k, the reaction proceeds more quickly. Reaction rate coefficients are measured in the laboratory for various reactions by, for instance, measuring the temporal change in [A] under constant [B] at a given temperature T. Reaction rate coefficients are generally temperature dependent.

The chemical reaction (3.1) can alternatively be interpreted as molecule A approaching and colliding with molecule B in free space. During the collision, the chemical bonds are rearranged, producing the final product molecules, C and D. In this microscopic view, the chemical reaction is a collision problem at least initially, and the cross-section σ (cm^{-2}) for the reaction can hence be defined. This cross-section equals the collisional cross-section, if the reaction occurs for every collision. If the reaction occurs with a certain probability, the collisional cross-section should be multiplied by the efficiency to obtain the reaction cross-section.

The reaction rate coefficient k and the reaction cross-section σ are related. Provided that the relative velocity between molecule A and molecule B is ν, molecule A moves νdt relative to molecule B in an infinitesimal time of dt. As shown in Fig. 3.1, a volume of $\sigma\nu dt$ of molecule A will pass through the cross-section for target molecule B. Hence, the number of A molecules reacting with each B molecule is expressed as $[\mathrm{A}]\sigma\nu dt$. Because a unit volume contains B molecules with a density of [B], a decrease in the abundance of B molecules, $-d[\mathrm{B}]$, in the reaction can be written as:

$$-d[\mathrm{B}] = [\mathrm{A}][\mathrm{B}]\sigma\nu dt. \tag{3.4}$$

Comparing this relation with Eq. (3.2), we obtain:

$$k = \sigma\nu. \tag{3.5}$$

Note that σ is generally a function of ν, depending on the interaction potential between molecules A and B, as will be described in later sections.

In thermal equilibrium at T, the distribution of the relative speeds obeys the Maxwell–Boltzmann distribution:

$$f(\nu,T)d\nu = 4\pi\nu^2\left(\frac{\mu}{2\pi k_B T}\right)^{3/2}\exp\left(-\frac{\mu\nu^2}{2k_B T}\right)\,d\nu, \tag{3.6}$$

where k_B is Boltzmann constant. The reduced mass between A and B, μ, is represented by the masses of A and B, m_A and m_B, respectively:

$$\mu = \frac{m_A m_B}{m_A + m_B}. \tag{3.7}$$

Hence, the reaction rate at T is expressed as:

$$k(T) = 4\pi \left(\frac{\mu}{2\pi k_B T} \right)^{3/2} \int_0^\infty \sigma(\nu)\nu^3 \exp\left(-\frac{\mu \nu^2}{2k_B T} \right) d\nu. \tag{3.8}$$

If σ is independent of ν, we obtain:

$$k(T) = \sigma \left(\frac{8k_B T}{\pi\mu} \right)^{\frac{1}{2}}. \tag{3.9}$$

In this case, the reaction rate coefficient is just the product of σ and the average relative velocity $<\nu>$ at T:

$$< \nu >= \left(\frac{8k_\mathrm{B} T}{\pi\mu} \right)^{\frac{1}{2}}. \tag{3.10}$$

Note that products of a reaction are not always unique. For instance,

$$\mathrm{C}^+ + \mathrm{CH} \rightarrow \mathrm{C_2}^+ + \mathrm{H} \tag{3.11}$$

can compete with

$$\mathrm{C}^+ + \mathrm{CH} \rightarrow \mathrm{CH}^+ + \mathrm{C}. \tag{3.12}$$

The relative fraction that characterizes different channels is called the branching ratio. The branching ratio depends on the details of each reaction and is determined from laboratory experiments or estimated from theoretical considerations. The reaction rate coefficient for each reaction is the product of the total reaction rate coefficient, k, and the corresponding branching ratio. If the branching ratios for reactions (3.11 and 3.12) are f and $1 - f$, respectively, the actual reaction rate coefficients are kf and $k(1 - f)$, respectively.

3.2 Reactions in Interstellar Clouds

Interstellar clouds are in the "extremes" with regard to physical conditions with low temperature (10–100 K) and low density (10–10^7 cm^{-3}) in comparison with terrestrial conditions. A typical H_2 density of 10^4 cm^{-3} in molecular clouds corresponds to the number density of molecules under a “vacuum” of 3.8×10^{-10} Pa, which cannot be readily achieved in the laboratory. In this section, we consider constraints on chemical reactions in such extreme conditions.

What happens to two hydrogen atoms colliding with each other in the above conditions? During the collision, a hydrogen molecule is tentatively formed. However, this tentative molecule is not stable. It can barely discard the excess energy produced by its formation, unless a third body takes it away or the molecule spontaneously emits a photon. The probability that a collision with a third body will occur is almost negligible in interstellar conditions. If we assume that the relative velocity of the hydrogen atom of 0.3 km s^{-1} is at 10 K according to Eq. (3.10), the duration of the collision is roughly estimated to be 0.3 ps. Here, the size of the hydrogen atom is simply assumed to be 1 Å. The collision rate of two hydrogen atoms is approximately 10^{-7} s^{-1} for a density of 10^4 cm^{-3}, and hence the probability that a third-body collision occurs during the binary collision is as low as 3×10^{-20}. Similarly, the probability that a transient molecule emits a photon during the collision is very low. For this stabilization, infrared vibration-rotation transitions allowed by the electric quadrupole moment play an important role in the H_2case. However, the Einstein A coefficient for such a transition is roughly 10^{-6}–10^{-7} s^{-1} (Wolniewicz et al. 1998), and the probability of radiative stabilization is also on the order of $3 \times 10^{-19} - 3 \times 10^{-20}$. Because of these reasons, the molecule tentatively formed during the collision is eventually dissociated back into two hydrogen atoms. That is, a hydrogen molecule is not formed through a binary collision of hydrogen atoms as far as energy conservation holds during the collision (Fig. 3.2). In interstellar clouds, a hydrogen molecule is formed on dust grains from two hydrogen atom adsorbed there, with the dust grains acting as a third body. This process will be described in Chap. 6.

The situation is different in terrestrial conditions, where the density is much higher. At atmospheric pressure, the collision rate of two hydrogen atoms is as high as 10^8 s^{-1}, and the resultant probability of the third-body collision is as high as 3×10^{-5}.

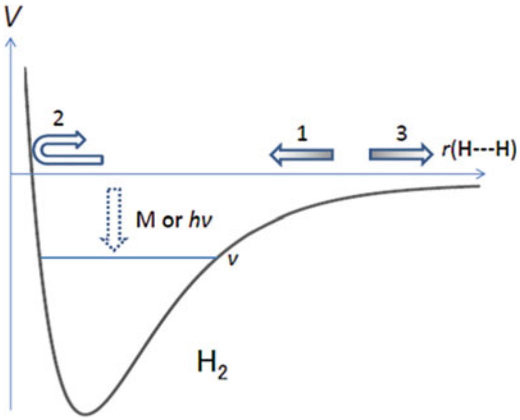

Fig. 3.2 Collision between two H atoms proceeds from steps 1 to 3, but does not form H_2 unless stabilized by the third body (M) or photon emission occurs

For the reason discussed above, a binary reaction forming a single product species, such as

$$\mathrm{A} + \mathrm{B} \rightarrow \mathrm{C}, \tag{3.13}$$

does not proceed efficiently. It should be noted, however, that a radiative association process that stabilizes the product by emitting photons becomes efficient for larger molecules (Sect. 3.4). Similarly, the electron recombination reaction that gives a single neutral species such as

$$\mathrm{A}^+ + \mathrm{e} \rightarrow \mathrm{A} \tag{3.14}$$

is usually slow, although it is important for electron recombination of atomic ions.

Thus, the most general type of binary reactions that are effective in interstellar conditions is:

$$\mathrm{A} + \mathrm{B} \rightarrow \mathrm{C} + \mathrm{D}, \tag{3.15}$$

which gives two or more product species. In this case, the redundant energy produced by the reaction can be taken away as the kinetic energy of the two products moving in opposite directions. Several examples include:

$$\mathrm{OH} + \mathrm{C} \rightarrow \mathrm{CO} + \mathrm{H}, \tag{3.16}$$

$$\mathrm{He}^+ + \mathrm{CO} \rightarrow \mathrm{C}^+ + \mathrm{O} + \mathrm{He}, \tag{3.17}$$

and

$$\mathrm{OH_3}^+ + \mathrm{e} \rightarrow \mathrm{H_2O} + \mathrm{H}. \tag{3.18}$$

This constraint mainly originates from the low density of interstellar clouds, which prohibits tertiary reactions.

Another constraint on reactions in interstellar clouds is that the reaction is exothermic and does not have energy barriers toward products. Because the gas kinetic temperature of interstellar clouds is as low as 10–100 K for most cases, endothermic reactions that require an external energy input do not proceed. Even for exothermic reactions, some reactions have an energy barrier toward the formation of products, which also requires an external energy input. If the barrier is sufficiently higher than the thermal energy of the reactants, such reactions do not proceed efficiently despite their exothermicity. An important exception is shocked regions, where the gas kinetic temperature temporarily increases up to a few 1000 K (Chap. 7). In this case, endothermic reactions as well as reactions with energy barriers can occur to some extent.

As seen above, gas-phase chemical reactions occurring in interstellar clouds are in a sense very simple: A molecule collides with another molecule to form product molecules. This type of chemical reaction is one of the most basic reactions. In laboratory experiments, various additional factors such as third-body effects (three-body reactions), catalytic effects of surfaces, and temperature effects make chemical processes much more complex. Such complex nature is sometimes useful for producing new types of molecules or in accelerating reactions. However, the complexity also hampers our understanding of chemical processes in a microscopic way, like a slow-motion movie. Thus, chemistry in interstellar clouds is inextricably linked to experimental and theoretical studies of molecular dynamics. In this sense, it can be said that an interstellar cloud is an ideal laboratory for chemical reactions.

3.3 Ion–Molecule Reactions

As discussed in the Introduction, an interstellar cloud is weakly ionized because of photoionization and cosmic-ray ionization. Hence, a cloud contains ionic species with a range of ionization degrees (10^{-4}–10^{-8}). In general, the ionization degree is as high as ~10^{-4} for diffuse clouds where the interstellar UV radiation can well penetrate. It is lower in dense clouds where only the cosmic ray contributes to the ionization. In such conditions, ion–molecule reactions play important roles in producing various molecules. Examples of this process include:

$$\mathrm{O^+ + H_2 \rightarrow OH^+ + H}, \tag{3.19}$$

$$\mathrm{C^+ + C_2H_2 \rightarrow C_3H^+ + H}, \tag{3.20}$$

and

$$\mathrm{He^+ + N_2 \rightarrow N^+ + N + He}. \tag{3.21}$$

An atomic or molecular ion produces an electric field around it. Provided that a molecule is located at a distance r from an ion, the electric field of the ion polarizes the molecule. The dipole moment thus induced is given as:

$$\mu_D^{\mathrm{induced}} = \frac{\alpha e}{r^2}, \tag{3.22}$$

where α represents the polarizability of the neutral molecule. In this case, the negative side of the dipole moment points toward the positive ion (and vice versa for the negative ion). An electrostatic attractive force between this oriented dipole moment and the ion is given by:

$$F = -\frac{2\alpha e^2}{r^5}. \tag{3.23}$$

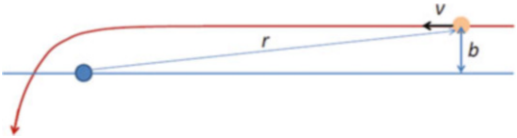

Fig. 3.3 Definition of the impact parameter *b*

By integrating from infinity to r, the potential energy for the charge-induced dipole interaction is represented as:

$$V = -\int_{\infty}^{r} F dr' = -\frac{\alpha e^2}{2r^4}. \tag{3.24}$$

That is, the interaction potential has a r^{-4} dependence and acts over relatively long ranges compared with the interaction between two neutral molecules (Sect. 3.4).

Next, we evaluate the collisional cross-section for the above potential using classical mechanics. Consider that the neutral species approaches from an infinite distance with a relative velocity ν and an impact parameter b (see Fig. 3.3). This system has an angular momentum, $L = \mu b \nu$, which is conserved during the collision. Here, μ is the reduced mass between A and B. For larger b, the system has a larger angular momentum. If b is larger than the critical value, b_0, the neutral species does not collide with the ion but simply recoils. Let us derive the b_0 value for the ion–molecule reaction below.

The centrifugal force at a distance r is given as:

$$F_{\mathrm{cent}} = \frac{L^2}{\mu r^3}. \tag{3.25}$$

The centrifugal potential is obtained by integrating the centrifugal force as:

$$V_{\mathrm{cent}} = -\int_{\infty}^{r} F_{\mathrm{cent}} dr = \frac{b^2}{r^2}\frac{\mu \nu^2}{2}. \tag{3.26}$$

Then, the effective potential for the collision is the sum of Eqs. (3.24 and 3.26) and written as:

$$V = -\frac{\alpha e^2}{2r^4} + \frac{b^2}{r^2}\frac{\mu \nu^2}{2}. \tag{3.27}$$

This potential has a centrifugal barrier (Fig. 3.4) of:

$$V_{\mathrm{barrier}} = \frac{b^4 \mu^2 \nu^4}{8\alpha e^2}. \tag{3.28}$$

If the initial energy is higher than this centrifugal barrier, collision then occurs. The maximum value of b for a given initial kinetic energy ($\mu \nu^2/2$) is:

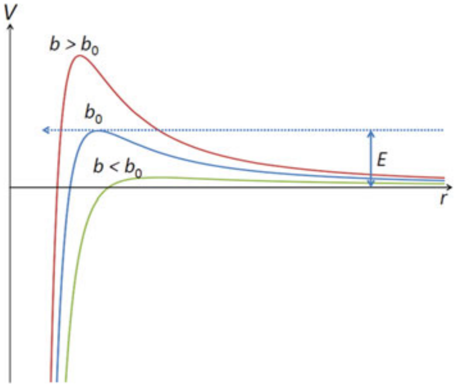

Fig. 3.4 The centrifugal barrier is higher for a larger impact parameter *b*. For a given initial energy, *E*, a reaction for which the impact parameter is smaller than a critical value, b_0, can actually take place

$$b_0^2 = \sqrt{\frac{4\alpha e^2}{\mu \nu^2}}. \tag{3.29}$$

The collisional cross-section follows:

$$\sigma = \pi b_0^2 = 2\pi e \sqrt{\frac{\alpha}{\mu \nu^2}}. \tag{3.30}$$

If no reaction barriers exist in the reaction after the collision and the reaction occurs in every collision, the reaction rate coefficient is derived using Eq. (3.8):

$$k_L = 2\pi e \sqrt{\frac{\alpha}{\mu}}. \tag{3.31}$$

This rate coefficient, called the Langevin rate coefficient for ion–molecule reactions (Langevin 1905), does not depend on temperature.

For the reaction:

$$\mathrm{H_2}^+ + \mathrm{H_2} \rightarrow \mathrm{H_3}^+ + \mathrm{H}, \tag{3.32}$$

the Langevin rate coefficient is calculated to be 2.1×10^{-9} cm^3 s^{-1}, where α is 0.79×10^{-24} cm^{-3}. This value is in excellent agreement with the experimental value of $(2.08 \pm 0.03) \times 10^{-9}$ cm^3 s^{-1} (Theard and Huntress Jr. 1974). The reaction rate coefficient is larger by two orders of magnitude than the coefficients of neutral–neutral reactions described in the next section. Because of these features, ion–molecule reactions play important roles in chemical processes in interstellar clouds.

Although the Langevin rate coefficient is independent of temperature, the actual rate coefficients determined by experiments sometimes show significant temperature dependencies. One of the explanations for the temperature dependence is the contribution of the permanent dipole moment of the neutral species. At high temperatures, neutral species rotate rapidly, and hence the permanent dipole moment averaged over various directions of the molecule will be zero. Then, the effect of the permanent dipole moment can be ignored. However, the situation differs at low temperatures. In this case, neutral species rotate slowly. If the rotational energy is comparable to the electrostatic energy between the ion charge and the dipole moment, the negative end of the permanent dipole moment tends to point toward the ion. Then, a strong attractive force showing a r^{-2} dependence emerges between the charge and the permanent dipole moment. Then, the effective potential including the centrifugal potential can be expressed as:

$$V = -\frac{\alpha e^2}{r^4} - \frac{e\mu_D}{r^2}\cos\theta + \frac{b^2}{r^2}\frac{\mu v^2}{2}, \tag{3.33}$$

where μ_D is the dipole moment of the neutral species and θ is the angle which the dipole moment makes with r. If the dipole moment is assumed to be locked to the ion, we can set $\theta = 0$. In this case, the cross-section is given by:

$$\sigma = 2\pi e\sqrt{\frac{\alpha}{\mu v^2}} + \frac{2\pi e\mu_D}{\mu v^2}, \tag{3.34}$$

and the reaction rate coefficient at a temperature T can be expressed as:

$$k = 2\pi e\left(\sqrt{\frac{\alpha}{\mu}} + \mu_D\sqrt{\frac{2}{\pi\mu k_B T}}\right). \tag{3.35}$$

The second term increases with decreasing temperature. For a molecule with a dipole moment of a few Debye, the second term typically becomes dominant over the first term at low temperatures, and the rate coefficient shows a temperature dependence of $T^{-1/2}$.

In actuality, a neutral molecule rotates, and hence θ should be nonzero. Hence, we introduce an additional constant, c $(0 \le c \le 1)$, representing the average orientation of the dipole moment, and revise the above:

$$k = 2\pi e\left(\sqrt{\frac{\alpha}{\mu}} + c\mu_D\sqrt{\frac{2}{\pi\mu k_B T}}\right). \tag{3.36}$$

Here, c represents the average of $\cos\theta$ and is approximately related to μ_D, α, and T. This theory is called the average dipole orientation (ADO) theory (Su and Bowers 1973). A revised theory considering the conservation of the angular momentum is called the advanced ADO (AADO) theory (Su et al. 1978). More rigorous calculations considering the rotational energy-level structure have been conducted for several reactions (e.g., Sakimoto 1985). The effect of the dipole moment on ion–

molecule reactions was carefully implemented in chemical models for interstellar clouds using the empirical relation (Herbst and Leung 1986).

Another origin of the temperature dependence of the reaction rate coefficients of ion–molecule reactions is the existence of reaction barriers. In some cases, the reaction requires rearrangements of chemical bonds after collision; the transition states of these rearrangements have higher energies than the initial energies of the reactants. In this case, the reaction rate coefficient can be represented as:

$$k = k_L \exp\left(-\frac{E_b}{k_B T}\right), \tag{3.37}$$

where E_b corresponds to the reaction barrier height. If such an energy barrier is lower than or comparable to the kinetic energy at room temperature, the reaction proceeds to some extent at room temperature. However, the reaction rate coefficient rapidly drops with decreasing temperature due to the existence of the reaction barrier. The same behavior is also seen in reactions with slight endothermicity. For this reason, laboratory measurements of reaction rate coefficients at low temperatures are of fundamental importance for judging whether the reactions can be effective in interstellar conditions.

In some reactions with a small reaction barrier, the reaction rate coefficient decreases with decreasing temperature, but then increases again at very low temperatures. An example of such a reaction is:

$$\mathrm{NH_3}^+ + \mathrm{H_2} \rightarrow \mathrm{NH_4}^+ + \mathrm{H}, \tag{3.38}$$

which is an important reaction for the gas-phase production of NH_3 in interstellar clouds (Barlow and Dunn 1987; Fig. 3.5). This reaction is exothermic by 0.9 eV, but has a small barrier of 0.089 eV according to the temperature dependence around room temperature. When the interaction between NH_3^+ and H_2 is considered, a shallow attractive potential exists as the result of the charge-induced dipole interaction and the reaction barrier. At low temperature, the H_2 molecule is trapped in the shallow potential, which makes a temporary complex NH_3^+-H_2. The reaction can proceed during its lifetime by overcoming the reaction barrier by quantum tunneling (Fig. 3.5, right panel). Because this process is more effective at lower temperatures, the reaction rate coefficient steeply becomes larger again at very low temperatures. Theoretical considerations of the rate coefficient of reaction (3.38) are reported by Herbst et al. (1991). A similar situation is observed in the $C_2H_2^+ + H_2$ reaction (Hawley and Smith 1992).

As shown above, a reaction at low temperature sensitively reflects the potential energy surface of the reaction. For this reason, interstellar chemistry is strongly related to reaction dynamics studies in molecular science.

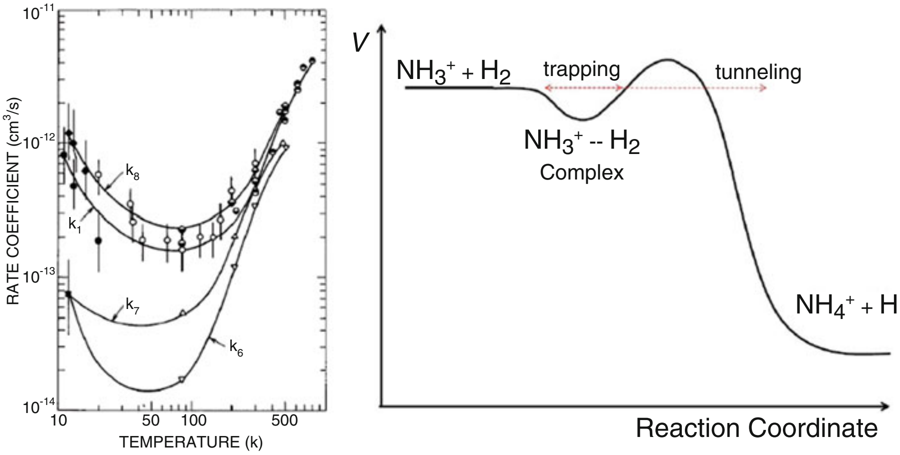

Fig. 3.5 (*Left*) Reaction rate coefficient of the $NH_3^+ + H_2$ reaction (k_1), the $ND_3^+ + H_2$ reaction (k_8), the $NH_3^+ + D_2$ reaction (k_6), and the $ND_3^+ + D_2$ reaction (k_7) as a function of temperature (Barlow and Dunn 1987). The rate coefficient decreases with decreasing temperature around room temperature because of the existence of a small barrier. When the temperature decreases further, the rate coefficient increases sharply due to the complex formation mechanism. The strong isotope effect is seen between H_2 and D_2. (*Right*) Schematic of the reaction potential curve

3.4 Neutral–Neutral Reactions

In addition to ion–molecule reactions, reactions between two neutral species also play an important role in producing molecules in interstellar clouds. Some examples include:

$$CH + O \rightarrow CO + H, \tag{3.39}$$

$$NO + N \rightarrow N_2 + O, \tag{3.40}$$

and

$$C_2H_2 + CN \rightarrow HC_3N + H. \tag{3.41}$$

They are exothermic without reaction barriers. Unlike ion–molecule reactions, rate coefficients for neutral–neutral reactions (in particular those for radical–radical reactions) are difficult to measure in the laboratory. Neutral–neutral reactions often have reaction barriers for a reason to be stated later. Hence, using these reactions in chemical models requires careful considerations. Ab initio quantum chemical calculations are helpful for investigating the presence or absence of reaction barriers. Now, the importance of neutral–neutral reactions in interstellar clouds is widely recognized (e.g., Herbst et al. 1994).

First, an electrostatic interaction between two neutral molecules (atoms) is considered. The following three mechanisms are mainly responsible for the interaction: (1) dipole–dipole interactions, (2) dipole-induced dipole interactions, and (3) dispersion forces. Here, we ignore the electric multipole interactions, which are typically smaller than the three interactions discussed above.

If both molecules have a permanent electric dipole moment, an attractive force appears between the dipole moments. Here, the local spherical coordinates $(\rho_1, \theta_1, \varphi_1)$ and $(\rho_2, \theta_2, \varphi_2)$ originating from the centers of mass for molecules 1 and 2, respectively, are defined, where the intermolecular distance is denoted by r. Here, the azimuthal angles φ_1 and φ_2 are defined as the angle about the axis connecting the two centers of mass. The dipole–dipole interaction energy is then given as:

$$E_{dd} = \frac{\mu_{D1}\mu_{D2}}{r^3}\,[\sin\theta_1 \sin\theta_2 \cos(\varphi_1 - \varphi_2) - 2\cos\theta_1 \cos\theta_2], \tag{3.42}$$

where the directions of the dipole moments, μ_{D1} and μ_{D2}, are (θ_1, φ_1) and (θ_2, φ_2), respectively. For a random orientation of dipole moments, the average interaction energy between the two molecules is:

$$V = < E_{dd} \exp\left(-\frac{E_{dd}}{kT}\right) > = < E_{dd} > - \frac{< E_{dd}^2 >}{kT} + \ldots, \tag{3.43}$$

where we assume $E_{dd} \ll kT$ for the expansion of the exponential term. When various orientations of the two dipole moments are averaged, the first term disappears, and we obtain:

$$V = -\frac{2\mu_{D1}^2 \mu_{D2}^2}{3k_B T r^6}. \tag{3.44}$$

Hence, the interaction potential is proportional to r^{-6}, which is short-ranged in comparison with ion–molecule reactions. Note that the two dipole moments will tend to lock to each other at low temperature, if the dipole moments are sufficiently large. In this case, the potential is proportional to r^{-3}.

The second interaction is the dipole-induced dipole interaction. The permanent dipole of molecule 1 produces an electric field (F_1) at molecule 2, which creates the induced dipole moment in molecule 2. This situation is the same as a dielectric material in an electric field, and hence the interaction potential is given as:

$$V = -\frac{\alpha_2 < F_1^2 >}{2}, \tag{3.45}$$

where α_2 is the polarizability of molecule 2, and $< >$ represents the average over the various directions of the dipole moment of molecule 1. If molecule 2 also has a dipole moment, it induces the dipole moment in molecule 1. When this effect is taken into account, we have:

$$V = -\frac{\mu_{D1}^2\alpha_2 + \mu_{D2}^2\alpha_1}{r^6}, \tag{3.46}$$

where the following relation is employed as $< F_i^2 >= 2\mu_{Di}^2 r^{-6}$ $(i = 1, 2)$. Again, the potential is proportional to r^{-6}, but is independent of temperature.

The third interaction is a quantum mechanical interaction called the "dispersion interaction." Although it cannot adequately be described by classical mechanics, a qualitative picture of the dispersion interaction is as follows. Because atoms and molecules consist of nuclei and electrons, they produce an instantaneous dipole moment when electrons move asymmetrically with respect to the nuclei. Such an instantaneous dipole moment produces an electric field at another molecule and induces a dipole moment there. The dipole moments of the original and neighboring molecules instantaneously interact with each other, creating an attractive force between the two molecules (atoms). The derivation of this force is beyond the scope of this book and is found elsewhere (Atkins and Friedman 2011). The interaction potential between two neutral molecules can be approximately represented as:

$$V = -\frac{3I_1I_2\alpha_1\alpha_2}{2(I_1 + I_2)r^6}, \tag{3.47}$$

where I_1 and I_2 are the ionization potentials for molecules 1 and 2, respectively. The interaction potential also has a r^{-6} dependence. Unlike the previous two interactions, this interaction is effective even between two nonpolar molecules without permanent dipole moments.

As described above, all of the interactions between the neutral species are proportional to r^{-6}. Among the three interactions, the dispersion interaction is usually dominant. When the interaction potential is assumed to be

$$V = -\frac{\beta}{r^6}, \tag{3.48}$$

the cross-section is derived in a similar way as described for ion–molecule reactions:

$$\sigma = \left(\frac{3\sqrt{3}}{2}\right)^{2/3} \pi \left(\frac{2\beta}{\mu v^2}\right)^{1/3}. \tag{3.49}$$

The reaction rate coefficient is found to be:

$$k = 2^{\frac{11}{2}}\Gamma\left(\frac{2}{3}\right)\left(\frac{\pi}{\mu}\right)^{\frac{1}{2}}\left(\beta^2 k_B T\right)^{\frac{1}{6}}, \tag{3.50}$$

where $\Gamma(x)$ is the gamma function. The rate coefficient weakly depends on temperature. A typical reaction rate coefficient for a neutral–neutral reaction is $10^{-11}\ \mathrm{cm}^3\ \mathrm{s}^{-1}$, which is smaller than ion–molecule reaction rate coefficients by two orders of magnitude.

The above rate coefficient is valid when the interaction is completely governed by the potential function of Eq. (3.48). However, molecules are not point masses, and hence the sizes of molecules must be considered. Because the cross-section is often smaller than or comparable to the cross-section assuming a rigid-body collision without any attractive force, the geometrical cross-section model is often used for evaluating the reaction rate coefficient of neutral–neutral reactions.

Here, a molecule is approximated by a sphere, the radius of which is regarded as being of molecular size. If the radii for molecule 1 and molecule 2 are denoted as a_1 and a_2, respectively, then, a collision occurs between the two if the impact parameter b is less than the sum of a_1 and a_2. Hence the cross-section is simply given by:

$$\sigma = \pi d^2, \tag{3.51}$$

where $d = a_1 + a_2$. If the reaction is assumed to occur for every collision, the reaction rate coefficient is represented by:

$$k = d^2 \left(\frac{8\pi k_B T}{\mu} \right)^{\frac{1}{2}}, \tag{3.52}$$

in accordance with Eq. (3.9). The rate coefficient is proportional to $T^{1/2}$ in this case. In actual neutral–neutral reactions, reaction rate coefficients and their temperature dependencies vary from reaction to reaction, depending on various factors such as molecular asymmetry and the stereochemical effect not considered here.

Neutral–neutral reactions often have reaction barriers. Because the interaction potential is weak and short-ranged in comparison with ion–molecule reactions, the energy gain due to collisions is relatively small. For this reason, if the reaction requires rearrangements of chemical bonds, transition states for the rearrangements can have higher energies than the initial energies of the reactants. Generally speaking, radical–radical reactions tend to proceed without reaction barriers, because the unpaired electrons of both radicals can form chemical bonds directly. Similarly, reactions between a radical species and a closed-shell molecule with π electrons can sometimes proceed without reaction barriers, because the unpaired electron of the radical can form a chemical bond with an electron of the π orbital. In contrast, reactions between closed-shell molecules, as well as those between a radical species and a saturated closed-shell molecule, usually have a high reaction barrier. However, it should be noted that the situation differs from reaction to reaction; each reaction should be investigated in detail.

3.5 Radiative Association Reactions

When a molecule that is tentatively formed during a collision process emits a photon before dissociating into its initial reactants, the molecule is stabilized to give an associated product:

$$\mathrm{A} + \mathrm{B} \rightarrow \mathrm{AB} + h\nu. \tag{3.53}$$

This reaction is called the "radiative association reaction." A similar process for electron recombination of atomic (or molecular) ions given by:

$$\mathrm{A}^+ + \mathrm{e} \rightarrow \mathrm{A} + h\nu \tag{3.54}$$

is called the "radiative electron recombination reaction." A process forming a negative ion by electron attachment given by:

$$\mathrm{A} + \mathrm{e} \rightarrow \mathrm{A}^- + h\nu \tag{3.55}$$

is called the "radiative electron attachment reaction."

These processes can be approximated by the scheme:

$$\mathrm{A} + \mathrm{B} \rightleftarrows \mathrm{AB}^* \rightarrow \mathrm{AB} + h\nu. \tag{3.56}$$

The rate coefficients for the forward and backward reactions for the first step are represented by k_1 and k_{-1}, respectively, and the rate coefficient for the second step is denoted by k_2. Then, the total reaction rate coefficient for production of AB is:

$$k = \frac{k_1 k_2}{k_{-1} + k_2}. \tag{3.57}$$

In this equation, k_1 equals the collisional rate coefficient between A and B, which was discussed in previous sections.

As discussed above, the backward reaction from AB* to A + B is very fast for a diatomic molecule such as H_2. In this case, only one vibrational mode is available for a reservoir of excess energy in molecular formation, and hence the excess energy is directly used to dissociate the molecule along its vibrational mode. In contrast, there are $(3N - 6)$ vibrational modes for a polyatomic molecule consisting of N atoms ($(3N - 5)$ for a linear molecule). When A and B collide with each other to form AB*, the excess energy is distributed across these vibrational modes. If the energy is sufficiently concentrated in one particular vibrational mode correlated with the (A + B) dissociation, the backward reaction occurs. The probability that AB* will follow this pathway among the many other pathways is smaller for larger molecules. Thus, the backward reaction rate coefficient k_{-1} rapidly decreases with increasing vibrational degrees of freedom.

This picture can be verified by the following simplified consideration. Suppose that the excess energy (E) in AB* corresponds to n vibrational quanta distributed over s different modes, where the vibrational energy ($h\nu$) is simply assumed to be identical for all of the modes; that is, $E = nh\nu$. Furthermore, AB* is assumed to be dissociated back to A + B, when m quanta out of n quanta is in a certain mode leading to the dissociation of AB*. This probability is given by:

$$p = \frac{(n-m+s-1)!n!}{(n+s-1)!(n-m)!} \sim \left(\frac{n-m}{n}\right)^{s-1} = \left(\frac{E-E_0}{E}\right)^{s-1}, \tag{3.58}$$

where $E_0 = mh\nu$. Here, we assume that n and m are much larger than s. The probability rapidly decreases with increasing s. The lower probability of the backward reaction means that AB* has more chances to stabilize as AB by emitting photons.

Additionally, k_2 depends on the transition probability. If there are electronic states below the state for AB*, an electronic transition can occur to stabilize AB*. If no electronic states exist, the vibrational transitions are major routes to stabilization. The oscillator strengths of these transitions depend on molecules, and hence k_2 also differs from molecule to molecule. A typical rate for electric transitions is 10^6 s^{-1}, but the rate can be as low as 10^2–10^3 s^{-1} for infrared vibration-rotation transitions. Nevertheless, it can be said that k_2 is generally larger for larger molecules because a larger molecule has more radiative pathways by which to stabilize.

As discussed above, the rate coefficient for radiative association reactions approaches the collisional rate for larger molecules. For instance, the rate coefficient is on the order of 10^{-16} cm^3 s^{-1} for

$$C^+ + H_2 \rightarrow CH_2^+ + h\nu, \tag{3.59}$$

and it is as fast as 10^{-11} cm^{-3} s^{-1} for

$$CH_3{}^+ + HCN \rightarrow CH_3CNH^+ + h\nu. \tag{3.60}$$

The reaction rate coefficient generally shows a temperature dependence of T^{-p} ($p > 0$), and hence reactions are faster at lower temperatures. This is due to a longer duration time of collision at lower temperature.

3.6 Dissociative Electron Recombination

A reaction between a molecular ion and an electron giving two or more product species is called dissociative electron recombination:

$$A^+ + e \rightarrow B + C. \tag{3.61}$$

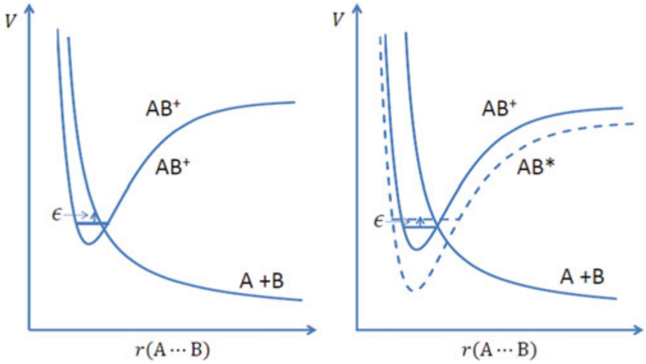

Fig. 3.6 Two mechanisms for dissociative electron recombination. (*Left*) Direct dissociation through the potential crossing between the ionic bound state (AB^+) and the neutral repulsive state (A+B). (*Right*) Dissociation through the Rydberg state (AB*). Small thermal energy is represented by ϵ

In interstellar clouds, this reaction plays an important role in producing neutral species from their parent molecular ions formed by ion–molecule reactions. In this reaction, an electron is first captured by the molecular ion to form a neutral molecule in its high electronic state, whose potential curve crosses over the potential curve of the initial molecular ion. If this neutral state is repulsive, the molecule is dissociated into fragments (Fig. 3.6, left panel). In some cases, the first neutral state after the capture of an electron would be the Rydberg state, which is a bound state. Even in this case, the molecule dissociates if a repulsive potential curve crosses over the potential curve of the Rydberg state. This situation is schematically shown in Fig. 3.6 (right panel).

In contrast to the other reactions introduced in the previous sections, the derivation of the rate coefficients for dissociative electron recombination reactions requires quantum treatments, which is beyond the scope of this book (e.g., Thomas 2008; Bates 1950). The derivation of the rate coefficients gives an approximate rate coefficient of 10^{-7} cm^3 s^{-1} and a temperature dependence of $T^{-1/2}$.

An important issue for dissociative electron recombination is the branching ratio to different products. For instance, the recombination of the $OH_3{}^+$ ion produces the following products:

$$OH_3{}^+ + e \rightarrow H_2O + H \tag{3.62}$$

$$\rightarrow OH + H_2 \tag{3.63}$$

$$\rightarrow OH + H + H \tag{3.64}$$

$$\rightarrow O + H_2 + H. \tag{3.65}$$

The branching ratios are very important, because they are directly related to the abundances of neutral species produced. However, the branching ratios are hard to measure in the laboratory, and their estimation is also a nonroutine analysis in theoretical approaches. Hence, an equal branching ratio has often been assumed for all possible channels. Owing to recent developments in laboratory experiments, including storage-ring experiments, the branching ratio has now been measured with sufficient accuracy. The branching ratios of Eqs. (3.62, 3.63, 3.64, and 3.65) are reported to be 0.25 ± 0.01, 0.14 ± 0.01, 0.60 ± 0.02, and 0.013 ± 0.005, respectively (Jensen et al. 2000). This result emphasizes that accurate measurements of recombination reactions for various fundamental ions are indispensable.

3.7 Photodissociation and Photoionization

Interstellar space is generally filled with UV radiation emitted by stars. This radiation is called interstellar UV radiation. When a molecule is exposed to interstellar UV radiation, the molecule is dissociated (*photodissociation*) and/or ionized (*photoionization*). These processes are mainly important in a diffuse molecular cloud and/or the periphery of a molecular cloud, where the interstellar UV radiation can penetrate. The UV radiation is particularly significant if a cloud is illuminated by nearby OB main-sequence stars. Such regions where photoprocesses are strongly active are called *photodissociation regions* or *photon-dominated regions* (PDRs).

The typical intensity of the interstellar UV radiation in the solar neighborhood is on the order of 10^5 photons $\mathrm{cm}^{-2}\ \mathrm{s}^{-1}\mathrm{\AA}^{-1}$ and is wavelength dependent. It vanishes below wavelengths of 912 Å, which corresponds to the ionization potential of the hydrogen atom (13.60 eV). Because the hydrogen atom is abundant in interstellar space, UV photons with energies higher than 13.60 eV are completely absorbed by hydrogen atoms. The predicted intensity at longer wavelengths depends on the grain models adopted (grain abundance and size distribution). The intensity differs by at most a factor of 2 among models. To account for the different intensities of the interstellar UV radiation in different conditions, an additional factor, G_0, is introduced to scale the intensity. In a PDR illuminated by nearby OB main-sequence stars, G_0 can be as high as 10^4–10^5 (Tielens and Hollenbach 1985a, b).

In addition to the interstellar UV radiation, there are two other sources of UV radiation in interstellar clouds. One is cosmic ray-induced UV radiation. When cosmic rays penetrate through a cloud, they ionize the surrounding H_2 gas and produce energetic electrons. These electrons excite the H_2 molecules, resulting in UV emission. This process is called cosmic ray-induced UV radiation (Prasad and Tarafdar 1983; Gredel et al. 1989). UV photons thus produced can contribute to photoprocesses deep within a molecular cloud, where interstellar UV radiation from outside is completely attenuated. Another important source is shock-induced Lyman-α emission (1216 A), which is caused by the recombination of H^+ ions or the collisional excitation of H atoms in a strong shocked region (Hollenbach and McKee 1979; Neufeld and Dalgarno 1989). A shock-induced Lyman-α emission is almost monochromatic, so that photodissociation rate by this radiation depends on molecular species.

Photodissociation processes can be classified into several categories based on their detailed mechanisms. The three major processes are depicted in Fig. 3.7. One process is direct dissociation, in which a molecule is excited by UV radiation to a repulsive electronic state. This step represents a bound-free transition, and hence the photodissociation can occur in a broad band of UV radiation (Fig. 3.7, left panel and Fig. 3.8, left panel). Another process is the so-called predissociation. In this case, a molecule is first excited by UV radiation to a rovibronic level of a bound electronic state. If the rovibronic level is coupled to repulsive states, the excited molecule will be dissociated with a certain probability depending on the strength of the coupling and the radiation lifetime. Hence, photodissociation is strongly wavelength dependent, and a molecule is photodissociated at the transition frequencies

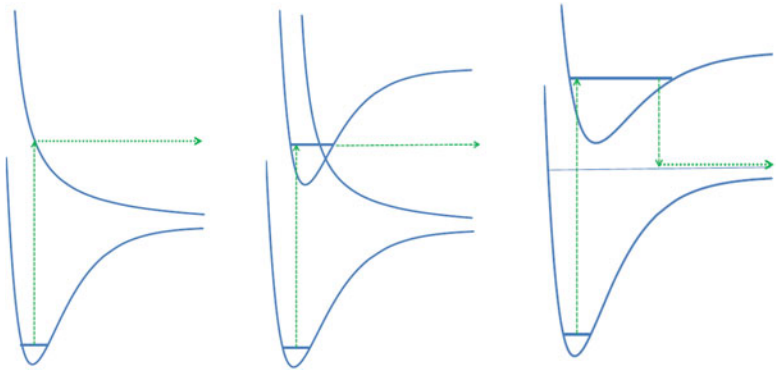

Fig. 3.7 Three typical photodissociation scenarios: (*left*) direct dissociation, (*center*) predissociation, and (*right*) excitation to the electronic state followed by fluorescent emission to the continuum of the lower state

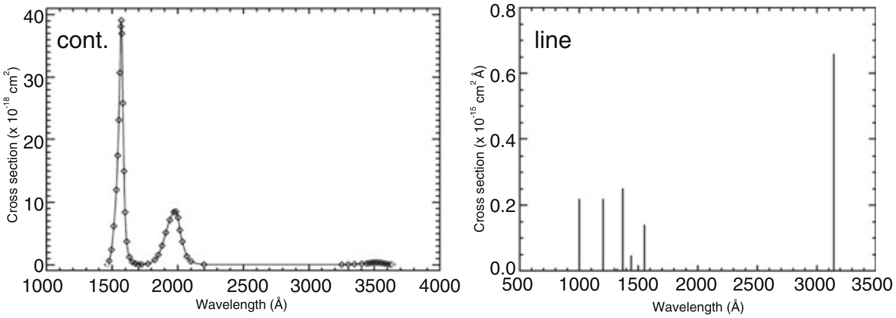

Fig. 3.8 Photodissociation cross-section for CH. Both direct photodissociation (*left*) and predissociation (*right*) occur simultaneously. Reproduced from http://home.strw.leidenuniv.nl/~heays/photo/showfile.php?showfile=ch.pd with permission by van Dishoeck (Original data: van Dishoeck 1987)

from the ground electronic state to the electronically excited state (Fig. 3.7, center panel, and Fig. 3.8, right panel). A third process is the excitation of a molecule to a bound electronic state, followed by fluorescent decay to continuum levels of the ground electronic state (Fig. 3.7, right panel). For instance, H_2 molecules are mainly photodissociated via this mechanism. Note that two or more of these channels are simultaneously possible in interstellar conditions.

Because photodissociation is a unimolecular reaction, the rate equation is simply given as:

$$\frac{d[\mathrm{A}]}{dt} = -k_d[\mathrm{A}], \tag{3.66}$$

where k_d is the rate coefficient for photodissociation in units of s^{-1}. A photodissociation rate coefficient from the lower state l can be evaluated using direct dissociation:

$$k_{dl} = \int \sigma_l(\lambda)I(\lambda)f_l d\lambda, \tag{3.67}$$

where σ_l is the photodissociation cross-section for the lower state l, I is the intensity of UV radiation, and f_l is the fractional population of the state l relative to the total population in the ground state. For predissociation, the rate coefficient is:

$$k_{dl} = \frac{\pi e^2}{mc^2}\sum_u \lambda_{ul}^2 x_{ul} I(\lambda_{ul}) f_l\, \eta_u, \tag{3.68}$$

where λ_{ul} represents the wavelength of the line transition from the lower state l to the upper state u, x_{ul} the oscillator strength of the corresponding transition, and η_u the efficiency of the predissociation for the upper state u. The summation should extend over the available upper states. The total photodissociation rate coefficient follows accordingly:

$$k_d = \sum_l k_{dl}\,. \tag{3.69}$$

If a single electron oscillator is considered for simplicity, the oscillator strength is on the order of unity. This situation corresponds to the strongest absorption case. If the upper state is predissociative and only one state is responsible for the upper and lower states, the photodissociation rate can readily be evaluated to be $10^{-9}\ \mathrm{s}^{-1}$ for typical levels of interstellar UV radiation (10^5 photons $\mathrm{cm}^{-2}\ \mathrm{s}^{-1}\ \mathrm{A}^{-1}$) using Eq. (3.68). Here, the wavelength of the photodissociating photons is assumed to be 1000 Å. In actuality, the oscillator strength is less than unity, and the efficiency of photodissociation can also be lower. Hence, the photodissociation rate estimated above should be regarded as an upper limit.

The interstellar UV radiation is attenuated in the interior of a molecular cloud. The attenuation is caused by dust grains, and hence it can be scaled using visual extinction, A_ν, from the cloud surface. The photodissociation rate in the interior of a molecular cloud should be corrected by this factor. Therefore, the effective photodissociation rate coefficients take the form:

$$k = k_0 \exp(-\gamma A_\nu), \tag{3.70}$$

where k_0 is the unattenuated photodissciation rate coefficient for the interstellar UV radiation. The coefficient γ depends on molecular species and also on the grain model adopted. The k_0 and γ values are tabulated for fundamental molecules (e.g., van Dishoeck 1988; UMIST Database). The k_0 value ranges from 10^{-9} to 10^{-11} s^{-1} for most cases.

For abundant species, the molecules residing near the cloud surface consume the photons for photodissociation, and hence molecules of the same species in the interior of the cloud can escape from photodissociation. This process is called self-shielding. The self-shielding effect is significant for predissociative spectral lines whose optical depth is high. In particular, this effect cannot be ignored for H_2 and CO. This effect is very important in determining the H_2 column density based on the CO observation particularly for external galaxies (e.g., Shetty et al. 2011; Feldman et al. 2012). Furthermore, if the photons that are dissociating a less abundant species are consumed by the photodissociation of the abundant species, such as H_2 and CO, through accidental overlapping of transition frequencies, the photodissociation of the less abundant species is suppressed. This process is called mutual shielding. In this case, the effective γ value depends on the abundance of the molecule considered, as well as the abundances of other abundant molecules. For detailed modeling of diffuse interstellar clouds, translucent clouds, and photodissociation regions, these shielding effects are considered carefully.

The self-shielding effect differs among isotopic species. For instance, in the solar neighborhood, ^{13}CO and C^{18}O are less abundant than ^{12}CO by factors of 59 and 560, respectively. Therefore, the self-shielding effect is less significant for ^{13} CO and much less significant for C^{18}O. Because of this difference, ^{13}CO and C^{18}O are selectively photodissociated in interiors of clouds. Photodissociation is more efficient for C^{18}O than for ^{13}CO, and hence the ^{13}CO/C^{18}O ratio tends to be higher than the normal ^{13}C/^{18}O ratio (Fig. 3.9). Such isotope-selective photodissociation is actually observed for translucent clouds (e.g., Visser et al. 2009).

The interstellar UV radiation not only dissociates molecules but also ionizes atoms and molecules. Ionization by photons is called photoionization. This process is important for atoms and molecules whose ionization potentials are lower than 13.60 eV. Carbon (C), silicon (Si), sulfur (S), and phosphorus (P) atoms are ionized by interstellar UV radiation; He, N, and O are not. The photoionization of atoms determines the degree of ionization of diffuse clouds, translucent clouds, and PDRs, as will be described in Chap. 4. Photoionization rate coefficients can be represented by Eq. (3.70). The unattenuated rate coefficients and the γ values are tabulated in

Fig. 3.9 Schematic of isotope-selective photodissociation

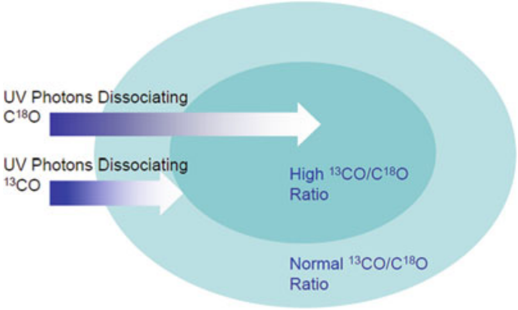

the literature, where these values depend on the grain model adopted (van Dishoeck 1988; UMIST Database).

The photoionization process of molecules can be classified into two categories. One category corresponds to direct ionization, where the absorption of a UV photon yields the corresponding ion in its various rovibronic levels:

$$\mathrm{M} + h\nu \rightarrow \mathrm{M}^{+}(e, \nu, r) + \mathrm{e}. \tag{3.71}$$

The excess energy is removed by an electron ejected from the parent molecule. The other category is excitation of parent molecules to their highly electronic excited states above the ionization potential and subsequent autoionization during the spontaneous emission lifetime and the dissociation lifetime of the excited state:

$$\mathrm{M} + h\nu \rightarrow \mathrm{M}^{*} \rightarrow \mathrm{M}^{+}(e, \nu, r) + \mathrm{e}. \tag{3.72}$$

Photoionization may sometimes cause further dissociation of the product ion, a process called dissociative photoionization.

Photoionization is largely controlled by photoabsorption, and hence the unattenuated photoionization rate coefficient is roughly comparable in magnitude to the unattenuated photodissociation rate coefficient (10^{-9}–10^{-11} s^{-1}). It should be noted that some molecules can be photodissociated but not photoionized. For instance, the H_2, CO, and N_2 molecules are subject to photodissociation. However, they are not ionized by interstellar UV radiation because their ionization potentials (15.4, 14.0, and 15.6 eV, respectively) exceed the ionization potential of H atoms (13.60 eV) (Chap. 4).

3.8 Timescale of Chemical Reactions

Let us consider a binary reaction given by:

$$\mathrm{A} + \mathrm{B} \rightarrow \mathrm{C} + \mathrm{D}. \tag{3.73}$$

When we focus on the abundance of A, the rate equation for this reaction is:

Fig. 3.10 Temporal variation of the abundance of A. The reaction timescale is defined by τ

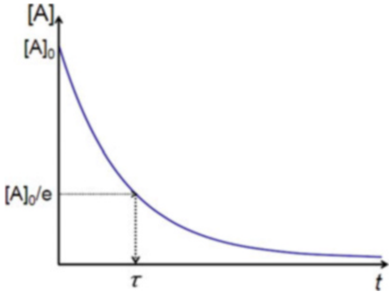

$$\frac{d[\mathrm{A}]}{dt} = -k[\mathrm{A}][\mathrm{B}], \tag{3.74}$$

where k is the rate coefficient for the reaction. In an actual interstellar cloud, A is formed and lost by many pathways. However, we focus here only on the above reaction. The abundance of B is assumed to remain constant during the reaction, which is particularly true if B is an abundant species. Under these assumptions, the temporal variation of the abundance of A is written as:

$$[\mathrm{A}] = [\mathrm{A}]_0 \exp(-k[\mathrm{B}]t), \tag{3.75}$$

where $[\mathrm{A}]_0$ represents the initial abundance of A at $t = 0$. This equation implies that the abundance becomes $1/e$ of the initial abundance at $\tau = 1/k[B]$ (Fig. 3.10). We define this time as the timescale of the reaction. This timescale provides us with a semiquantitative idea of how long a particular chemical reaction takes. As an example, we consider the ion–molecule reaction:

$$\mathrm{O}^+ + \mathrm{H}_2 \rightarrow \mathrm{OH}^+ + \mathrm{H}, \tag{3.76}$$

where the reaction rate coefficient is 1.6×10^{-9} cm^3 s^{-1}. If the H_2 density is 10^4 cm^{-3}, as is typical for a dense molecular cloud, the timescale for the above reaction is 6×10^4 s (about 17 h).

For unimolecular reactions such as photodissociation and photoionization, the rate equation is:

$$\frac{d[\mathrm{A}]}{dt} = -k[\mathrm{A}]. \tag{3.77}$$

In this case, the temporal variation of the abundance of A takes the form:

$$[\mathrm{A}] = [\mathrm{A}]_0 \exp(-k[\mathrm{B}]t), \tag{3.78}$$

and hence the timescale of the reaction is $\tau = 1/k$. If the photodissociation rate is 10^{-10} s^{-1}, the timescale for photodissociation is 10^{10} s (~300 year).

3.9 Timescale for Chemical Equilibrium

Consider reaction scheme:

$$A \rightleftharpoons B, \tag{3.79}$$

where B is formed from A, and A is reformed from B. The effective reaction rate coefficients from A to B and from B to A are represented by k_f and k_b, respectively. Note that these reactions are not always single reactions, but can be a series of binary and unimolecular reactions. Even in the binary reaction cases, the effective reaction rate coefficient can be defined by assuming a constant abundance of the reaction partner. By focusing on the abundance of A, the rate equation becomes:

$$\frac{d[\mathrm{A}]}{dt} = -k_f[\mathrm{A}] + k_b\,[\mathrm{B}]. \tag{3.80}$$

At $t = 0$, the abundance of A is assumed to be C_0; the abundance of B is assumed to be 0. Namely, all of the molecules are A molecules at the initial time step. After a sufficiently long period of time, this system will reach chemical equilibrium. In chemical equilibrium, the left-hand side of Eq. (3.80) vanishes, and hence we obtain:

$$\frac{[\mathrm{B}]}{[\mathrm{A}]} = \frac{k_f}{k_b}. \tag{3.81}$$

If A and B are the major species in the system and one molecule of A is formed from one molecule of B, we can assume that the total abundances of [A] and [B] are conserved:

$$[\mathrm{A}] + [\mathrm{B}] = C_0. \tag{3.82}$$

Then, the equilibrium abundances of A and B are given as:

$$[\mathrm{A}] = \frac{k_b}{k_f + k_b}\,C_0 \tag{3.83}$$

and

$$[\mathrm{B}] = \frac{k_b}{k_f + k_b}\,C_0, \tag{3.84}$$

respectively.

In principle, an infinite period of time is necessary to achieve chemical equilibrium. However, we can estimate a practical timescale for chemical equilibrium using the following consideration. Eqs. (3.80, 3.82) are rewritten as:

$$\frac{d[\mathrm{A}]}{dt} = -(k_f + k_b)[\mathrm{A}] + k_b C_0. \tag{3.85}$$

The formal solution of this differential equation is:

$$[\mathrm{A}] = \frac{k_b}{k_f + k_b} C_0 + \frac{k_f}{k_f + k_b} \ C_0 \exp\left[-\left(k_f + k_b\right)t\right], \tag{3.86}$$

where we assume that $[\mathrm{A}] = C_0$ and $[\mathrm{B}] = 0$ at $t = 0$ (Fig. 3.11). If the e-folding time is employed as the timescale for chemical equilibrium, we find:

$$t_{eq} = \frac{1}{k_f + k_b}. \tag{3.87}$$

Because the timescales for the forward and backward reactions are $t_f = 1/k_f$ and $t_b = 1/k_b$, respectively, the following important relation is obtained:

$$\frac{1}{t_{eq}} = \frac{1}{t_f} + \frac{1}{t_b}. \tag{3.88}$$

Namely, the timescale for chemical equilibrium is determined by the shorter timescale of the forward and backward reactions.

Problems

3.1 Consider two hydrogen molecules with a separation of 10 nm. Evaluate the dispersion force between them. Here, the polarizability and the ionization potential of H_2 are 0.79×10^{-24} cm^{-3} and 15.43 eV, respectively.

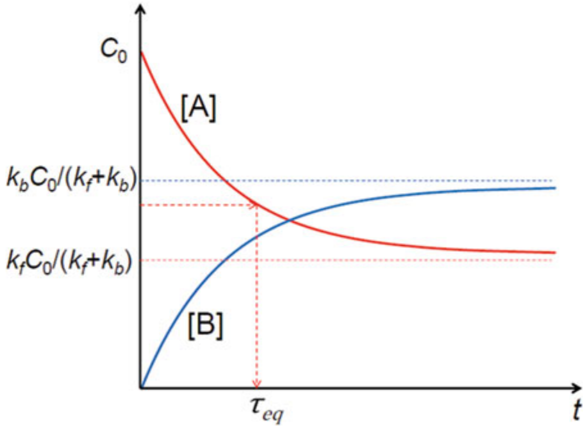

Fig. 3.11 Timescale for chemical equilibrium

3.2 Consider an attractive potential between two molecules of the form:

$$V = -\frac{\beta}{r^n} \quad (n \geq 3).$$

Show that the reaction rate coefficient between the molecules has a temperature dependence of:

$$k \propto T^{-\frac{2}{n}+\frac{1}{2}}.$$

3.3 Provided that an atom M has an ionization potential of 11 eV and a constant photoionization cross-section of 10^{-16} cm^2 above the ionization potential, derive the photodissociation rate coefficient for interstellar UV radiation. Here, the interstellar UV radiation flux is assumed to be constant below 13.60 eV (10^5 photons $\mathrm{cm}^{-2}\ \mathrm{s}^{-1} \text{Å}^{-1}$).

3.4 Derive Eq. (3.6) for the distribution of relative velocity from the original Maxwell distribution:

$$f(\nu, T)d\nu = 4\pi\nu^2 \left(\frac{m}{2\pi k_B T}\right)^{3/2} \exp\left(-\frac{m\nu^2}{2k_B T}\right) d\nu,$$

where m is the mass of a particle.

3.5 Consider a molecular cloud for which H_2 density is 10^4 cm^{-3} and temperature is 10 K. What are the mean free path and the mean free time of H_2 molecules in this cloud? Here, species other than H_2 molecules can be ignored.

3.6 Consider the ion–molecule reaction:

$$\mathrm{C^+ + H_2O \rightarrow HCO^+ + H}.$$

The polarizability of H_2O is 1.5×10^{-24} cm^3; its dipole moment is 1.94 D. Evaluate the Langevin rate coefficient, as well as the rate coefficient assuming a locking dipole moment (Eq. 3.35). Compare these values with the experimental value at 27 K (12×10^{-9} $\mathrm{cm}^3\ \mathrm{s}^{-1}$).

References

P. Atkins, R. Friedman, *Molecular Quantum Mechanics*, 5th edn. (Oxford University Press, Oxford, 2011), p. 413

S.E. Barlow, G.H. Dunn, Int. J. Mass Spectrom. Ion Processes **80**, 227 (1987)

D.R. Bates, Phys. Rev. **78**, 492 (1950)

R. Feldman, N.Y. Gnedin, A.V. Kravstsov, Astrophys. J. **747**, 124 (2012)

R. Gredel, S. Lepp, A. Dalgarno, E. Herbst, Astrophys. J. **347**, 289 (1989)

M. Hawley, M.A. Smith, J. Chem. Phys. **96**, 1121 (1992)

E. Herbst, C.M. Leung, Astrophys. J. **310**, 378 (1986)

E. Herbst, D.J. DeFrees, D. Talbi, F. Pauzat, W. Koch, A.D. McLean, J. Chem. Phys. **94**, 7842 (1991)

E. Herbst, H.H. Lee, D.A. Howe, T.J. Millar, Mon. Not. R. Astr. Soc. **268**, 335 (1994)

D. Hollenbach, C.F. McKee, Astrophys. J. Suppl. **41**, 555 (1979)

M.J. Jensen, R.C. Bilodeau, C.P. Safvan, K. Seiersen, L.H. Andersen, Astrophys. J. **543**, 764 (2000)

P. Langevin, Ann. Chim. Phys. **5**, 245 (1905)

D.A. Neufeld, A. Dalgarno, Astrophys. J. **340**, 869 (1989)

S.S. Prasad, S.P. Tarafdar, Astrophys. J. **267**, 603 (1983)

K. Sakimoto, CPL **116**, 86 (1985)

R. Shetty, S.C. Glover, C.P. Dullemond, R.S. Klessen, Mon Not. R. Astr. Soc. **412**, 1686 (2011)

T. Su, M.T. Bowers, J. Chem. Phys. **58**, 3027 (1973)

T. Su, E.C.F. Su, M.T. Bowers, J. Chem. Phys. **69**, 2243 (1978)

L.P. Theard, W.T. Huntress Jr., J. Chem. Phys. **60**, 2840 (1974)

R.D. Thomas, Mass Spectrometry Rev. **27**, 485 (2008)

A.G.G.M. Tielens, D. Hollenbach, Astrophys. J. **291**, 747 (1985a)

A.G.G.M. Tielens, D. Hollenbach, Astrophys. J. **291**, 722 (1985b)

E.F. van Dishoeck, J. Chem. Phys. **86**, 196 (1987)

E.F. van Dishoeck, in *Rate Coefficients in Astrochemistry*, ed. by T.J. Millar, D.A. Williams. (Kluwer, Dordrecht, 1988), p. 49

R. Visser, E.F. van Dishoeck, J.H. Black, Astron. Astrophys. **503**, 323 (2009)

L. Wolniewicz, I. Simbotin, A. Dalgarno, Astrophys. J. Suppl. **115**, 293 (1998)

Chapter 4
Chemistry of Diffuse Clouds

4.1 Physical Conditions in Diffuse Clouds

A *diffuse cloud* is defined as an interstellar cloud whose typical H_2 (or H) density ranges from a few 10 cm^{-3} to a few 100 cm^{-3} (Fig. 1.1). Because such a cloud usually has a typical visual extinction A_v (see Chap. 1 for definition) of a few magnitudes at most, the interstellar UV radiation penetrates deeply into the cloud. Photodissociation and photoionization are important processes there, and hence the cloud can be regarded as a PDR (See Sect. 3.7). Hydrogen molecules are formed from hydrogen atoms reacting on dust grain surfaces; they are partly photodissociated by the interstellar UV radiation. Hence, hydrogen atoms and hydrogen molecules coexist in a diffuse cloud, depending on the cloud's visual extinction and density. Historically, a diffuse cloud was recognized as a weak extinction feature at optical wavelengths against background stars, where extinction appears as the reddening of starlight. The first interstellar molecule, CN, was detected by observing its electronic transition (B-X) at UV wavelengths toward ζ Ophiuchi, as introduced in Chap. 1.

The temperature of a diffuse cloud is determined by the balance between heating and cooling. In a diffuse cloud, interstellar UV radiation plays a major role in heating. When UV radiation ($h\nu$) is absorbed by dust grains, a photoelectron is ejected. Its kinetic energy is given as $h\nu - W$, where W is the work function of dust grains. Because W is on the order of a few eV, a substantial fraction of the photon energy will be carried by the ejected electron. The electron collides with a H_2 molecule (or H atom) and transfers a part of its kinetic energy to the H_2 molecule (or H atom). This process is called photoelectric heating and is an important heating mechanism in diffuse clouds (Fig. 4.1). Cosmic-ray heating also contributes in diffuse clouds, but its contribution is relatively minor.

On the other hand, diffuse clouds are cooled by various radiation processes. In particular, the fine-structure transitions of C^+ ($^2P_{3/2} - {}^2P_{1/2}$; 158 μm) and O ($^3P_1 - {}^3P_2$;63 μm) dominate the contributions to cooling (Fig. 4.2). When H atoms and H_2

S. Yamamoto, *Introduction to Astrochemistry*, Astronomy and Astrophysics Library 7, DOI 10.1007/978-4-431-54171-4_4

Fig. 4.1 Schematic of the mechanism of photoelectric heating

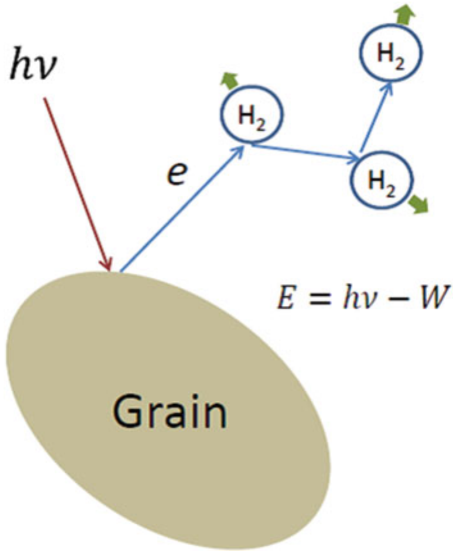

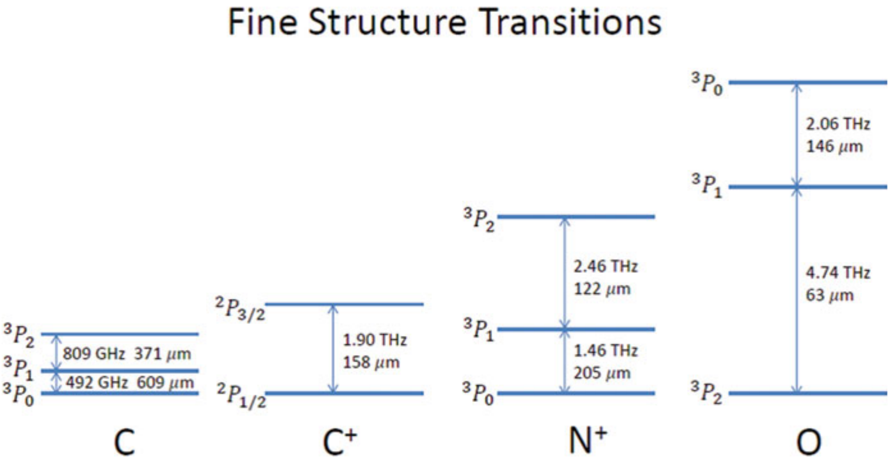

Fig. 4.2 Energy levels of the three fundamental atoms and ions

molecules collide with C^+ and O atoms, the latter are excited by energy transfer to the upper fine-structure levels of their electronic ground state. Through fine-structure transitions, the energy obtained through collisions is subsequently dispersed away from the cloud. Additionally, the rotational transitions of CO, as well as thermal emission of dust grains, also contribute to cooling. As a result, the kinetic temperature of the gas in a diffuse cloud becomes 20–100 K. It should be noted that this temperature can be regarded as the gas temperature. The gas temperature is different from the dust temperature in a diffuse cloud because of weak coupling

Table 4.1 Ionization potentials of the light atoms (eV)

Atom	IP	Atom	IP
H	13.598	Na	5.139
He	24.587	Mg	7.646
C	11.260	Si	8.151
N	14.534	P	10.486
O	13.618	S	10.360
F	17.422	Cl	12.967
Ne	21.564	Fe	7.870

between the gas and the dust grains due to low density. For a diffuse cloud, the gas is photoelectrically heated (the grains are also heated by direct absorption of UV photons). Typically, the gas temperature is higher than the dust temperature in a diffuse cloud.

A diffuse cloud is weakly ionized, with the degree of ionization being governed by photoionization. Cosmic rays give a minor contribution to the degree of ionization, as long as the visual extinction is lower than a few magnitudes. Interstellar UV radiation with an energy higher than 13.60 eV is absent in the interstellar medium, because it is absorbed by the overwhelming number of H atoms. Among the abundant second-row elements, the ionization potential of C atoms (11.30 eV) is lower than that of H atoms (13.60 eV); the ionization potentials of N and O atoms are higher than that of H (Table 4.1). Hence, carbon mainly exists as C^+ because of photoionization. In contrast, nitrogen and oxygen escape from photoionization, and they mainly exist as neutral atoms. In this book, the gas-phase abundance of C relative to the number of H nuclei is set at 7×10^{-5}, unless otherwise noted. This ratio is much lower than the cosmic abundance of C relative to H, 3.6×10^{-4}, because the depletion of C onto dust grains is taken into account. The degree of ionization relative to the total number of H nuclei is thus presumed to be 7×10^{-5}. Other elements such as S, Si, magnesium (Mg), and Fe with ionization potentials lower than 13.60 eV (Table 4.1) also contribute to the degree of ionization. However, their contributions are relatively minor in comparison with that of C, because these elements are heavily depleted on grains (Jenkins 2009).

In this chapter, we adopt a typical H_2 density of 100 cm^{-3}, a typical temperature of 100 K, and a visual extinction (A_v) of 1 magnitude, unless otherwise stated. Furthermore, the dominant form of hydrogen is assumed for simplicity to be H_2. Hence, the degree of ionization relative to H_2 is 1.4×10^{-4}. The gas-phase abundances of N and O relative to H_2 are set to 4.3×10^{-5} and 3.5×10^{-4}, respectively.

4.2 Molecules Detected in Diffuse Clouds

Historically, molecules in diffuse clouds were first detected in optical absorption spectra against bright stars corresponding to electronic transitions of molecules. Several fundamental molecules such as H_2, CO, C_2, CN, CH, OH, CH^+, and NH

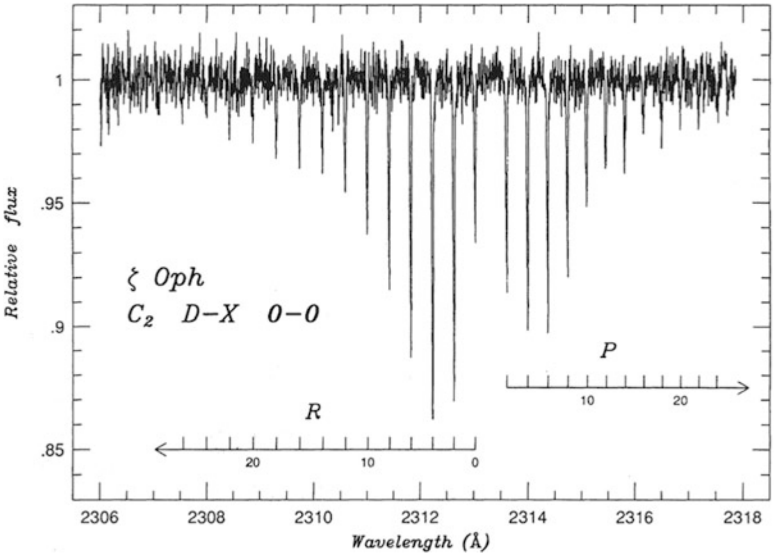

Fig. 4.3 UV spectrum of C_2 in a diffuse cloud toward ζ Oph. The P and R branch lines are well resolved. Note that only the transitions from even *J* levels of the ground electronic state are seen, because the odd *J* levels are missing owing to the Bose statistics of the two identical carbon atoms (Reprinted with permission from Lambert et al. (1995). Copyright 1995 American Astronomical Society)

have been detected in this way. The only polyatomic molecule detected by optical observations is C_3. These are "classical" diffuse-cloud species, which certainly exist in a cloud with an A_v less than 1. An example of the spectrum of C_2 observed toward ζ Ophiuchi is shown in Fig. 4.3. Dissociation energies of most molecules are typically less than 13.60 eV (see Table 4.2). Hence, molecules are readily photodissociated, which prevents molecular growth.

Many molecules have now been identified in diffuse clouds by observations in infrared and radio wavelengths. Infrared vibration-rotation lines of H_3^+ were detected toward bright infrared sources (e.g., McCall et al. 1998, 2002). In the radio-frequency band, absorption lines of polyatomic molecules such as HCN, HCO^+, and H_2CO in diffuse galactic-arm clouds have been detected toward continuum sources (e.g., Nyman 1983, Godard et al. 2010). These polyatomic molecules are difficult to identify using optical observations because of the predissociative nature of their electronic excited states. Hence, infrared/radio detections are essential for detecting these species in diffuse clouds. Recently, new interstellar species such as HF, OH^+, H_2O^+, and H_2Cl^+ were detected by observing their absorption lines in the submillimeter-wave and THz-wave regimes using ESA's *Herschel* Space Telescope (Sonnentrucker et al. 2010; Gerin et al. 2010; Lis et al. 2010; Neufeld et al. 2010). The light hydrides, XH_n, where X represents a heavy atom, usually have a ground-state rotational transition in the

Table 4.2 Ionization potentials (IP) and dissociation energies (DE) of molecules (eV)

Molecule	IP	DE
CH	10.64	3.47
OH	12.9	4.39
HF	16.04	5.87
HCl	12.75	4.43
SH	10.43	3.6
C_2	12.15	6.21
CN	14.17	7.76
CO	14.01	11.09
N_2	15.59	9.76
NO	9.26	6.50
O_2	12.07	5.12
CS	11.33	7.35
SO	10.3	5.36
PN	11.85	6.4
CH_2	10.40	4.34
CH_3	9.84	4.72
CH_4	14.40	4.49
C_2H	11.6	4.85
C_2H_2	10.51	5.71
C_3	12.97	7.3
CO_2	13.78	5.45
H_2O	12.61	5.12
NH_3	10.85	(4.4)
HCN	13.60	5.2
CH^+		4.09
OH^+		5.1
$C_2{}^+$		5.3
CO^+		8.34

submillimeter-wave and THz-wave regions. Because their Einstein A coefficient is usually large because of their high transition frequency (Eq. (2.30)), their critical density is too high to be observed in a diffuse cloud in emission (Eq. (2.50)). Hence, these transitions are usually detected in absorption against bright continuum sources. As an example, OH^+ and H_2O^+ spectra observed toward W49N are shown in Fig. 4.4. The C_3 molecule can be detected in the THz regime for a special reason. C_3 is a linear triatomic molecule without a permanent dipole moment, and hence rotational transitions are not allowed. However, the bending vibration mode (ν_2) is extremely low at 60 cm^{-1}. By taking advantage of this characteristic, its vibration-rotation transitions were detected in absorption in the 1.9 THz region toward bright continuum sources. In contrast to classical diffuse-cloud species, the physical conditions of sources where the above species are detected by radio observations are not well characterized in many cases; the actual visual extinction may be higher than 1 in some cases. Molecules detected in diffuse clouds are listed

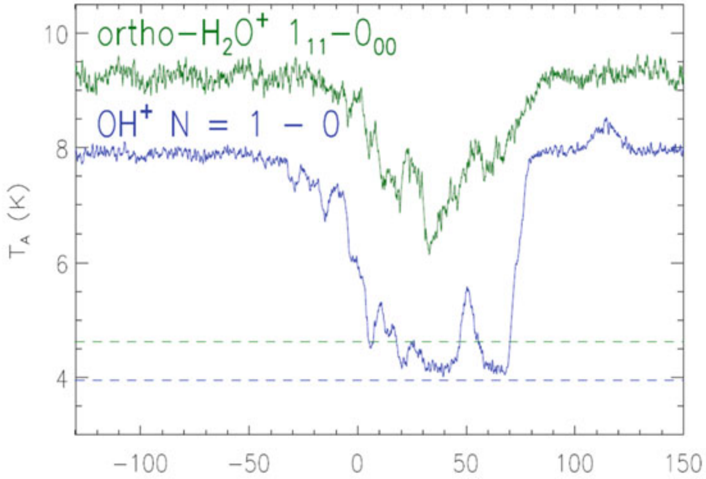

Fig. 4.4 THz spectrum of H_2O^+ and OH^+ observed toward W49N with the *Herschel* Space Telescope (Neufeld et al. 2010). Absorption peaks from various molecular clouds in our Galaxy along the line of sight can be seen (Reprinted with permission from Neufeld et al. (2010). Copyright 2010 European Southern Observatory)

in Table 4.3; additional observational details can be found in Snow and McCall (2006).

4.3 Carbon Chemistry

In this section, we consider the major formation pathways of carbon-bearing molecules in a step-by-step way. In a diffuse cloud, the dominant form of carbon in the gas phase is C^+. Hence, the reaction of C^+ with H_2 molecules has to be examined first, because H_2 is the most abundant molecule in collision with C^+. However, the ion–molecule reaction,

$$C^+ + H_2 \rightarrow CH^+ + H, \tag{4.1}$$

is known to be endothermic by 0.4 eV (4600 K), so that this reaction does not proceed at typical temperatures of diffuse clouds (100 K). Hence, we have to invoke the following radiative association reaction:

$$C^+ + H_2 \rightarrow CH_2{}^+ + h\nu. \tag{4.2}$$

The rate coefficient of this reaction is evaluated to be as small as $8 \times 10^{-16}\,\mathrm{cm^3\,s^{-1}}$ at 100 K (for details, see Kinetic Database for Astrochemistry (KIDA) database

Table 4.3 Molecules detected in diffuse clouds

Molecule	Method	Molecule	Method
H_2	O	HCl^+	R
$H_3{}^+$	IR	H_2Cl^+	R
CH	O, R	C_2	O
CH^+	O, R	C_2H	O, R
NH	O, R	CN	O, R
NH_2	R	HCN	R
NH_3	R	HNC	R
OH	O, R	N_2	O
OH^+	R	CO	OR
H_2O^+	R	HCO^+	R
H_2O	R	HOC^+	R
$OH_3{}^+$	R	H_2CO	R
HF	R	C_3	O, R
SH	R	$c-C_3H_2$	R
SH^+	R	CS	R
H_2S	R	SO_2	R
HCl	R	CF^+	R
HCO	R	$c-C_3H$	R

O: Detection in the optical and ultraviolet region. IR: Detection in the infrared region

R: Detection in the radio region including submillimeter wave and THz wave

(Wakelam et al. 2012)). Nevertheless, this reaction is important as a first step in the synthesis of organic molecules.

As discussed in Sect. 3.7, the timescale for this reaction is:

$$\tau = \frac{1}{k[H_2]}, \tag{4.3}$$

where k is the rate coefficient for reaction (4.2). Using the above value for the rate coefficient, the timescale is found to be 10^{13} s (3×10^5 yr) for a H_2 density of 10^2 cm^{-3}.

It should be noted that the radiative association reactions with abundant atoms such as:

$$C^+ + O \rightarrow CO^+ + h\nu \tag{4.4}$$

$$C^+ + N \rightarrow CN^+ + h\nu \tag{4.5}$$

are generally as slow as 10^{-18} cm^3 s^{-1}, because only one vibrational mode is available (see Sect. 4.4). Hence, these pathways cannot be the main reaction pathways for C^+.

Alternatively, C^+ can recombine with an electron to form a neutral carbon atom:

$$C^+ + e \rightarrow C + h\nu. \tag{4.6}$$

This process is a radiative recombination process with a rate coefficient of 2.8×10^{-12} cm^3 s^{-1}. From the degree of ionization (1.4×10^{-4}), the electron abundance is estimated to be 1.4×10^{-2} cm^{-3} for a H_2 density of 100 cm^{-3}. Therefore, the timescale for the electron recombination is 3×10^{13} s, which is comparable with the timescale for reaction (4.2). However, even if radiative recombination occurs, the C atom thus formed will further be photoionized to recover C^+:

$$C + h\nu \rightarrow C^+ + e. \tag{4.7}$$

The timescale of the photoionization can be as short as 10^{11} s. Hence, reaction (4.6) does not contribute to the formation of molecules through C. Based on these considerations, the major reaction pathway for C^+ is reaction (4.2), which gives $CH_2{}^+$.

Next, we consider in a similar way the reaction of $CH_2{}^+$. There are five major reaction channels for $CH_2{}^+$:

$$CH_2{}^+ + H_2 \rightarrow CH_3{}^+ + H \tag{4.8}$$

$$CH_2{}^+ + e \rightarrow CH + H \tag{4.9}$$

$$\rightarrow C + H_2 \tag{4.10}$$

$$\rightarrow C + H + H \tag{4.11}$$

and

$$CH_2{}^+ + h\nu \rightarrow CH^+ + H, \tag{4.12}$$

where the rate coefficients for the reactions are given in Table 4.6. Reaction (4.8) is the ion–molecule reaction with H_2, which proceeds at the Langevin rate. Reactions (4.9), (4.10), and (4.11) are electron recombination reactions, where the branching ratios to the three product channels are different (see Table 4.6). The sum of the rate coefficients for the three product channels is 1.2×10^{-6} cm^3 s^{-1} at 100 K. In contrast, reaction (4–12) is a photodissociation process.

The reaction timescales for the ion–molecule reaction with H_2, the electron recombination reaction, and the photodissociation are evaluated to be 6×10^6 s, 6×10^7, and 10^{10} s, respectively, where the H_2 density and the degree of ionization are assumed to be 100 cm^{-3} and 1.4×10^{-4}, respectively. The photodissociation rate for $CH_2{}^+$ is assumed to be the typical photodissociation rate of simple molecules. By comparing these timescales, one can see that the ion–molecule reaction with H_2 is much faster than the other processes. Reactions with other species such as O atoms are also subdominant, because their abundance relative to H_2 is as low as 3.5×10^{-4}. Therefore, $CH_2{}^+$ mainly reacts with H_2 molecules to produce $CH_3{}^+$. Electron recombination, photodissociation, and other reactions are minor processes for $CH_2{}^+$. In general, if a molecular ion can react with H_2 at the Langevin rate, this reaction represents the main reaction process for the molecular ion.

The next step is CH_3^+ reactions. There are five reaction pathways to consider:

$$CH_3{}^+ + H_2 \rightarrow CH_5{}^+ + h\nu \tag{4.13}$$

$$CH_3{}^+ + e \rightarrow CH_2 + H \tag{4.14}$$

$$\rightarrow CH + H_2 \tag{4.15}$$

$$\rightarrow CH + H + H \tag{4.16}$$

and

$$CH_3{}^+ + h\nu \rightarrow CH_2{}^+ + H. \tag{4.17}$$

Rate coefficients are listed in Table 4.6. Note that the ion–molecule reaction

$$CH_3{}^+ + H_2 \rightarrow CH_4{}^+ + H \tag{4.18}$$

is endothermic by 2.7 eV, because CH_3^+ is a stable molecular ion with a closed shell. Because this ion–molecule reaction does not proceed, the radiative association reaction with H_2 to form CH_5^+ (reaction 4.13) has to be considered. However, the rate coefficient for the radiative association is 4×10^{-15} cm^3 s^{-1}, and the timescale for this reaction is evaluated to be 2.5×10^{12} s for typical diffuse clouds. The timescale for this reaction is much longer than the timescale of the electron recombination reactions (9×10^7 s), which are calculated from the sum of the rate coefficients for the three branching pathways (reactions (4.14), (4.15), and (4.16); 7.8×10^{-7} cm^3 s^{-1}). Hence, the electron recombination is a dominant reaction pathway for CH_3^+ and produces the neutral species CH and CH_2. Photodissociation of CH_3^+ (reaction 4.17) can occur to some extent and produce CH_2^+ ions. Because CH_2^+ immediately reacts with H_2 to recover CH_3^+, the CH_3^+ photodissociation does not make a significant contribution to the loss of CH_3^+.

The neutral species formed by the electron recombination of CH_3^+ are subject to photodissociation:

$$CH_2 + h\nu \rightarrow CH + H \tag{4.19}$$

and

$$CH + h\nu \rightarrow C + H. \tag{4.20}$$

Eventually, C^+ is recovered by photoionization of C atoms by reaction (4.7). The timescale for photodissociation is typically on the order of 10^{10}–10^{11} s. In contrast, the following reactions with C^+ and O produce larger molecules:

$$CH + C^+ \rightarrow C_2{}^+ + H \tag{4.21}$$

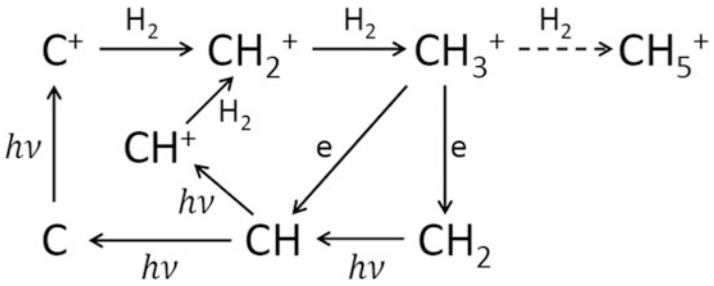

Fig. 4.5 Basic carbon chemistry in a diffuse cloud. Further growth to C_2 species and coupling with oxygen and nitrogen chemistry is not indicated

$$CH + O \rightarrow CO + H, \tag{4.22}$$

and

$$CH_2 + O \rightarrow CO + H + H \tag{4.23}$$

$$\rightarrow CO + H_2 \tag{4.24}$$

$$\rightarrow HCO + H \tag{4.25}$$

$C_2{}^+$ ions react with H_2 with the Langevin rate coefficient to produce C_2H^+, and then C_2H^+ is further hydrogenated to form $C_2H_2{}^+$. The electron recombination of $C_2H_2{}^+$ produces the neutral species C_2H and C_2. However, the timescales of reaction (4.21) are evaluated to be 10^{11} s; the timescales of reaction (4.22) and the sum of reactions (4.23, 4.24, and 4.25) are estimated to be 4.3×10^{11} s and 1.1×10^{11} s, respectively. Here, we assume that the abundance of oxygen atoms relative to H_2 is 3.5×10^{-4}. Hence, reaction pathways that produce larger species compete with photodissociation pathways. Even if large molecules are produced, they will be efficiently photodissociated. For this reason, large molecules are generally deficient in diffuse clouds. Figure 4.5 highlights the major processes of basic carbon chemistry in a diffuse cloud.

As demonstrated above, major reactions can be traced by considering the reaction timescales. Needless to say, subdominant reactions are also occurring in addition to the dominant reactions; these subdominant processes are important for producing some molecules. In chemical model calculations, all of the possible reactions are involved to evaluate molecular abundances. However, it should be stressed that the above consideration is useful in understanding which chemical processes are actually occurring in diffuse clouds.

4.4 Oxygen Chemistry

Because the ionization potential of the O atom is slightly higher than that of H atoms, oxygen mainly exists as neutral atoms in a diffuse cloud. The O atoms do not react with H_2 at low temperature, and hence the O atoms have to be ionized to react with H_2. In a diffuse cloud, the degree of ionization is largely governed by photoionization. Although cosmic-ray ionization only makes a minor contribution to the degree of ionization, it plays an important role in the formation of molecules via the production of H^+ and $H_2{}^+$:

$$H_2 + \text{cosmic rays} \rightarrow H^+ + H + e \tag{4.26}$$

$$\rightarrow H_2{}^+ + e \tag{4.27}$$

The rates for reactions (4.26 and 4.27) are assumed to be $2.9 \times 10^{-19}\ s^{-1}$ and $1.2 \times 10^{-17}\ s^{-1}$, respectively, in this book. Note that H^+ and $H_2{}^+$ are not produced by photoionization. Hence, cosmic-ray ionization is unique in producing these species. $H_2{}^+$ ions react with H_2 to give $H_3{}^+$ ions:

$$H_2{}^+ + H_2 \rightarrow H_3{}^+ + H. \tag{4.28}$$

The $H_3{}^+$ ion is a physically stable ion, which has a regular triangle configuration of three hydrogen nuclei. Although the H^+ ion does not react with H_2, it can ionize O by charge transfer:

$$H^+ + O \rightarrow O^+ + H. \tag{4.29}$$

This reaction is endothermic by 0.02 eV (230 K), which corresponds to the difference in ionization potentials between H and O. This endothermicity can be overcome by the thermal kinetic energy of the reactants at 100 K. The O^+ ion that is formed by reaction (4.29) successively reacts with H_2 at Langevin rates:

$$O^+ + H_2 \rightarrow OH^+ + H \tag{4.30}$$

$$OH^+ + H_2 \rightarrow OH_2{}^+ + H \tag{4.31}$$

and

$$OH_2{}^+ + H_2 \rightarrow OH_3{}^+ + H. \tag{4.32}$$

As discussed in Sect. 4.3, reactions with H_2 dominate a given ionic species when the reactions proceed at the Langevin rate. Therefore, reactions (4.30, 4.31, and 4.32) are major chemical processes, although photodissociation and electron recombination will make supplemental contributions. In addition to the reactions starting from O^+, the OH^+ ion formed by the reaction:

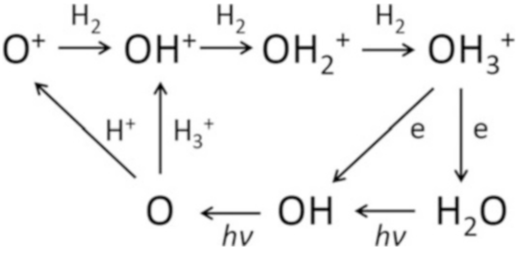

Fig. 4.6 Basic oxygen chemistry in diffuse clouds

$$O + H_3^+ \rightarrow OH^+ + H_2 \tag{4.33}$$

also plays an important role. The OH^+ ion is hydrogenated by reactions (4.31 and 4.32) to form OH_3^+.

The OH_3^+ ion formed in the above reactions is a protonated H_2O molecule, which is isoelectronic with NH_3. It is therefore a physically stable ion that does not react further with H_2, even through radiative association. Hence, OH_3^+ is subject to an electron recombination reaction to yield the neutral species OH and H_2O:

$$OH_3^+ + e \rightarrow H_2O + H \tag{4.34}$$

$$\rightarrow OH + H_2 \tag{4.35}$$

$$\rightarrow OH + H + H \tag{4.36}$$

$$\rightarrow O + H_2 + H \tag{4.37}$$

where the branching ratio is given in Sect. 3.6. The above series of reactions is known as the major formation route for H_2O and OH in the gas phase. The H_2O and OH molecules are broken up by photodissociation, thereby recovering the O atoms. The basic oxygen chemistry is depicted in Fig. 4.6.

An important molecule connecting carbon chemistry and oxygen chemistry is CO, which is produced by the following reactions:

$$CH_3^+ + O \rightarrow HCO^+ + H_2 \tag{4.38}$$

$$C^+ + OH \rightarrow CO^+ + H \tag{4.39}$$

$$CO^+ + H_2 \rightarrow HCO^+ + H \tag{4.40}$$

and

$$HCO^+ + e \rightarrow CO + H. \tag{4.41}$$

As discussed in Sect. 4.3, reaction (4.38) competes with the electron recombination reaction and hence is a minor pathway for the loss reaction of CH_3^+. Similarly, reaction (4.39) competes with the photodissociation of OH. The timescale for OH to react with C^+ is evaluated to be 10^{11} s, which is comparable to the timescale for photodissociation. However, these reactions are important formation mechanisms for CO as well as other processes such as neutral–neutral reactions (reactions (4.22, 4.23, and 4.24)). The CO molecule is mainly destroyed by photodissociation in diffuse clouds.

4.5 Nitrogen Chemistry

Because the ionization potential of N atoms (14.534 eV) is substantially higher than that of H atoms, nitrogen mainly exists as neutral N atoms in diffuse clouds. Hence, the formation of nitrogen-bearing molecules has to start from a reaction of N atoms with other species. Because N atoms do not react with H_3^+, unlike the O atoms, they first react with neutral species:

$$\mathrm{CH_2 + N \rightarrow HCN + H} \tag{4.42}$$

$$\mathrm{C_2 + N \rightarrow CN + C} \tag{4.43}$$

and

$$\mathrm{CH + N \rightarrow CN + H,} \tag{4.44}$$

although all of these processes compete with photodissociation. The HCN and CN molecules thus formed are subject to photodissociation:

$$\mathrm{HCN} + h\nu \rightarrow \mathrm{CN + H} \tag{4.45}$$

and

$$\mathrm{CN} + h\nu \rightarrow \mathrm{C + N.} \tag{4.46}$$

In contrast, hydrogenation of N atoms is not easy in interstellar conditions, because there is no efficient pathway to form N^+. A possible mechanism is:

$$\mathrm{He^+ + CN \rightarrow N^+ + C + He,} \tag{4.47}$$

where He^+ is formed by cosmic-ray ionization. Alternatively, N^+ can be formed by direct ionization of N atoms by cosmic ray-induced UV radiation. Once N^+ is formed, the following hydrogenation reactions proceed successively:

$$\mathrm{N^+ + H_2 \rightarrow NH^+ + H,} \tag{4.48}$$

$$\mathrm{NH^+ + H_2 \rightarrow {NH_2}^+ + H,} \tag{4.49}$$

and

$$NH_2{}^+ + H_2 \rightarrow NH_3{}^+ + H. \tag{4.50}$$

The next hydrogenation reaction,

$$NH_3{}^+ + H_2 \rightarrow NH_4{}^+ + H, \tag{4.51}$$

has an activation barrier of 0.089 eV (1000 K), so that the reaction rate at 100 K is as low as 2×10^{-13} cm^3 s^{-1} (see Sect. 3.3). The timescale of this reaction is 5×10^{10} s, which is much longer than the timescale for electron recombination (1.3×10^8 s):

$$NH_3{}^+ + e \rightarrow NH_2 + H \tag{4.52}$$

$$\rightarrow NH + H + H \tag{4.53}$$

The neutral molecules thus produced are destroyed by photodissociation. Hence, NH_3, which is produced by electron recombination of $NH_4{}^+$, is not efficiently produced in diffuse clouds. Note that reaction (4.48), the first step of the above series of reactions to form NH_3, is known to be endothermic by 0.019 eV (220 K). However, this reaction proceeds in diffuse clouds with kinetic temperatures of 100 K. In contrast, the situation differs for a cold molecular cloud, as will be discussed in Chap. 5.

4.6 Chemical Model of a Diffuse Cloud

In the previous sections, chemical processes have been discussed for each category of chemical elements in order to trace the major formation routes of molecules. However, it is necessary to treat all chemical reactions simultaneously in simulations of chemical compositions in diffuse clouds. To this end, rate equations for a number of species have to be prepared. Focusing on species A, the rate equation takes the form:

$$\frac{d[A]}{dt} = k_1[B][C] - k_2[A][D] - k_3[A] + \ldots. \tag{4.54}$$

When n species including a free electron are considered, n rate equations can be set up.

These are essentially nonlinear differential equations. In a diffuse cloud, the major destruction process is photodissociation, whose timescale is typically 10^{10} s. However, the timescale for formation of molecules is much longer. For instance, the $C^+ + H_2$ reaction is a bottleneck for carbon chemistry. For C^+, the timescale for the reaction with H_2 is 10^{13} s. For O, the timescale of the charge transfer eq. $O + H^+ \rightarrow O^+ + H$ (reaction (4.29)) and that of the proton transfer reaction $H_3{}^+ + O \rightarrow OH^+ + H_2$ (reaction (4.33)) are also as long as 10^{13} s. Hence, the timescale for chemical equilibrium is determined by the timescale for destruction, which is 10^{10} s (~300 year), according to Eq. (3.88). This timescale is very short in comparison with the dynamical timescale of the cloud, i.e., the free-fall time, which is given as:

$$t_{ff} = \left(\frac{3\pi}{32G\rho_0}\right)^{\frac{1}{2}} = 3.4 \times 10^5 \left(\frac{10^4\ \mathrm{cm}^{-3}}{n(\mathrm{H}_2)}\right)^{\frac{1}{2}}\ \text{year}, \tag{4.55}$$

where G stands for the gravitational constant and ρ_0 is the initial mass density. For uniform clouds with a H_2 density of 10^2 cm^{-3}, the free-fall time is 3.4×10^6 year. (1.1×10^{14} s). Therefore, the chemical composition can follow changes in physical conditions. Thus, the chemical composition of a diffuse cloud is approximately in a steady state.

In the steady-state approximation, the left-hand-side term of Eq. (4.54) can be ignored. Hence, the set of rate equations simplifies to a set of (nonlinear) simultaneous equations. Vanishing abundances for all species represent a trivial solution, but are physically meaningless. Hence, a conservation equation for each element should be added to constrain the total abundance of the elements. If the number of chemical elements is m, the total number of equations becomes $n+m$. However, only $n-m-1$ equations are independent if charge conservation is considered. The equations can be solved numerically for given elemental abundances and physical conditions (density, temperature, UV radiation strength, and visual extinction).

An example of a model calculation for two representative diffuse clouds is given in Tables 4.4 and 4.5 along with the observational results. Table 4.4 shows the results of the classical but representative model toward ζ Oph reported by van Dishoeck and Black (1986). These authors considered the density structure of a cloud using a polytropic equation with a negative index and calculated chemical composition as well as the level populations of H_2 molecules and a few dominant atomic ions. Approximately 500 reactions for 120 species were considered for the chemical network of the model. This model represents one of the most comprehensive models of diffuse clouds. The atomic and molecular abundances calculated by the model mostly agree with the observed abundances. Nevertheless, the calculated CH^+ abundance significantly differs from observations. Table 4.5 includes the model toward ζ Per reported by Le Petit et al. (2004). These authors considered a two-phase model, which consists of a diffuse phase and a dense phase with number densities of H nuclei of 100 cm^{-3} and 2×10^4 cm^{-3}, respectively. The goal of this model was to obtain better fits to observational results, including H_3^+ abundances. The chemical model employs about 1000 reactions of about 100 species. The CH^+ abundance is again underestimated in the model. By including shocks, the model produces better agreement with the observed abundances.

Table 4.4 An example of the chemical model for the ζ Oph diffuse cloud[a]

Species	Model[b]	Observation[b]
H	5.1(20)	(5.2+−0.2)(20)
H_2	4.2(20)	(4.3+−0.3)(20)
C^+	4.2(17)	(9.3+−4.5)(17)
C	3.3(15)	(3.2+−0.6)(15)
CH	1.8(13)	(2.5+−0.1)(13)
CH^+	2.8(10)	(2.9+−0.1)(13)
C_2	1.7(13)	(1.5+−0.2)(13)
O	6.9 (17)	(7.1+−0.5)(17)
OH	4.5(13)	(4.8+−0.5)(13)
CO	1.9(14)	(2.0+−0.3)(14)
N	8.0(16)	(5.2+−3.3)(16)
CN	1.4(12)	(2.5+−0.1)(12)

[a] van Dishoeck and Black (1986). Various models with different parameters are given, among which Model G is presented here as an example. The cosmic-ray ionization rate is assumed to be 8×10^{-17} s^{-1}. The number density of the hydrogen nuclei is 350 cm^{-3}, and the temperature at the cloud center is 30 K. The UV radiation field is assumed to be three times the standard interstellar UV radiation

[b] $a(b)$ denotes $a \times 10^b$

Table 4.5 An example of the chemical model for the ζ Per diffuse cloud[a, b]

Species	Diffuse phase	Dense phase	Total	Observation
H	3.5(20)	1.4(17)	3.5(20)	5.7(20) 7.1(20)
H_2	4.5(20)	1.1(19)	4.6(20)	3.2(20) 7.1(20)
HD	1.5(16)	3.9(13)	1.5(16)	2.0(15) 1.1(16)
C^+	1.6(17)	1.2(15)	1.6(17)	1.8(17)
C	1.4(15)	1.6(15)	2.8(15)	2.9(15) 3.6(15)
CO	3.5(14)	7.9(13)	4.2(14)	5.4(14) –
CH	2.4(12)	5.6(12)	8.0(12)	1.9(13) 2.0(13)
CH^+	2.2(10)	2.7(08)	2.2(10)	3.5(12) –
C_2	1.9(11)	1.9(13)	1.9(13)	1.6(13) 2.2(13)
C_3	3.1(08)	2.1(12)	2.1(12)	1.0(12)
CN	6.6(10)	1.9(12)	1.9(12)	2.7(12) 3.3(12)
NH	3.5(11)	1.2(09)	3.5(11)	9.0(11) –
O	4.0(17)	7.2(15)	4.0(17)	0.2(18) 1.0(18)
OH	4.9(13)	1.1(09)	4.9(13)	4.0(13) –
$H_3{}^+$	2.9(13)	5.0(09)	2.9(13)	8.0(13) –

[a] Le Petit et al. (2004). The model assumes the two phases: a diffuse cloud ($n_H \sim 100$ cm^{-3}) and a dense cloud ($n_H \sim 2 \times 10^4$ cm^{-3}). The observed value indicates the possible range

[b] $a(b)$ denotes $a \times 10^b$

4.7 CH$^+$ Problem

Conventional chemical models predict a lower abundance of CH$^+$. This result occurs because CH$^+$ is not on the main path of the carbon chemistry discussed above. Because the C$^+$ + H$_2$ reaction to form CH$^+$ is endothermic (reaction 4.1), CH$^+$ is mainly formed by the photoionization of CH:

$$\mathrm{CH} + h\nu \rightarrow \mathrm{CH}^+ + \mathrm{e}, \tag{4.56}$$

whose rate coefficient is denoted as k_{pi}. Destruction of CH$^+$ occurs mainly via the reaction of H$_2$:

$$\mathrm{CH}^+ + \mathrm{H}_2 \rightarrow \mathrm{CH_2}^+ + \mathrm{H}. \tag{4.57}$$

The rate coefficient of this reaction is denoted as k_r. Under the steady-state approximation, we obtain:

$$k_{pi}[\mathrm{CH}] = k_r[\mathrm{CH}^+][\mathrm{H}_2]. \tag{4.58}$$

Here, the electron recombination reaction:

$$\mathrm{CH}^+ + \mathrm{e} \rightarrow \mathrm{C} + \mathrm{H} \tag{4.59}$$

makes a minor contribution in loss of CH$^+$ and hence for simplicity is ignored. Because CH is produced through sequential reactions starting from the C$^+$ + H$_2$ reaction with a rate coefficient of k_{ra}, we can assume that every C$^+$ + H$_2$ reaction yields CH at the simplest approximation. CH is destroyed by photodissociation. With the rate coefficient of the photodissociation denoted by k_{pd}, we obtain the approximate relation:

$$k_{ra}[\mathrm{C}^+][\mathrm{H}_2] = k_{pd}[\mathrm{CH}]. \tag{4.60}$$

The fractional abundance of CH, [CH]/[H$_2$], is then:

$$\frac{[\mathrm{CH}]}{[\mathrm{H}_2]} = \frac{k_{ra}[\mathrm{C}^+]}{k_{pd}} \sim 5.5 \times 10^{-8}, \tag{4.61}$$

which agrees well with the observed abundance in diffuse clouds (Tables 4.4 and 4.5). Indeed, a good correlation between the CH column density and the H$_2$ column density in diffuse clouds has been established (e.g., Federman 1982; Sheffer et al. 2008; Sakai et al. 2012) (Fig. 4.7). The [CH$^+$]/[H$_2$] ratio is then obtained using Eqs. (4.58 and 4.61):

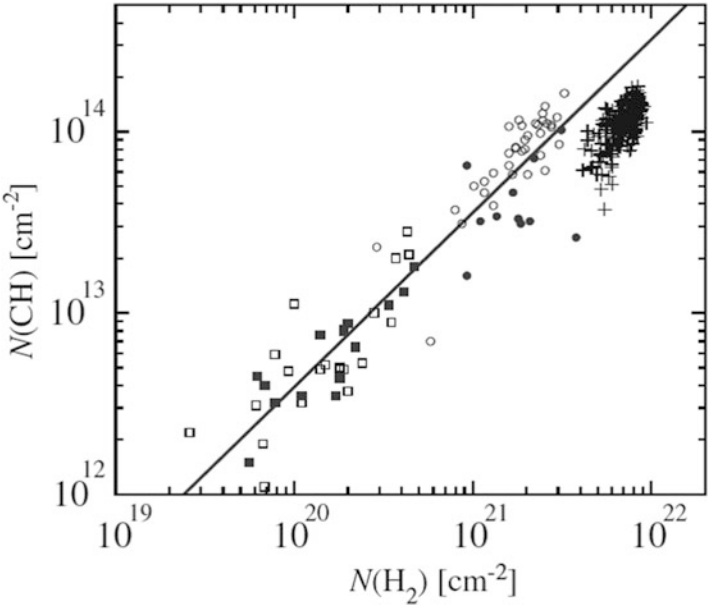

Fig. 4.7 Correlation between the column density of CH and that of CO in diffuse clouds observed with optical and radio observations. A good correlation can be seen in the low-$N(H_2)$ regime. However, a possible turnover may exist in the high-column density regime, which corresponds to denser clouds (Reprinted with permission from Sakai et al. (2012). Copyright 2012 European Southern Observatory)

$$\frac{[\mathrm{CH}^+]}{[\mathrm{H}_2]} = \frac{k_{pi}k_{ra}[\mathrm{C}^+]}{k_r k_{pd}[\mathrm{H}_2]} \sim 1.4 \times 10^{-11}, \tag{4.62}$$

where we assume that [C^+]~[e]. This value is much lower than the observed abundance (Tables 4.4 and 4.5).

Hence, additional considerations are necessary for the production of CH^+. To overcome the endothermicity of reaction (4.1), increasing the temperature of the cloud is necessary, at least temporarily. The most probable mechanism for increasing the temperature is shocks induced by cloud–cloud collisions or turbulence. Because the endothermicity of reaction (4.1) is 0.4 eV, which corresponds to 4600 K, a shock velocity of 10–15 km s^{-1} is sufficient for this reaction to overcome the endothermicity for adiabatic shock (Sect. 7.9). In this mechanism, CH^+ is formed in regions of the clouds that are influenced by shocks. The correlation between the CH^+ column density and the H_2 column density is indeed weak in comparison with the CH column density (Sheffer et al. 2008). Furthermore, an apparent velocity shift is observed between the CH and CH^+ lines (Crane et al. 1995) (Fig. 4.8), which also supports the idea of enhancement by shocks.

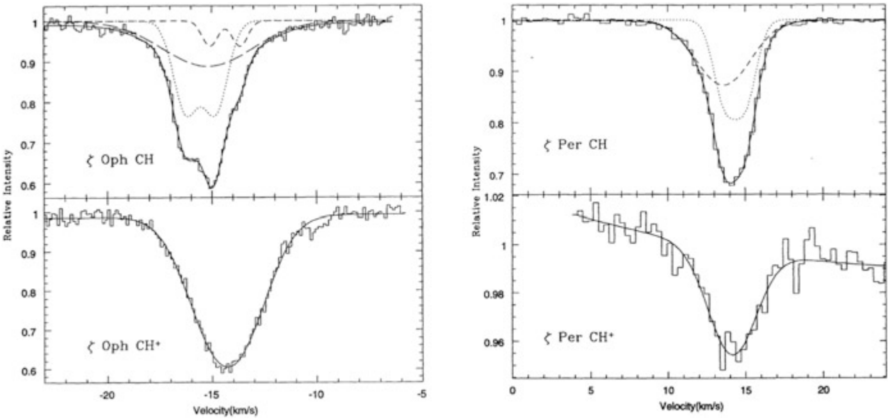

Fig. 4.8 Comparison of the spectral line profile of the rovibronic lines of CH and CH^+ observed toward ζ Oph and ζ Per. The difference between CH and CH^+ is evident, which may be related to the shock enhancement of CH^+ (Reprinted with permission from Crane et al. (1995). Copyright 1995 American Astronomical Society)

4.8 H_3^+ Problem

The H_3^+ ion is a fundamental ionic species in diffuse clouds, which is mainly formed by cosmic-ray ionization and then in subsequent ion–molecule reactions with H_2 (reactions (4.27 and 4.28)). This species does not give ordinary rotational spectra because of a lack of a permanent dipole moment. Instead, infrared vibration-rotation transitions are possible, which were first observed in the laboratory by Oka (1980). McCall et al. (1998, 2002) detected infrared vibration-rotation transition lines of H_3^+ in absorption toward various molecular clouds against bright infrared sources. An example of the H_3^+ spectrum is shown in Fig. 4.9. The H_3^+ column density is found to be unexpectedly high; for instance, it is 3.8×10^{14} cm^{-2} toward Cyg OB2 12 (McCall et al. 1998).

The H_3^+ abundance can be estimated from the following simple consideration (McCall et al. 2002). The H_3^+ ion is formed by reactions (4.27 and 4.28) and destroyed by the dissociative recombination reaction or by the proton transfer reaction with CO:

$$H_3{}^+ + e \rightarrow H_2 + H \tag{4.63}$$

$$\rightarrow H + H + H \tag{4.64}$$

$$H_3{}^+ + CO \rightarrow HCO^+ + H_2. \tag{4.65}$$

By considering reactions (4.27, 4.28, 4.63, 4.64, and 4.65), the H_3^+ abundance can be represented as:

Fig. 4.9 Infrared absorption spectra of H_3^+ observed toward three infrared sources (Indriolo et al. 2007) (Reprinted with permission from Indriolo et al. (2007). Copyright 2007 American Astronomical Society)

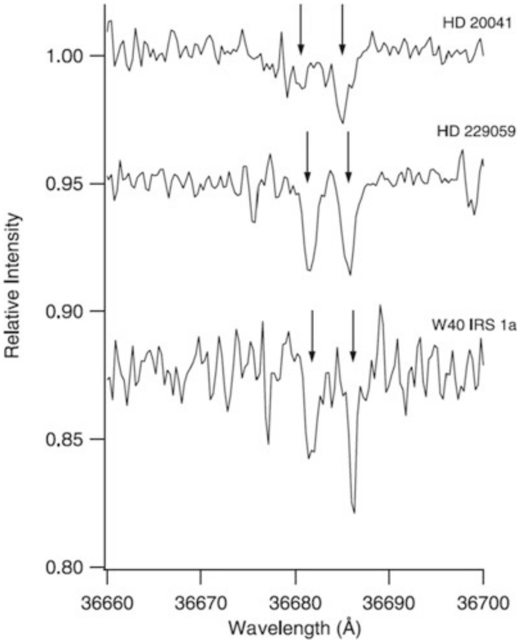

$$[\mathrm{H}_3^+] = \frac{\zeta[\mathrm{H}_2]}{k_r[e] + k_{\mathrm{co}}[\mathrm{CO}]}, \tag{4.66}$$

where ζ denotes the cosmic-ray ionization rate for reaction (4.27), and k_r and k_{co} represent the rate coefficients for the sum of reactions (4.63 and 4.64) and reaction (4.65), respectively. In a diffuse cloud, the first term in the denominator is dominant because of the high electron abundance. Hence, the following relation holds to a good approximation:

$$[\mathrm{H}_3^+] = \frac{\zeta[\mathrm{H}_2]}{k_r[\mathrm{e}]}. \tag{4.67}$$

The $[\mathrm{e}]/[\mathrm{H}_2]$ ratio is the degree of ionization (10^{-4}) for diffuse clouds. When we employ 10^{-17} s^{-1} for ζ and 1.2×10^{-7} cm^3 s^{-1} for k_r (the sum of the rate coefficients of reactions (4.63 and 4.64)), the $[\mathrm{H}_3^+]$ abundance should be approximately 6×10^{-7} cm^{-3}. This value is independent of density. We then can estimate the necessary "line-of-sight length" of the diffuse cloud where H_3^+ is detected. This is as long as 210 pc toward Cyg OB2 12.

The above estimation means that the $[\mathrm{H}_3^+]$ abundance derived above is underestimated. The degree of ionization, the $[\mathrm{e}]/[\mathrm{H}_2]$ ratio, was confirmed toward ζ Per by observations of C^+; the electron recombination rate k_r was measured accurately in the laboratory. Hence, it is suggested that the cosmic-ray ionizationrate

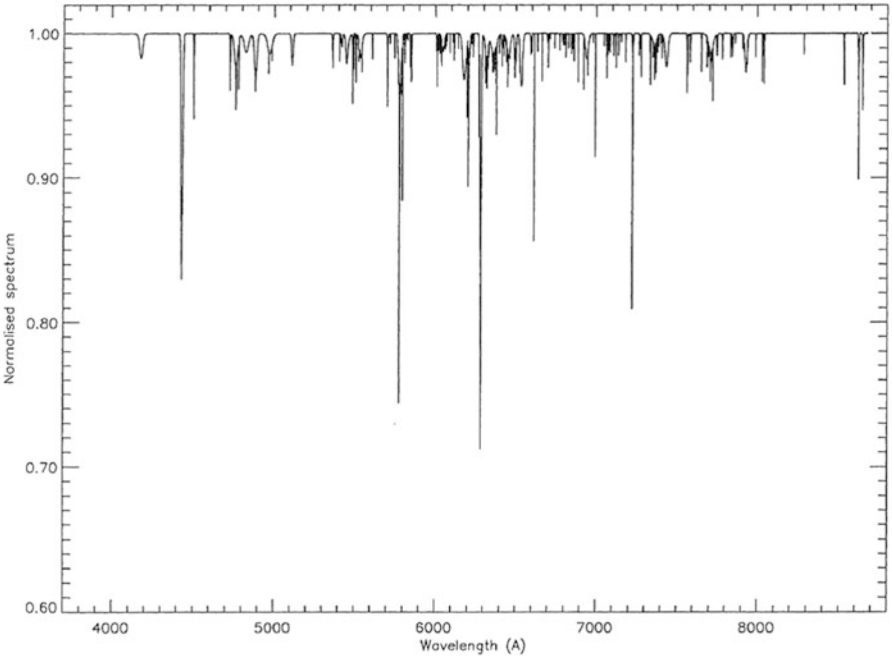

Fig. 4.10 Composite spectrum of DIBs (Reprinted with permission from Jenniskens and Desert (1994). Copyright 1994 European Southern Observatory)

is higher for diffuse clouds. This assumption may be reasonable, because low-energy cosmic rays that cannot penetrate into dense molecular clouds can contribute to the degree of ionization of diffuse clouds. According to the recent H_3^+ observations, the ζ value is derived to be $3.5^{+5.3}_{-3.0} \times 10^{-16}$ s^{-1} (Indriolo and McCall 2012).

4.9 Diffuse Interstellar Bands

In the visible spectrum observed toward field stars, hundreds of absorption features caused by diffuse clouds along the line of sight are reported that cannot be assigned to transitions of any known molecules or solid particles (Fig. 4.10) (e.g., Tielens 2014; Snow and Destree 2011; Snow and McCall 2006; Sarre 2006; Tielens and Snow 1995; Jenniskens and Desert 1994). These features are called "diffuse interstellar bands" (DIBs). Since their first report in 1922 (Heger 1922; Merrill 1934), DIBs have been a long-standing problem in astronomy and for spectroscopy. There was a debate as to whether the carriers were molecules or solid particles. Now, the carriers of DIBs are thought to be large molecules or molecular ions. Indeed, some DIBs show a broad spectral feature characteristic of rotational envelopes of vibronic transitions (e.g., Oka et al. 2013). So far, a few proposals

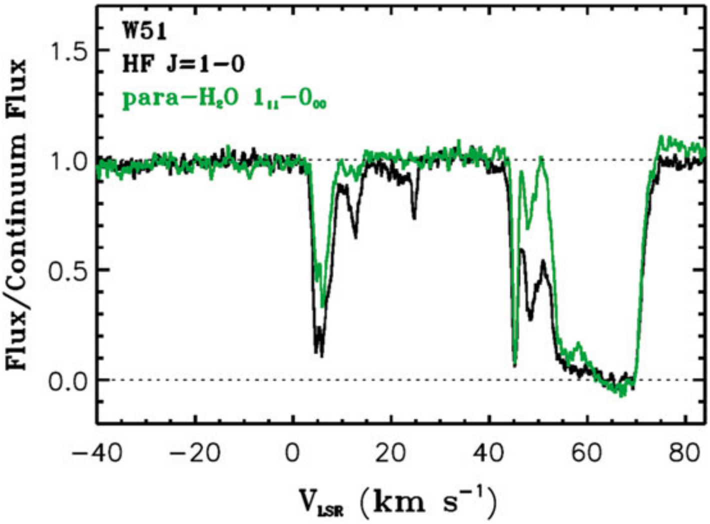

Fig. 4.11 THz spectra of HF and H_2O toward the Galactic continuum source W51 (Reprinted with permission from Sonnentrucker et al. (2010). Copyright 2010 European Southern Observatory)

for carriers of DIBs have been reported based on laboratory spectroscopic studies. Proposed carriers include C_7^-, HC_5N^+, HC_4H^+, and *l*-C_3H_2. However, none of these candidates have signatures that exactly match with the observations (Tielens 2014). Recently, $C_{60}{}^+$, which was identified as a carrier of DIBs at 963.3 nm and 957.8 nm based on its laboratory spectrum in the Ar matrix (Foing and Ehrenfreund 1994), was confirmed by laboratory spectroscopic measurements of $C_{60}{}^+$ in the gas phase (Campbell et al. 2015; Walker et al. 2015).

From an astronomy perspective, various observational efforts have been undertaken to classify DIBs based on correlations (e.g., Thorburn et al. 2003; McCall et al. 2010). Some DIBs are correlated with the intensity of the C_2 band; some are correlated with the H column density rather than the H_2 column density. Despite these efforts, the carrier of DIBs has not been identified. Full identification of DIBs will be a real challenge for astronomy and spectroscopy.

Problems

4.1 The heats of formation of C^+, CH^+, and H are known to be 1798, 1619, and 216 kJ mol^{-1}, respectively. Evaluate the endothermic energy for the $C^+ + H_2 \rightarrow CH^+ + H$ reaction in units of eV. Note that the heat of formation of H_2 is zero by definition.

4.2 With the Herschel Space Telescope, HF has been detected in some diffuse clouds (Fig. 4.11). In a diffuse cloud, the F atom can react with a H_2 molecule to give HF, although the reaction has a slight reaction barrier:

$$F + H_2 \rightarrow HF + H.$$

The rate coefficient for this reaction is given by:

$$k_1 = 1.0 \times 10^{-10} \exp\left(-\frac{400\text{K}}{T}\right) \text{cm}^3\text{s}^{-1}.$$

Moreover, HF is lost by reacting with C^+ to form CF^+:

$$C^+ + HF \rightarrow CF^+ + H.$$

The rate coefficient for this reaction is:

$$k_2 = 7.2 \times 10^{-9} \left(\frac{T}{300\text{K}}\right)^{-0.5} \text{cm}^3\text{s}^{-1}.$$

The CF^+ ion that is produced recombines with an electron to reproduce the F atom. The rate coefficient for the recombination is:

$$k_3 = 5.2 \times 10^{-8} \left(\frac{T}{300\text{K}}\right)^{-0.8} \text{cm}^3\text{s}^{-1}.$$

HF is also destroyed by photodissociation for which the rate coefficient is:

$$k_4 = 1.17 \times 10^{-10} \exp(-2.0 A_v) \text{ cm}^3\text{s}^{-1}.$$

By considering the above reactions among F, HF, and CF^+, evaluate the abundances of F, HF, and CF^+ relative to H_2 in a diffuse cloud under the steady-state approximation, where the elemental abundance of F atoms relative to H_2 is set to 3.6×10^{-8}.

4.3 Consider the basic carbon chemistry shown in Fig. 4.5.
   (a) Set up the rate equations for the species indicated in Fig. 4.5 (except for ${CH_5}^+$), and solve the equations numerically using the steady-state approximation. Assume that the H_2 density, temperature, and visual extinction are 100 cm^{-3}, 100 K, and 1 magnitude, respectively. The rate constants that are necessary for the calculation are listed in Table 4.6. Ignore the photodissociation of H_2 for simplicity. Compare your result with that of Table 4.7.
   (b) Using your result, estimate the formation and destruction rates of ${CH_2}^+$.

Table 4.6 Rate coefficients of some reactions appearing in the text[a]

Reaction	Rate	Rate ($A_v = 1$, $T = 100$ K)	Reaction no.
$C + h\nu \rightarrow C^+ + e$	$2.2 \times 10^{-10} \exp(-2.96A_v)\ \text{s}^{-1}$	$1.1 \times 10^{-11}\ \text{s}^{-1}$	4.7
$C^+ + e \rightarrow C + h\nu$	$2.36 \times 10^{-12} \left(\frac{T}{300}\right)^{-0.3} \exp\left(-\frac{17.6}{T}\right)$ $\text{cm}^3\ \text{s}^{-1}$	$2.8 \times 10^{-12}\ \text{cm}^3\ \text{s}^{-1}$	4.6
$C^+ + H_2 \rightarrow CH_2{}^+ + h\nu$	$2.0 \times 10^{-16} \left(\frac{T}{300}\right)^{-1.3} \exp\left(-\frac{23}{T}\right)$ $\text{cm}^3\ \text{s}^{-1}$	$6.6 \times 10^{-16}\ \text{cm}^3\ \text{s}^{-1}$	4.2
$CH^+ + H_2 \rightarrow CH_2{}^+ + H$	$1.2 \times 10^{-9}\ \text{cm}^3\ \text{s}^{-1}$	$1.2 \times 10^{-9}\ \text{cm}^3\ \text{s}^{-1}$	4.57
$CH^+ + e \rightarrow C + H$	$1.5 \times 10^{-7} \left(\frac{T}{300}\right)^{-0.4}\ \text{cm}^3\ \text{s}^{-1}$	$2.3 \times 10^{-7}\ \text{cm}^3\ \text{s}^{-1}$	4.59
$CH_2{}^+ + H_2 \rightarrow CH_3{}^+ + H$	$1.6 \times 10^{-9}\ \text{cm}^3\ \text{s}^{-1}$	$1.6 \times 10^{-9}\ \text{cm}^3\ \text{s}^{-1}$	4.8
$CH_2{}^+ + e \rightarrow CH + H$	$1.60 \times 10^{-7} \left(\frac{T}{300}\right)^{-0.6}\ \text{cm}^3\ \text{s}^{-1}$	$3.1 \times 10^{-7}\ \text{cm}^3\ \text{s}^{-1}$	4.9
$\rightarrow C + H_2$	$7.68 \times 10^{-8} \left(\frac{T}{300}\right)^{-0.6}\ \text{cm}^3\ \text{s}^{-1}$	$1.5 \times 10^{-7}\ \text{cm}^3\ \text{s}^{-1}$	4.10
$\rightarrow C + H + H$	$4.03 \times 10^{-7} \left(\frac{T}{300}\right)^{-0.6}\ \text{cm}^3\ \text{s}^{-}-^{1}$	$7.8 \times 10^{-7}\ \text{cm}^3\ \text{s}^{-1}$	4.11
$CH_3{}^+ + e \rightarrow CH_2 + H$	$7.75 \times 10^{-8} \left(\frac{T}{300}\right)^{-0.5}\ \text{cm}^3\ \text{s}^{-1}$	$1.3 \times 10^{-7}\ \text{cm}^3\ \text{s}^{-1}$	4.14
$\rightarrow CH + H_2$	$1.95 \times 10^{-7} \left(\frac{T}{300}\right)^{-0.5}\ \text{cm}^3\ \text{s}^{-1}$	$3.4 \times 10^{-7}\ \text{cm}^3\ \text{s}^{-1}$	4.15
$\rightarrow CH + H + H$	$2.00 \times 10^{-7} \left(\frac{T}{300}\right)^{-0.4}\ \text{cm}^3\ \text{s}^{-1}$	$3.1 \times 10^{-7}\ \text{cm}^3\ \text{s}^{-1}$	4.16
$CH_2 + h\nu \rightarrow CH + H$	$4.9 \times 10^{-10} \exp(-1.67A_v)\ \text{s}^{-1}$	$9.2 \times 10^{-11}\ \text{s}^{-1}$	4.19
$CH + h\nu \rightarrow C + H$	$6.6 \times 10^{-10} \exp(-1.15A_v)\ \text{s}^{-1}$	$2.1 \times 10^{-10}\ \text{s}^{-1}$	4.20
$CH + h\nu \rightarrow CH^+ + e$	$5.5 \times 10^{-10} \exp(-2.84A_v)\ \text{s}^{-1}$	$3.2 \times 10^{-11}\ \text{s}^{-1}$	4.56
$H + H \rightarrow H_2$	$4.4 \times 10^{-18} \sqrt{T}\ \text{cm}^3\ \text{s}^{-1}$ [b]	$4.4 \times 10^{-17}\ \text{cm}^3\ \text{s}^{-1}$	
$O^+ + H_2 \rightarrow OH^+ + H$	$1.7 \times 10^{-9}\ \text{cm}^3\ \text{s}^{-1}$	$1.7 \times 10^{-9}\ \text{cm}^3\ \text{s}^{-1}$	4.30
$O + H_3{}^+ \rightarrow OH^+ + H_2$	$7.98 \times 10^{-10} \left(\frac{T}{300}\right)^{-0.16} \exp\left(-\frac{1.40}{T}\right)$ $\text{cm}^3\ \text{s}^{-1}$	$9.38 \times 10^{-10}\ \text{cm}^3\ \text{s}^{-1}$	4.33
$OH^+ + H_2 \rightarrow OH_2{}^+ + H$	$1.01 \times 10^{-9}\ \text{cm}^3\ \text{s}^{-1}$	$1.01 \times 10^{-9}\ \text{cm}^3\ \text{s}^{-1}$	4.31
$OH_2{}^+ + H_2 \rightarrow OH_3{}^+ + H$	$6.40 \times 10^{-10}\ \text{cm}^3\ \text{s}^{-1}$	$6.40 \times 10^{-10}\ \text{cm}^3\text{s}^{-1}$	4.32
$OH_3{}^+ + e \rightarrow H_2O + H$	$7.09 \times 10^{-8} \left(\frac{T}{300}\right)^{-0.5}\ \text{cm}^3\ \text{s}^{-1}$	$1.22 \times 10^{-7}\ \text{cm}^3\ \text{s}^{-1}$	4.34
$\rightarrow OH + H_2$	$5.37 \times 10^{-8} \left(\frac{T}{300}\right)^{-0.5}\ \text{cm}^3\ \text{s}^{-1}$	$9.30 \times 10^{-8}\ \text{cm}^3\ \text{s}^{-1}$	4.35
$\rightarrow OH + H + H$	$3.05 \times 10^{-7} \left(\frac{T}{300}\right)^{-0.5}\ \text{cm}^3\ \text{s}^{-1}$	$5.28 \times 10^{-7}\ \text{cm}^3\ \text{s}^{-1}$	4.36
$\rightarrow O + H_2 + H$	$5.60 \times 10^{-9} \left(\frac{T}{300}\right)^{-0.5}\ \text{cm}^3\ \text{s}^{-1}$	$9.70 \times 10^{-9}\ \text{cm}^3\ \text{s}^{-1}$	4.37
$H_2O + h\nu \rightarrow OH + H$	$8.0 \times 10^{-10} \exp(-2.20A_v)\ \text{s}^{-1}$	$8.86 \times 10^{-11}\ \text{s}^{-1}$	
$OH + h\nu \rightarrow O + H$	$3.9 \times 10^{-10} \exp(-2.20A_v)\ \text{s}^{-1}$	$4.32 \times 10^{-11}\ \text{s}^{-1}$	
$O + H^+ \rightarrow O^+ + H$	$6.86 \times 10^{-10} \left(\frac{T}{300}\right)^{0.26} \exp\left(-\frac{224.3}{T}\right)$ $\text{cm}^3\ \text{s}^{-1}$	$5.46 \times 10^{-11}\ \text{cm}^3\ \text{s}^{-1}$	4.29
$H_2 + cr \rightarrow H^+ + H + e$	$2.9 \times 10^{-19}\ \text{s}^{-1}$	$2.9 \times 10^{-19}\ \text{s}^{-1}$	4.26
$H_2 + cr \rightarrow H_2{}^+ + e$	$1.2 \times 10^{-17}\ \text{s}^{-1}$	$1.2 \times 10^{-17}\ \text{s}^{-1}$	4.27
$H_2{}^+ + H_2 \rightarrow H_3{}^+ + H$	$2.08 \times 10^{-9}\ \text{cm}^3\ \text{s}^{-1}$	$2.08 \times 10^{-9}\ \text{cm}^3\ \text{s}^{-1}$	4.28

[a] The rate coefficients are mostly taken from the UMIST Database for Astrochemistry (McElroy et al. 2013). The unit of T is K

[b] The rate coefficient of H_2 production per H atom per number density of H nucleus ([H]+2[H_2]). See Eq. (6.38)

Table 4.7 Calculated abundances of molecules for simple carbon chemistry (cm^{-3})[a]

Species	Abundance
H	0.178
H_2	99.9
C	0.127(−3)
C^+	0.139(−1)
CH^+	0.105(−8)
$CH_2{}^+$	0.590(−8)
$CH_3{}^+$	0.869(−7)
CH_2	0.175(−5)
CH	0.402(−5)
e	0.139(−1)

[a] The result of the simple model for Problem 3, calculated using the rate coefficient listed in Table 4.6. The temperature is assumed to be 100 K. The number density of the H nuclei is 200 cm^{-3}, and the visual extinction is 1 magnitude. The carbon abundance relative to the H nuclei is set to be 1.4×10^{-4}. The format $a(b)$ denotes $a \times 10^b$

References

E.K. Campbell, M. Holz, D. Gerlich, J.P. Maier, Nature **523**, 322 (2015)

P. Crane, D.L. Lambert, Y. Sheffer, Astrophys. J. Suppl. **99**, 107 (1995)

S.R. Federman, Astron. Astrophys. **257**, 125 (1982)

B.H. Foing, P. Ehrenfreund, Nature **369**, 296 (1994)

M. Gerin, M. De Luca, J. Black, et al., Astron. Astrophys. **518**, L110 (2010)

B. Goddard, E. Falgarone, M. Gerin, P. Hily-Brant, M. De Luca, Astron. Astrophys. **520**, A20 (2010)

M.L. Heger, Lick Obs. Bull. **10**, 141 (1922)

N. Indriolo, B.J. McCall, Astrophys. J. **745**, 91 (2012)

N. Indriolo, T.R. Geballe, T. Oka, B.J. McCall, Astrophys. J. **671**, 1736 (2007)

E.B. Jenkins, Astrophys. J. **700**, 1299 (2009)

P. Jenniskens, F.-X. Desert, Astron. Astrophys. Suppl. **106**, 39 (1994)

D.L. Lambert, Y. Sheffer, S.R. Federman, Astrophys. J. **438**, 740 (1995)

F. Le Petit, E. Roueff, E. Herbst, Astron. Astrophys. **417**, 993 (2004)

D.C. Lis, J.C. Pearson, D.A. Neufeld, et al., Astron. Astrophys. **521**, L9 (2010)

B.J. McCall, T.R. Geballe, K.H. Hinkle, T. Oka, Science **279**, 1910 (1998)

B.J. McCall, K.H. Hinkle, T.R. Geballe, G.H. Moriarty-Schieven, N.J. Evans II, K. Kawaguchi, S. Takano, V.V. Smith, T. Oka, Astrophys. J. **567**, 391 (2002)

B.J. McCall, M.M. Drosback, J.A. Thorburn, D.G. York, S.D. Friedman, L.M. Hobbs, B.L. Rachford, T.P. Snow, P. Sonnentrucker, D.E. Welty, Astrophys. J. **708**, 1628 (2010)

D. McElroy, C. Walsh, A. J. Markwick, M. A. Cordiner, K. Smith, T. J. Millar, Astron. Astrophys. **550**, A36 (2013). http://udfa.ajmarkwick.net/

P.W. Merrill, Publ. Astron. Soc. Pac. **46**, 206 (1934)

D.A. Neufeld, J.R. Goicoechea, P. Sonnentrucker, et al., Astron. Astrophys. **521**, L10 (2010)

L.-A. Nyman, Astron. Astrophys. **120**, 307 (1983)

T. Oka, Phys. Rev. Lett. **45**, 531 (1980)

T. Oka, D.E. Welty, S. Johnson, D.G. York, J. Dahlstrom, L.M. Hobbs, Astrophys. J. **773**, 42 (2013)

N. Sakai, H. Maezawa, T. Sakai, K.M. Menten, S. Yamamoto, Astron. Astrophys. **546**, A103 (2012)

P.J. Sarre, J. Mol. Spectrosc. **238**, 1 (2006)

Y. Sheffer, M. Rogers, S.R. Federman, N.P. Abel, R. Gredel, D.L. Lambert, G. Shaw, Astrophys. J. **687**, 1075 (2008)

T.P. Snow, B.J. McCall, Annu. Rev. Astron. Astrophys. **44**, 367 (2006)

T.P. Snow, J.D. Destree, in '*PAHs and the Universe*', 2011, ed. by C. Joblin, A.G.G.M. Tielens EAS Publ. Ser. **46**, p. 341

P. Sonnentrucker, D.A. Neufeld, T.G. Phillips, et al., Astron. Astrophys. **521**, L12 (2010)

J.A. Thorburn, L.M. Hobbs, B.J. McCall, T. Oka, D.E. Welty, S.D. Friedman, T.P. Snow, P. Sonnentrucker, D.G. York, Astrophys. J. **584**, 339 (2003)

A.G.G.M. Tielens, in *Proceedings IAU Symposium No. 297*, eds by Cami, J., Cox, N.L.J., (2014) p. 399

A.G.G.M. Tielens, T.P. Snow, *The diffuse interstellar bands* (Kluwer, Dordrecht, 1995)

E.F. van Dishoeck, J.H. Black, Astrophys. J. Suppl. **62**, 109 (1986)

V. Wakelam et al., Astrophys. J. Suppl. **199**, 21 (2012)

G.A. Walker, D.A. Bohlender, J.P. Maier, E.K. Campbell, Astrophys. J. **812**, L8 (2015)

Chapter 5
Chemistry of Molecular Clouds I: Gas Phase Processes

5.1 Physical Conditions in Molecular Clouds

Although diffuse clouds are generally in pressure equilibrium, they can start to collapse because of gravitational instability (Jeans instability) or cloud–cloud collisions, for instance. Interstellar UV radiation penetrates deeply in diffuse clouds and partly dissociates H_2 molecules. As the cloud density increases, interstellar UV radiation becomes shielded at the center of the cloud. As a result, photodissociation of H_2 molecules is inefficient in the interiors of a cloud, and most of the hydrogen exists in the form of H_2. Such clouds are referred to as *molecular clouds*. The H_2 density of a molecular cloud typically ranges from 10^2–10^6 cm^{-3}. The visual extinction, A_v, is larger than a few magnitudes, which corresponds to a H_2 column density of a few times 10^{21} cm^{-2} or higher. Molecular clouds are often called dark clouds because nearby molecular clouds can be recognized as dark patches obscuring the light of background stars. The sizes of molecular clouds range from 0.1 to 10 pc. Isolated small molecular clouds are called Bok globules and have masses around a few $M_\odot$. Large molecular clouds extending over 10 pc are called giant molecular clouds (GMCs) and have masses as high as 10^5–10^6 $M_\odot$.

The gas kinetic temperature of a molecular cloud is determined by the thermal balance between heating and cooling processes. Because interstellar UV radiation does not contribute to cloud heating, cosmic-ray heating plays a major role. For this reason, heating is not as efficient in molecular clouds as in diffuse clouds, where photoelectric heating by interstellar UV radiation is efficient. The major cooling processes in molecular clouds are via molecular line emissions and dust continuum emissions. Because the H_2 molecule does not contribute to cooling via line emission, the rotational emissions of the next abundant molecule, CO, is an important cooling mechanism. Note that the infrared vibration–rotation lines allowed by an electric quadrupole moment can contribute in special conditions such as cloud peripheries and shocked regions, where excitation of these transitions effectively occurs. From the balance of these heating and cooling mechanisms, the gas kinetic

S. Yamamoto, *Introduction to Astrochemistry*, Astronomy and Astrophysics Library 7, DOI 10.1007/978-4-431-54171-4_5

temperature of molecular clouds is maintained at around 8–15 K, unless other heating mechanisms, such as heating by newborn stars, contribute. This temperature is much lower than that of a diffuse cloud (100 K). In the following sections, we adopt 10 K as a representative temperature of a molecular cloud.

Because of the high visual extinction of molecular clouds, optical absorption spectroscopy—mainly employed for identification of molecules in a diffuse cloud—cannot be used for a molecular cloud. Infrared absorption spectroscopy is often useful to identify the major constituents of gaseous molecules and solid materials contained in dust grains and mantles. Principally, radio observation of rotational emission lines is the most important technique for investigating in detail the chemical compositions of molecular clouds. Because the typical rotational energy level spacing of molecules is on the order of a few K, rotational levels are readily excited by collisions with H_2 molecules, even in the low-temperature conditions of molecular clouds. The subsequent emission can thus be observed with radio telescopes.

The structures, physical conditions, and distributions of molecular clouds have extensively been studied by observing rotational emission lines of CO. Rotational transitions of CO have small Einstein A coefficients because of the small dipole moment, resulting in low critical densities (Sect. 2.3). Hence, the rotational transitions of CO are conveniently used to trace a wide range of densities that cover the diffuse peripheries of clouds to the deep interiors of molecular clouds. Observations of CO and its rare isotopic species (^{13}CO, C^{18}O, and C^{17}O) have been conducted toward various sources, including the Milky Way and external galaxies (e.g., Dame et al. 1987; Bally et al. 1987; Mizuno et al. 1995; Kuno et al. 2007; Fukui et al. 2008).

The dense part of a molecular cloud, where the H_2 density is higher than ~10^4 cm^{-3}, is called the *dense core*. A dense core is usually a region of a complex structure within a molecular cloud, but isolated cores such as Bok globules also exist. Nearby dense cores are recognized as dark patches in optical images; initial systematic radio studies of dense cores were conducted using rotational emission of CO, NH_3, and HC_3N toward such optical features (e.g., Myers et al. 1983, Benson and Myers 1989). Dense cores have generally been observed using rotational emission of, for example, NH_3, CS, CCS, $H^{13}CO^+$, and N_2H^+, which have high critical densities (10^4 cm^{-3} or higher). Thermal emission from dust grains in the millimeter-wave and submillimeter-wave regimes is also a good tracer of dense cores, because such cores are usually optically thin in dust emission. Recent advances in millimeter-wave and submillimeter-wave bolometer cameras made it possible to conduct large-scale surveys of dense cores from their dust emissions (e.g., Kirk et al. 2006; Palmeirim et al. 2013).

Because dense cores are the birthplaces of new stars (Beichman et al. 1986), the physical conditions and dynamics of dense cores have been extensively studied in relation to star-formation physics. Dense cores have typical masses of 1–10 $M_\odot$ and typical sizes of 0.1 pc. Spectral line widths of the high-density tracers listed above typically range from 0.1 to 1 km s^{-1} in dense cores. The turbulent velocity width Δv_{turb} is calculated from the observed velocity width Δv_{obs} by correcting the thermal velocity width $\Delta v_{\mathrm{thermal}}$:

$$\Delta v_{\mathrm{obs}}^2 = \Delta v_{\mathrm{turb}}^2 + \Delta v_{\mathrm{thermal}}^2, \tag{5.1}$$

and

$$\Delta v_{\mathrm{thermal}}^2 = \frac{8(\ln 2) k_{\mathrm{B}} T}{m}, \tag{5.2}$$

where Δv_{obs}, Δv_{turb}, and $\Delta v_{\mathrm{thermal}}$ each refers to the full-width half maximum of the corresponding distribution of the line-of-sight component of Doppler velocity (Myers 1983), and m and k_B represent the mass of the observed molecule and Boltzmann constant, respectively. The turbulent velocity often exceeds the adiabatic sound speed of H_2 gas (0.22 km s^{-1} at 10 K). Hence, supersonic turbulence often exists in dense cores. Dense cores are gravitationally bound in general and are subject to gravitational contraction with timescales on the order of the free-fall time, given by Eq. (4.55). The timescale is 3.4×10^5 year for a H_2 density of 10^4 cm $^{-3}$. Because turbulence and magnetic fields will support a dense core against gravitational contraction, the actual lifetime would be longer than the free-fall time by a factor of a few. Dense cores before they harbor protostars are called *starless cores* or *prestellar cores*. If protostars are associated with dense cores, they are called *protostellar cores*. In the following sections, we consider a representative starless core with a H_2 density of 10^4 cm^{-3} and a visual extinction of 10 magnitudes (a H_2 column density of 10^{22} cm^{-2}). Chemical processes in protostellar cores will be presented in Chap. 7.

5.2 Molecules in Molecular Cloud Cores

The chemistry of starless cores is an important area of astrochemistry. Although chemical compositions have been studied toward many starless cores using radio observations, these compositions are mostly discussed based on observations of just a few abundant molecules, except for a few representative sources. One of the well-studied starless cores in chemistry is the Taurus Molecular Cloud-1 CP (TMC-1 CP). This core is a very famous source of rich chemistry. Since its discovery by Morris et al. (1976), many new interstellar molecules have been detected in TMC-1 CP. Its chemical composition was studied in an unbiased way using a spectral scan with a wide frequency range (a spectral line survey). A compressed spectrum toward TMC-1 CP in the frequency range of 8–50 GHz observed with the Nobeyama 45 m telescope is shown in Fig. 5.1. Two series of regularly spaced lines with spacing of about 9 GHz and 3.4 GHz can readily be recognized, which are ascribed to the rotational spectral lines of HC_3N and HC_5N. Table 5.1 lists representative molecules detected in TMC-1 CP and their column densities. When

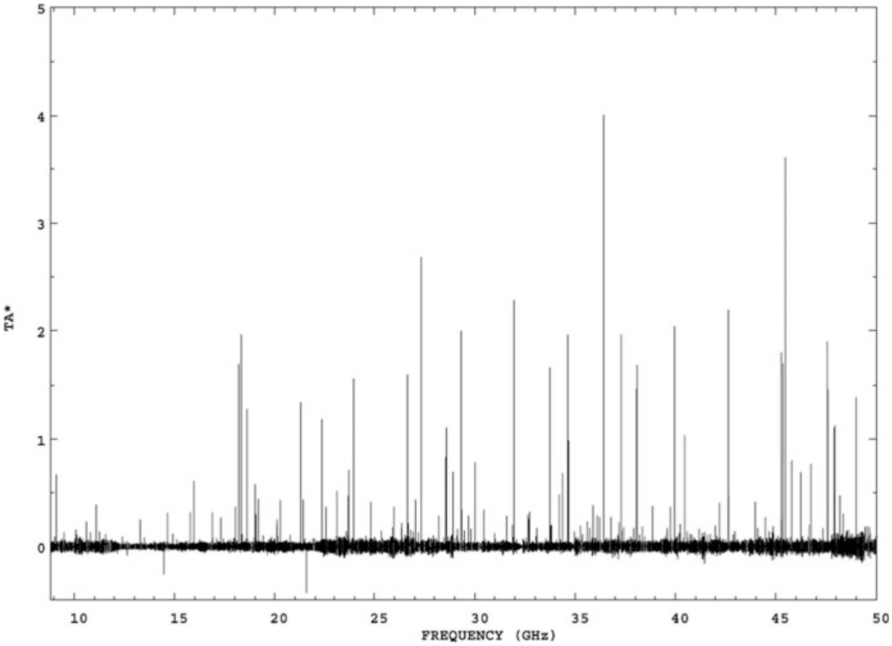

Fig. 5.1 Compressed spectrum observed toward the cold starless core TMC-1. Regular progressions of rotational spectral lines of HC_3N and HC_5N are clearly seen (Reprinted with permission from Kaifu et al. 2004)

Table 5.1 is compared with a list of interstellar molecules (Table 1.2), one can see that various series of carbon-chain molecules such as HC_nN, C_nH, C_nH_2 (cumulene type), C_nN, C_nO, and C_nS are dominant in TMC-1 CP. It should be noted that the negative ions (anions) C_6H^- and C_8H^- have also been detected in TMC-1 CP. The existence of a variety of carbon-chain molecules is the most characteristic feature of the chemical composition of starless cores. TMC-1 CP had long been the brightest source of carbon-chain molecules until the recent discovery of a brighter source, Lupus-1A (Sakai et al. 2010b) (Fig. 5.2).

However, starless cores do not all have uniform chemical compositions; significant chemical differences are observed among cores. An example is shown in Fig. 5.3. L1521B is a starless core in the Taurus region for which the chemical composition is similar to that of TMC-1 (CP). Spectral lines of carbon-chain molecules are strong in L1521B. In contrast, L134N looks quite different from L1521B, because the spectral lines of carbon-chain molecules are not as bright as those in L1521B. In particular, the lines of HC_5N are almost absent. However, the NH_3 line is brighter than in TMC-1 (CP) and L1521B. These trends are difficult to explain solely based on differences in physical conditions. The temperature of starless cores is usually around 10 K and does not vary much. The critical densities of the lines shown in Fig. 5.3 are all around 10^4 cm^{-3}, and hence the lines trace a

Table 5.1 Column densities of molecules reported for TMC-1

Molecule	Column density	Reference
SO	1.4×10^{13}	a
NS	6.8×10^{12}	b
OH	1.5×10^{15}(narrow)	c
N_2H^+	2.9×10^{12}	a
NH_3	1.9×10^{14}	d
H_2S	$<4.7\times10^{12}$	e
CN	7.8×10^{12}	a
$C^{18}O$	3.3×10^{15}	a
$C^{34}S$	7.3×10^{12}	g
CH	0.41×10^{14}(narrow)	f
	1.6×10^{14}(broad)	
$H^{13}CN$	3.7×10^{12}	g
$HN^{13}C$	6.2×10^{12}	g
$H^{13}CO^+$	1.4×10^{12}	a
HNCO	4×10^{12}	h
HCNO	$<1.4\times10^{10}$	h
HOCN	$<1.9\times10^{10}$	i
HNCS	$<2\times10^{12}$	j
HCOOH	$<7\times10^{12}$	j
H_2CN	1.5×10^{11}	k
$H_2{}^{13}CO$	3×10^{11}(NH_3 peak)	l
H_2CS	6.1×10^{13}	m
NH_2CHO	$<1\times10^{12}$	j
CH_3OH	1.7×10^{13}	a
CH_3SH	$<4\times10^{12}$	j
CCO	6×10^{11}	n
CCS	6.6×10^{13}	d
CCH	$>6.7\times10^{14}$	o
CH_2CN	$(2-10)\times10^{13}$	p
H_2CCO	1.1×10^{13}	j
CH_3CN	6.7×10^{12}	q
CH_3CHO	6×10^{12}	r
$HCOOCH_3$	$<8\times10^{12}$	j
C_3N	7×10^{12}	s
C_3O	1.4×10^{12}	t
C_3S	1.3×10^{12}	d
c-C_3H	6×10^{12}, 1.03×10^{13}	u, v
l-C_3H	8.4×10^{11}	v
HC_3N	1.7×10^{14}	d
HNC_3	3.8×10^{11}	w
HCCNC	2.9×10^{11}	x
c-C_3H_2	5.8×10^{13}	v

(continued)

Table 5.1 (continued)

Molecule	Column density	Reference
l-C_3H_2	2.5×10^{12}	y
$HCCCNH^+$	1.0×10^{12}	z
HCCCHO	1.5×10^{12}	aa
CH_3CCH	2.0×10^{14}	ab
C_3H_6	4×10^{13}	ac
C_4H	2.9×10^{14}	o
C_4H^-	$< 3.7\times10^{10}$	ad
l-C_4H_2	7.1×10^{12}	o
C_5H	1.7×10^{12}	o
HC_5N	6.3×10^{13}	ae
CH_3C_3N	1.8×10^{12}	af
CH_3C_4H	1.8×10^{12}	ag
C_6H	3.0×10^{12}	ah
C_6H^-	1.2×10^{11}	ai
l-C_6H_2	1.8×10^{11}	ah
CH_3C_5N	7.4×10^{11}	af
HC_7N	2.3×10^{13}	o
CH_3C_6H	3×10^{12}	ag
C_8H	4.6×10^{11}	ai
C_8H^-	2.1×10^{10}	ai
HC_9N	4.8×10^{12}	o

[a] Pratap et al. ApJ, 486, 862 (1997)
[b] McGonagle et al. ApJ, 422, 621 (1994)
[c] Harju et al. A&A, 353, 1065 (2000)
[d] Suzuki et al. ApJ, 392, 551 (1992)
[e] Minh et al. ApJ, 345, L63 (1989)
[f] Sakai et al. A&A, 546, A103 (2012)
[g] Hirota et al. ApJ, 503, 717 (1998)
[h] Marcelino et al. ApJ, 690, L27 (2009)
[i] Marcelino et al. A&A, 516, A105 (2010)
[j] Irvine et al. ApJ, 342, 871 (1989)
[k] Ohishi et al. ApJ, 427, L51 (1994)
[l] Minh et al. A&A, 298, 213 (1995)
[m] Minowa et al. ApJ, 491, L63 (1997)
[n] Ohishi et al. ApJ, 380, L39 (1991)
[o] Sakai et al. ApJ, 672, 371 (2008)
[p] Irvine et al. ApJ, 334, L107 (1988a)
[q] Matthews and Sears ApJ, 267, L53 (1983)
[r] Matthews et al. ApJ, 290, 609 (1985)
[s] Friberg et al. ApJ, 241, L99 (1980)
[t] Brown et al. ApJ, 297, 302 (1985)
[u] Yamamoto et al. ApJ, 322, L55 (1987)
[v] Fosse et al. ApJ, 552, 168 (2001)
[w] Kawaguchi et al. ApJ, 396, L49 (1992a)
[x] Kawaguchi et al. ApJ, 386, L51(1992b)
[y] Cernicharo et al. ApJ,368,L39(1991)
[z] Kawaguchi et al. ApJ, 420, L95 (1994)

(continued)

Table 5.1 (continued)

[aa]Irvine et al. ApJ, 335, L89 (1988b)
[ab]Irvine et al. ApJ, 248, L113 (1981)
[ac]Marcelino et al. ApJ, 665, L127 (2007)
[ad]Agundez et al. A&A, 478, L19 (2008)
[ae]Takano et al. ApJ, 361, L15 (1990)
[af]Snyder et al. ApJ, 647, 412 (2006)
[ag]Remijan et al. ApJ, 643, L37 (2006)
[ah]Sakai et al. ApJ, 667, L65 (2007)
[ai]Brunken et al. ApJ, 664, L43 (2007)

similar density region in each cloud. Chemical diversity is clearly evident among starless cores.

Such chemical differentiation is also seen within starless cores. Figure 5.4 shows integrated intensity maps of CCS and NH_3 of a filamentary cloud including TMC-1, which is called the TMC-1 ridge (Hirahara et al. 1992). The CCS emission is bright in the southern part of the TMC-1 ridge, particularly toward TMC-1 CP (labeled D); the NH_3 emission is intense in the northern region of the TMC-1 ridge. Such a chemical gradient was first recognized by Little et al. (1979) based on observations of HC_5N and NH_3, and it was later studied by several authors (Olano et al. 1988; Tolle et al. 1981; Hirahara et al. 1992; Pratap et al. 1997). Figure 5.5 shows integrated intensity maps of CCS and N_2H^+ toward the starless core, L1544 (e.g., Aikawa et al. 2001). The CCS emission is weak toward the center of the core, which is the peak of the dust continuum emission. Conversely, the N_2H^+ emission is strong and centrally condensed. Hence, a systematic chemical gradient from the outer to the inner region of the core is evident for L1544. These trends will be discussed later in light of chemical processes in molecular clouds.

5.3 H_3^+ Chemistry

Because interstellar UV radiation does not penetrate molecular clouds, the ionization source is cosmic rays (c.r.):

$$H_2 + \text{c.r.} \rightarrow {H_2}^+ + e \tag{5.3}$$

$$\rightarrow H^+ + H + e. \tag{5.4}$$

The rate coefficients for reactions (5.3) and (5.4) are 1.2×10^{-17} s^{-1} and 2.9×10^{-19} s^{-1}, respectively. The ${H_2}^+$ ion reacts immediately with H_2 to form ${H_3}^+$:

$${H_2}^+ + H_2 \rightarrow {H_3}^+ + H, \tag{5.5}$$

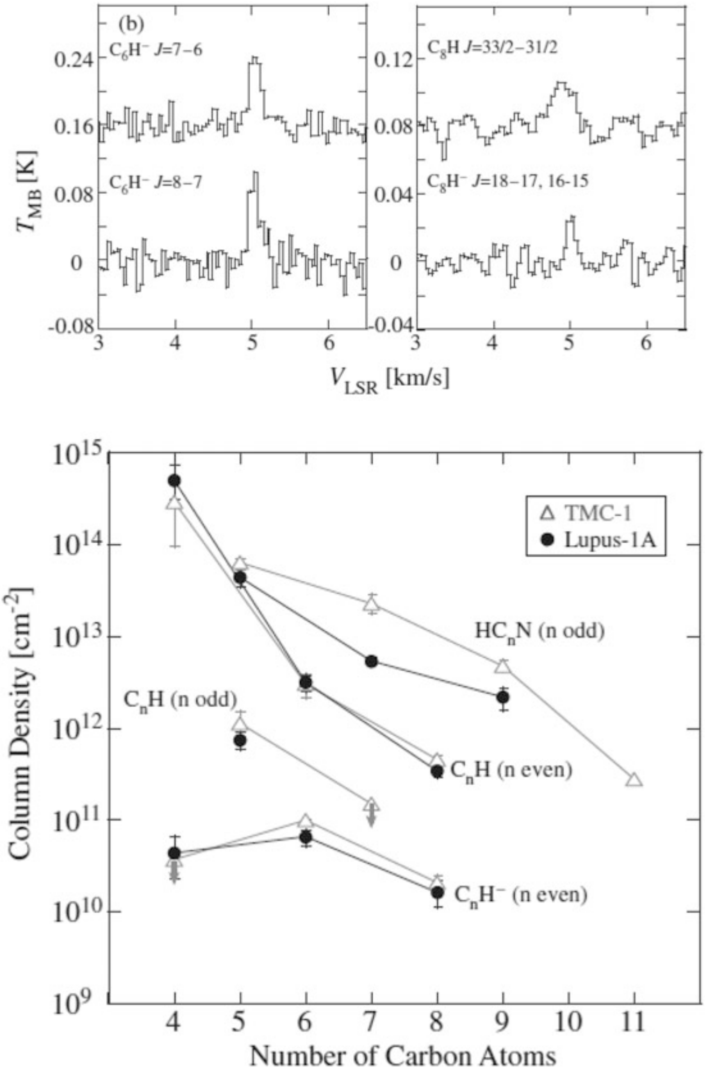

Fig. 5.2 (*Top panels*) Spectra of carbon-chain anions, C_6H^- and C_8H^-, and C_8H observed toward the starless core Lupus-1A. The spectral line profile of C_8H is broadened due to unresolved hyperfine structure. (*Bottom panels*) The column densities of various carbon-chain molecules observed toward TMC-1 and Lupus-1A are plotted versus the number of carbon atoms (chain length). The chemical compositions of these two starless cores are quite similar. Reprinted with permission from Sakai et al. (2010b) (Copyright 2010 American Astronomical Society)

which proceeds at the Langevin rate (2.1×10^{-9} cm^3 s^{-1}). Because the Langevin rate is independent of temperature, the timescale of this reaction for H_2^+ can be as fast as 5×10^4 s (about half a day) for a H_2 density of 10^4 cm^{-3}, even at 10 K.

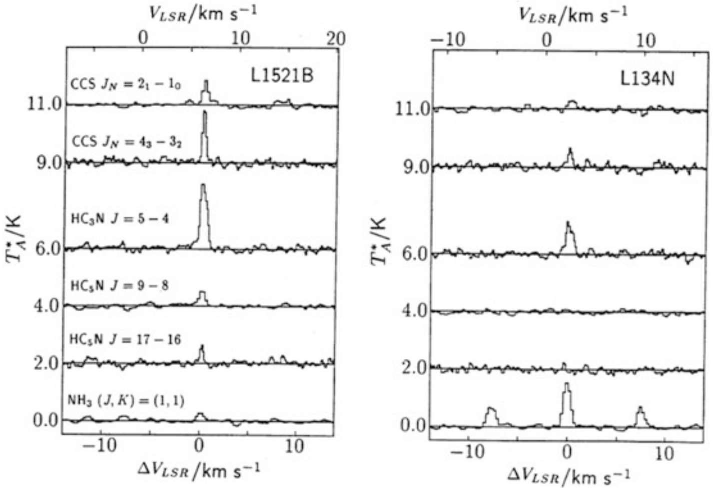

Fig. 5.3 Examples of chemical diversity in starless cores. Carbon-chain molecules such as CCS and HC_3N are abundant in L1521B; NH_3 is rather deficient. In L134N, the opposite trend persists (Suzuki et al. 1992) (Reprinted with permission from Suzuki et al. (1992). Copyright 1992 American Astronomical Society)

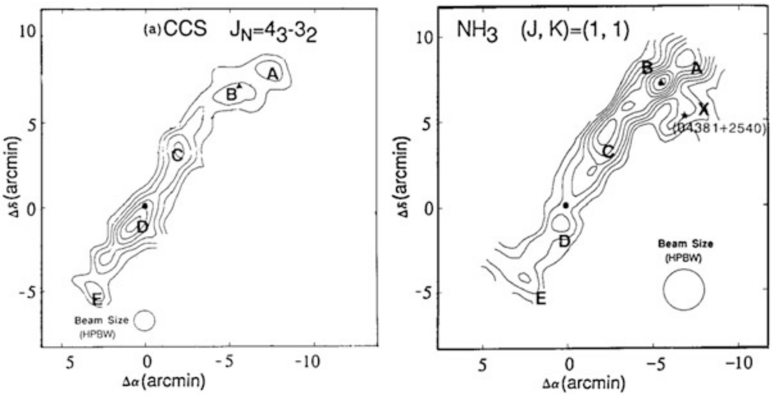

Fig. 5.4 Maps of the CCS (J_N=4_3–3_2) and NH_3 (*J, K*=1, 1) lines observed toward the TMC-1 ridge. The letters (**a**–**e**) indicate the positions of dense cores; D corresponds to TMC-1 (CP). The CCS emission is bright in the southeast (*bottom left*) part of the ridge; NH_3 emission is bright in the northwest (*top right*) part of the ridge. This trend can be interpreted in terms of chemical evolution. In accordance with the chemical evolutionary scenario, the southeastern part of the ridge is younger than the northwestern part. Hence, the TMC-1 ridge is gravitationally collapsing from the northwest to the southeast. It should be noted that the protostar IRAS 04381+2540 is located in the northern region of the ridge (Reprinted with permission from Hirahara et al. (1992). Copyright 1992 American Astronomical Society)

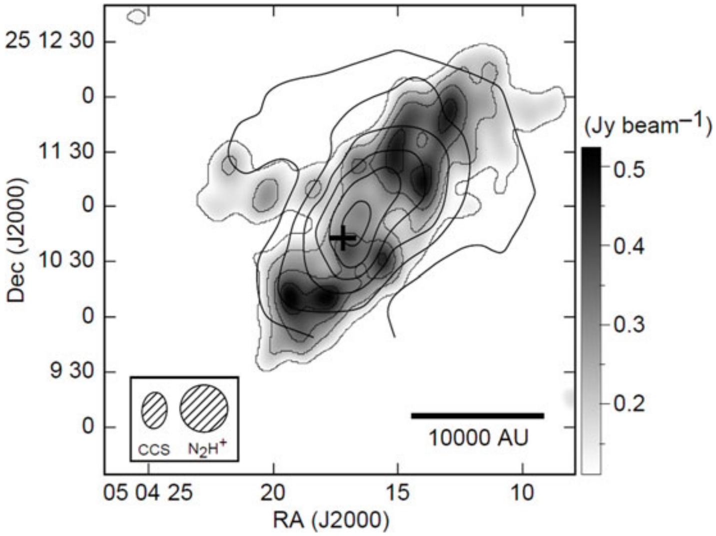

Fig. 5.5 Distributions of CCS (*gray scale*) and N_2H^+ (*contours*) in the starless core L1544. CCS tends to be less abundant in the center (the peak position of dust continuum emission (DP)); N_2H^+ is centrally concentrated (Reprinted with permission from Aikawa et al. (2001). Copyright 2001 American Astronomical Society)

The H_3^+ ion initiates the formation of various molecules. First, a proton is transferred from H_3^+ to the other molecule (A):

$$H_3^+ + A \rightarrow AH^+ + H_2. \tag{5.6}$$

Whether this reaction proceeds or not depends on the proton affinity of A. The proton affinity is a measure of the energy released in the reaction of the proton to an atom or a molecule. A larger proton affinity means higher stability of the protonated species. Hence, this reaction (5.6) is exothermic, if the proton affinity of A is larger than that of H_2. The reaction then proceeds at the Langevin rate. Because the gas kinetic temperature is 10 K in molecular clouds, the reaction does not proceed at all if the reaction is endothermic. Table 5.2 lists the proton affinities of various atoms and molecules. Most of the atoms and molecules have proton affinities higher than that of H_2. Important exceptions to this trend are He, H, and N. Hence, proton transfer from H_3^+ to various species can proceed at the low-temperature conditions of molecular clouds. The AH^+ ion further reacts with species B to form more complex ions (a condensation reaction):

$$AH^+ + B \rightarrow AB^+ + H. \tag{5.7}$$

This reaction has to be exothermic to proceed. Then, AB^+ reacts with an electron to form neutral species C and D via dissociative recombination:

Table 5.2 Proton affinities of atoms and molecules[a]

Species	Proton affinity (eV)
He	1.84
H	2.65
N	3.55
CH_3	3.69[b]
O_2	4.36
H_2	4.38
HF	5.01
O	5.02
N_2	5.12
NO	5.51
CO_2	5.60
CH_4	5.63
HCl	5.76
OH	6.15
CO	6.15
CN	$>$6.16
C_2H_6	6.18
C	6.42[b]
HCO	6.59
C_2H_2	6.64
C_2	6.8[b]
S	6.88
SO_2	6.97
C_2H_4	7.05
H_2O	7.16
H_2S	7.30
HCN	7.39
H_2CO	7.39
CH	7.54[b]
C_2H	7.80
CH_3OH	7.81
C_3	7.95
CH_3CHO	7.96
HNC	8.00
NH_2	8.01
$HCOOCH_3$	8.11
CS	8.20
CH_2	8.48[b]
Si	8.67
NH_3	8.84
CCS	9.01
c-C_3H_2	9.85

[a] Calculated from the dissociation energy and the ionization potentials listed in Table 4.2

[b] Hunter and Lias (1998)

Table 5.3 Rate coefficients of some reactions appearing in the text[a]

Reaction	Rate coefficient	Rate coefficient ($T = 10$K)	Reaction no.
$H_2 + cr \rightarrow H_2^+ + e$	$1.2 \times 10^{-17} s^{-1}$	$1.2 \times 10^{-17} s^{-1}$	5.3
$H_2^+ + H_2 \rightarrow H_3^+ + H$	$2.1 \times 10^{-9} cm^3\ s^{-1}$	$2.1 \times 10^{-9} cm^3\ s^{-1}$	5.5
$H_3^+ + CO \rightarrow HCO^+ + H_2$	$2.7 \times 10^{-9} cm^3\ s^{-1}$	$2.7 \times 10^{-9} cm^3\ s^{-1}$	5.9
$H_3^+ + O \rightarrow OH^+ + H_2$	$1.4 \times 10^{-9} cm^3\ s^{-1}$	$1.4 \times 10^{-9} cm^3\ s^{-1}$	5.10, 5.72
$HCO^+ + e \rightarrow CO + H$	$2.4 \times 10^{-7} \left(\frac{T}{300}\right)^{-0.69} cm^3\ s^{-1}$	$2.5 \times 10^{-6} cm^3\ s^{-1}$	
$OH_3^+ + e \rightarrow H_2O + H$	$7.09 \times 10^{-8} \left(\frac{T}{300}\right)^{-0.5} cm^3\ s^{-1}$	$3.9 \times 10^{-7} cm^3\ s^{-1}$	
$\rightarrow OH + H_2$	$5.37 \times 10^{-8} \left(\frac{T}{300}\right)^{-0.5} cm^3\ s^{-1}$	$2.9 \times 10^{-7} cm^3\ s^{-1}$	
$\rightarrow OH + H + H$	$3.05 \times 10^{-7} \left(\frac{T}{300}\right)^{-0.5} cm^3\ s^{-1}$	$1.7 \times 10^{-6} cm^3\ s^{-1}$	
$\rightarrow O + H_2 + H$	$5.60 \times 10^{-9} \left(\frac{T}{300}\right)^{-0.5} cm^3\ s^{-1}$	$3.1 \times 10^{-8} cm^3\ s^{-1}$	
$He + cr \rightarrow He^+ + e$	$1.3 \times 10^{-17} s^{-1}$	$1.3 \times 10^{-17} s^{-1}$	5.30
$He^+ + CO \rightarrow C^+ + O + He$	$1.6 \times 10^{-9} cm^3\ s^{-1}$	$1.6 \times 10^{-9} cm^3\ s^{-1}$	5.31
$H_3^+ + C \rightarrow CH^+ + H_2$	$2.0 \times 10^{-9} cm^3\ s^{-1}$	$2.0 \times 10^{-9} cm^3\ s^{-1}$	5.36
$CH^+ + H_2 \rightarrow CH_2^+ + H$	$1.2 \times 10^{-9} cm^3\ s^{-1}$	$1.2 \times 10^{-9} cm^3\ s^{-1}$	5.37
$CH_2^+ + H_2 \rightarrow CH_3^+ + H$	$1.6 \times 10^{-9} cm^3\ s^{-1}$	$1.6 \times 10^{-9} cm^3\ s^{-1}$	5.38
$CH_3^+ + H_2 \rightarrow CH_5^+ + h\nu$	$3.9 \times 10^{-16} \left(\frac{T}{300}\right)^{-2.3} \exp\left(-\frac{21.3}{T}\right) cm^3\ s^{-1}$	$1.2 \times 10^{-13} cm^3\ s^{-1}$	5.39
$CH_3^+ + e \rightarrow CH_2 + H$	$7.75 \times 10^{-8} \left(\frac{T}{300}\right)^{-0.5} cm^3\ s^{-1}$	$4.2 \times 10^{-7} cm^3\ s^{-1}$	5.40
$\rightarrow CH + H_2$	$1.95 \times 10^{-7} \left(\frac{T}{300}\right)^{-0.5} cm^3\ s^{-1}$	$1.1 \times 10^{-6} cm^3\ s^{-1}$	5.41
$\rightarrow CH + H + H$	$2.00 \times 10^{-7} \left(\frac{T}{300}\right)^{-0.4} cm^3\ s^{-1}$	$7.8 \times 10^{-7} cm^3\ s^{-1}$	5.42
$CH_3^+ + O \rightarrow HCO^+ + H_2$	$4.0 \times 10^{-10} cm^3\ s^{-1}$	$4.0 \times 10^{-10} cm^3\ s^{-1}$	5.43
$\rightarrow H_2CO^+ + H$	$4.0 \times 10^{-11} cm^3\ s^{-1}$	$4.0 \times 10^{-11} cm^3\ s^{-1}$	5.44, 5.82
$CH_5^+ + e \rightarrow CH_4 + H$	$1.40 \times 10^{-8} \left(\frac{T}{300}\right)^{-0.52} cm^3\ s^{-1}$	$8.2 \times 10^{-8} cm^3\ s^{-1}$	5.45
$\rightarrow CH_3 + H_2$	$1.40 \times 10^{-8} \left(\frac{T}{300}\right)^{-0.52} cm^3\ s^{-1}$	$8.2 \times 10^{-8} cm^3\ s^{-1}$	5.46
$\rightarrow CH_3 + H + H$	$1.96 \times 10^{-7} \left(\frac{T}{300}\right)^{-0.52} cm^3\ s^{-1}$	$1.1 \times 10^{-6} cm^3\ s^{-1}$	5.47
$\rightarrow CH_2 + H_2 + H$	$4.76 \times 10^{-8} \left(\frac{T}{300}\right)^{-0.52} cm^3\ s^{-1}$	$2.8 \times 10^{-7} cm^3\ s^{-1}$	5.48
$\rightarrow CH + H_2 + H_2$	$8.40 \times 10^{-9} \left(\frac{T}{300}\right)^{-0.4} cm^3\ s^{-1}$	$4.9 \times 10^{-8} cm^3\ s^{-1}$	5.49
$CH_5^+ + O \rightarrow CH_3O^+ + H_2$	$4.4 \times 10^{-12} cm^3\ s^{-1}$	$4.4 \times 10^{-12} cm^3\ s^{-1}$	5.50
$\rightarrow OH_3^+ + CH_2$	$2.2 \times 10^{-10} cm^3\ s^{-1}$	$2.2 \times 10^{-10} cm^3\ s^{-1}$	5.51
$CH_5^+ + CO \rightarrow HCO^+ + CH_4$	$1.0 \times 10^{-9} cm^3\ s^{-1}$	$1.0 \times 10^{-9} cm^3\ s^{-1}$	5.52
$CH + O \rightarrow CO + H$	$6.02 \times 10^{-11} \left(\frac{T}{300}\right)^{0.1} \exp\left(\frac{4.5}{T}\right) cm^3\ s^{-1}$	$6.7 \times 10^{-11} cm^3\ s^{-1}$	5.53
$CH_2 + C \rightarrow C_2H + H$	$1.0 \times 10^{-10} cm^3\ s^{-1}$	$1.0 \times 10^{-10} cm^3\ s^{-1}$	5.54

(continued)

Table 5.3 (continued)

Reaction	Rate coefficient	Rate coefficient ($T = 10$K)	Reaction no.
$CH_3 + O \rightarrow H_2CO + H$	$1.3 \times 10^{-10} cm^3\ s^{-1}$	$1.3 \times 10^{-10} cm^3\ s^{-1}$	5.55, 5.84
$CH_3 + C \rightarrow C_2H_2 + H$	$1.0 \times 10^{-10} cm^3\ s^{-1}$	$1.0 \times 10^{-10} cm^3\ s^{-1}$	5.56
$C^+ + CH_4 \rightarrow C_2H_3^+ + H$	$1.0 \times 10^{-9}\ cm^3\ s^{-1}$	$1.0 \times 10^{-9}\ cm^3\ s^{-1}$	5.57
$\rightarrow C_2H_2^+ + H_2$	$3.9 \times 10^{-10}\ cm^3\ s^{-1}$	$3.9 \times 10^{-10}\ cm^3\ s^{-1}$	5.58
$C_3H^+ + H_2 \rightarrow C_3H_2^+ + H$	$5.2 \times 10^{-12}\ cm^3\ s^{-1}$	$5.2 \times 10^{-12}\ cm^3\ s^{-1}$	5.64
$C_3H^+ + H_2 \rightarrow C_3H_3^+ + h\nu$	$1.69 \times 10^{-12} \left(\frac{T}{300}\right)^{-1.0} cm^3\ s^{-1}$	$5.1 \times 10^{-11} cm^3\ s^{-1}$	5.65
$OH + O \rightarrow O_2 + H$	$3.69 \times 10^{-11} \left(\frac{T}{300}\right)^{-0.27} \exp\left(-\frac{12.9}{T}\right)$ $cm^3\ s^{-1}$	$2.5 \times 10^{-11} cm^3\ s^{-1}$	5.73
$OH + C \rightarrow CO + H$	$1.0 \times 10^{-10} cm^3\ s^{-1}$	$1.0 \times 10^{-10} cm^3\ s^{-1}$	5.74
$C + O_2 \rightarrow CO + O$	$5.56 \times 10^{-11} \left(\frac{T}{300}\right)^{0.41} \exp\left(\frac{26.9}{T}\right)$ $cm^3\ s^{-1}$	$2.0 \times 10^{-10} cm^3\ s^{-1}$	5.75
$C^+ + OH \rightarrow CO^+ + H$	$7.7 \times 10^{-10} \left(\frac{T}{300}\right)^{-0.5} cm^3\ s^{-1}$	$4.2 \times 10^{-9} cm^3\ s^{-1}$	5.76
$C^+ + H_2O \rightarrow HCO^+ + H$	$9.0 \times 10^{-10} \left(\frac{T}{300}\right)^{-0.5} cm^3\ s^{-1}$	$4.9 \times 10^{-9} cm^3\ s^{-1}$	5.77
$C^+ + O_2 \rightarrow CO + O^+$	$4.5 \times 10^{-10}\ cm^3\ s^{-1}$	$4.5 \times 10^{-10}\ cm^3\ s^{-1}$	5.78
$\rightarrow CO^+ + O$	$3.4 \times 10^{-10}\ cm^3\ s^{-1}$	$3.4 \times 10^{-10}\ cm^3\ s^{-1}$	5.79
$CO^+ + H_2 \rightarrow HCO^+ + H$	$7.5 \times 10^{-10}\ cm^3\ s^{-1}$	$7.5 \times 10^{-10}\ cm^3\ s^{-1}$	5.80
$CH_3^+ + H_2O \rightarrow CH_3OH_2^+ + h\nu$	$2.0 \times 10^{-12} cm^3\ s^{-1}$	$2.0 \times 10^{-12} cm^3\ s^{-1}$	5.87
$N^+ + H_2 \rightarrow NH^+ + H$	$1.0 \times 10^{-9} \exp\left(-\frac{85}{T}\right) cm^3\ s^{-1}$	$2.0 \times 10^{-13} cm^3\ s^{-1}$	5.95
$NH^+ + H_2 \rightarrow NH_2^+ + H$	$1.3 \times 10^{-9} cm^3\ s^{-1}$	$1.3 \times 10^{-9} cm^3\ s^{-1}$	5.96
$NH_2^+ + H_2 \rightarrow NH_3^+ + H$	$2.7 \times 10^{-10} cm^3\ s^{-1}$	$2.7 \times 10^{-10} cm^3\ s^{-1}$	5.97
$NH_3^+ + H_2 \rightarrow NH_4^+ + H$	$3.09 \times 10^{-13} \left(\frac{T}{300}\right)^{1.08} \exp\left(\frac{50.9}{T}\right)$ $cm^3\ s^{-1}$	$1.3 \times 10^{-12} cm^3\ s^{-1}$	5.98
$SH^+ + H_2 \rightarrow H_3S^+ + h\nu$	$2.4 \times 10^{-16} \left(\frac{T}{300}\right)^{-0.8} cm^3\ s^{-1}$	$3.6 \times 10^{-15} cm^3\ s^{-1}$	5.126
$SH^+ + e \rightarrow S + H$	$2.0 \times 10^{-7} \left(\frac{T}{300}\right)^{-0.5}\ cm^3\ s^{-1}$	$1.1 \times 10^{-6} cm^3\ s^{-1}$	

[a] The rate coefficients are mostly taken from the UMIST Database for Astrochemistry (McElroy et al. 2013). The unit of T is K.

$$AB^+ + e \rightarrow C + D. \tag{5.8}$$

This series of reactions starting from H_3^+ is called H_3^+ chemistry, which plays a dominant role in producing various molecules in the gas phase.

The degree of ionization of molecular clouds is determined by the rate of cosmic-ray ionization. In molecular clouds, CO molecules and O atoms are generally abundant; these species represent the main reactants for H_3^+:

$$H_3{}^+ + CO \rightarrow HCO^+ + H_2, \tag{5.9}$$

$$H_3{}^+ + O \rightarrow OH^+ + H_2. \tag{5.10}$$

Then, the OH^+ ion is successively hydrogenated to form $OH_3{}^+$, as described in Sect. 4.4. The HCO^+ and $OH_3{}^+$ ions recombine with an electron to form neutral species. The rate equation for an electron can therefore be written as:

$$\frac{d[\mathrm{e}]}{dt} = \zeta[\mathrm{H_2}] - k_r\{[\mathrm{HCO^+}] + [\mathrm{OH_3}{}^+]\}[\mathrm{e}], \tag{5.11}$$

where ζ is the cosmic-ray ionization rate (1.2×10^{-17} s^{-1}) for reaction (5.3), and k_r is the average rate coefficient for the electron recombination reaction of HCO^+ and $OH_3{}^+$ (2.5×10^{-6} cm^3 s^{-1} at 10 K). Because these two ions are dominant carriers of positive charge, we can approximate the charge balance by writing:

$$[\mathrm{HCO^+}] + [\mathrm{H_3O^+}] = [\mathrm{e}]. \tag{5.12}$$

In the steady-state approximation, the degree of ionization is represented as:

$$\frac{[\mathrm{e}]}{[\mathrm{H_2}]} = \sqrt{\frac{\zeta}{k_r[\mathrm{H_2}]}}. \tag{5.13}$$

The degree of ionization is calculated to be 2×10^{-8} for a H_2 density of 10^4 cm^{-3}, which is almost four orders of magnitude lower than the degree of ionization observed in diffuse clouds. The degree of ionization is inversely proportional to the square root of the H_2 density and hence decreases for denser parts of clouds.

In focusing on $H_3{}^+$ in reactions (5.3, 5.5, 5.9, and 5.10), we obtain the following rate equation:

$$\frac{d[\mathrm{H_3^+}]}{dt} = \zeta[\mathrm{H_2}] - k_{\mathrm{CO}}[\mathrm{H_3^+}][\mathrm{CO}] - k_{\mathrm{O}}[\mathrm{H_3^+}][\mathrm{O}], \tag{5.14}$$

where k_{CO} is the rate coefficient for reaction (5.9) (2.7×10^{-9} cm^3 s^{-1} at 10 K), and k_{O} is the rate coefficient for reaction (5.10) (1.4×10^{-9} cm^3 s^{-1} at 10 K). Here, all of the $H_2{}^+$ ions are assumed to be converted to $H_3{}^+$ through reaction (5.5), to a good approximation. Under the steady-state approximation, we obtain:

$$[\mathrm{H_3^+}] = \frac{\zeta[\mathrm{H_2}]}{k_{\mathrm{CO}}[\mathrm{CO}] + k_{\mathrm{O}}[\mathrm{O}]}. \tag{5.15}$$

By assuming CO and O abundances relative to H_2 of 1.4×10^{-4} and 2.1×10^{-4}, respectively (the sum of the two abundances is assumed to equal the oxygen abundance of 3.5×10^{-4}), we obtain an $[H_3{}^+]$ abundance of 1.8×10^{-5} cm^{-3}, which is independent of H_2 density. The fractional abundance of ${H_3}^+$ relative to H_2 is 1.8×10^{-9} for a cloud with a H_2 density of 10^4 cm^{-3}.

5.4 Destruction of Molecules

Because photodissociation processes are almost negligible in molecular clouds, molecules can survive for much longer time in molecular clouds than in diffuse clouds. The main destruction mechanism of molecules in molecular clouds is reactions with ions such as He^+ and H^+. In particular, reactions with He^+ efficiently destroy molecules. When He^+ collides with a neutral molecule, it extracts one electron from the target neutral molecule and ionizes the molecule. In this process, the difference in the ionization potentials between He (24.6 eV) and the target neutral molecule is mostly assimilated as electronic excitation of the ionized molecule, which further leads to dissociation. For instance:

$$\mathrm{He^+ + CO \rightarrow C^+ + O + He,} \tag{5.16}$$

$$\mathrm{He^+ + H_2O \rightarrow OH^+ + H + He,} \tag{5.17}$$

$$\mathrm{He^+ + HCN \rightarrow C^+ + H + N + He.} \tag{5.18}$$

In contrast, reactions with H^+ are rather mild because of the lower ionization potential of H (13.60 eV). The H^+ ion only ionizes the molecule, without dissociating it in many cases. For instance:

$$\mathrm{H^+ + OH \rightarrow OH^+ + H,} \tag{5.19}$$

$$\mathrm{H^+ + H_2O \rightarrow H_2O^+ + H,} \tag{5.20}$$

$$\mathrm{H^+ + H_2CO \rightarrow H_2CO^+ + H.} \tag{5.21}$$

A fraction of the ionized species return to neutral species:

$$\mathrm{OH^+ + H_2 \rightarrow H_2O^+ + H,} \tag{5.22}$$

$$\mathrm{H_2O^+ + H_2 \rightarrow {OH_3}^+ + H,} \tag{5.23}$$

$$\mathrm{{OH_3}^+ + e \rightarrow OH + H + H,} \tag{5.24}$$

$$\mathrm{\rightarrow OH + H_2} \tag{5.25}$$

$$\mathrm{\rightarrow H_2O + H} \tag{5.26}$$

$$\mathrm{H_2CO^+ + H_2 \rightarrow H_2COH^+ + H,} \tag{5.27}$$

$$\mathrm{H_2COH^+ + e \rightarrow H_2CO + H.} \tag{5.28}$$

Hence, destruction by H^+ is not as effective as that by He^+.

The H_3^+ ion and HCO^+ ion also contribute to the dissociation of molecules through proton transfer and subsequent electron recombination. For instance:

$$H_3{}^+ + H_2O \rightarrow OH_3{}^+ + H_2. \tag{5.29}$$

The OH_3^+ ion yields H_2O or OH via electron recombination. Therefore, a reaction with H_3^+ (HCO^+ as well) dissociates a H_2O molecule into OH and H with some probability.

Destruction by ions such as He^+, H^+, H_3^+, and HCO^+ is called ionic destruction. Its timescale can be estimated as follows. We only consider reactions with He^+ for simplicity, because reactions with H^+ and H_3^+ make minor contributions. In particular, H^+ cannot disassociate CO, because the ionization potential of CO is higher than that of H. He^+ is formed by cosmic-ray ionization and is lost by reactions with neutral molecules other than H_2, where the CO molecule can be assumed to be the most abundant neutral molecule ($[CO]/[H_2] \sim 1.4 \times 10^{-4}$):

$$\mathrm{He} + \mathrm{c.r.} \rightarrow \mathrm{He}^+ + \mathrm{e}, \tag{5.30}$$

$$\mathrm{He}^+ + \mathrm{CO} \rightarrow \mathrm{C}^+ + \mathrm{O} + \mathrm{He}, \tag{5.31}$$

for which the rate equation for He^+ is

$$\frac{d[\mathrm{He}^+]}{dt} = \zeta_{\mathrm{He}}[\mathrm{He}] - k_{\mathrm{He}}[\mathrm{He}^+][\mathrm{CO}], \tag{5.32}$$

where ζ_{He} is the cosmic-ray ionization rate for He (reaction (5.30)) and k_{He} is the rate coefficient for reaction (5.31). Note that ζ_{He} is the effective ionization rate including ionization by cosmic-ray-induced photons. The abundance of He^+ can then be obtained under the steady-state approximation:

$$[\mathrm{He}^+] = \frac{\zeta_{\mathrm{He}}[\mathrm{He}]}{k_{\mathrm{He}}[\mathrm{CO}]}. \tag{5.33}$$

The steady-state condition is really a rough approximation in this case, because it is later shown that the molecular cloud chemistry is not always in chemical equilibrium. However, we employ this approximation for a simple estimation of the $[He^+]$ abundance. The timescale for destruction by He^+ is:

$$t = \frac{1}{k_{\mathrm{He}}[\mathrm{He}^+]} = \frac{[\mathrm{CO}]}{\zeta_{\mathrm{He}}[\mathrm{He}]}. \tag{5.34}$$

When ζ_{He} is assumed to be $6.5 \times 10^{-18}\ \mathrm{s}^{-1}$, the timescale is evaluated to be 3×10^6 year. Here, [CO]/[He] is assumed to be 7×10^{-4}. This timescale is much longer than the photodissociation timescale in a diffuse cloud (10^2 year).

The corresponding timescale for reactions with H^+ is comparable to or shorter than that for reactions with He^+. However, the destruction efficiency is not very high. Hence, the destruction timescale of neutral molecules in molecular clouds can roughly be approximated by the above timescale for He^+ destruction.

In addition to ionic destruction, cosmic-ray-induced photodissociation plays an important role (Sect. 3.7). Gredel et al. (1987, 1989) presented quantitative treatments of this process and listed its efficiency for various molecules. According to their result, the rate coefficient for the cosmic-ray-induced photodissociation rate for the CO molecule is 7 times the total cosmic-ray ionization rate (7ζ) for a cloud temperature of 10 K and grain albedo of 0.5 (Gredel et al. 1987). When we assume the total cosmic-ray ionization rate of 1.2×10^{-17} s^{-1}, the cosmic-ray-induced photodissociation rate of CO is 8×10^{-17} s^{-1}. In the UMIST database, the rate coefficient for this process for various molecules is simply assumed to be 1.3×10^{-17} s^{-1}. Even if we employ a rate coefficient of 8×10^{-17} s^{-1} for CO, its timescale is as long as 4×10^8 year. Hence, this process only makes a supplementary contribution to the destruction of CO molecules.

5.5 Carbon Chemistry

Here, we discuss the formation of organic molecules in molecular clouds. We assume the diffuse cloud condition as the initial condition, where the major form of carbon is C^+. The degree of ionization is initially 1.4×10^{-4}. The C^+ ion is neutralized by radiative recombination in capturing an electron to yield the neutral carbon atom, C, in a relatively short timescale (800 year), and the reaction of C and ${H_3}^+$ initiates the formation of various organic molecules. Additionally, the radiative association reaction between C^+ and H_2 also contributes to the formation of organic molecules. Hence, we consider the following starting processes for carbon chemistry:

$$C^+ + H_2 \rightarrow {CH_2}^+ + h\nu, \tag{5.35}$$

$$C + {H_3}^+ \rightarrow CH^+ + H_2. \tag{5.36}$$

The CH^+ ion reacts with H_2 to produce ${CH_2}^+$ at the Langevin rate:

$$CH^+ + H_2 \rightarrow {CH_2}^+ + H. \tag{5.37}$$

As discussed in Sect. 4.3, if a reaction between an ion and H_2 proceeds at the Langevin rate, the reaction is the most important reaction for the ion. This statement is also true for a molecular cloud, because the H_2 density is higher, and the electron abundance is lower than in a diffuse cloud. Hence, the ${CH_2}^+$ ion thus produced via reactions (5.35, 5.36, and 5.37) reacts with H_2 to form ${CH_3}^+$:

$$CH_2{}^+ + H_2 \rightarrow CH_3{}^+ + H. \tag{5.38}$$

Because the reaction of $CH_3{}^+$ and H_2 is a slow radiative association reaction, it competes with the electron recombination reaction:

$$CH_3{}^+ + H_2 \rightarrow CH_5{}^+ + h\nu, \tag{5.39}$$

$$CH_3{}^+ + e \rightarrow CH_2 + H, \tag{5.40}$$

$$\rightarrow CH + H_2 \tag{5.41}$$

$$\rightarrow CH + H + H. \tag{5.42}$$

Reaction (5.39) also competes with reactions with oxygen atoms, which are the abundant neutral species:

$$CH_3{}^+ + O \rightarrow HCO^+ + H_2 \tag{5.43}$$

$$\rightarrow H_2CO^+ + H. \tag{5.44}$$

The rate coefficient for reaction (5.39) is $3.9 \times 10^{-16}(T/300)^{-2.3} \exp(-21.3/T)$ cm^3 s^{-1}. Hence, the timescale for the reaction for $CH_3{}^+$ is 8×10^8 s for a H_2 density of 10^4 cm^{-3} at 10 K. For comparison, the timescale for electron recombination (the sum of reactions (5.40, 5.41, and 5.42)) is 2×10^9 s at 10 K, where the degree of ionization obtained above for a H_2 density of 10^4 cm^{-3} is employed. Because the rate coefficients for reactions (5.43) and (5.44) are 4×10^{-10} cm^3 s^{-1} and 4×10^{-11} cm^3 s^{-1}, respectively, the timescale for reactions (5.43 and 5.44) with the oxygen atom is 1×10^9 s for a H_2 density of 10^4 cm^{-3}, where the fractional abundance of oxygen atoms is assumed to be the same as the elemental abundance of 2.1×10^{-4}. Hence, reactions with H_2 to form $CH_5{}^+$ compete with the electron recombination and reactions with oxygen atoms. In contrast, electron recombination is a dominant pathway for $CH_3{}^+$ in diffuse clouds, as described in Sect. 4.3. This fact is apparently due to the higher electron abundance and lower H_2 density in diffuse clouds.

The $CH_5{}^+$ ion thus formed no longer reacts with H_2 and hence is subject to an electron recombination reaction to form the neutral species CH_3 and CH_4:

$$CH_5{}^+ + e \rightarrow CH_4 + H \tag{5.45}$$

$$\rightarrow CH_3 + H_2 \tag{5.46}$$

$$\rightarrow CH_3 + H + H \tag{5.47}$$

$$\rightarrow CH_2 + H_2 + H \tag{5.48}$$

$$\rightarrow CH + H_2 + H_2. \tag{5.49}$$

The sum of the reaction rates for all of the branching channels (5.45, 5.46, 5.47, 5.48, 5.49) is 1.5×10^{-6} cm^3 s^{-1} at 10 K. The timescale for electron recombination is therefore 10^9 s. Among the product hydrocarbons, CH and CH_2 are detected in molecular clouds via radio observations; CH_3 and CH_4 are identified using high-resolution infrared observations.

The CH_5^+ ion can also react with an O atom:

$$CH_5{}^+ + O \rightarrow CH_3O^+ + H_2 \tag{5.50}$$

$$\rightarrow OH_3{}^+ + CH_2. \tag{5.51}$$

The rate coefficients for reactions (5.50) and (5.51) are 4.4×10^{-12} cm^3 s^{-1} and 2.2×10^{-10} cm^3 s^{-1}, respectively. Hence, the timescale of the reaction with the O atom is estimated to be 1.3×10^9 s, which is comparable to that of electron recombination. Moreover, the reaction with CO proceeds at the Langevin rate (1.0×10^{-9} cm^3 s^{-1}) to form CH_4:

$$CH_5{}^+ + CO \rightarrow HCO^+ + CH_4. \tag{5.52}$$

This reaction proceeds because the proton affinity of CH_4 is lower than that of CO, as listed in Table 5.2. Similar proton transfer reactions with other species such as C and OH also contribute to loss of CH_5^+. The timescale for reaction (5.52) for CH_5^+ is 7×10^8 s as long as the abundance of CO relative to H_2 is 1.4×10^{-4}. The timescale is also comparable to the timescale of electron recombination. It should be noted that both reactions (5.45 and 5.52) yield CH_4 as a by-product.

The neutral species, CH, CH_2, CH_3, and CH_4, are primarily lost by reaction with ions. As discussed above, the ionic destruction is very slow, and hence these molecules are subject to further reactions in making more complex molecules. This situation represents another difference in the chemistry between diffuse clouds and molecular clouds. In diffuse clouds, molecular complexity is not increased efficiently because of fast photodissociation processes. In contrast, larger molecules can form in molecular clouds.

Because CH, CH_2, and CH_3 are free radicals with one or two unpaired electrons, these species efficiently react with O or C atoms without energy barriers. Some examples of this process include:

$$CH + O \rightarrow CO + H, \tag{5.53}$$

$$CH_2 + C \rightarrow C_2H + H, \tag{5.54}$$

$$CH_3 + O \rightarrow H_2CO + H, \tag{5.55}$$

$$CH_3 + C \rightarrow C_2H_2 + H. \tag{5.56}$$

Because the rate coefficients for reactions (5.53, 5.54, 5.55, and 5.56) are 9.4×10^{-11} cm^3 s^{-1}, 1.0×10^{-10} cm^3 s^{-1}, 1.3×10^{-10} cm^3 s^{-1}, and 1.0×10^{-10} cm^3 s^{-1}, respectively, at 10 K, the timescale for these reactions is on the order of 10^{10} s. This timescale is much shorter than that of the ionic destruction of these species. In contrast, CH_4 is a chemically stable molecule, and the reaction with O or C atoms does not proceed at low temperature because of the activation barrier. Instead, CH_4 can react with C^+ to form $C_2H_3{}^+$ and $C_2H_2{}^+$:

$$C^+ + CH_4 \rightarrow C_2H_3{}^+ + H, \tag{5.57}$$

$$C^+ + CH_4 \rightarrow C_2H_2{}^+ + H_2. \tag{5.58}$$

Here, molecular ions with two carbon atoms are produced. The $C_2H_2{}^+$ ion reacts with H_2 to form $C_2H_3{}^+$:

$$C_2H_2{}^+ + H_2 \rightarrow C_2H_3{}^+ + H \tag{5.59}$$

The $C_2H_3{}^+$ ion react no further with H_2. Instead, it recombines with an electron to produce the neutral species C_2H and C_2H_2 (acetylene). These two molecules are common in molecular clouds, although C_2H_2 has been identified only by infrared observations. It should be noted that reactions (5.54) and (5.56) also contribute to the formation of C_2H and C_2H_2, respectively. Furthermore, the reaction of $CH_3{}^+$ with the C atom produces $C_2H_2{}^+$, which also yields C_2H and C_2H_2 via reaction (5.59) and subsequent electron recombination.

Because the ionic destruction of these neutral species is slow, their molecular complexity is able to increase further. C_2H and C_2H_2 will react with C^+ to form $C_3{}^+$ and C_3H^+:

$$C^+ + C_2H \rightarrow C_3{}^+ + H, \tag{5.60}$$

$$C^+ + C_2H_2 \rightarrow C_3H^+ + H. \tag{5.61}$$

The reaction of a C atom with $C_2H_3{}^+$ also contributes to the formation of more complex molecules:

$$C_2H_3{}^+ + C \rightarrow C_3H_2{}^+ + H. \tag{5.62}$$

The $C_3{}^+$ ion reacts with H_2:

$$C_3{}^+ + H_2 \rightarrow C_3H^+ + H. \tag{5.63}$$

Then, C_3H^+ reacts with H_2 in two ways:

$$C_3H^+ + H_2 \rightarrow C_3H_2{}^+ + H, \tag{5.64}$$

$$C_3H^+ + H_2 \rightarrow C_3H_3{}^+ + h\nu, \tag{5.65}$$

where the rate coefficients for reaction (5.64) and (5.65) are 5.2×10^{-12} cm^3 s^{-1} and 5.1×10^{-11} cm^3 s^{-1} , respectively, at 10 K. Note that the reaction of the $C_3H_2{}^+$ ion with H_2,

$$C_3H_2{}^+ + H_2 \rightarrow C_3H_3{}^+ + H, \tag{5.66}$$

has an activation barrier and does not proceed efficiently in cold clouds. The $C_3H_3{}^+$ ion is a physically stable ion and has two geometrical isomers, a cyclic one and a linear one. The former isomer is more energetically stable than the latter. The C_3H_3 $^+$ ion reacts no further with H_2, and it is subject to an electron recombination reaction to form the neutral species *l*-C_3H_2 and c-C_3H_2. Here, "*l*-" and "c-" denote the linear and cyclic isomers, respectively. Similarly the electron recombination of $C_3H_2{}^+$ gives *l*-C_3H and c-C_3H. We note that neutral–neutral reactions such as

$$C + C_2H_2 \rightarrow \text{c-}C_3H + H, \tag{5.67}$$

$$CH + CH \rightarrow C_2H + H, \tag{5.68}$$

$$CH + C_2H \rightarrow c-C_3H(\text{or } \ell-C_3H) + H, \tag{5.69}$$

and

$$C_2H_2 + CH \rightarrow c-C_3H_2 + H \tag{5.70}$$

also contribute to the formation of C_3H_m (m=1,2).

Molecular complexity increases by reactions with C^+ and/or C (Fig. 5.6). Here, we stress that molecules formed in this scheme are all (highly) unsaturated. This lack of saturation occurs because the hydrogenation reaction of the hydrocarbon ions does not proceed at some point. For species with two carbon atoms, $C_2H_3{}^+$ is a very stable ion, and further hydrogenation does not occur. For species with three

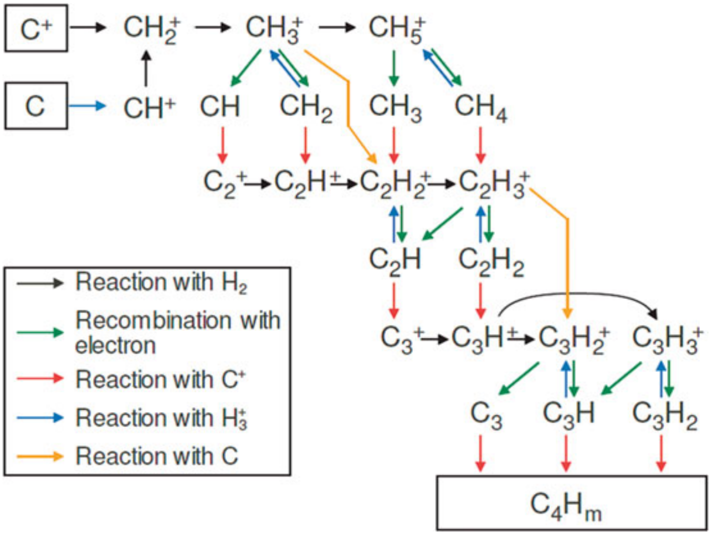

Fig. 5.6 Schematic of the carbon chemistry in molecular clouds. Major reaction pathways are indicated (Reprinted with permission from Sakai and Yamamoto 2013)

carbon atoms, $C_3H_3^+$ is a very stable ion, and hydrogenation is terminated at this ion. A similar situation occurs for longer species. The $C_4H_2^+$ and C_5H^+ ions are terminals for the C_4 and C_5 species, respectively. The existence of such stable ions is an important reason why highly unsaturated species such as carbon-chain molecules are preferentially formed in cold molecular clouds. For larger species, condensation reactions between small, unsaturated molecules and their ions are more important. Even in this case, the building blocks are mostly unsaturated molecules and ions, and hence the products should also be highly unsaturated. This trend is also true for neutral–neutral reactions between unsaturated molecules.

In short, hydrogenation in the gas phase can only proceed through ion–molecule reaction with H_2. In this process, existence of stable ions prevents further hydrogenation, resulting in production of highly unsaturated molecules. In contrast, hydrogenation by the H atom does not proceed efficiently in the gas phase. Such a reaction produces only a single product and is prohibited by the reason mentioned in Sect. 3.2. This is in great contrast to the grain-surface chemistry, as described in Chap. 6.

5.6 Oxygen Chemistry and Its Relation to Carbon Chemistry

In contrast to the diffuse cloud case, the charge transfer reaction:

$$H^+ + O \rightarrow O^+ + H \tag{5.71}$$

is not effective in cold molecular clouds (10 K) because of its endothermicity (0.04 eV). Hence, H_3^+ chemistry is a dominant contributor to the hydrogenation of oxygen atoms:

$$H_3^+ + O \rightarrow OH^+ + H_2. \tag{5.72}$$

Subsequent reactions with H_2 described in Sect. 4.4 yield the OH_3^+ ion, which produces H_2O and OH via electron recombination reactions with branching ratios of 0.25 and 0.74, respectively (Sect. 3.6). This process represents the main formation route of H_2O in the gas phase at low temperature. OH and H_2O molecules are widely seen in molecular clouds. We remark that H_2O is also efficiently formed on dust grains, as will be described later (Chap. 6).

The OH molecule reacts with O to form O_2 molecules:

$$OH + O \rightarrow O_2 + H. \tag{5.73}$$

Because this reaction is a radical–radical reaction with a reaction rate coefficient of 2.8×10^{-11} cm^3 s^{-1} at 10 K, it proceeds even in a cold molecular cloud. The O_2 molecule has now been confirmed toward ρ-Oph A via observations of its magnetic dipole-allowed transitions in the millimeter- and submillimeter-wave regions with the *Odin* and *Herschel* satellites (Larsson et al. 2007; Liseau et al. 2012); its fractional abundance relative to H_2 is reported to be 5×10^{-8}.

Oxygen chemistry is inextricably linked to carbon chemistry. In particular, the following formation processes of CO are important:

$$\mathrm{OH + C \rightarrow CO + H}, \tag{5.74}$$

$$\mathrm{C + O_2 \rightarrow CO + O}, \tag{5.75}$$

$$\mathrm{OH + C^+ \rightarrow CO^+ + H}, \tag{5.76}$$

$$\mathrm{H_2O + C^+ \rightarrow HCO^+ + H}, \tag{5.77}$$

$$\mathrm{O_2 + C^+ \rightarrow CO + O^+} \tag{5.78}$$

$$\mathrm{\rightarrow CO^+ + O}, \tag{5.79}$$

where CO^+ and HCO^+ form CO via reactions:

$$\mathrm{CO^+ + H_2 \rightarrow HCO^+ + H}, \tag{5.80}$$

$$\mathrm{HCO^+ + e \rightarrow CO + H}. \tag{5.81}$$

We note that CO is also formed through various other reactions, including reaction (5.53).

Some oxygen-containing organic molecules are produced in the gas phase. For instance, H_2CO can be formed through reactions:

$$\mathrm{CH_3{}^+ + O \rightarrow H_2CO^+ + H}, \tag{5.82}$$

$$\mathrm{CH_5{}^+ + O \rightarrow H_3CO^+ + H_2}, \tag{5.83}$$

$$\mathrm{CH_3 + O \rightarrow H_2CO + H}, \tag{5.84}$$

where H_2CO^+ and H_3CO^+ yield H_2CO:

$$\mathrm{H_2CO^+ + H_2 \rightarrow H_3CO^+ + H}, \tag{5.85}$$

$$\mathrm{H_3CO^+ + e \rightarrow H_2CO + H}. \tag{5.86}$$

However, the formation of CH_3OH is controversial. The formation was initially proposed to follow the reactions

$$\mathrm{CH_3{}^+ + H_2O \rightarrow CH_3OH_2{}^+} + h\nu, \tag{5.87}$$

$$\mathrm{CH_3OH_2{}^+ + e \rightarrow CH_3OH + H}. \tag{5.88}$$

However, the radiative association reaction (5.87) is very slow, and the electron recombination reaction of $CH_3OH_2{}^+$ mainly causes cleavage of the C–O bond (Geppert et al. 2006). Hence, the yield of CH_3OH through this process is not high enough to explain the observed abundance of CH_3OH in cold molecular clouds. It is now thought that CH_3OH is mainly formed on dust grains and that it is liberated into the gas phase by thermal and nonthermal desorption processes. This point is described later in Chap. 6.

Oxygen is usually the most abundant heavy element in interstellar clouds. Hence, oxygen atoms can still be the most abundant gas-phase O-bearing species with a fractional abundance on the order of 10^{-4}, unless they are depleted onto dust grains. The reaction with the O atom is an important destruction process for many molecules, in particular free radical species. For instance, reactions (5.53) and (5.82) can be regarded as the destruction of CH and CH_3^+, respectively. A timescale for this destruction of CH by O atoms is 4×10^9 s for a H_2 density of 10^4 cm^{-3}, which is shorter than the timescale for ionic destruction by He^+ (5×10^{13} s). Here, we consider that a molecule reacts with O atoms with a reaction rate coefficient, k. The reaction with O atoms becomes a dominant destruction process for the molecule if the following condition is fulfilled:

$$kn(H_2) \gg 10^{-10}\ s^{-1}. \tag{5.89}$$

For this reasons, reactions with O atoms are thought to be an important destruction process for carbon-chain radicals. For instance, it is assumed that C_n (n =even) can react with O with rate coefficients of 10^{-10} cm^3 s^{-1}, although the C_n (n =even) + O reaction has a reaction barrier of 900 K (UMIST database). Similarly, long carbon-chain radicals, C_nH (n>3) and C_nN, are assumed to react with O atoms. These reactions all form CO:

$$C_n + O \rightarrow C_{n-1} + CO, \tag{5.90}$$

$$C_nH + O \rightarrow C_n + OH, \tag{5.91}$$

and

$$C_nN + O \rightarrow C_{n-1}N + CO. \tag{5.92}$$

Without these reactions, longer chains are overproduced in the chemical models in comparison with observations. Hence, the destruction process of carbon-chain molecules is an outstanding problem in astrochemistry.

5.7 Nitrogen Chemistry

Because the proton affinity of nitrogen atoms is lower than that of H_2 molecules, H_3^+ chemistry starting from $N + H_3^+$ does not occur. It was once proposed that the reaction

$$\mathrm{N} + \mathrm{H_3}^+ \rightarrow \mathrm{NH_2}^+ + \mathrm{H} \tag{5.93}$$

may occur. However, the rate coefficient for this reaction turned out to be insignificant, and this reaction does not contribute to nitrogen chemistry (Scott et al. 1998). It is currently thought that reactions between N_2 and He^+ would produce N^+, which causes the following hydrogenation processes (Galloway and Herbst 1989):

$$\mathrm{N_2} + \mathrm{He}^+ \rightarrow \mathrm{N}^+ + \mathrm{N} + \mathrm{He}, \tag{5.94}$$

$$\mathrm{N}^+ + \mathrm{H_2} \rightarrow \mathrm{NH}^+ + \mathrm{H}, \tag{5.95}$$

$$\mathrm{NH}^+ + \mathrm{H_2} \rightarrow \mathrm{NH_2}^+ + \mathrm{H}, \tag{5.96}$$

$$\mathrm{NH_2}^+ + \mathrm{H_2} \rightarrow \mathrm{NH_3}^+ + \mathrm{H}, \tag{5.97}$$

$$\mathrm{NH_3}^+ + \mathrm{H_2} \rightarrow \mathrm{NH_4}^+ + \mathrm{H}, \tag{5.98}$$

$$\mathrm{NH_4}^+ + \mathrm{e} \rightarrow \mathrm{NH_2} + \mathrm{H_2}, \tag{5.99}$$

$$\rightarrow \mathrm{NH_3} + \mathrm{H}. \tag{5.100}$$

The reaction (5.95) is slightly endothermic by 0.019 eV and hence at first glance does not proceed in cold molecular clouds. However, the N^+ ions formed from N_2 have kinetic energies from the excess energy of the reaction, which can be used to overcome the slight endothermicity of the reaction. Because H_2 molecules are a dominant species, the N^+ ion formed from N_2 first collides with a H_2 molecule before losing its kinetic energy. Excitation of the fine structure levels of N^+ ($^3P_1$ and $^3P_2$) and existence of ortho H_2 molecule also contribute to overcome the endothermicity. The further hydrogenation reactions after NH^+ proceed with the Langevin rate coefficient, except for the $NH_3{}^+ + H_2$ reaction. As discussed in Sect. 3.3, the reaction rate coefficient for this reaction decreases with decreasing temperature, but it increases at very low temperatures because of the formation of the intermediate complex. In addition to the above series of reactions, the following reactions will form $NH_2{}^+$:

$$\mathrm{N_2} + \mathrm{H_3}^+ \rightarrow \mathrm{N_2H}^+ + \mathrm{H_2} \tag{5.101}$$

$$\mathrm{N_2H}^+ + \mathrm{e} \rightarrow \mathrm{NH} + \mathrm{H} \tag{5.102}$$

$$\mathrm{NH} + \mathrm{H_3}^+ \rightarrow \mathrm{NH_2}^+ + \mathrm{H_2} \tag{5.103}$$

The $NH_2{}^+$ ion thus formed also contribute to form NH_2 and NH_3 by reactions (5.97, 5.98, 5.99 and 5.100). This route via N_2H^+ is effective, when CO is heavily depleted onto dust grains (Chap. 6). Since CO is the main destroyer for N_2H^+, its depletion extends the lifetime of N_2H^+. Then, N_2H^+ has more chances to encounter with electrons for reaction (5.102). In these ways, NH_3 and NH_2 can be formed in the gas phase.

We note that N_2 molecules are the starting molecules in the above scheme. Therefore, an obvious question is how N_2 is formed in cold interstellar clouds.

There are several channels for producing N_2, although all of these channels are not straightforward. One representative route is through CN; another route is through NO. The CN route is:

$$CH + N \rightarrow CN + H, \tag{5.104}$$

$$C_2 + N \rightarrow CN + C, \tag{5.105}$$

$$C + NO \rightarrow CN + O, \tag{5.106}$$

and

$$CN + N \rightarrow N_2 + C. \tag{5.107}$$

The alternative NO route is:

$$OH + N \rightarrow NO + H, \tag{5.108}$$

$$N + O_2 \rightarrow NO + H, \tag{5.109}$$

and

$$NO + N \rightarrow N_2 + O. \tag{5.110}$$

Because these reactions are relatively slow, the formation of N_2 is also slow. For this reason, NH_3 and N_2H^+ gradually become abundant in the late stages of chemical evolution.

HCN and HNC are, for instance, formed from CN as:

$$CN + H_3{}^+ \rightarrow HCN^+ + H_2 \tag{5.111}$$

$$HCN^+ + H_2 \rightarrow HCNH^+ + H \tag{5.112}$$

$$HCNH^+ + e \rightarrow HCN + H \tag{5.113}$$

$$\rightarrow HNC + H. \tag{5.114}$$

Although HNC is less stable by 0.49 eV than HCN, the abundance of HNC is comparable to or higher than that of HCN in cold molecular clouds (e.g., Hirota et al. 1998). This fact means the branching ratio of reactions (5.99a and 5.99b) would be close to unity.

Cyanopolyynes ($HC_{2n}CN$) (and their geometrical isomers) can be formed by reactions of HCN with hydrocarbon ions. For instance, the ion–molecule reaction pathway to forming HC_3N is

$$C_2H_2{}^+ + HCN \rightarrow HCCCNH^+ + H \tag{5.115}$$

$$\rightarrow HCCNCH^+ + H, \tag{5.116}$$

$$HCCCNH^+ + e \rightarrow HC_3N + H, \tag{5.117}$$

$$\rightarrow HNC_3 + H, \tag{5.118}$$

$$\rightarrow C_3N + H + H, \tag{5.119}$$

$$HCCNCH^+ + e \rightarrow HCCNC + H. \tag{5.120}$$

Note that HNC_3 and HCCNC, which are isomers of HC_3N, are also detected in cold molecular clouds (Kawaguchi et al. 1992a, b). Furthermore, HC_3N also forms via a neutral–neutral reaction (Sims et al. 1993; Woon and Herbst 1997):

$$C_2H_2 + CN \rightarrow HC_3N + H. \tag{5.121}$$

The contribution of this process to HC_3N formation is supported by observations of the ^{13}C isotopic species of HC_3N (Takano et al. 1998).

5.8 Sulfur Chemistry

Sulfur is a relatively abundant chemical element (Table 1.1), and various sulfur-bearing molecules are known to exist in interstellar molecules (Table 1.2). Although oxygen and sulfur belong to the same group in the periodic table, their astrochemical behaviors are significantly different. The ionization potential of sulfur atoms (10.4 eV) is less than that of hydrogen atoms (13.6 eV), and hence sulfur atoms can readily be ionized in interstellar conditions. For instance, the following reactions ionize sulfur:

$$H^+ + S \rightarrow S^+ + H \tag{5.122}$$

$$C^+ + S \rightarrow S^+ + C. \tag{5.123}$$

However, the S^+ ion does not react with H_2 at low temperatures because of the reaction endothermicity. Even the radiative association reaction

$$S^+ + H_2 \rightarrow H_2S^+ + h\nu \tag{5.124}$$

does not occur (Prasad and Huntress 1982). Furthermore, the reaction of H_2S^+ with H_2 is highly endothermic. Hence, the S^+ ion does not contribute to the production of H_2S and SH. The situation is significantly different for O^+ ions, which can efficiently form H_2O and OH. Instead, $H_3{}^+$ chemistry commences to produce H_2S and SH as:

$$H_3{}^+ + S \rightarrow SH^+ + H_2. \tag{5.125}$$

Since SH^+ does not react with H_2 because of the endothermicity of the reaction, its radiative association reaction is important:

$$SH^+ + H_2 \rightarrow H_3S^+ + h\nu. \tag{5.126}$$

The reaction rate for this reaction is 3.6×10^{-15} cm^3 s^{-1} at 10 K, and the timescale of this reaction is evaluated to be 3×10^{10} s for a H_2 density of 10^4 cm^{-3}. For comparison, the timescale for electron recombination of SH^+ is calculated to be 5×10^9 s, using a rate coefficient of 1.1×10^{-6} cm^3 s^{-1} and assuming an electron abundance of 2×10^{-4} cm^{-3}. The timescale of electron recombination is shorter than that of radiative association. Hence, the H_3S^+ formation (reaction (5.126)) is a minor process for the loss of SH^+. Nevertheless, this route represents the only way to produce H_3S^+ from S atoms in the gas phase of cold molecular clouds.

The product ion, H_3S^+, is a stable ion that is isoelectronic with PH_3, and hence it does not react with H_2. H_2S and SH are therefore formed by dissociative electron recombination reactions of H_3S^+:

$$H_3S^+ + e \rightarrow H_2S + H \tag{5.127}$$

$$\rightarrow SH + H_2 \tag{5.128}$$

$$\rightarrow SH + H + H \tag{5.129}$$

$$\rightarrow S + H_2 + H. \tag{5.130}$$

The branching ratios for reactions (5.127, 5.128, 5.129, and 5.130) are 0.17, 0.58, 0.15, and 0.10, respectively, according to laboratory measurements of dissociative recombination reactions of D_3S^+ (Kaminska et al. 2008). Because of the slow radiative association reaction (5.126) and the small branching ratio yielding H_2S, the production efficiency of H_2S is not very high in the gas phase. It is known that the observed abundance of H_2S in cold clouds cannot be explained by this mechanism. Hence, H_2S is thought to be produced mainly on dust grains and liberated into the gas phase by thermal and nonthermal processes (Sect. 6.6).

Because S^+ ions do not react with H_2, S^+ has a greater probability of reacting with hydrocarbons that make up various sulfur-bearing organic molecules. For instance, the following reactions contribute to form the abundant sulfur-bearing molecules CS, H_2CS, CCS, and C_3S:

$$S^+ + CH \rightarrow CS^+ + H, \tag{5.131}$$

$$CS^+ + H_2 \rightarrow HCS^+ + H, \tag{5.132}$$

$$S^+ + CH_2 \rightarrow HCS^+ + H, \tag{5.133}$$

$$S^+ + CH_4 \rightarrow H_3CS^+ + H, \tag{5.134}$$

$$S^+ + C_2H_2 \rightarrow HCCS^+ + H, \tag{5.135}$$

$$S^+ + C_3H_2 \rightarrow HC_3S + +H, \tag{5.136}$$

$$\mathrm{HCS^+ + e \rightarrow CS + H}, \tag{5.137}$$

$$\mathrm{H_3CS^+ + e \rightarrow H_2CS + H}, \tag{5.138}$$

$$\mathrm{HCCS^+ + e \rightarrow CCS + H}, \tag{5.139}$$

and

$$\mathrm{HC_3S^+ + e \rightarrow C_3S + H}. \tag{5.140}$$

In addition to S^+ ions, S atoms play an important role in producing sulfur-bearing molecules via ion–molecule and neutral–neutral reactions. For instance, the following reaction of S with $CH_3{}^+$ produces H_2CS^+:

$$\mathrm{S + CH_3{}^+ \rightarrow H_2CS^+ + H}. \tag{5.141}$$

A subsequent hydrogenation reaction,

$$\mathrm{H_2CS^+ + H_2 \rightarrow H_3CS^+ + H}, \tag{5.142}$$

and the electron recombination reaction (5.138) eventually make H_2CS. Although reaction (5.141) is a minor pathway among various reaction of $CH_3{}^+$, it is useful for sulfur chemistry.

Neutral–neutral reactions such as

$$\mathrm{CH + S \rightarrow CS + H}, \tag{5.143}$$

$$\mathrm{CCH + S \rightarrow CCS + H}, \tag{5.144}$$

$$\mathrm{OH + S \rightarrow SO + H}, \tag{5.145}$$

$$\mathrm{O_2 + S \rightarrow SO + O}, \tag{5.146}$$

and

$$\mathrm{SO + OH \rightarrow SO_2 + H} \tag{5.147}$$

are exothermic and free of reaction barriers and hence play important roles in sulfur chemistry in cold molecular clouds. The reaction

$$\mathrm{CH + CS \rightarrow CCS + S} \tag{5.148}$$

is proposed as the main production pathway for producing CCS based on observations of its ^{13}C isotopic species (Sakai et al. 2007). According to these authors' results, the abundances of the two ^{13}C isotopic species of CCS, ^{13}CCS and C^{13}CS, differ significantly, indicating that the two carbon atoms making up CCS are not equivalent. Specifically, the two carbon atoms have to come from different molecular species or from nonequivalent positions of a single molecule. Hence, reaction

(5.135), for instance, is not the main route. Such nonequivalence of carbon atoms in carbon-chain molecules has been recognized for HC_3N, CCH, c-C_3H_2, C_3S, and C_4H (Takano et al. 1990; Sakai et al. 2010a, 2013; Yoshida et al. 2015).

5.9 Anion Chemistry

Although the dominant carriers of negative charge are electrons, negatively charged molecules are expected to exist in molecular clouds. The existence of an observable amount of anion molecules was theoretically predicted by Herbst (1981). However, laboratory spectroscopic studies of molecular anions have been very difficult to conduct, and the rotational transition frequencies of most molecular anions were not known accurately at that time. Hence, astronomical observations of molecular anions were also very difficult (e.g., Morisawa et al. 2005). In 2006, McCarthy and collaborators succeeded in detecting the rotational spectrum of C_6H^- in the laboratory. Based on their result, they subsequently found that a series of unidentified lines observed in the envelope of the evolved star, IRC+10,216, originate from C_6H^-. Furthermore, they detected C_6H^- lines toward the starless core TMC-1. This observation represented the first detection of an anion molecule in molecular clouds. The $[C_6H^-]/[C_6H]$ ratio is 0.04 (Table 5.1). Following the detection of C_6H^-, C_8H^- was detected in TMC-1 (Brunken et al. 2007). Additionally, C_4H^- was detected in the starless core Lupus-1A, which is a carbon-chain-rich cloud-like TMC-1 (Fig. 5.2) (Sakai et al. 2010b). Although CN^-, C_3N^-, and C_5N^- were detected in IRC+10,216 (Agundez et al. 2010; Thaddeus et al. 2008; Cernicharo et al. 2008), they have not yet been detected in molecular clouds.

Because carbon-chain molecules (C_nH) have large electron affinities, their anions, C_nH^-, are mainly formed by radiative electron-attachment reactions:

$$C_nH + e \rightarrow C_nH^- + h\nu (n = 4, 6, \text{and } 8). \tag{5.149}$$

Dissociative electron-attachment reactions may also contribute to their formation:

$$C_nH_2(\text{cumulene type}) + e \rightarrow C_nH^- + H(n = 6 \text{ and } 8). \tag{5.150}$$

In this case, C_nH_2 has to be a cumulene-type geometrical isomer. For an acetylene-type isomer, the reaction is endothermic. On the other hand, C_nH^- is destroyed by reactions with H, O, and positive M^+ ions:

$$C_nH^- + H \rightarrow C_nH_2(\text{cumulene type}) + e, \tag{5.151}$$

$$C_nH^- + O \rightarrow \text{products} + e, \tag{5.152}$$

and

$$C_nH^- + M^+ \rightarrow \text{products}. \tag{5.153}$$

Considering the formation and destruction processes of C_nH^-, the steady-state abundance is written:

$$\frac{[C_nH^-]}{[C_nH]} = \frac{k_{ra}[e]}{k_H[H] + k_O[O] + k_M[M^+]}, \tag{5.154}$$

where k_{ra} denotes the rate coefficient of reaction (5.149), and k_H, k_O, and k_M represent the rate coefficients of reactions (5.151), (5.152), and (5.153), respectively. Here, we ignored the dissociative association reaction (5.150). The value of the rate coefficient of k_{ra} is highly uncertain, because it has not yet been measured in the laboratory and has accordingly only a theoretical estimate. In comparison, the rate coefficients of k_H and k_O are expected to be close to the Langevin rate coefficient, because reactions (5.150), (5.151), and (5.152) are initiated by charge-induced dipole interactions. The rate coefficient of k_M can reasonably be estimated from that of the neutralization reaction. Here, we assume that $k_H \sim k_O \sim 10^{-9}$ cm^3 s^{-1}, $k_M \sim 4 \times 10^{-7}$ cm^3 s^{-1}, [H] ~ [O] ~ 1 cm^{-3}, and [e] ~ [M$^+$] ~ 10^{-3} cm^{-3} for order-of-magnitude estimates of the $[C_6H^-]/[C_6H]$ ratio. Then, k_{ra} of 6×10^{-8} cm^3 s^{-1} is required to reproduce the $[C_6H^-]/[C_6H]$ ratio observed in TMC-1. The radiative electron attachment is indeed very fast for C_6H. This rate coefficient for the radiative electron-attachment reaction is roughly consistent with the theoretical prediction by Herbst and Osamura (2008) (3×10^{-7} cm^3 s^{-1} at 10 K). The situation is notably different for C_4H^-. The $[C_4H^-]/[C_4H]$ ratio is less than 5.2×10^{-5} in TMC-1 (Agundez et al. 2008); it is 8.8×10^{-5} in Lupus-1A (Sakai et al. 2010b). Using the above equation, we recover the rate coefficient for the radiative electron-attachment reaction for C_4H smaller by two orders of magnitude than the rate coefficient for C_6H. This result arises because radiative stabilization is faster for a larger molecule (Sect. 3.5).

In molecular clouds, dust grains tend to be negatively charged because a solid particle typically has a large electron affinity. This situation is in contrast to the diffuse cloud case, where dust grains are positively charged because of photoionization. The existence of C_nH^- in starless cores may be consistent with this trend: C_nH molecules can be regarded as "very small dust grains" with positive electron affinities. If a substantial number of negative charges are carried by molecular anions, the recombination processes of atomic ions will be significantly affected. Detecting other molecular anions is therefore of fundamental importance in astrochemistry.

5.10 Gas-Phase Chemical Models and Comparisons with Observations

First, we estimate the timescale for chemical equilibrium. Because molecular formation starts from reactions with H_3^+, the formation timescale is roughly the same as the timescales for the reactions of H_3^+ with C (reaction 5.36) and H_3^+ with O (reaction 5.72). Then, the reactions generally proceed quickly to yield various neutral species, including CO. The timescale of reactions (5.36 and 5.72) is given as

$$t = \frac{1}{k\left[H_3^+\right]}, \tag{5.155}$$

where k is the reaction rate coefficient for reactions (5.36 and 5.72) and can be approximated as 2×10^{-9} cm^3 s^{-1}. The H_3^+ abundance can be approximated to be 1.8×10^{-5} cm^{-3}, as discussed in Sect. 5.3. Hence, the timescale is 9×10^5 year. The formation timescale is noted to be independent of H_2 density in this approximation, because the H_3^+ abundance is independent of H_2 density, as seen in Eq. (5.15). The destruction timescale of molecules is, for example, 3×10^6 year for He^+ destruction, and is longer than the formation timescale (Sect. 5.4). The destruction timescale is also independent of H_2 density. Hence, the timescale for chemical equilibrium is roughly evaluated to be 7×10^5 year, according to Eq. (3.88). This timescale is much longer than that for diffuse clouds (typically 300 year), where the short timescale of the photodissociation process makes the equilibrium timescale short.

The timescale for chemical equilibrium is longer than the free-fall time. According to Eq. (4.55), the free-fall time is 3.4×10^5 year for a H_2 density of 10^4 cm^{-3}. Hence, the chemical composition of molecular clouds does not always reach its equilibrium value before gravitational collapse. The actual lifetime of a cloud against collapse could be longer than the free-fall time because of various supporting mechanisms, including magnetic fields and turbulent motion. In this case, chemical compositions would approach those in chemical equilibrium. In contrast to diffuse clouds where the steady-state approximation typically holds, it is crucially important to simulate the evolution of chemical compositions for molecular clouds. The rate equations have to be solved as a set of simultaneous (nonlinear) differential equations.

The time-dependent chemical models can be categorized into two types. One type includes the "pseudo-time-dependent" model. In this model, the temporal variation of chemical compositions is calculated as a function of time assuming a constant H_2 density and temperature. This model is useful for exploring the general trends of chemical compositions and the role of particular reactions in forming particular molecules. This assumption is a good approximation for starless cores, and hence the results are used for critical comparisons with the chemical compositions of cold starless cores such as TMC-1. The other type includes the full time-dependent model, which considers the dynamical evolution of clouds and also the

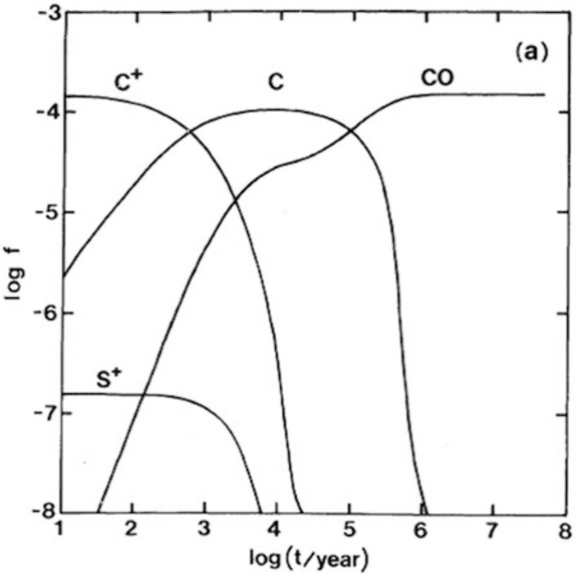

Fig. 5.7 Temporal variation of the fractional abundances of C^+, C, and CO in a molecular cloud for a H_2 density of 10^4 cm^{-3}, a temperature of 10 K, and a visual extinction of 10 magnitudes, calculated using the pseudo-time-dependent model. The diffuse cloud condition is employed as the initial conditions (i.e., all carbon atoms are ionized; oxygen and nitrogen atoms are neutral). After shutting off the UV radiation ($t = 0$), the major form of carbon in the gas phase changes from C^+ to C and then from C to CO within a timescale of a several 10^5 year. Carbon-chain molecules are preferentially formed in the early stages before the carbon atoms are locked up as CO, as shown in Fig. 5.9 (Reprinted with permission from Suzuki et al. (1992). Copyright 1992 American Astronomical Society)

effect of star formation. This treatment is more realistic than the pseudo-time-dependent model and can trace chemical evolution toward star formation. Because this model treats the coupling between physics and chemistry, the chemical composition depends on the physical evolution of the cloud. The interpretation of the chemical composition is therefore more complicated.

Figure 5.7 shows an example of the pseudo-time-dependent model, showing the change in the dominant form of carbon. For the initial conditions, the chemical composition of a diffuse cloud is employed to simulate chemical evolution from a diffuse cloud to a molecular cloud. In particular, hydrogen is assumed to be in molecular form, and the other elements in atomic form. Some elements (e.g., He, O, N, and fluorine (F)) with ionization potentials higher than that of H (13.60 eV) are neutral; other elements (C, Si, P, and S) with ionization potentials lower than that of H are ionized. After the UV radiation is shielded at $t = 0$, the C^+ ion recombines with electrons to form C, and then C is locked up as CO through various chemical reactions. The formation timescale of CO is approximately 9×10^5 year. This change in the major form of carbon causes systematic temporal variations in the chemical compositions of molecular clouds. Organic molecules, including carbon-chain molecules, are abundant at early times when C is abundant, but they become

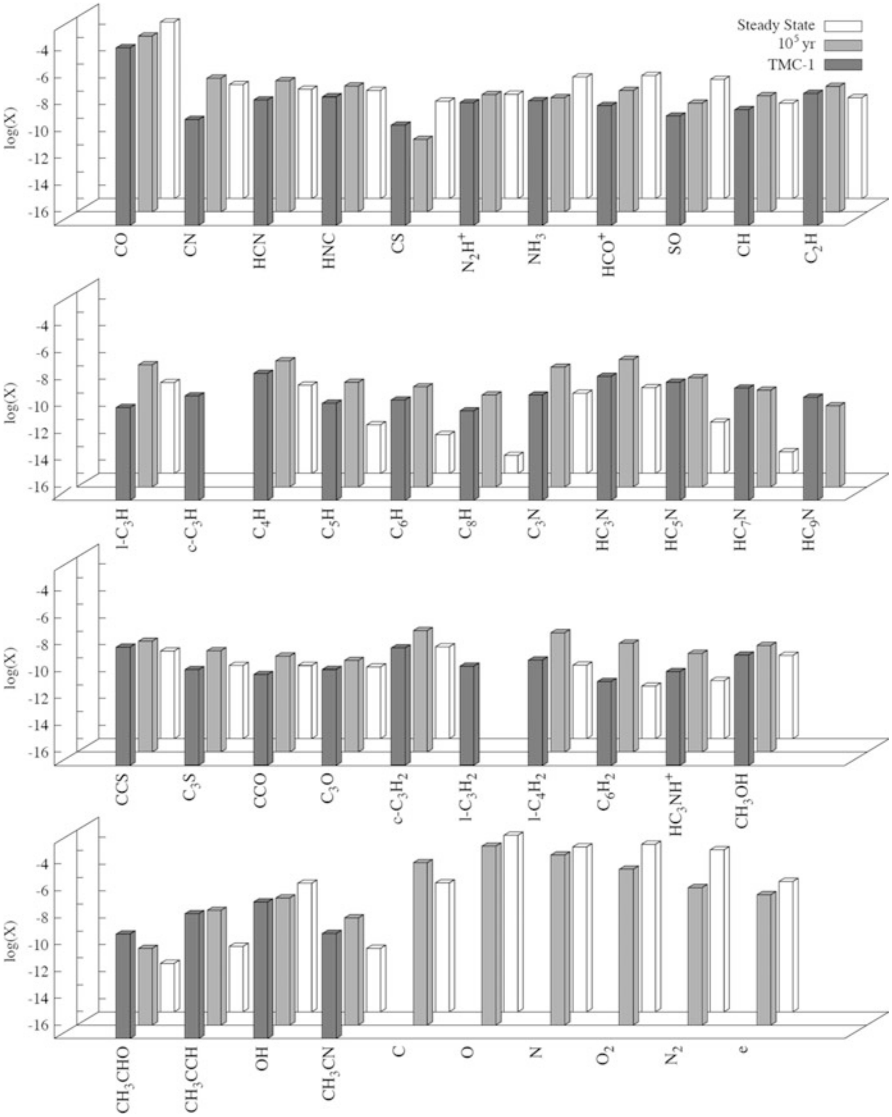

Fig. 5.8 Fractional abundances of selected molecules observed in TMC-1 and comparison with model calculation. Observed abundances are calculated from the column densities (Table 5.1) by assuming the H_2 column density of 10^{22} cm^{-2}. For comparison, results of the pseudo-time-dependent model by Lee et al. (1996) (the abundances at 10^5 year and in the steady state) are shown

deficient in the steady state. The nitrogen-containing species such as NH_3 and N_2H^+ become more abundant at later stages, because they are not directly related to the carbon chemistry and are formed slowly. These features can be seen in the detailed pseudo-time-dependent calculation (Fig. 5.8).

The non-equilibrium nature of chemical compositions of molecular clouds is indeed seen in observations. The chemical composition of TMC-1 (CP) is compared with the chemical model calculations in Fig. 5.8. The chemical composition of TMC-1 (CP) is poorly reproduced by the steady-state abundances; it can reasonably be explained by the abundances at early times (1×10^5 year).

The chemical compositions of molecular cloud cores systematically differ from source to source. Figure 5.9 shows the correlation diagram of the column densities of carbon-chain molecules (CCS and HC_3N) and NH_3. The column densities of CCS and HC_3N show a good correlation; the column densities of CCS and NH_3 show significant scatter. In these diagrams, the open circles and open triangles represent the evolved cores in which star formation has already taken place. In such star-forming cores, the carbon-chain molecules CCS and HC_3N are generally deficient, whereas NH_3 is abundant. This observational result is consistent with the picture of non-equilibrium chemistry.

Chemical differentiation between carbon-chain molecules and NH_3/ N_2H^+ observed in the TMC-1 ridge and L1544 can be explained in terms of chemical evolution. In the TMC-1 ridge case, the northern region, where NH_3 is abundant, is more chemically evolved than the southern region, where CCS and other carbon-chain molecules are also abundant (Fig. 5.4). This result means that dense core formation has been progressing from north to south in the TMC-1 ridge (Hirahara et al. 1992). Indeed, the young protostar IRAS 04381+2540 is associated with the NH_3 peak in the northern region of the ridge. Although other interpretations of chemical differentiation in TMC-1 have been proposed, such as the C/O abundance gradient and the effect of magneto-hydrodynamics waves from IRAS 04381+2540 (Pratap et al. 1997; Markwick et al. 2000), chemical evolution can naturally account for observations of the TMC-1 ridge, as well as chemical differentiation in other regions. Large-scale maps of the atomic carbon obtained using the Mount Fuji submillimeter-wave telescope revealed that the direction of chemical evolution seen in the C/CO ratio is consistent with the direction inferred from the carbon-chain molecules and NH_3/N_2H^+ (Fig. 5.10) (Maezawa et al. 1999). Recent observations of CH, which is a reaction intermediate in the formation of CO from C, shows that the CH distribution indeed bridges the distributions of atomic carbon and CO (Sakai et al. 2012). This result further supports the picture of chemical evolution.

As for L1544 (Fig. 5.5), CCS is apparently deficient in the central part of the core; N_2H^+ is enhanced there. This result can naturally be interpreted as a collapsing core, where the central part is more chemically evolved than the peripheries. This gradation in chemical evolution is not only the result of the chemical evolutionary effect in the gas phase but also to the depletion of molecules onto dust grains. This effect will be described in Chap. 6.

Problems

5.1 Evaluate the proton affinity of CH using the dissociation energy of CH_2 and the ionization potentials of H and CH_2 listed in Table 4.2. In the same way, evaluate the proton affinities of CH_2 and CH_3.

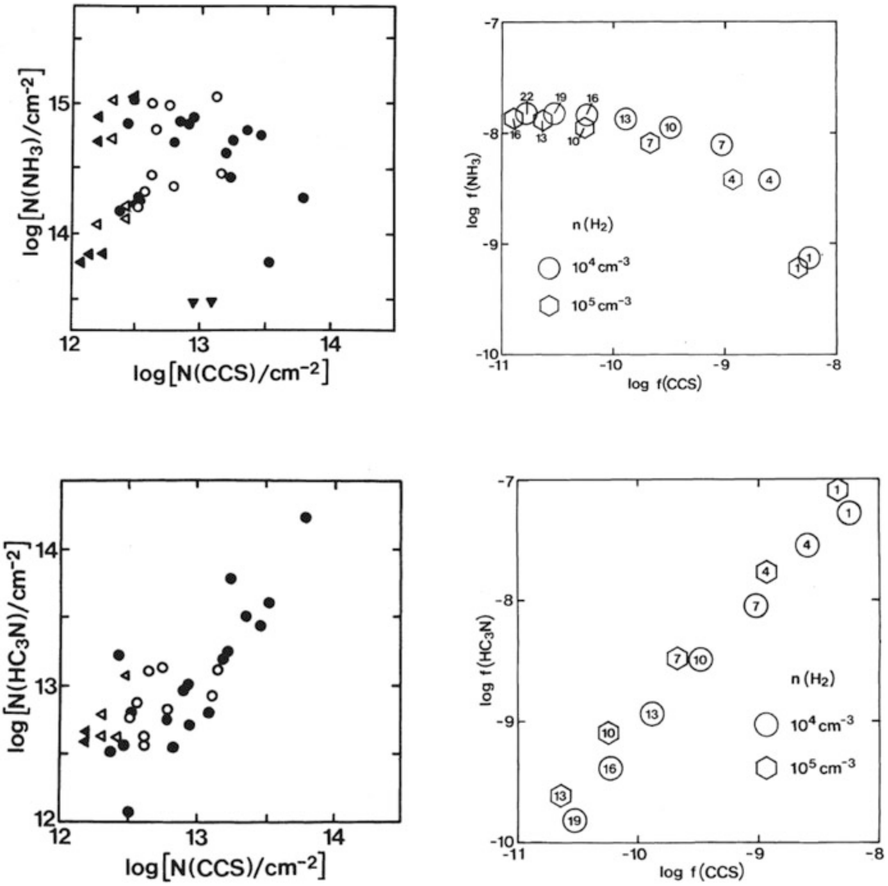

Fig. 5.9 (*Left panels*) Correlation diagrams between NH_3 and CCS and between HC_3N and CCS observed toward dense cores. *Filled marks* represent starless cores; *open circles* represent star-forming cores. *Triangles* represent upper limits. Although the abundances of the carbon-chain molecules HC_3N and CCS are well correlated, the abundances of NH_3 and CCS are not. (*Right panels*) The observed trends can be reproduced using chemical model calculations (the pseudo-time-dependent model). The numbers in the symbols represent the time, in units of 10^5 year, after shut-off of UV radiation. The chemical model can reproduce both the correlation between HC_3N and CCS and the lack of a correlation between NH_3 and CCS. Furthermore, evolved cores (star-forming cores) tend to be located in the *upper left* corner in the NH_3–CCS diagram and the *lower left* corner in the HC_3N–CCS diagram. Carbon-chain molecules are abundant in early stages; NH_3 is abundant in late stages (Reprinted with permission from Suzuki et al. (1992). Copyright 1992 American Astronomical Society)

5.2 We consider a molecular cloud where the cosmic-ray ionization rate is 100 times higher than in the normal molecular clouds discussed in this chapter. For simplicity, the density and temperature of the molecular cloud are assumed to be 10^4 cm^{-3} and 10 K, respectively.

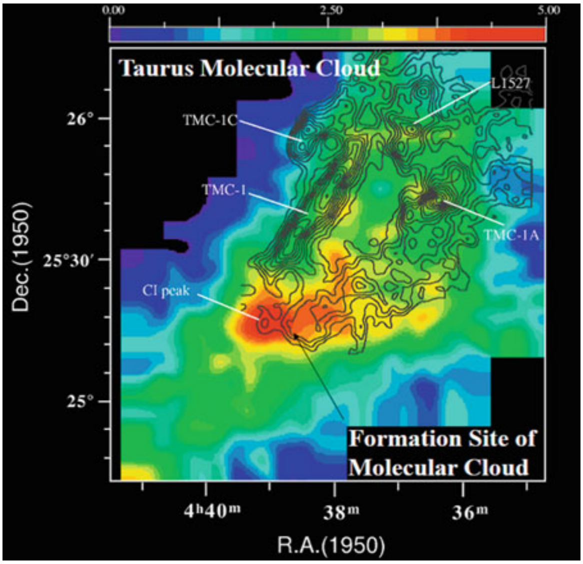

Fig. 5.10 Intensity distribution of the $^3P_1$–$^3P_0$ fine structure line of atomic carbon [C I] at 492 GHz observed toward the Heiles Cloud 2 (HCL2) region involving the TMC-1 ridge with the Mount Fuji submillimeter-wave telescope (color). The superposed contour map is the intensity distribution of $C^{18}O$ (J=1–0). Atomic carbon is preferentially distributed around the southern region of HCL2; CO mainly exists in the northern region. Hence, the global direction of chemical evolution proceeds from the northern region to the southern region, which is consistent with the direction of the chemical evolution seen in the TMC-1 ridge (see Fig. 5.3 and the text) (Reprinted with permission from Maezawa et al. (1999). Copyright 1999 American Astronomical Society)

(a) Calculate the degree of ionization of the cloud, and the abundances of H_3^+ and He^+.
(b) Evaluate the time necessary for chemical equilibrium.
(c) Discuss the major reactions for CH_3^+. How does the high cosmic ionization rate affect the reaction pathways?

5.3 As for Problem 2, we turn to examining chemical processes in low-metallicity conditions. Abundances of all of the heavy elements (C, N, O, and so on) relative to H_2 are assumed to be lower by a factor of 10 than those employed in the text. For simplicity, the density and the temperature are assumed to be 10^4 cm^{-3} and 10 K, respectively.

(a) Calculate the degree of ionization, and the abundances of H_3^+ and He^+.
(b) Evaluate the time necessary for chemical equilibrium.
(c) Discuss the major reactions for CH_3^+. How does the low metallicity affect the reaction pathways?

5.4 There are two stable carbon isotopes, ^{12}C and ^{13}C, where the elemental abundance ratio of $[^{12}C]/[^{13}C]$ is assumed to be 59 in the local interstellar medium. Here, we consider a mechanism that makes the [^{12}C]/[^{13}C] ratio in molecules different from this elemental abundance ratio. Because the major form of carbon is CO, the main reservoir of ^{13}C is ^{13}CO. The ^{12}C^{+} and ^{13}C^{+} ions are formed by the destruction reactions of ^{12}CO and ^{13}CO by He^{+}:

$$^{12}\mathrm{CO} + \mathrm{He}^{+} \rightarrow {}^{12}\mathrm{C}^{+} + \mathrm{O} + \mathrm{He},$$
$$^{13}\mathrm{CO} + \mathrm{He}^{+} \rightarrow {}^{13}\mathrm{C}^{+} + \mathrm{O} + \mathrm{He}.$$

The rate coefficients of these reactions are the same as that for reaction (5.31). The ^{12}C^{+} and ^{13}C^{+} ions thus formed are used for producing various carbon-bearing molecules through reactions:

$$^{12}\mathrm{C}^{+} + \mathrm{H}_2 \rightarrow {}^{12}\mathrm{CH_2}^{+} + h\nu,$$
$$^{13}\mathrm{C}^{+} + \mathrm{H}_2 \rightarrow {}^{13}\mathrm{CH_2}^{+} + h\nu.$$

The rate coefficient is 1.7×10^{-15} cm^{3} s^{-1} at 10 K (Table 4.6) for both reactions. However, ^{13}C^{+} is lost by the following isotope exchange reaction:

$$^{13}\mathrm{C}^{+} + {}^{12}\mathrm{CO} \rightarrow {}^{12}\mathrm{C}^{+} + {}^{13}\mathrm{CO},$$

whose reaction rate coefficient is assumed to be 1×10^{-9} cm^{3} s^{-1}. This reaction is exothermic only by 35 K, and hence the backward reaction rate can be approximated to be $1 \times 10^{-9} \exp(-35/T)$ cm^{3} s^{-1}. For this reason, the [^{12}C^{+}]/[^{13}C^{+}] ratio differs from the elemental ^{12}C/^{13}C ratio, which affects the ^{12}C/^{13}C ratios in various molecules. By adopting a steady-state approximation, derive a relation between the [^{12}C^{+}]/[^{13}C^{+}] ratio and the [^{12}CO]/[^{13}CO] ratio as a function of temperature. The ^{13}C isotopic species are thus expected to be "diluted" in molecular clouds in general (Langer et al. 1984), which is actually observed for carbon-chain molecules in TMC-1 (Sakai et al. 2010a).

5.5 In deriving the anion-to-neutral ratio of Eq. (5.154), include the effect of the dissociative attachment reaction (5.150). If the rate coefficient of the reaction (5.150) is assumed to be 3×10^{-6} cm^{3} s^{-1} at 10 K (Herbst and Osamura 2008), how does the inclusion of reaction (5.150) affect the C_6H^{-}/C_6H ratio? Use the abundances of C_6H and C_6H_2 (cumulene type) in TMC-1 (Table 5.1) for your evaluation.

References

M. Agundez, J. Cernicharo, M. Guelin, M. Gerin, M.C. McCarthy, P. Thaddeus, Astron. Astrophys. **478**, L19 (2008)

M. Agundez, J. Cernicharo, M. Guelin, C. Kahane, E. Roueff, J. Klos, F.J. Aoiz, F. Lique, J. Marcelino, J.R. Goicoechea, M. Gonzalez Garcia, C.A. Gottlieb, M. McCarthy, P. Thaddeus, Astron. Astrophys. **517**, L2 (2010)

Y. Aikawa, N. Ohashi, S. Inutsuka, E. Herbst, S. Takakuwa, Astrophys. J **552**, 639 (2001)

J. Bally, W.D. Langer, A.A. Stark, R.W. Wilson, Astrophys. J. **312**, L45 (1987)

C.A. Beichman, P.C. Myers, J.P. Emerson, S. Harris, R. Mathieu, P.J. Benson, R.E. Jennings, Astrophys. J. **307**, 337 (1986)

P.J. Benson, P.C. Myers, Astrophys. J. Suppl. **71**, 89 (1989)

R.D. Brown, P.D. Godfrey, D.M. Cragg, E.H.N. Rice, W.M. Irvine, P. Friberg, H. Suzuki, M. Ohishi, N. Kaifu, M. Morimoto, Astrophys. J. **297**, 302 (1985)

S. Brunken, H. Gupta, C.A. Gottlieb, M.C. McCarthy, P. Thaddeus, Astrophys. J. **664**, L43 (2007)

J. Cernicharo, C.A. Gottlieb, M. Guelin, T.C. Killian, G. Paubert, P. Thaddeus, J.M. Vrtilek, Astrophys. J. **368**, L39 (1991)

J. Cernicharo, M. Guelin, M. Agundez, M. McCarthy, P. Thaddeus, Astrophys. J. **688**, L83 (2008)

T.M. Dame, H. Ungerechts, R.S. Cohen, E.J. de Geus, I.A. Grenier, J. May, D.C. Murphy, L.-A. Nyman, P. Thaddeus, Astrophys. J. **322**, 706 (1987)

D. Fosse, J. Cernicharo, M. Gerin, P. Cox, Astrophys. J. **552**, 168 (2001)

P. Friberg, A. Hjalmarson, W.M. Irvine, M. Guelin, Astrophys. J. **241**, L99 (1980)

Y. Fukui et al., Astrophys. J. Suppl. **178**, 56 (2008)

E.T. Galloway, E. Herbst, Astron. Astrophys. **211**, 413 (1989)

W.D. Geppert, M. Hamberg, R.D. Thomas, et al., Faraday Discuss. **133**, 177 (2006)

R. Gredel, S. Lepp, A. Dalgarno, Astrophys. J. **323**, L137 (1987)

R. Gredel, S. Lepp, A. Dalgarno, E. Herbst, Astrophys. J. **347**, 289 (1989)

J. Harju, A. Winnberg, J.G.A. Wouterloot, Astron. Astrophys. **353**, 1065 (2000)

E. Herbst, Nature **289**, 656 (1981)

E. Herbst, Y. Osamura, Astrophys. J. **679**, 1670 (2008)

Y. Hirahara, H. Suzuki, S. Yamamoto, et al., Astrophys. J. **394**, 539 (1992)

T. Hirota, S. Yamamoto, H. Mikami, M. Ohishi, Astrophys. J. **503**, 717 (1998)

E.P.L. Hunter, S.G. Lias, J. Phys. Chem. Ref. Data **27**, 413 (1998)

W.M. Irvine, B. Hoglund, P. Friberg, J. Askne, J. Ellder, Astrophys. J. **248**, L113 (1981)

W.M. Irvine et al., Astrophys. J. **334**, L107 (1988a)

W.M. Irvine, R.D. Brown, D.M. Cragg, P. Friberg, P.D. Godfrey, N. Kaifu, H.E. Matthews, M. Ohishi, H. Suzuki, H. Takeo, Astrophys. J. **335**, L89 (1988b)

W.M. Irvine, P. Friberg, N. Kaifu, K. Kawaguchi, Y. Kitamura, H.E. Matthews, Y. Minh, S. Saito, N. Ukita, S. Yamamoto, Astrophys. J. **342**, 871 (1989)

N. Kaifu, M. Ohishi, K. Kawaguchi, S. Saito, S. Yamamoto, T. Miyaji, K. Miyazawa, S. Ishikawa, C. Nomaru, S. Harasawa, M. Okuda, H. Suzuki, Publ. Astron. Soc. Japan **56**, 69 (2004)

M. Kaminska, E. Vigren, V. Zhaunerchyk, et al., Astrophys. J. **681**, 1717 (2008)

K. Kawaguchi et al., Astrophys. J. **396**, L49 (1992a)

K. Kawaguchi, M. Ohishi, S. Ishikawa, N. Kaifu, Astrophys. J. **386**, L51 (1992b)

K. Kawaguchi, Y. Kasai, S. Ishikawa, M. Ohishi, N. Kaifu, T. Amano, Astrophys. J. **420**, L95 (1994)

H. Kirk, D. Johnstone, J. Di Francesco, Astrophys. J. **646**, 1009 (2006)

N. Kuno et al., Publ. Astron. Soc. Japan **59**, 117 (2007)

W.D. Langer, T.E. Graedel, M.A. Frerking, P.B. Armentrout, Astrophys. J. **277**, 581 (1984)

B. Larsson, R. Liseau, L. Pagani, et al., Astron. Astrophys. **466**, 999 (2007)

H.-H. Lee, R.P.A. Bettens, E. Herbst, Astron. Astrophys. Suppl. **119**, 111 (1996)

R. Liseau, P.F. Goldsmith, B. Larsson, et al., Astron. Astrophys. **54**, A73 (2012)

L.T. Little, G.H. Macdonald, P.W. Riley, D.N. Matheson, Mon. Not. R. Astr. Soc. **189**, 539 (1979)

H. Maezawa, M. Ikeda, T. Ito, et al., Astrophys. J. **524**, L129 (1999)

N. Marcelino, J. Cernicharo, M. Agundez, E. Roueff, M. Gerin, J. Martin-Pintado, R. Mauersberger, C. Thum, Astrophys. J. **665**, L127 (2007)

N. Marcelino, J. Cernicharo, B. Tercero, E. Roueff, Astrophys. J. **690**, L27 (2009)

N. Marcelino, S. Brunken, J. Cernicharo, D. Quan, E. Roueff, E. Herbst, P. Thaddeus, Astron. Astrophys. **516**, A105 (2010)

A.J. Markwick, T.J. Millar, S.B. Charnley, Astrophys. J. **535**, 256 (2000)

H.E. Matthews, T.J. Sears, Astrophys. J. **267**, L53 (1983)

H.E. Matthews, P. Friberg, W.M. Irvine, Astrophys. J. **290**, 609 (1985)

D. McGonagle, W.M. Irvine, M. Ohishi, Astrophys. J. **422**, 621 (1994)

D. McElroy, C. Walsh, A.J. Markwick, M.A. Cordiner, K. Smith, T.J. Millar, Astron. Astrophys. **550**, 36 (2013)

Y.C. Minh, W.M. Irvine, L.M. Ziurys, Astrophys. J. **345**, L63 (1989)

Y.C. Minh, J.E. Dickens, W.M. Irvine, D. McGonagle, Astron. Astrophys. **298**, 213 (1995)

H. Minowa, M. Satake, T. Hirota, S. Yamamoto, M. Ohishi, N. Kaifu, Astrophys. J. **491**, L63 (1997)

A. Mizuno, T. Onishi, Y. Yonekura, T. Nagahama, H. Ogawa, Y. Fukui, Astrophys. J. **445**, L161 (1995)

Y. Morisawa, H. Hoshina, Y. Kato, Z. Simizu, S. Kuma, N. Sogoshi, M. Fushitani, S. Watanabe, Y. Miyamoto, T. Momose, Y. Kasai, K. Kawaguchi, PASJ **57**, 325 (2005)

M. Morris, B.E. Turner, P. Palmer, B. Zuckerman, Astrophys. J. **205**, 82 (1976)

P.C. Myers, Astrophys. J. **270**, 105 (1983)

P.C. Myers, R.A. Linke, P.J. Benson, Astrophys. J. **264**, 517 (1983)

M. Ohishi, H. Suzuki, S. Ishikawa, C. Yamada, H. Kanamori, W.M. Irvine, R.D. Brown, P.D. Godfrey, N. Kaifu, Astrophys. J. **380**, L39 (1991)

M. Ohishi, D. McGonagle, W.M. Irvine, S. Yamamoto, S. Saito, Astrophys. J. **427**, L51 (1994)

C.A. Olano, C.M. Walmsley, T.L. Wilson, Astron. Astrophys. **196**, 194 (1988)

P. Palmeirim et al., Astron. Astrophys. **550**, 38 (2013)

S.S. Prasad, W.T. Huntress Jr., Astrophys. J. **260**, 590 (1982)

P. Pratap, J.E. Dickens, R.L. Snell, M.P. Miralles, E.A. Bergin, W.M. Irvine, F.P. Schloerb, Astrophys. J. **486**, 862 (1997)

A.J. Remijan, J.M. Hollis, L.E. Snyder, P.R. Jewell, F.J. Lovas, Astrophys. J. **643**, L37 (2006)

N. Sakai, M. Ikeda, M. Morita, T. Sakai, S. Takano, S. Yamamoto, Astrophys. J. **663**, 1174 (2007)

N. Sakai, T. Sakai, T. Hirota, S. Yamamoto, Astrophys. J. **672**, 371 (2008)

N. Sakai, O. Saruwatari, .T. Sakai, T. Takano, S. Yamamoto, Astron. Astrophys. **512**, A31 (2010a)

N. Sakai, T. Shiino, T. Hirota, T. Sakai, S. Yamamoto, Astrophys. J. **718**, L49 (2010b)

N. Sakai, H. Maezawa, T. Sakai, K.M. Menten, S. Yamamoto, Astron. Astrophys. **546**, A103 (2012)

N. Sakai, S. Takano, T. Sakai, S. Shiba, Y. Sumiyoshi, Y. Endo, S. Yamamoto, J. Phys. Chem. **117**, 9831 (2013)

N. Sakai, S. Yamamoto, Chem. Rev. **113**, 8981 (2013)

G.B.I. Scott., D.A. Fairley, C.G. Freeman, M.J. McEwan, V.G. Anicich, J. Chem. Phys **109**, 9010 (1998)

I.R. Sims, J.-L. Queffelec, D. Travers, B.R. Rowe, L.B. Herbert, J. Karthauser, I.W.M. Smith, Chem. Phys. Lett. **211**, 461 (1993)

L.E. Snyder, J.M. Hollis, P.R. Jewell, F.J. Lovas, A. Remijan, Astrophys. J. **647**, 412 (2006)

H. Suzuki, S. Yamamoto, M. Ohishi, et al., Astrophys. J. **392**, 551 (1992)

S. Takano, H. Suzuki, M. Ohishi, S. Ishikawa, N. Kaifu, Y. Hirahara, A. Masuda, Astrophys. J. **361**, L15 (1990)

S. Takano, A. Masuda, Y. Hirahara, et al., Astron. Astrophys. **329**, 1156 (1998)

P. Thaddeus, C.A. Gottlieb, H. Gupta, S. Brunken, M. McCarthy, M. Agundez, M. Guelin, J. Cernicharo, Astrophys. J. **677**, 1132 (2008)

F. Tolle, H. Ungerechts, C.M. Walmsley, G. Winnewisser, E. Chunchwell, Astron. Astrophys. **95**, 143 (1981)

D.E. Woon, E. Herbst, Astrophys. J. **477**, 204 (1997)

S. Yamamoto, S. Saito, M. Ohishi, H. Suzuki, S. Ishikawa, N. Kaifu, A. Murakami, Astrophys. J. **322**, L55 (1987)

K. Yoshida, N. Sakai, T. Tokudome, A. Lopez-Sepulcre, Y. Watanabe, T. Takano, B. Lefloch, C. Ceccarelli, R. Bachiller, E. Caux, C. Vastel, S. Yamamoto, Astrophys. J. **807**, 66 (2015)

Chapter 6
Chemistry of Molecular Clouds II: Gas–Grain Processes

6.1 Roles of Dust Grains in Astrochemistry

Interstellar matter is composed of molecular and atomic gas and dust grains. Dust grains mainly consist of nonvolatile silicate (e.g., $Mg_{2x}Fe_{2\text{-}2x}SiO_4$, olivines; $Mg_xFe_{1\text{-}x}SiO_3$, pyroxenes) and carbonaceous compounds including polycyclic aromatic hydrocarbons (PAHs), and have a typical radius of 0.1 μm (grain cores). In molecular clouds, the grain core is surrounded by grain mantle, which consists of H_2O ice containing various molecules. Dust grains scatter and absorb interstellar UV radiation. As a result, molecules that reside deep inside of molecular clouds can avoid photodissociation and/or photoionization and can survive for a much longer time than in diffuse clouds. This process ensures more complex molecules, as indeed found in molecular clouds. Furthermore, ionization of the gas is dominated by cosmic-ray ionization, because photoionization is inefficient because of UV shielding by dust grains. The degree of ionization is accordingly lower in molecular clouds than in diffuse clouds. The difference in the degree of ionization is responsible for the difference in molecular formation pathways, as described in Chaps. 4 and 5. Dust grains in molecular clouds tend to be negatively charged, whereas dust grains are positively charged in diffuse clouds because of photoionization.

In addition to these fundamental effects, dust grains play an important role in production of molecules. Dust grains absorb atoms and molecules on their surface, thereby providing opportunities for chemical reactions to take place. Such surface reactions make further chemical complexity. This chapter describes the role of dust grains on chemical compositions of molecular clouds.

S. Yamamoto, *Introduction to Astrochemistry*, Astronomy and Astrophysics
Library 7, DOI 10.1007/978-4-431-54171-4_6

6.2 Depletion of Atoms and Molecules onto Dust Grains

In cold molecular clouds, molecules are adsorbed on dust grains when they collide with them. Molecules are typically adsorbed on dust grains by van der Waals forces or electrostatic force (physisorption). In some cases, molecules are more strongly bound to the surface by forming chemical bonds (chemisorption). Here, we mainly consider the physisorption. Adsorbed molecules can be desorbed thermally. The balance between adsorption and desorption determines the adsorption temperature, below which the corresponding species is adsorbed on dust grains efficiently and is removed from the gas phase. This process is referred to as *depletion*. Conversely, the corresponding species on dust grains is liberated into the gas phase above the adsorption temperature. Hence, the adsorption temperature is also called the desorption temperature.

Let us evaluate the adsorption temperature. First, we consider the adsorption process. Because dust grains have a typical size of 0.1 μm and are much larger than molecules, the geometrical cross section of dust grains can be applied to estimate the depletion. If we assume that a dust grain is a sphere of radius a, the geometrical cross section is given as:

$$\sigma = \pi a^2. \tag{6.1}$$

In reality, dust grains do not have the same radius, but have a size distribution (Problem 1). However, for simplicity, this effect is not considered here. We here focus on a particular molecular species, X. The number of the molecules colliding with a particular dust grain per unit time is represented as follows:

$$R_{\text{ads}} = n(\text{X}) S\sigma < v >, \tag{6.2}$$

where $n(\text{X})$ denotes the number density of X in the gas phase, $<v>$ is the average speed of a molecule, and S is the sticking probability. The sticking probability accounts for the probability that a molecule is adsorbed in a collision with dust grains. A sticking probability of unity means that a molecule is adsorbed in every collision. We assume here a sticking probability of unity for simplicity.

Adsorbed molecules can be desorbed thermally. The rate of thermal desorption depends on the desorption energy, E_d, which depends on molecular species as well as surface conditions of dust grains (Table 6.1). The number of molecules desorbed thermally from a particular grain is given as:

$$R_{\text{des}} = N_s(\text{X})\nu_0 \exp\left(-\frac{E_d}{k_B T}\right), \tag{6.3}$$

where v_0 is the characteristic frequency for the vibrational mode that leads to desorption, and $N_s(\text{X})$ denotes the number of molecules X on a particular dust

Table 6.1 Desorption energies and various timescales for some atoms and molecules

Species	E_d/K[a]	10 K	t_{hop} /s[b] 20 K	40K	10 K	t_{evap} /s[c] 20K	40K	t_{qt}/s[d]	t_{acc}/s[e] 10 K
H	450	1.7×10^{-3}	2.3×10^{-8}	8.2×10^{-11}	1.0×10^{7}	1.8×10^{-3}	2.3×10^{-6}	1.3×10^{-10}	6.9×10^{4}
H_2	430	9.3×10^{-4}	2.0×10^{-8}	9.3×10^{-11}	2.0×10^{6}	9.3×10^{-4}	2.0×10^{-8}	2.0×10^{-9}	9.8×10^{4}
OH	2850	3.7×10^{49}	4.3×10^{18}	1.4	2.9×10^{111}	3.7×10^{49}	4.3×10^{18}	1.4×10^{15}	2.9×10^{5}
H_2O	5700	2.1×10^{111}	2.7×10^{49}	3.1×10^{18}	1.2×10^{235}	2.1×10^{111}	2.7×10^{49}	3.2×10^{27}	2.9×10^{5}
N_2	1000	5.5×10^{9}	7.6×10^{-2}	2.8×10^{-7}	2.8×10^{31}	5.5×10^{9}	7.6×10^{-2}	7.8×10^{8}	3.7×10^{5}
CO	1150	9.2×10^{12}	3.0	1.7×10^{-6}	8.6×10^{37}	9.2×10^{12}	3.0	2.4×10^{10}	3.7×10^{5}
CH_4	1300	1.2×10^{16}	9.1×10^{1}	8.0×10^{-6}	2.0×10^{44}	1.2×10^{16}	9.1×10^{1}	6.8×10^{5}	2.8×10^{5}
H_2CO	2050	2.5×10^{32}	1.4×10^{10}	1.0×10^{-1}	8.2×10^{76}	2.5×10^{32}	1.4×10^{10}	6.5×10^{18}	3.8×10^{5}
CH_3OH	5530	5.8×10^{107}	5.3×10^{47}	5.0×10^{17}	7.0×10^{227}	5.8×10^{107}	5.3×10^{47}	1.4×10^{40}	3.9×10^{5}
$HCOOCH_3$	6300	3.9×10^{124}	1.5×10^{56}	9.7×10^{21}	2.5×10^{261}	3.9×10^{124}	1.5×10^{56}	3.0×10^{64}	5.4×10^{5}
CH_3OCH_3	3150	1.9×10^{56}	1.2×10^{22}	9.6×10^{4}	4.8×10^{124}	1.9×10^{56}	1.2×10^{22}	2.3×10^{35}	4.7×10^{5}
C	800	1.8×10^{5}	3.7×10^{-4}	1.7×10^{-6}	4.3×10^{22}	1.8×10^{5}	3.7×10^{-4}	1.3	2.4×10^{5}
O	800	2.1×10^{5}	4.3×10^{-4}	2.0×10^{-6}	4.9×10^{22}	2.1×10^{5}	4.3×10^{-4}	1.2×10^{2}	2.8×10^{5}

[a] Desorption energy

[b] Hopping timescale from one site to another, assuming that $E_b = E_d/2$

[c] Evaporation timescale

[d] Timescale for quantum tunneling from one site to another

[e] Accretion timescale of molecules onto a single grain. The gas-phase abundance is set to 1 cm^{-3}

grain. This frequency (ν_0) can be estimated with a formula obtained from the harmonic oscillator approximation:

$$\nu_0 = \left(2n_{\mathrm{site}}E_d/\pi^2 m\right)^{1/2}, \tag{6.4}$$

where n_{site} is the surface density of the adsorbing sites (1.5×10^{15} cm^{-2}) and m is the mass of the absorbed molecule (Hasegawa et al. 1992) (see Sect. 6.3 for definition of the adsorption site). A typical frequency is 10^{12} Hz.

In the steady state, R_{ads} is balanced by R_{des}, and hence we obtain the relation:

$$\frac{N_s(\mathrm{X})}{n(\mathrm{X})} = \frac{\sigma < v >}{\nu_0 \exp\left(-\frac{E_d}{k_B T}\right)}. \tag{6.5}$$

N_s(X) is related to the number of molecules X on dust grains in a unit volume, n_s(X), as:

$$n_s(\mathrm{X}) = N_s(\mathrm{X})n_g, \tag{6.6}$$

where n_g is the number of grains in a unit volume. Then, we obtain:

$$\frac{n_s(\mathrm{X})}{n(\mathrm{X})} = \frac{n_g N_s(\mathrm{X})}{n(\mathrm{X})} = \frac{\Sigma n_0 < v >}{\nu_0 \exp\left(-\frac{E_d}{k_B T}\right)}. \tag{6.7}$$

Here, Σ is the effective collision area of dust per H nucleus:

$$\Sigma = \frac{n_g \sigma}{n_0}, \tag{6.8}$$

where n_0 represents the number density of H nuclei ($n_0 = n(\mathrm{H}) + 2n(\mathrm{H_2})$). Σ is estimated to be 3×10^{-22} cm^{-2}. If the size distribution of grains is considered, it is 6×10^{-22} cm^{-2} (See Problem 6.1). When the right-hand side of Eq. (6.7) is equal to unity, the gas-phase abundance and the solid-phase abundance on dust grains become comparable. The temperature that satisfies this condition can be regarded as the adsorption temperature. When we assume n_{site} to be 1.5×10^{15} cm^{-2}, the critical temperature of CO is calculated to be 20 K using a desorption energy of 1150 K, as shown in Fig. 6.1. In contrast, the critical temperature of H_2 is found to be 7 K when we employ a desorption energy of 430 K. The adsorption temperature depends on the grain-surface conditions, as well as cloud density. However, the adsorption temperature is only weakly affected by these factors.

If the grain temperature is the same as the gas kinetic temperature, molecules other than H_2, H, and He will be depleted onto dust grains at 10 K in the steady state. Next, we evaluate the timescale required for a molecule to be depleted onto a dust grain. The depletion rate for a molecule can be represented as:

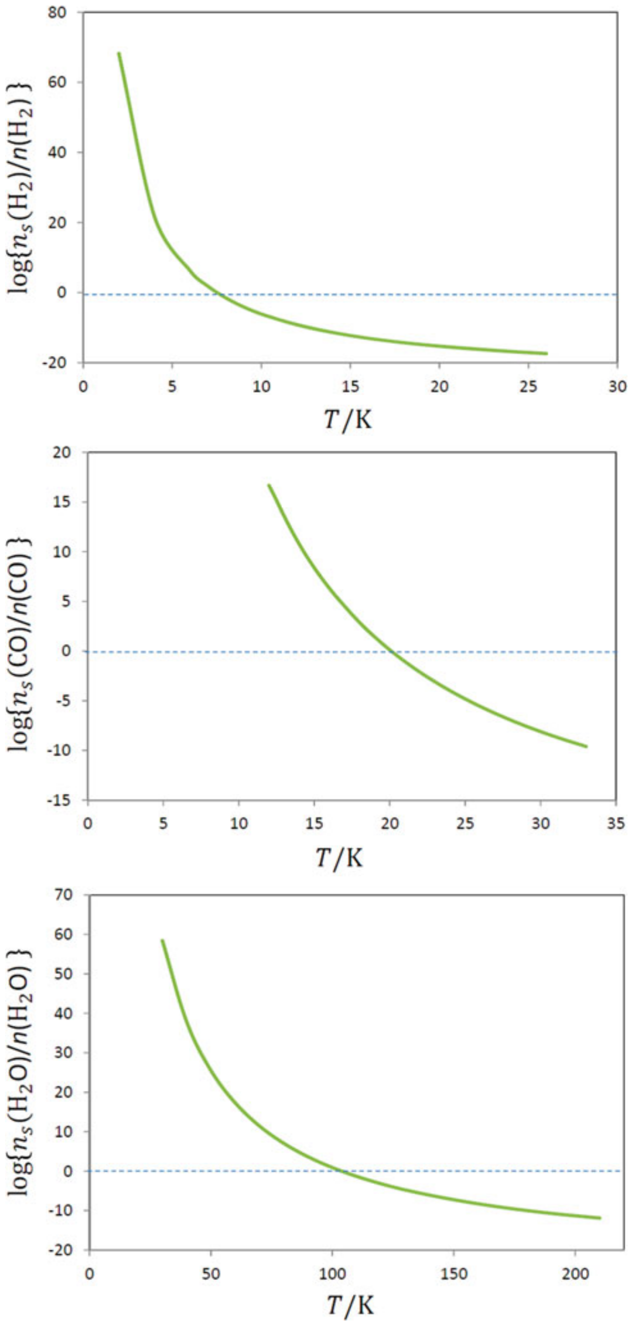

Fig. 6.1 Ratio of the gas-phase abundance and the solid-phase abundance of CO (*upper panel*) and H_2O (*lower panel*) as a function of temperature. The temperature at which the ratio is unity can be regarded as the desorption temperature. The H_2 density is 10^4 cm^{-3}. The desorption temperature weakly depends on H_2 density (Chap. 8)

$$R_{\mathrm{dep}} = n(\mathrm{H_2}) f_g S\sigma < v > , \tag{6.9}$$

where f_g is the fractional abundance of dust grains (2×10^{-12}) relative to H_2. Assuming that the sticking probability is unity and $a \sim 0.1$ μm, we obtain:

$$R_{\mathrm{dep}} \sim 5 \times 10^{-18} n(\mathrm{H_2}) \mathrm{s}^{-1}, \tag{6.10}$$

for CO molecules at 10 K; if the size distribution is considered, it is given as:

$$R_{\mathrm{dep}} \sim 1 \times 10^{-17} n(\mathrm{H_2}) \mathrm{s}^{-1}. \tag{6.11}$$

The timescale for depletion (τ_d) is therefore the inverse of R:

$$\tau_d \sim \frac{3 \times 10^9}{n(\mathrm{H_2})} \text{ year.} \tag{6.12}$$

Apparently, the above derivation is an order-of-magnitude estimation and is based on many simplified assumptions. Indeed, a rough estimation,

$$\tau_d \sim \frac{10^9}{n(\mathrm{H_2})} \text{ year} \tag{6.13}$$

is often used (e.g., Caselli et al. 1999). Nevertheless, the timescale can be as short as 10^5 year. for an H_2 density of 10^4 cm^{-3}. This timescale is comparable to or even shorter than the timescale for chemical equilibrium or the dynamical timescale (Chap. 5). Hence, the depletion of molecules has a substantial impact on chemical compositions in the gas phase. This fact is particularly important in the late stages of the starless core phase.

Depletion of CO onto dust grains was demonstrated observationally toward the starless core, L1544, by Caselli et al. (1999). These authors observed the $C^{17}O$ ($J = 1 - 0$) line toward this source and compared its distribution with that of the dust continuum emission, which is known to trace the total H_2 column density along the line of sight. As shown in Fig. 6.2, the intensity of the $C^{17}O$ ($J = 1 - 0$) line apparently becomes weaker toward the peak of dust continuum emission than toward the surrounding positions. Because the $C^{17}O$ ($J = 1 - 0$) line is optically thin, this result cannot be interpreted as an optical depth effect. One can therefore conclude that the relatively weak intensity of the $C^{17}O$ ($J = 1 - 0$) emission toward the dust continuum peak originates from the depletion of CO onto dust grains. Such evidence for CO depletion has been found toward many sources (e.g., Tafalla et al. 2004, 2006; Bacmann et al. 2002; Pagani et al. 2005; Maret et al. 2013), and it is now established that CO depletion is a general feature of evolved starless cores.

CO depletion has a large impact on chemical compositions of molecular clouds. A good example is the enhancement of N_2H^+ and HCO_2^+. The proton affinities of

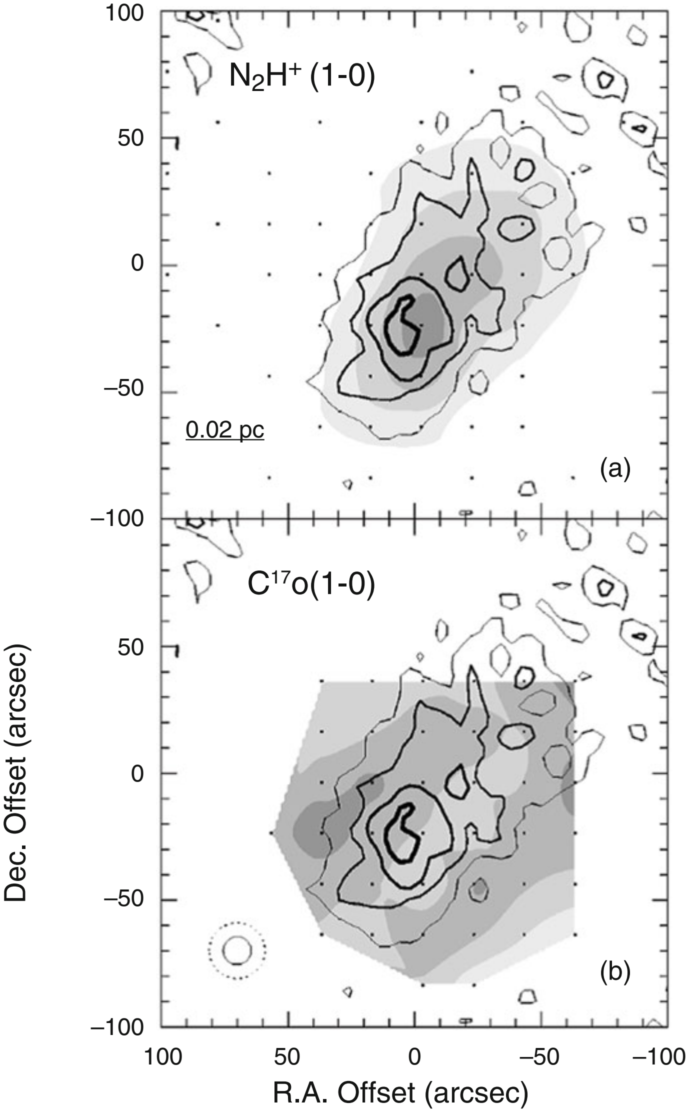

Fig. 6.2 Distributions of N_2H^+ (*upper panel*: gray scale) and $C^{17}O$ (*lower panel*: gray scale) superimposed on the distribution of dust continuum (*contours*) observed toward the starless core L1544. The intensity of the dust continuum emission can be regarded as a measure of the total column density of H_2. The $C^{17}O$ distribution clearly shows depletion toward the continuum peak, in contrast to N_2H^+ (Reprinted with permission from Caselli et al. (1999). Copyright 1999 American Astronomical Society)

N_2 and CO_2 are lower than that of CO, and hence CO is the main destructor of these ions:

$$N_2H^+ + CO \rightarrow HCO^+ + N_2, \tag{6.14}$$

$$HCO_2{}^+ + CO \rightarrow HCO^+ + CO_2. \tag{6.15}$$

The removal of CO from the gas phase extends the lifetime of these ions and enhances their abundances. This implies that N_2H^+ is abundant in high-density regions where CO is significantly depleted. Indeed, the N_2H^+ ($J = 1 - 0$) emission has a peak toward the dust continuum peak in L1544 (Aikawa et al. 2001). We note that N_2 itself is also depleted onto dust grains in high-density regions. However, the extension of the lifetime of N_2H^+ overcomes the depletion effect, yielding a N_2H^+ emission peak toward the dust continuum peak. Enhancement of N_2H^+ due to CO depletion makes the NH_3 abundance higher, as described in Sect. 5.7. Another effect of CO depletion is the enhancement of deuterium fractionation in various molecules. This topic will be discussed in Sect. 6.7.

6.3 Grain-Surface Reactions

Depleted molecules do not stay on dust grains as they are, but are instead subject to grain-surface reactions. For such reactions, atoms and molecules adsorbed on dust grains have to move on the surface to encounter a reaction partner (Fig. 6.3). This reaction mechanism is called the Langmuir–Hinshelwood mechanism. A second mechanism in which gaseous atoms and molecules directly hit atoms and molecules

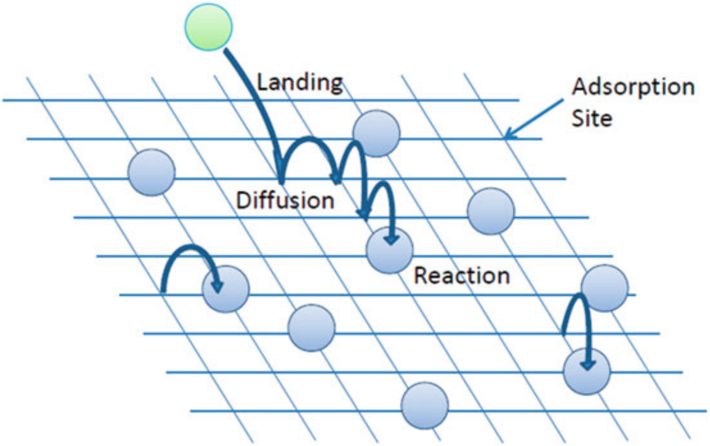

Fig. 6.3 Schematic of surface reactions via the Langmuir–Hinshelwood mechanism. A diffusive species such as H scans the site by thermal diffusion and quantum tunneling to find a reaction partner

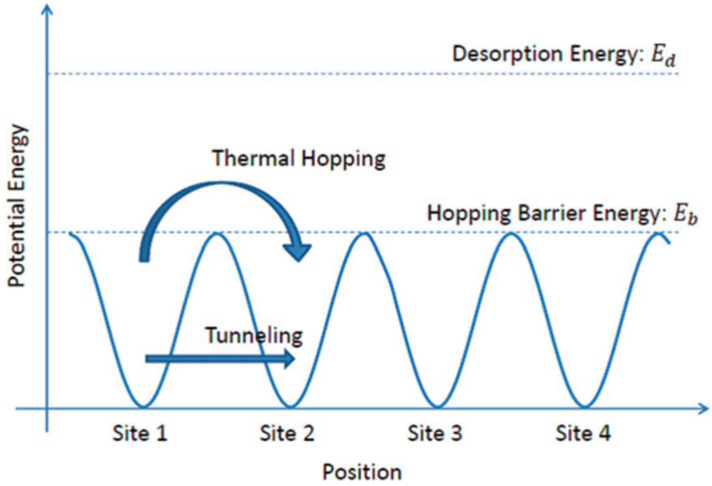

Fig. 6.4 Schematic of the surface potential for an adsorbed molecule/atom. The molecule/atom is adsorbed at an adsorption site, which is the surface potential minimum, with a binding energy of E_d. The molecule/atom moves from one adsorption site to another adsorption site via thermal hopping with a barrier of E_b or via quantum tunneling

on dust grains to form products is called the Rideal mechanism, which is less important in interstellar clouds. Hence, surface mobility is an important factor in grain-surface reactions. Atoms and molecules are typically adsorbed on “sites,” which are the local minima of the interaction potential of atoms and molecules with the surface (Fig. 6.4). The density of sites and their distribution depend on the surface. The motion of atoms and molecules on a surface can be represented classically in terms of a hopping motion from one site to another. During this hopping, atoms and molecules have to overcome a potential barrier between the sites. When the barrier height is assumed to be E_b, the timescale of the hopping motion can be classically represented as:

$$\frac{1}{t} = \nu_0 \exp\left(-\frac{E_b}{k_B T}\right), \tag{6.16}$$

where ν_0 is the characteristic frequency used in the desorption process. E_b depends on various factors, including the interaction potential and surface conditions; it is often assumed to be $E_d/2$ for simplicity. The ratio between E_b and E_d is, however, quite ambiguous and is often used as an adjusting parameter in chemical models. At 10 K, the timescale for molecules to hop from one site to another can be as short as 1.7×10^{-3} s for H atoms; the timescale is 9.2×10^{12} s for CO molecules (Table 6.1). It should be noted that the mobility of atoms and molecules increases with increasing temperature. For instance, the timescale for CO decreases to 3.0 s at 20 K. At the same time, one has to realize that hopping can compete with desorption process at higher temperatures.

For light species such as H atoms, quantum effects are thought to be important. For instance, H atoms could tunnel through a barrier between the two sites with a certain probability. The relevant timescale can be written as:

$$t_q = \frac{1}{\nu_0 \exp\left\{-\frac{2a}{\hbar}(2mE_b)^{1/2}\right\}}, \tag{6.17}$$

obtained using a simple one-dimensional rectangular barrier with a constant height of E_b and a width of a. The typical timescale is 1.3×10^{-4} s for H atoms, assuming a typical a of 1 Å. This timescale is shorter than the classical hopping rate at 10 K. However, it was found based on laboratory experiments that the migration of H atoms is not as fast as that expected based on tunneling (Katz et al. 1999). Hence, it is now assumed that classical hopping plays a major role in the migration of H atoms on dust surfaces. In any case, we can say that H atoms can readily move around the grain surface, even at 10 K.

When we assume that the number of sites on a grain surface is 10^6, the time required for H atoms to scan all of the sites is roughly evaluated to be 1.7×10^3 s. This time is called the diffusion timescale $t_{\rm diff}$, which is approximated as a product of the hopping timescale $t_{\rm hop}$ and the number of sites on the surface n_s:

$$t_{\rm diff} = t_{\rm hop}\, n_s. \tag{6.18}$$

Of course, this process competes with the desorption timescale. When the temperature is below 15 K, H atoms can scan all of the adsorption sites before desorption. However, mobility is quite low for heavy atoms and molecules at 10 K. Hence, we can assume that the heavy atoms almost stay at their sites and wait for H atoms for reactions.

Next, we consider a grain-surface reaction between species i and j. The numbers of species i and j on a single grain are denoted by N_i^S and N_j^S, respectively. Denoting the diffusion timescales for the i and j species by $t_{\rm diff}(i)$ and $t_{\rm diff}(j)$, respectively, the number of reactions between species i and j occurring per unit volume and unit time can be written as:

$$R_{ij} = k_{ij}\left\{\frac{1}{t_{\rm diff}(i)} + \frac{1}{t_{\rm diff}(j)}\right\} N_i^S N_j^S n_g. \tag{6.19}$$

The coefficient, k_{ij}, is the probability that the reaction occurs between i and j when they encounter each other at a site on a grain. The numbers of solid-phase species i and j per unit volume, n_i^S and n_j^S, respectively, are related to N_i and N_j according to:

$$n_i^S = n_g N_i, \quad n_j^S = n_g N_j. \tag{6.20}$$

Hence, Eq. (6.15) can be rewritten as:

$$R_{ij} = K_{ij} n_i^S n_j^S, \tag{6.21}$$

where K_{ij} can be regarded as the effective rate coefficient for the reaction between the grain-surface species i and j. It is defined as:

$$K_{ij} = k_{ij} \left\{ \frac{1}{t_{\mathrm{diff}}(i)} + \frac{1}{t_{\mathrm{diff}}(j)} \right\} \frac{1}{n_g}, \tag{6.22}$$

where the units are cm^3 s^{-1}.

The reaction probability k_{ij} is an important factor for grain-surface reactions. The probability can typically be regarded as being equal to unity for radical–radical reactions such as:

$$\mathrm{H} + \mathrm{OH} \rightarrow \mathrm{H_2O}, \tag{6.23}$$

$$\mathrm{H} + \mathrm{HCO} \rightarrow \mathrm{H_2CO}. \tag{6.24}$$

In contrast to gas-phase reactions, the grain surface can be a "third body" that absorbs the excess reaction energy. Hence, the reaction yielding only one product species can proceed on the grain surface. However, reactions between closed-shell molecules and radicals typically possess an activation energy barrier (reaction barrier) E_a. Hence, the reaction probability becomes less than unity because of the Boltzmann factor necessary to overcome the activation barrier. For reactions involving H and H_2, quantum tunneling is thought to be important. In this case, k_{ij} can be written as:

$$k_{ij} = \exp\left\{ -\frac{2a}{\hbar} (2mE_{\mathrm{a}})^{1/2} \right\}. \tag{6.25}$$

Reactions between closed-shell species generally have very high activation energies and will not proceed on grain surfaces at low temperatures.

The above formulation of grain-surface reactions using the rate equation has an apparent limitation. The rate equation method is based on the macroscopic number of molecules. This implicit assumption holds true for gas-phase reactions, as well as surface reactions on very large grains. However, it does not hold true for small grains because of their discrete nature. The average number of molecules on dust grains is less meaningful if the number is much less than unity. In particular, the reaction timescale of reactive species such as H, t_{react}, is much shorter than the interval of accretion of the next H atom, t_{int}. In this case, the reaction probability of H atoms during the interval is evaluated to be $t_{\mathrm{int}}/t_{\mathrm{react}}$, which exceeds unity. Despite having no more available H atoms on a grain surface, the reaction will continue with the certain rate given in the rate equation method. Thus, the rate equation method tends to overestimate the reaction. In reality, the reaction rate of H atoms with other species is not governed by the reaction rate (or diffusion rate), but rather by the accretion rate of H atoms. For multiple reaction pathways for H atoms, the sum of their reaction probabilities has to be less than unity during the accretion interval.

This situation for the rate equation method can be explained in a different way (Garrod 2008). The number of molecules on dust grains should fluctuate, and the production rate of molecules should be expressed by the average of many dust grains. The average production rate for the reactions of species i and j on a single grain can then be given as:

$$\left\langle \frac{R_{ij}}{n_g} \right\rangle = k_{ij} \left\{ \frac{1}{t_{\mathrm{diff}}(i)} + \frac{1}{t_{\mathrm{diff}}(j)} \right\} \langle N_i^S N_j^S \rangle, \tag{6.26}$$

where $\langle Q \rangle$ represents the average of quantity Q over many dust grains. If $\langle N_i N_j \rangle = \langle N_i \rangle \times \langle N_j \rangle$, the rate equation method discussed above can be applied. This assumption is valid if there is no correlation between N_i and N_j. However, an anticorrelation develops if the reaction between the two species is fast. In this case, $\langle N_i \rangle \times \langle N_j \rangle$ is larger than $\langle N_i N_j \rangle$, and the production rate is overestimated. This situation is particularly significant when both N_i and N_j are less than unity.

To fully account for the discrete nature of grains, a Monte Carlo approach is necessary. In this case, reactions of a molecule (or an atom) falling onto a dust grain are traced by probabilities. A difference in the results between the rate equation method and the Monte Carlo method was pointed out by Tielens and Hagen (1982), Caselli et al. (1998), and others. However, it is not easy to implement the Monte Carlo method for a large chemical model network dealing with complex molecules. Hence, many proposals to mitigate the limitation of the rate equation method have been developed.

One proposal is the modified rate approach (e.g., Caselli et al. 1998; Garrod 2008). To suppress the overreaction of reactive species such as H, reaction rates between H atoms and other species are artificially slowed down to the rate that is the faster of the accretion and evaporation rates of H atoms. In most cases, the reaction of H atoms is then determined by the accretion rate. Apparently, this modified rate approach depends on the surface mobility of the reactive species. The modified rate approach is often employed in gas–grain chemical models. The moment equation method and the master equation method (e.g., Stantcheva et al. 2002; Lipshtat and Biham 2003; Du and Parise 2011) are also proposed to deal with the stochastic effects of dust grains.

6.4 Formation of H_2 Molecules on Grain Surfaces

Because H atoms and H_2 molecules have a high surface mobility, they play a major role in grain-surface reactions. In particular, H atoms are a key species for hydrogenation reactions because of their high reactivity. Table 6.1 lists the diffusion timescales at a few representative temperatures. C, O, and N atoms can also move from site to site to some extent. However, the diffusion timescales of other species such as CO, H_2O, and N_2 are very long at 10 K. Furthermore, the evaporation timescale of H atoms is 10^7 s at 10 K, which is much longer than the accretion and diffusion times. Hence, all H atoms react with the other species on dust grains. From this point of view, hydrogenation reactions are the most important processes in grain-surface chemistry. We note that the situation is different for higher temperatures. At 40 K, the evaporation time is 2.3×10^{-6} s, which is shorter than the diffusion time of 8.2×10^{-5} s. At higher temperatures, the mobility of heavy species increases, and hence hydrogenation reactions are less important.

Here, we describe a few examples of grain-surface chemistry. First, we present the formation of H_2 molecule from H atoms:

$$\mathrm{H(g)} \rightarrow \mathrm{H(s)}, \tag{6.27}$$

$$\mathrm{H(s)} \rightarrow \mathrm{H(g)}, \tag{6.28}$$

$$\mathrm{H(s)} + \mathrm{H(s)} \rightarrow \mathrm{H_2(s)}, \tag{6.29}$$

$$\mathrm{H_2(s)} \rightarrow \mathrm{H_2(g)}. \tag{6.30}$$

The gas-phase and surface species are denoted by (g) and (s), respectively. The rate coefficients for reactions (6.27, 6.28, and 6.29) are denoted as $k_{\mathrm{ad,\,H}}$, $k_{\mathrm{des,\,H}}$, and k_{HH}, respectively. Then, the rate equations for H_2(g) and H(s) are represented as:

$$\frac{d[\mathrm{H_2(g)}]}{dt} = k_{\mathrm{HH}}[\mathrm{H(s)}]^2 \tag{6.31}$$

and

$$\frac{d[\mathrm{H(s)}]}{dt} = k_{\mathrm{ad,H}}[\mathrm{H(g)}] - k_{des,\mathrm{H}}[\mathrm{H(s)}] - 2k_{\mathrm{HH}}[\mathrm{H(s)}]^2, \tag{6.32}$$

where

$$k_{\mathrm{ad,H}} = n_g \sigma < v(\mathrm{H}) > , \tag{6.33}$$

$$k_{\mathrm{des,H}} = \nu_0 \exp\left(-\frac{E_d}{kT}\right), \tag{6.34}$$

and

$$k_{\mathrm{HH}} = \frac{2}{t_{\mathrm{diff}}(\mathrm{H}) n_g}. \tag{6.35}$$

Here, H_2 molecules formed on dust grains are assumed to be liberated into the gas phase immediately. When the steady-state condition is applied to Eq. (6.32), we obtain the following relation:

$$k_{\mathrm{ad,H}}[\mathrm{H(g)}] - k_{\mathrm{des,H}}[\mathrm{H(s)}] - 2k_{\mathrm{HH}}[H(s)]^2 = 0. \tag{6.36}$$

At 10 K, the last term dominates over the second term (Table 6.1). Hence, we ignore the second term and obtain the formation rate of H_2 molecules:

$$R(\mathrm{H_2}) = \frac{d[\mathrm{H_2(g)}]}{dt} = \frac{1}{2}k_{\mathrm{ad,H}}[\mathrm{H(g)}]. \tag{6.37}$$

Hence, each H atom adsorbed onto a dust grain produces (half of a) H_2 molecule. Using Eq. (6.33), the formation rate of H_2 molecules is reduced to:

$$R(\mathrm{H_2}) = 4.4 \times 10^{-18}\sqrt{T/\mathrm{K}}\, n_0[\mathrm{H(g)}] \left(\mathrm{cm^{-3}s^{-1}}\right). \tag{6.38}$$

Here, n_0 denotes the total number density of hydrogen nuclei ($[\mathrm{H}] + 2[\mathrm{H_2}]$). We remark that the timescale for desorption of H atoms rapidly becomes shorter for higher temperatures. In this case, [H(s)] becomes almost zero, and H_2 formation does not occur. However, the above estimate of the evaporation timescale of H atoms is based on physisorption, where the interatomic or intermolecular forces are responsible for binding H atoms on dust grains. In reality, chemisorption of H atoms on dust grains, which has a higher desorption energy, contributes at high temperature, and the evaporation timescale does not become as short as expected based on physisorption (Cazaux and Tielens 2004). Hence, the H_2 formation rate is also regulated by the accretion rate of H atoms onto dust grains, and Eq. (6.33) holds even at high temperatures.

6.5 Formation of Various Molecules on Grain Surfaces

Next, we consider carbon chemistry. In the early stages of chemical evolution, carbon can exist in its atomic form. It is depleted onto dust grains, and CH_4 is produced via reactions:

$$\mathrm{C} + \mathrm{H} \rightarrow \mathrm{CH}, \tag{6.39}$$

$$\mathrm{CH} + \mathrm{H} \rightarrow \mathrm{CH_2}, \tag{6.40}$$

$$\mathrm{CH_2} + \mathrm{H} \rightarrow \mathrm{CH_3}, \tag{6.41}$$

$$\mathrm{CH_3} + \mathrm{H} \rightarrow \mathrm{CH_4}. \tag{6.42}$$

These are all radical–radical reactions on dust grains, and we expect no activation barrier for them. For CH_x ($x = 0$–3), the hydrogenation reaction competes with the reaction of O atoms. The gas-phase abundance of H atoms is approximately 1 $\mathrm{cm^{-3}}$ in molecular clouds, which is almost independent of the H_2 density. The gas-phase abundance of O atoms is about 2 $\mathrm{cm^{-3}}$ for a H_2 density of 10^4 $\mathrm{cm^{-3}}$, if the fractional abundance of O relative to H_2 is assumed to be 2.1×10^{-4} (see Chap. 5). Hence, the accretion times of H and O atoms are estimated to be 7×10^4 s and 1.4×10^5 s, respectively. Because the diffusion rate of H is much faster than that of O, the hydrogenation reaction is a dominant pathway for CH_x ($x = 0 - 3$).

In the later stages of chemical evolution, C atoms are nearly completely converted into CO molecules in the gas phase. The CO molecules are then adsorbed onto dust grains and are subject to grain-surface reactions. Again, the hydrogenation reactions are dominant pathways:

$$\mathrm{CO + H \rightarrow HCO,} \tag{6.43}$$

$$\mathrm{HCO + H \rightarrow H_2CO,} \tag{6.44}$$

$$\mathrm{H_2CO + H \rightarrow CH_3O,} \tag{6.45}$$

$$\mathrm{CH_3O + H \rightarrow CH_3OH.} \tag{6.46}$$

Because CO and H_2CO are closed-shell molecules, reactions (6.43) and (6.45) have activation barriers of about 2000 K. At 10 K, quantum tunneling effects may play important roles for these two reactions. In contrast, reactions (6.44) and (6.46) are radical–radical reactions without an activation barrier. A series of these reactions was studied in laboratory experiments, and they are confirmed to work even at 10 K (Watanabe and Kouchi 2002; Watanabe et al. 2003).

H_2O molecules are formed on grain surfaces by the hydrogenation of O atoms:

$$\mathrm{O + H \rightarrow OH,} \tag{6.47}$$

$$\mathrm{OH + H \rightarrow H_2O.} \tag{6.48}$$

Both reactions are radical–radical reactions without an activation energy barrier. Although these reactions are the main pathways to produce H_2O, another pathway contributes as well.

$$\mathrm{O + O \rightarrow O_2,} \tag{6.49}$$

$$\mathrm{O_2 + H \rightarrow HO_2,} \tag{6.50}$$

$$\mathrm{HO_2 + H \rightarrow H_2O_2,} \tag{6.51}$$

$$\mathrm{H_2O_2 + H \rightarrow H_2O + OH.} \tag{6.52}$$

The contribution of this process is expected to be higher for higher H_2 densities. Figure 6.5 summarizes the production mechanism of H_2O on dust grains.

Similarly, N atoms are also hydrogenated successively to form NH_3:

$$\mathrm{N + H \rightarrow NH,} \tag{6.53}$$

$$\mathrm{NH + H \rightarrow NH_2,} \tag{6.54}$$

$$\mathrm{NH_2 + H \rightarrow NH_3.} \tag{6.55}$$

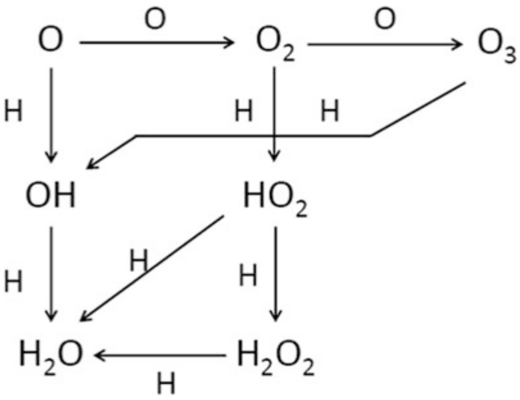

Fig. 6.5 Pathways from O to H_2O through grain-surface reactions

All of these reactions are radical–radical reactions, and no activation barriers are expected.

In addition to simple hydrogenation reactions, reactions with C, O, and N atoms can proceed to some extent. These processes contribute to form complex molecules. Furthermore, radical–radical reactions play an important role in producing complex organic molecules. Examples of these processes include:

$$\mathrm{HCO} + \mathrm{CH_3O} \rightarrow \mathrm{HCOOCH_3}, \tag{6.56}$$

$$\mathrm{CH_3} + \mathrm{CH_3O} \rightarrow (\mathrm{CH_3})_2\mathrm{O}, \tag{6.57}$$

$$\mathrm{OH} + \mathrm{HCO} \rightarrow \mathrm{HCOOH}. \tag{6.58}$$

Radicals are formed as intermediates in hydrogenation processes. Additionally, photodissociation of molecules by cosmic ray-induced UV radiation contributes to the formation of radicals. For low A_v, photodissociation of molecules by external UV radiation will also contribute to their production. The radicals thus formed can also react with each other to form larger species, although hydrogenation processes are the most important pathways for them.

The hydrogenation of molecules larger than CO is also expected. For instance, hydrogenation of HC_3N produces C_2H_3CN and C_2H_5CN:

$$\mathrm{HC_3N} + \mathrm{H} \rightarrow \mathrm{H_2C_3N}, \tag{6.59}$$

$$\mathrm{H_2C_3N} + \mathrm{H} \rightarrow \mathrm{C_2H_3CN}, \tag{6.60}$$

$$\mathrm{C_2H_3CN} + \mathrm{H} \rightarrow \mathrm{C_2H_4CN}, \tag{6.61}$$

$$\mathrm{C_2H_4CN} + \mathrm{H} \rightarrow \mathrm{C_2H_5CN}. \tag{6.62}$$

where H_2C_3N and C_2H_4CN are free radicals. This scheme is suggested to be a possible pathway to form C_2H_5CN on dust grains (Blake et al. 1987; Caselli et al. 1993).

6.6 Desorption of Molecules by Nonthermal Processes

Except for H_2, molecules formed on grain-surface reactions stay on the grain surface at 10 K, because thermal evaporation is negligibly slow. Grain-surface molecules will be liberated into the gas phase by thermal heating, shock heating, or sputtering caused by various processes associated with star formation. Such processes will be described in Chap. 7. Even at 10 K, there exist desorption processes that liberate the grain-surface molecules into the gas phase. One process is desorption by excess energy of chemical reactions; another process is desorption by cosmic rays or cosmic ray-induced UV radiation. For low A_v, photodesorption by external UV radiation will also contribute to the desorption of molecules.

First, we consider desorption by excess chemical reaction energy. In association reactions, an excess energy of a few eV will be released. This energy, E, is typically much larger than the binding energy, E_D, of the product molecule on the grain surface. In considering the statistical partition of the excess energy for the $(s-1)$ vibrational modes of the product molecule and one dissociation mode between the molecule and the surface, the probability of dissociation is:

$$P = \left(\frac{E - E_D}{E}\right)^{s-1}. \tag{6.63}$$

This equation is similar to Eq. (3.57). Because $E - E_D$ is typically very close to E, the probability of dissociation is close to unity. If so, the product molecule is desorbed with a probability of almost 100 %. However, this consideration is too simplified. It is necessary to consider energy transfer to the surface, which significantly lowers the probability. In this case, we consider a hypothetical molecule composed of the product molecule and a finite area of the surface. When all of the vibrational degrees of freedom of the surface atoms and molecules are counted, the effective s value for the hypothetical molecule would be enormous. Even if $(E - E_D)/E$ is close to unity, the probability of dissociation can be very low in this case. The fraction of molecules desorbed in their formation is thus taken as a parameter for the model. A fraction of 0.01–0.01 is typically assumed (Garrod et al. 2007).

The second process is desorption by cosmic rays, which can be divided into two different mechanisms. One mechanism is instantaneous heating of dust grains by a direct hit of cosmic rays. This mechanism is particularly significant for small grains, whose heat capacity is small. Another mechanism is desorption by cosmic ray-induced UV radiation. The rate coefficients of the former processes have been reported in the literature (Hasegawa and Herbst 1993), although they involve many assumptions.

In cosmic ray-induced desorption (both of the above two mechanisms), the desorption rate of species X on dust grains is approximately proportional to the cosmic-ray ionization rate, as far as the abundance of species X on dust grains is constant. Then, the following rate relation holds for the abundance of X:

$$\frac{d[\mathrm{X}]}{dt} = \beta\zeta[\mathrm{H}_2] - k_{ad,X}[\mathrm{X}] \tag{6.64}$$

Here, ζ is the cosmic-ray ionization rate, β the constant of proportionality, and $k_{\mathrm{ad,X}}$ the rate coefficient for the depletion of X onto dust grains, which is similar to Eq. (6.33). In the steady state, the abundance of X is constant regardless of the H_2 density, because $k_{\mathrm{ad,\,X}}$ is proportional to the abundance of grains and thereby the H_2 density. The abundance of some major solid molecules (e.g., H_2O and CH_3OH) can be regarded to be constant over a most part of a cloud, and, hence, distribution of the molecules evaporated by the cosmic ray-induced desorption is expected to be different in a cloud from that of molecules formed by gas-phase reactions.

An important result indicating the formation of complex organic molecules in cold molecular clouds and their liberation by nonthermal processes into the gas phase was shown, for instance, by detection of $HCOOCH_3$ and $(CH_3)_2O$ toward a starless core by Bacmann et al. (2012). It is likely that complex organic molecules were already formed on dust grains in a starless core phase to some extent. Note that the importance of the gas-phase production of these complex organic molecules is recently suggested by Vasyunin et al. (2013).

6.7 Observation of Grain Mantles

The existence of various molecules on dust grains has been demonstrated by infrared observations. By detecting absorption features of vibrational bands of molecules, it is possible to determine the species and their abundances of grain cores and grain mantles. For such observations, infrared sources embedded in molecular clouds are typically used as radiation sources for absorption spectroscopy. Hence, it is very difficult to observe solid-phase abundances in purely starless clouds. Nevertheless, we can study the composition of grain mantles even toward star-forming regions harboring luminous infrared sources, because the envelope of these sources is still cold and preserves the conditions of starless cores. Although such an envelope may not be very dense, absorption spectroscopy can still trace the envelope, unlike emission spectroscopy.

Figure 6.6 shows examples of absorption spectra taken toward representative star-forming regions (Gibb et al. 2004). Absorption by H_2O, CO_2, and CO is clearly seen. For the high-mass star-forming region AFGL2591, the CO absorption does not exhibit a single-peaked profile, but rather shows rotational substructure. This result means that CO molecules are in the gas phase in this source. We can infer that H_2O and CO_2 are in the solid phase from their spectral features. Grain mantle species that have definitively been identified thus far in this way are H_2O, CO, CO_2, CH_4, CH_3OH, H_2CO, HCOOH, NH_3, XCN, NCO-, where H_2O is the most abundant species.

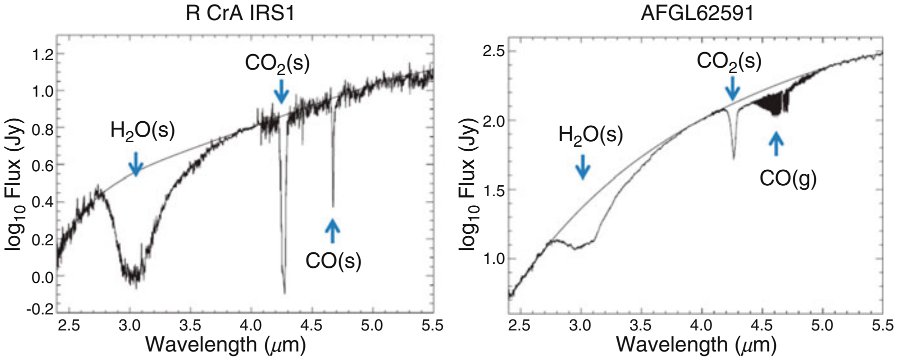

Fig. 6.6 Infrared spectra observed toward R CrA IRS1 and AFGL2591 with the Infrared Space Observatory. Absorption features of solid H_2O and CO_2 are seen in both sources. An absorption feature of solid CO is also seen in R CrA IRS1; an absorption feature of gaseous CO exhibiting rotational structure is seen in AFGL2591 (Reprinted with permission from Gibb et al. (2004). Copyright 2004 American Astronomical Society)

Infrared observations of dust grains are an important technique for investigating the chemical compositions of dust grains. However, the identification of molecules via infrared observations is limited to simple species. Vibrational bands are observed in infrared spectroscopy of interstellar dust grains. Although the vibrational frequencies are specific to molecular species in principle, they are similar among molecules that have similar molecular structures. Furthermore, the spectral width of vibrational bands is intrinsically broad because of the inhomogeneous broadening of solid species. The minor constituents of grain mantles are thus difficult to identify by infrared observations, because their absorptions are often buried in overwhelming absorptions by major species.

6.8 Gas–Grain Models

Many chemical models, including grain-surface reactions, have been reported. Earlier works on the subject include studies by Allen and Robinson (1977), Tielens and Hagen (1982), and Hasegawa et al. (1992). For instance, Hasegawa et al. (1992) constructed a gas–grain model involving a large number of species using the rate equation method and demonstrated the impact that grain-surface reactions have on the chemical compositions of molecular clouds. Although the Monte Carlo approach considering the discrete nature of grains is essential for some cases, its implementation in a large chemical model is not practical. Hence, modification of the rate equation methods has been investigated extensively (Caselli et al. 1998, 2002a; Garrod 2008). A chemical model involving gas–grain interactions is now becoming standard, and many studies have been done for molecular clouds at various physical conditions. The depletion of molecules onto dust grains is widely

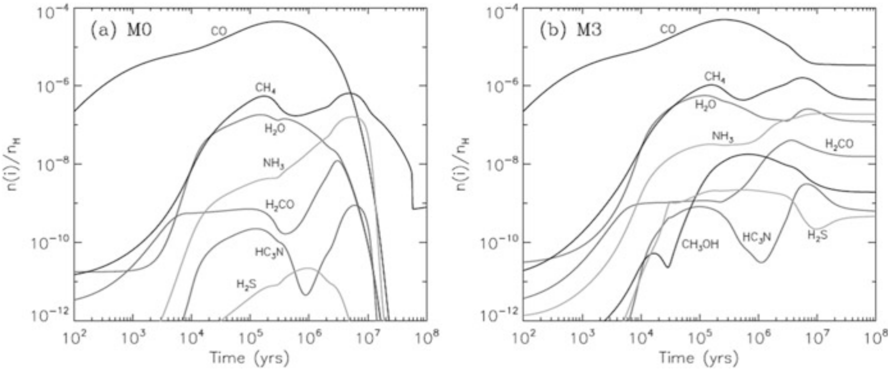

Fig. 6.7 Results from the pseudo-time-dependent model considering gas–grain interactions. Model M0 (*left panel*) assumes no desorption by the surplus reaction energies; model M3 (*right panel*) assumes that 10 % of the surplus reaction energies are used for desorption. The second peak of the carbon-bearing molecule appears at a few times 10^6 year, after CO depletion, although chemical compositions in later stages ($>10^6$ year) depend on the desorption efficiency of surface molecules (Reprinted with permission from Garrod et al. (2007). Copyright 2007 European Southern Observatory)

recognized as playing an important role in the chemical evolution of molecular clouds. Here, we introduce two examples of such calculations.

The first calculation is the pseudo-time-dependent calculation, where a temporal change in chemical compositions is calculated assuming a constant density and temperature. Figure 6.7 shows the result reported by Garrod et al. (2007). Among various parameters of grain-surface processes, they examined the effect of desorption by excess energy of chemical reactions. The left panel shows a case in which such a mechanism does not work; the right panel shows a case in which 1 % of the excess energy is used for desorption. From the left panel, the temporal change in chemical compositions of the gas-phase species exhibits two peaks. The early peak corresponds to the peak that is seen in the pure gas-phase model (Sect. 5.10). This peak is mainly caused by chemical evolutionary effects, where organic molecules, particularly carbon-chain molecules, appear in the early stages before carbon atoms have been locked up in CO. After 1 Myr (10^6 year), the depletion of molecules becomes significant, and the abundances of most molecules decrease. However, a second peak of organic molecules appears after a few Myr, because of the evaporation of hydrocarbons produced on grain-surface reactions, which are liberated into the gas phase by nonthermal desorption. The second peak is expected to appear at a later time than the dynamical timescale. Hence, it has not clearly been identified in observations. Nevertheless, the second peak may contribute to the chemical compositions of star-forming cores.

The second example is a chemical model coupled with the dynamical contraction of a cloud (Fig. 6.8). Aikawa et al. (2005) calculated the temporal change in chemical compositions for such a gravitationally contracting core using a gas–grain model. According to their results, carbon-chain molecules such as CCS appear in the early stages, and they are depleted onto dust grains or broken up by chemical reactions in

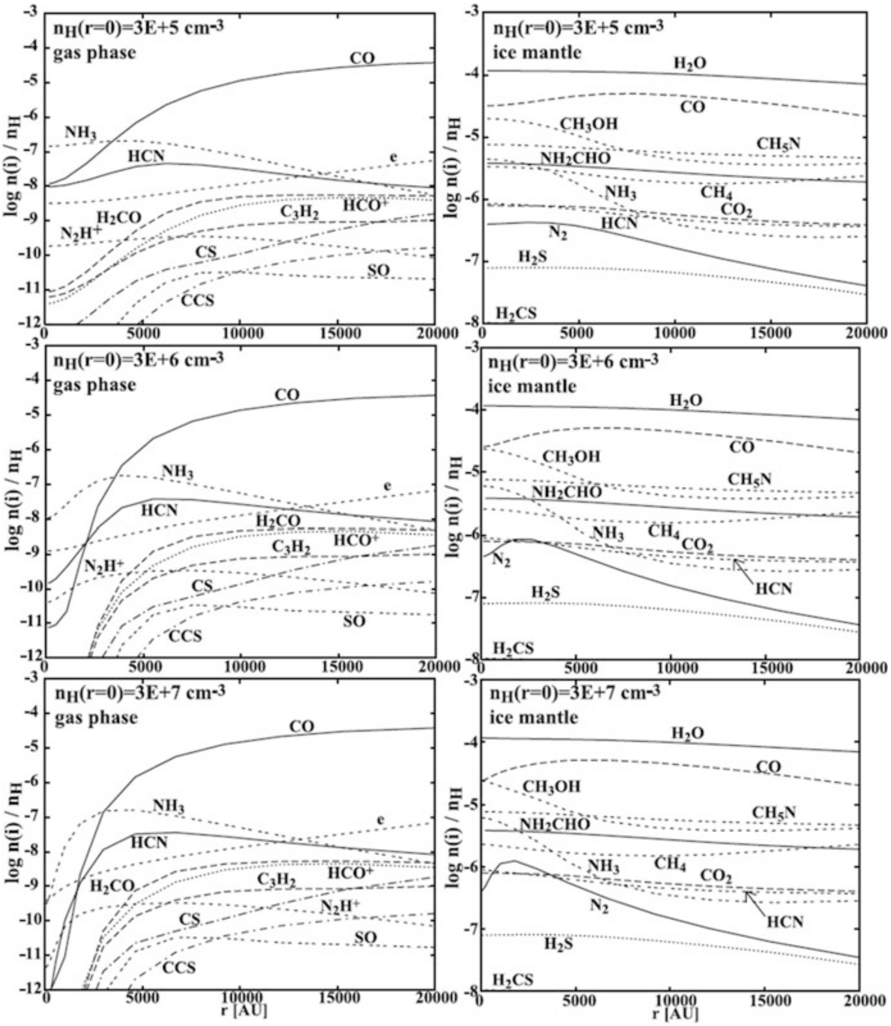

Fig. 6.8 Results from gas–grain chemical models considering the dynamical evolution of a molecular cloud core. A spherical cloud close to the critical Bonnor–Ebert sphere (Bonnor 1956) is considered, and molecular abundances are plotted as a function of the distance to the core center. The top, middle, and bottom panels represent the chemical compositions, when the central densities are 3×10^5, 3×10^6, and 3×10^7 cm^{-3} at 1.05×10^6, 1.15×10^6, and 1.17×10^6 year, respectively. The *left* panels show the gas-phase abundances; the *right* panels show the solid-phase abundances. In the gas phase, CO and CCS show significant depletion toward the center; N_2H^+ and NH_3 tend to be more abundant even in the inner region (<5000 AU) (Reprinted with permission from Aikawa et al. (2005). Copyright 2005 American Astronomical Society)

the later stages. Conversely, NH_3 and N_2H^+ appear in the later stages. This result is qualitatively similar to that derived from the pure gas-phase model under constant physical conditions (Sect. 5.10), but it provides a more complete picture of the chemistry of starless cores. Indeed, the calculations of Aikawa et al. (2005) explain the distributions of CCS and N_2H^+ in the starless core L1544 (Fig. 5.5).

In contrast to the pure gas-phase models, the gas–grain models contain many assumptions about surface reactions, adsorption and desorption procedures, and photoprocesses. For these reasons, the results are often dependent on the choice of model. When the results of a particular model are compared with observations, it is necessary to recognize the assumptions employed in the model.

6.9 Deuterium Fractionation

A good example showing the importance of gas–grain interactions is deuterium fractionation. The cosmic abundance of D relative to H is $(1.52 \pm 0.08) \times 10^{-5}$ (Linsky 2003), and deuterium atoms mainly exist as HD in molecular clouds. Hence, the $[HD]/[H_2]$ ratio is 3×10^{-5}. It is well known that the abundance ratios of deuterated molecules other than HD relative to those of corresponding normal species can be as high as 0.01–0.1 in cold molecular clouds (Table 6.2). These abundance ratios are much higher than the cosmic D/H ratio mentioned above. This phenomenon is called *deuterium fractionation* (e.g., Watson 1974, 1976; Millar et al. 1989; Gerlich and Schlemmer 2002; Walmsley et al. 2004; Albertsson et al.

Table 6.2 Deuterium fractionation ratios of various molecules in the starless cores TMC-1 and L1544

	TMC-1	L1544
NH_2D/NH_3	0.00085[a]	0.13[b]
N_2D^+/N_2H^+	0.04[a]	0.2[c]
DCN/HCN	0.023[d]	–
DNC/HNC	0.028[e]	0.034[e]
DCO^+/HCO^+	0.027[f]	0.04[c]
$HDCO/H_2CO$	0.0595[a]	0.0595[a]
D_2CO/H_2CO	–	0.04[g]
$HDCS/H_2CS$	0.02[h]	–
$c\text{-}C_3HD/c\text{-}C_3H_2$	0.0475[a]	0.12–0.17[i]
$c\text{-}C_3D_2/c\text{-}C_3H_2$	–	0.012–0.021[i]
DC_3N/HC_3N	0.0145[a]	–
CH_3CCD/CH_3CCH	0.0395[j]	–
CH_2DCCH/CH_3CCH	0.081[j]	–
C_4D/C_4H	0.043[k]	–
DC_5N/HC_5N	0.016[a]	–

[a] Turner (2001), [b] Shah and Wootten (2001), [c] Caselli et al. (2002a, b), [d] Wootten 1987, [e] Hirota et al. (2001), [f] Butner et al. (1995), [g] Bacmann et al. (2003), [h] Minowa et al. (1997), [i] Spezzano et al. (2013), [j] Markwick et al. (2002), [k] Turner (1989)

2013). The basic mechanism responsible for deuterium fractionation includes the following gas-phase reactions:

$$H_3{}^+ + HD \rightarrow H_2D^+ + H_2 + 230K, \tag{6.65}$$

$$CH_3{}^+ + HD \rightarrow CH_2D^+ + H_2 + 370K, \tag{6.66}$$

$$C_2H_2{}^+ + HD \rightarrow C_2HD^+ + H_2 + 550K. \tag{6.67}$$

These reactions are exothermic as the products have a lower zero-point vibrational energy than the reactants; here H_2 is assumed to be in the para-state. Hence, the backward reactions barely occur at low temperatures (10 K) because of endothermicity, and deuterium atoms are fractionated into H_2D^+, CH_2D^+, and C_2HD^+. In most cases, the first reaction producing H_2D^+ is the most important. The fractionation through CH_2D^+ and C_2HD^+ is thought to be important in warm conditions (Roueff et al. 2007).

In general, reactions that can contribute to deuterium fractionation require the following two conditions. First, the corresponding reaction with H_2 does not proceed except for radiative association processes. If the reaction with H_2 occurs, the reaction with HD also occurs. In this case, the product is not fractionated in the deuterium abundance. Second, the reaction needs to form a transient complex of reactant molecules in order to ensure the mixing of H and D atoms. For instance, $H_5{}^+$, $CH_5{}^+$, and $C_2H_3{}^+$ are such transient complexes for reactions (6.65), (6.66), and (6.67), respectively.

Because the rate coefficient for reaction (6.65) is 3.5×10^{-10} cm^3 s^{-1} (Gerlich et al. 2002; Gerlich and Schlemmer 2002), the timescale for the forward reaction for $H_3{}^+$ is 3×10^{10} s. Here, we employ H_2 density of 10^4 cm^{-3}. If the rate coefficient of reaction (6.65) is denoted by k_f, the rate coefficient for the backward reaction

$$H_2D^+ + H_2 \rightarrow H_3{}^+ + HD - 230K \tag{6.68}$$

can be approximated as:

$$k_b = k_f \exp(-230/T) \tag{6.69}$$

where the entropy term is ignored. The timescale of the backward reaction is then 3×10^{15} s at 10 K; the timescale shortens to 3×10^{10} s and 10^8 s for 20 K and 40 K, respectively. Hence, low temperatures are essential for deuterium fractionation.

We remark that para-H_2 is assumed in the endothermic reaction (6.68). When ortho-H_2 is the reaction partner with H_2D^+, the backward reaction is exothermic if H_2D^+ is in the ortho-state (the 1_{10} rotational level). In this case, deuterium fractionation does not occur efficiently. The ortho-to-para ratio of H_2 is thought to be generally small (<0.01) in cold molecular clouds (Pagani et al. 2009; Dislaire et al. 2012), because the ortho-to-para conversion slowly occurs on dust grains and also by the gas-phase reactions with H^+ and $H_3{}^+$. Hence, the above endothermicity is assumed for reaction (6.68) in the following discussions. However, note that the contribution of ortho-H_2 needs to be considered for the deuterium fractionation processes particularly in warm regions.

The deuterium fractionation reaction (6.65) competes with the proton transfer reaction with the abundant molecule CO:

$$H_3{}^+ + CO \rightarrow HCO^+ + H_2 \tag{6.70}$$

For $H_3{}^+$, the timescale of this reaction is 10^9 s at H_2 density of 10^4 cm^{-3}, which is shorter than the timescale of the reaction with HD. Furthermore, $H_3{}^+$ is broken up by electron recombination:

$$H_3{}^+ + e \rightarrow H_2 + H. \tag{6.71}$$

Similarly, H_2D^+ is also destructed by the reaction of CO, the reaction of HD, and electron recombination:

$$H_2D^+ + CO \rightarrow HCO^+ + HD \tag{6.72}$$

$$\rightarrow DCO^+ + H_2, \tag{6.73}$$

$$H_2D^+ + HD \rightarrow HD_2{}^+ + H_2, \tag{6.74}$$

$$H_2D^+ + e \rightarrow H_2 + D \tag{6.75}$$

$$\rightarrow HD + H. \tag{6.76}$$

For this reason, the abundance of CO is a very important factor in deuterium fractionation. Although CO is the main destroyer for $H_3{}^+$ and H_2D^+, other gas-phase species having a proton affinity higher than that of H_2, such as O atoms, also contribute to destroy $H_3{}^+$ and H_2D^+. Considering reactions (6.65, 6.68, 6.72, 6.73, 6.74, 6.75, and 6.76), the $[H_2D^+]/[H_3{}^+]$ ratio is derived under the steady-state approximation as:

$$\frac{[H_2D^+]}{[H_3^+]} = \frac{k_f[HD]}{k_1[CO] + k_2[HD] + k_r[e] + k_b[H_2]}, \tag{6.77}$$

where k_1 and k_2 stand for the sum of the rate coefficients of reactions (6.72 and 6.73) and the rate coefficient of reaction (6.74), respectively. And k_r represents the total rate coefficient of the electron recombination reactions (6.75 and 6.76). As long as the abundance of CO (and the other species) relative to H_2 is 10^{-4}, the electron recombination reaction is a minor process in the breakup of $H_3{}^+$ and H_2D^+. In this case, we obtain a $[H_2D^+]/[H_3{}^+]$ ratio of 0.03.

The H_2D^+ ion thus formed donates its deuterium atom to various molecules:

$$H_2D^+ + X \rightarrow DX^+ + H_2. \tag{6.78}$$

This reaction proceeds at the Langevin rate for most cases. Thus, the deuterium fractionation of H_2D^+ is transferred to other molecules. For molecule X, the timescale for deuteration in its reaction with H_2D^+ is given as:

$$t = \frac{1}{k[\mathrm{H_2D^+}]}, \tag{6.79}$$

which can be as long as a few times 10^7 year. Hence, deuterium fractionation gradually proceeds with a timescale as in chemical equilibrium (Sect. 5.10).

The $[H_2D^+]/[H_3^+]$ ratio depends on the CO abundance and hence can be higher when CO is depleted onto dust grains. Depletion of CO indeed occurs in the late stages of a starless core (Sect. 6.2). If CO is completely removed from the gas phase, the main destruction process of H_3^+ is reactions with HD (Problem 6.5). Under this condition, the $[H_2D^+]/[H_3^+]$ ratio can be as high as 1.0. Hence, the deuterium fractionation is accelerated by CO depletion. Moreover, the main destruction process of H_2D^+ is reactions with HD, and hence the doubly deuterated species, HD_2^+, is enhanced. Similarly, the main breakup process of HD_2^+ is also reactions with HD to form D_3^+. D_3^+ disassociates by electron recombination reactions. This situation is shown in Fig. 6.9. H_2D^+ was detected for the first time toward the low-mass star-forming region NGC1333 IRAS4A (Stark et al. 1999). Later, H_2D^+ and HD_2^+ were observed in starless cores (Caselli et al. 2003; Vastel et al. 2004).

Significant deuterium fractionation is indeed observed toward evolved starless cores. A good example is again L1544, where a significant CO depletion is seen. The DCO^+/HCO^+ ratio tends to be higher toward the center of the core than toward the core periphery (Caselli et al. 2002a, b). As shown in Table 6.2, the deuterium fractionation ratios in L1544 are generally higher than those in the young starless core TMC-1 (CP). Furthermore, the deuterium fractionation ratio, DNC/HNC, shows a good correlation with the NH_3/CCS ratio, which is a good indicator of chemical evolution (Fig. 6.10). Hence, the deuterium fractionation ratio indeed increases as clouds evolve.

The deuterium fractionation in the gas phase also affects grain-surface reactions. In molecular clouds, hydrogen is in the form of H_2, and H atoms are mainly produced by the electron recombination of protonated ions (Problem 6.3). When

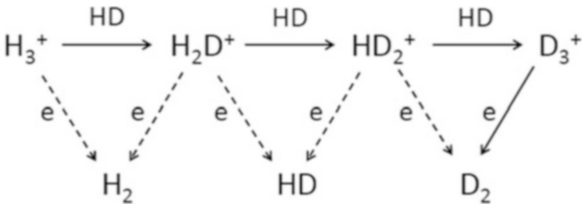

Fig. 6.9 Deuterium fractionation in highly depleted cold molecular clouds. Breakup of H_3^+, H_2D^+, and HD_2^+ is mainly due to HD under CO depletion. Electron recombination contributes to the breakup of these ions

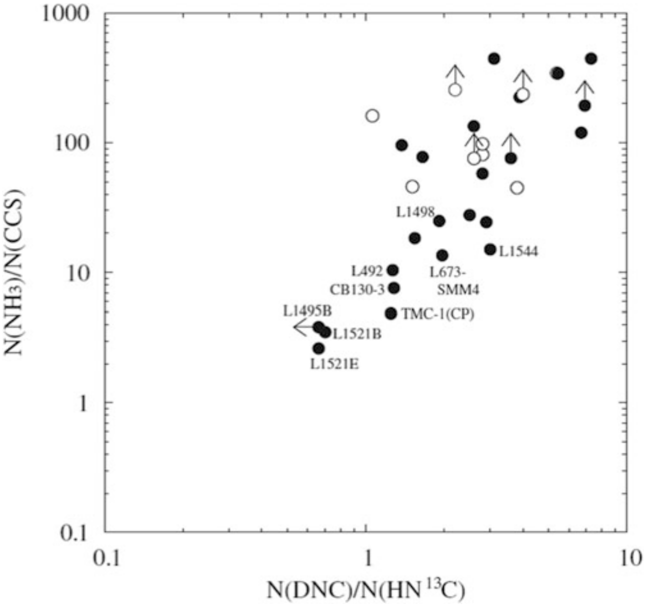

Fig. 6.10 Correlation between two evolutionary tracers, NH_3/CCS and DNC/$HN^{13}C$ (Reprinted with permission from Hirota et al. (2011). Copyright 2011 American Astronomical Society)

the deuterium is fractionated in these ions, the abundance of D atoms relative to H atoms is much higher than the cosmic D/H ratio. The atomic D/H ratio can be as high as 0.1–1 in molecular clouds. Because H and D atoms react with C, O, CO, and other molecules on grain surfaces, deuterium fractionation occurs for their products such as H_2O, CH_4, H_2CO, and CH_3OH. For instance, the hydrogenation and deuteration of CO were studied in the laboratory (Hidaka et al. 2009). The main processes are shown in Fig. 6.11. Multiply deuterated H_2CO and CH_3OH are formed on dust grains. These molecules mostly stay on the grains during the starless core phase, and they are liberated into the gas phase after the birth of a protostar, which is to be described in Sect. 7.4.1.

Many chemical models of deuterium fractionation have been reported (e.g., Taquet et al. 2014; Roueff et al. 2007). The dynamical model of a starless core is presented by Aikawa et al. (2005, 2012). The deuterium fractionation is higher in the interior of the core, which is chemically evolved and shows heavy CO depletion. This result is consistent with the observational results of starless cores discussed above.

Problems

6.1 Dust grains have a size distribution. The number of grains with a radius between a and $a + da$ is given as:

$$n(a)da = Aa^{-3.5}n_0da,$$

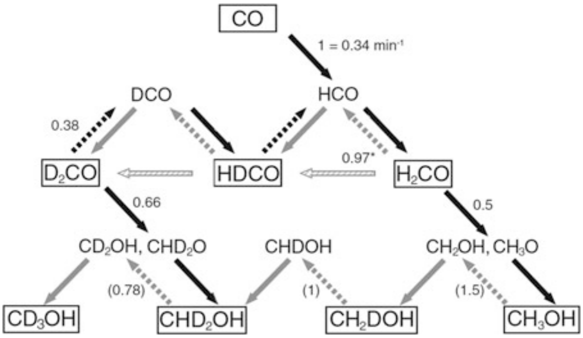

Fig. 6.11 Grain-surface reactions of CO with H and D atoms. The *solid black* and *gray arrows* indicate the addition reactions of H and D, respectively. The *dashed black* and *gray arrows* indicate abstraction reactions by H and D atoms, respectively, which form HD. The shaded arrows indicate H–D exchange reactions (Reprinted with permission from Hidaka et al. (2009). Copyright 2009 American Astronomical Society)

where n_0 is the number density of H nuclei ($n_0 = [\mathrm{H}] + 2[\mathrm{H_2}]$). This distribution is called the MRN distribution, named after three authors who published a seminal paper on this topic (Mathis et al. 1977). Here, grains are assumed to be spherical. For silicate grains, A is adopted to be 7.8×10^{-26} $\mathrm{cm}^{2.5}$/H nucleus.

(a) Calculate the dust surface area S per H nucleus and the total cross section Σ per H nucleus, assuming that the minimum and maximum radii of grains are 50 and 3000 Å, respectively. S and Σ are defined as:

$$S = \int_{a_\mathrm{min}}^{a_\mathrm{max}} 4\pi a^2 n(a) da$$

and

$$\Sigma = \int_{a_\mathrm{min}}^{a_\mathrm{max}} \pi a^2 n(a) da.$$

(b) Calculate the timescale of CO depletion using Σ obtained above, where the sticking probability is assumed to be unity.

6.2 The adsorption energy of H_2CO is 2050 K. Evaluate the desorption temperature of H_2CO. Additionally, estimate the diffusion timescales and desorption timescales of H_2CO at 10 K and 20 K.

6.3 We now turn to evaluating the abundance of H atoms in molecular clouds. In molecular clouds, H atoms are produced by cosmic-ray ionization of H_2 molecules and subsequent reactions. These reactions can be simplified as:

$$H_2 + \text{c.r.} \rightarrow {H_2}^+ + e$$
$${H_2}^+ + H_2 \rightarrow {H_3}^+ + H$$
$${H_3}^+ + A \rightarrow HA^+ + H_2$$
$$HA^+ + e \rightarrow A + H,$$

where A is a molecule with a proton affinity higher than that of H_2. As a result, one cosmic-ray hit on an H_2 molecule produces two H atoms. Although more than two H atoms can be produced in some cases, we simply assume the above condition. Considering that H atoms re-form H_2 molecules via grain-surface reactions, as discussed in Sect. 6.4, set up the rate equation for H atoms in molecular clouds and solve it to obtain the number density of H atoms in the gas phase under the steady-state approximation. Show that the number density of H atoms is about 1 cm^{-3} and is independent of the H_2 density.

6.4 Consider the formation of CH_3OH from CO on dust grains. The reactions of CO and H_2CO with H atoms have an activation barrier of 2000 K; the reactions of HCO and CH_3O have no activation barrier.

(a) Evaluate the reaction probabilities k_{ij} for the CO + H and H_2CO + H reactions assuming that the reactions occur via tunneling of the H atom through the activation barrier of 2000 K.
(b) Evaluate the [HCO]/[CO] ratio on dust grains in the steady-state approximation.
(c) Estimate the formation timescale of CH_3OH molecules on dust grains.

6.5 In heavy CO depletion on dust grains, the ${HD_2}^+$ and ${D_3}^+$ abundances are also enhanced from:

$$H_2D^+ + HD \rightarrow {HD_2}^+ + H_2$$
$${HD_2}^+ + HD \rightarrow {D_3}^+ + H_2$$
$${D_3}^+ + e \rightarrow D_2 + D.$$

(a) Assuming complete CO depletion, show that mainly HD destroys H_2D^+ and ${HD_2}^+$ rather than electrons. Here, assume the H_2 density of 10^6 cm^{-3}.
(b) By considering the above three reactions, derive the $[{HD_2}^+]/[H_2D^+]$ and $[{D_3}^+]/[{HD_2}^+]$ ratios under the steady-state approximation. Note that ${HD_2}^+$ is indeed detected in starless cores.

References

Y. Aikawa, N. Ohashi, S. Inutsuka, E. Herbst, S. Takakuwa, Astrophys. J. **552**, 639 (2001)

Y. Aikawa, E. Herbst, H. Roberts, P. Caselli, Astrophys. J. **620**, 330 (2005)

Y. Aikawa, V. Wakelam, F. Hersant, R.T. Garrod, E. Herbst, Astrophys. J. **760**, 40 (2012)

T. Albertsson, D.A. Semenov, A.I. Vasyunin, T. Henning, E. Herbst, Astrophys. J. Suppl. **207**, 27 (2013)

M. Allen, G.W. Robinson, Astrophys. J. **212**, 396 (1977)

A. Bacmann, B. Lefloch, C. Ceccarelli, A. Castets, J. Steinacker, L. Loinard, Astron. Astrophys. **39**, L6 (2002)

A. Bacmann, B. Lefloch, C. Ceccarelli, J. Steinacker, A. Castets, L. Loinard, Astrophys. J. **585**, L55 (2003)

A. Bacmann, V. Taquet, A. Faure, C. Kahane, C. Ceccarelli, Astron. Astrophys. **541**, L12 (2012)

G.A. Blake, E.C. Sutton, C.R. Masson, T.G. Phillips, Astrophys. J. **315**, 621 (1987)

W.B. Bonnor, Mon. Not. R. Astron. Soc. **116**, 351 (1956)

H.M. Butner, E.A. Lada, R.B. Loren, Astrophys. J. **448**, 207 (1995)

P. Caselli, T.I. Hasegawa, E. Herbst, Astrophys. J. **408**, 548 (1993)

P. Caselli, T.I. Hasegawa, E. Herbst, Astrophys. J. **495**, 309 (1998)

P. Caselli, C.M. Walmsley, M. Tafalla, L. Dore, P.C. Myers, Astrophys. J. **523**, L165 (1999)

P. Caselli, T. Stantcheva, O. Shalabiea, V.I. Shematovich, E. Herbst, Planet. Space Sci. **50**, 1257 (2002a)

P. Caselli, C.M. Walmsley, A. Zucconi, M. Tafalla, L. Dore, P.C. Myers, Astrophys. J. **565**, 344 (2002b)

P. Caselli, F.F.S. van der Tak, C. Ceccarelli, A. Bacmann, Astron. Astrophys. **403**, L37 (2003)

S. Cazaux, A.G.G.M. Tielens, Astrophys. J. **604**, 222 (2004)

V. Dislaire, P. Hily-Blant, A. Faure, S. Maret, A. Bacmann, G. Pineau des Forets, Astron. Astrophys. **537**, A20 (2012)

F. Du, B. Parise, Astron. Astrophys. **530**, A131 (2011)

R.T. Garrod, Astron. Astrophys. **491**, 239 (2008)

R.T. Garrod, V. Wakelam, E. Herbst, Astron. Astrophys. **467**, 1103 (2007)

D. Gerlich, S. Schlemmer, Planet. Space Sci. **50**, 1287 (2002)

D. Gerlich, E. Herbst, E. Roueff, Planet. Space Sci. **50**, 1275 (2002)

E.L. Gibb, D.C.B. Whittet, A.C.A. Boogert, A.G.G.M. Tielens, Astrophys. J. Suppl. **151**, 35 (2004)

T.I. Hasegawa, E. Herbst, Mon. Not. R. Astron. Soc. **261**, 83 (1993)

T.I. Hasegawa, E. Herbst, C.M. Leung, Astrophys. J. Suppl. **82**, 167 (1992)

H. Hidaka, M. Watanabe, A. Kouchi, N. Watanabe, Astrophys. J. **702**, 291 (2009)

T. Hirota, M. Ikeda, S. Yamamoto, Astrophys. J. **547**, 814 (2001)

T. Hirota, T. Sakai, N. Sakai, S. Yamamoto, Astrophys. J. **736**, 4 (2011)

N. Katz, I. Furman, O. Biham, V. Pirronello, G. Vidali, Astrophys. J. **522**, 305 (1999)

A. Lipshtat, O. Biham, Astron. Astrophys. **400**, 585 (2003)

J.L. Linsky, Space Sci. Rev. **106**, 49 (2003)

S. Maret, E.A. Bergin, M. Tafalla, Astron. Astrophys. **559**, A53 (2013)

A.J. Markwick, M. Ilgner, T.J. Millar, T. Henning, Astron. Astrophys. **358**, 632 (2002)

J.S. Mathis, W. Rumpl, K.H. Nordsieck, Astrophys. J. **217**, 425 (1977)

T.J. Millar, A. Bennett, E. Herbst, Astrophys. J. **340**, 906 (1989)

H. Minowa, M. Satake, T. Hirota, S. Yamamoto, M. Ohishi, N. Kaifu, Astrophys. J. **491**, L63 (1997)

L. Pagani, J.-R. Pardo, A.J. Apponi, A. Bacmann, S. Cabrit, Astron. Astrophys. **429**, 181 (2005)

L. Pagani, C. Vastel, E. Hugo, V. Kokoouline, C.H. Greene, A. Bacmann, E. Bayet, C. Ceccarelli, R. Peng, S. Schlemmer, Astron. Astrophys. **494**, 623 (2009)

E. Roueff, B. Parise, E. Herbst, Astron. Astrophys. **464**, 245 (2007)

R.Y. Shah, A. Wootten, Astrophys. J. **554**, 933 (2001)

S. Spezzano, S. Brunken, P. Schilke, P. Caselli, K.M. Menten, M.C. McCarthy, L. Bizzocchi, S.P. Trevino-Morales, Y. Aikawa, S. Schlemmer, Astrophys. J. **769**, L19 (2013)

T. Stantcheva, V.I. Shematovich, E. Herbst, Astron. Astrophys. **391**, 1069 (2002)
R. Stark, F.F.S. van der Tak, E.F. van Dishoeck, Astrophys. J. **521**, L67 (1999)
M. Tafalla, P.C. Myers, P. Caselli, C.M. Walmsley, Astron. Astrophys. **416**, 191 (2004)
M. Tafalla, J. Santiago-Garcia, P.C. Myers, P. Caselli, C.M. Walmsley, A. Crapsi, Astron. Astrophys. **455**, 577 (2006)
V. Taquet, S.B. Charnley, O. Sipila, Astrophys. J. **791**, 1 (2014)
A.G.G.M. Tielens, W. Hagen, Astron. Astrophys. **114**, 245 (1982)
B.E. Turner, Astrophys. J. **347**, L39 (1989)
B.E. Turner, Astrophys. J. Suppl. **136**, 579 (2001)
C. Vastel, T.G. Phillips, H. Yoshida, Astrophys. J. **606**, L127 (2004)
A.I. Vasyunin, E. Herbst, Astrophys. J. **769**, 34 (2013)
C.M. Walmsley, D.R. Flower, G. Pineau des Forets, Astron. Astrophys. **418**, 1035 (2004)
N. Watanabe, A. Kouchi, Astrophys. J. **571**, L173 (2002)
N. Watanabe, T. Shiraki, A. Kouchi, Astrophys. J. **588**, L121 (2003)
W.D. Watson, Astrophys. J. **188**, 35 (1974)
W.D. Watson, Rev. Mod. Phys. **48**, 513 (1976)
A. Wootten, in Astrochemistry, ed. by M.S. Vardya, S.P. Tarafdar (Reidel, Dordrecht, 1987), p. 311

Chapter 7
Chemistry of Star-Forming Regions

7.1 Introduction

Stars are born by gravitational contraction of molecular cloud cores. Evolution of a protostar depends on its mass. Roughly speaking, the formation processes of low-mass stars (< a few $M_\odot$) and those of high-mass stars (>8 $M_\odot$) differ significantly. In general, it typically takes 10^7–10^8 year for low-mass protostars to evolve into main-sequence stars; high-mass protostars evolve much faster (~10^5 year) (e.g., Zinnecker and Yorke 2007). High-mass protostars reach the main-sequence stage while they are still embedded in their parent molecular cloud cores. Hence, high-mass protostars have a significant effect on the physical and chemical state of their parent cores. In particular, high-mass stars radiate intense UV (far UV) radiation, which ionizes the surrounding gas to form H II regions. Furthermore, the surfaces of nearby clouds illuminated by the intense UV radiation become dense PDRs. In low-mass and intermediate-mass star-forming regions, H II regions are not usually formed, although PDRs often appear on much smaller scales.

Historically speaking, the chemistry of star-forming regions was first studied for high-mass star-forming regions because the formation sites of high-mass stars were often known as optical signposts (e.g., H II regions and reflection nebulae). Most high-mass star-forming regions were also known as bright sources of centimeter-wave continuum emission (free–free emission) from H II regions. One of the best studied sources is Orion KL (Kleinmann–Low object in Orion), which is the nearest high-mass star-forming region and the richest source of molecular emission (437 pc; Hirota et al. 2007). Orion KL is located in a filamentary molecular cloud behind the reflection nebula M42 illuminated by a cluster of high-mass stars (the Trapezium Cluster). Orion KL consists of a cluster of young, high-mass protostars being born in the densest part of filamentary clouds, as revealed by infrared

S. Yamamoto, *Introduction to Astrochemistry*, Astronomy and Astrophysics Library 7, DOI 10.1007/978-4-431-54171-4_7

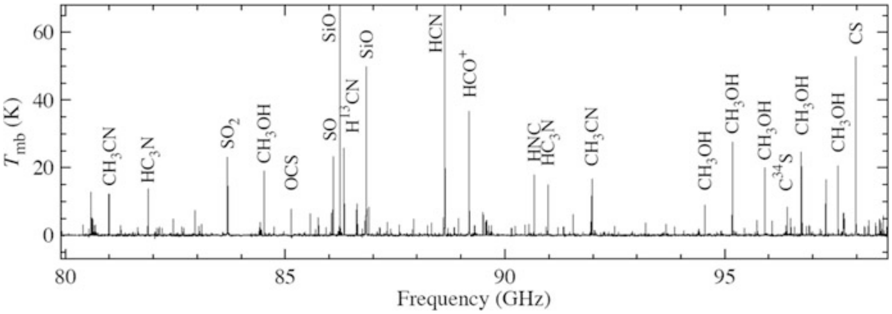

Fig. 7.1 A portion of the spectral line survey toward Orion KL with the Nobeyama 45m telescope (Watanabe, Y. private communication)

observations (Genzel and Stutzki 1989; Bally et al. 1987). Its chemical composition has been extensively studied since the early era of radio astronomy (e.g., Blake et al. 1987; Schilke et al. 1997a; Beuther et al. 2005; Tercero et al. 2010). The most characteristic feature of this source is the existence of various saturated complex organic molecules such as $HCOOCH_3$, $(CH_3)_2O$, C_2H_5CN, and C_2H_5OH, as well as sulfur-containing molecules such as SO and SO_2 and nonvolatile molecules such as SiO, SiS, and PN, in the hot and dense part of the source near the protostar. Such a region is generally called a *hot core*. In Orion KL, the small-scale chemical differentiation among the species noted above is seen, and the term “hot core” is used for a rather specialized region (Sect. 7.5.1). A number of spectral line survey observations have been conducted toward Orion KL (e.g., Blake et al. 1987; Turner 1989; Schilke et al. 1997a; Comito et al. 2005; Tercero et al. 2010; Crockett et al. 2014). An example of a spectral scan in Orion KL is shown in Fig. 7.1. In addition to Orion KL, high-mass protostellar sources were extensively observed to search for new interstellar molecules and to study the chemical composition of star-forming clouds.

In contrast, chemical studies of low-mass star-forming regions were relatively sparse before the 1990s. Because of the great success of the *Infrared Astronomical Satellite (IRAS)* in the 1980s, a number of low-mass protostars were identified in dense cores in molecular clouds. The chemical compositions of low-mass star-forming regions were studied using a few representative molecules such as NH_3, CS, and HC_3N (Benson and Myers 1989; Zhou et al. 1989; Suzuki et al. 1992). However, molecular emission is generally weaker in low-mass star-forming regions than in high-mass star-forming regions. As a result, not much attention was paid to the chemical compositions of low-mass star-forming regions. Considering that planetary systems can be formed around low-mass stars, chemical compositions of low-mass star-forming regions are of particular interest in understanding how chemical evolution progresses from molecular clouds to planetary systems. Hence, the observational chemical characterization of chemical compositions of low-mass protostellar sources was awaited.

A pioneering study in this direction was the spectral line survey of the low-mass protostar IRAS 16293-2422 (Blake et al. 1994; van Dishoeck et al. 1995). In this line survey extending from the millimeter-wave to submillimeter-wave range, sulfur-containing species such as SO and SO_2 were found to be very abundant in this source. The emission of SO and SO_2 was thought to arise from the hot and dense region around the protostar, which resembled the case of high-mass star-forming regions. The existence of such a hot region around the protostar was also inferred later from the analysis of submillimeter-wave lines of H_2CO and CH_3OH observed with single-dish observations (e.g., Ceccarelli et al. 1998; Schoier et al. 2002). The hot region around a low-mass protostar can be as small as a few tens of au, which is impossible to resolve with single-dish observations. However, detailed modeling of the emission was able to extract a hint of its existence.

In 2003, Cazaux et al. (2003) detected the spectral lines of saturated complex organic molecules (e.g., $HCOOCH_3$, $(CH_3)_2O$, C_2H_5CN) toward IRAS 16293-2422 and demonstrated that a hot core-like chemistry is indeed occurring even in low-mass star-forming regions. Such a hot and dense core around a low-mass protostar, which is characterized by the rich existence of complex organic molecules, is called a *hot corino*. The discovery of hot corinos attracted significant attention not only from researchers in the field of astrochemistry but also scientists in planetary science, because these complex molecules are thought to be related to the pre-solar organic materials found in meteorites. Since then, the chemical compositions of low-mass star-forming regions have been extensively studied for many sources.

In this chapter, we describe the chemistry of star-forming regions both for low-mass and high-mass sources with a particular emphasis on the microscopic chemical processes occurring in these regions.

7.2 Formation of Low-Mass Stars

The formation process of an isolated low-mass star has been extensively studied observationally and theoretically. Here, we describe a brief sketch of this process, which consists of the following three major steps:

(1) Starless core phase

This phase corresponds to dense parts of the molecular clouds before onset of star formation discussed in Chap. 5. Because radiative cooling by both spectral line and dust emissions is efficient during collapse, the temperature of the dense core remains constant (~10 K) (isothermal collapse). The duration for this phase is roughly comparable to the free-fall time. Because the dense core is supported by turbulence and magnetic fields, the actual duration time may be longer than the free-fall time. According to a statistical study by Evans et al. (2009), the duration time of starless cores is $(5 \pm 3) \times 10^5$ year.

(2) Protostar phase

When the H_2 density at the central part of the core exceeds 10^{11} cm^{-3}, the dust emission becomes opaque. In these conditions, a photon emitted from the central part of the core is reabsorbed within the cloud, and hence cooling efficiency diminishes. Then, the temperature of the central part of the core starts to rise. This high-temperature core is called the *first core* (e.g., Larson 1969; Masunaga et al. 1998). The temperature of the first core rapidly increases. When the central temperature exceeds 1500 K after a few 100 year after the formation of the first core, thermal dissociation of H_2 molecules begins. This process absorbs an enormous amount of energy, resulting in the acceleration of the gravitational contraction. This process is known as the second collapse. After this phase, the so-called *second core* is formed. This point in time marks the birth of the protostar.

Gas still accretes onto the protostar, and the protostar is growing. The protostar shines through the release of gravitational energy of the accreting material. Hence, this phase is called the main accretion phase. In general, the accreting material possesses angular momentum, and hence the accretion is not always spherical. A flattened infalling envelope and a protostellar disk will be formed around the protostar in accordance with conservation of angular momentum, through which the materials are delivered to the protostar. At the same time, an outflow is launched from the protostar perpendicular to the protostellar disk. This outflow is thought to be caused by the interplay between magnetic fields and the gas dynamics, which plays an important role in extracting angular momentum of the accreting material. The outflow usually consists of an inner ionized jet and the outer molecular outflow. The outflow velocity can be as high as few tens of km/s to 100 km/s. That is, the infalling motion and outflow are simultaneously occurring in the protostar phase (Bachiller 1996; Hartmann 2009; Tomisaka 2002; Machida and Hosokawa 2013; Shu et al. 1994a, b).

(3) T-Tauri star phase

The dynamical accretion of gas and dust onto the protostar almost ends with the dissipation or consumption of the envelope gas. Then, the protostar moves on to the next stage, called the *T-Tauri star phase* (Appenzeller and Mundt 1989). In this phase, the star is in quasi-static contraction. The central temperature of the star increases due to contraction, and the heat is transferred to the surface of the star by convection. This step is called Hayashi phase (Hayashi 1961, 1966), and the young stellar object in this phase is called a T-Tauri star. A T-Tauri star evolves into a main-sequence star after 10^7–10^8 year. Because most of the parent cloud has already been dissipated by the outflow and the other protostellar activities before this phase, only a small disk remains around the protostar. This disk is called a protoplanetary disk and marks the location where a planetary system can be formed. The protostellar disk formed in the protostellar phase is thought to evolve into a protoplanetary disk. The accretion of material from the protoplanetary disk onto the central star still continues in the initial stage of the T-Tauri phase (the classical T-Tauri stage), which explains the episodic energetic events found in T-Tauri stars

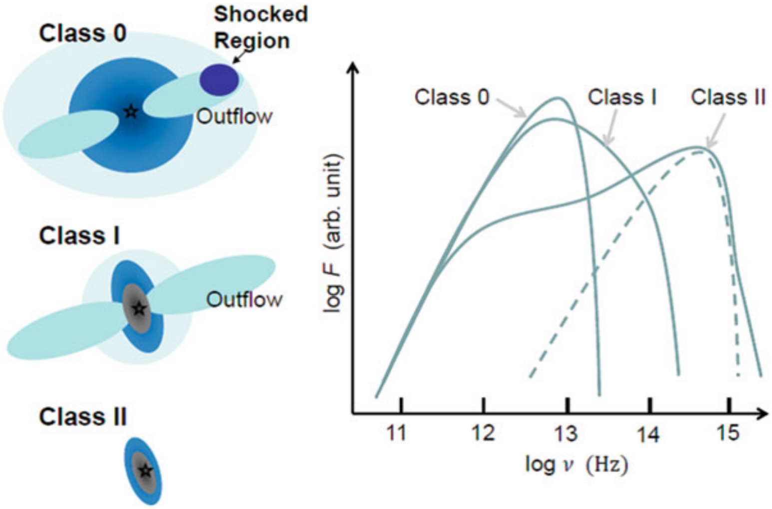

Fig. 7.2 Schematic SEDs for Class 0, Class I, and Class II protostars. The shape of the SED reflects the physical evolutionary stage of young stellar objects. The *dashed curve* represents the stellar blackbody and is dominant in the Class III source

such as UV excesses, X-ray emission, and flares. However, most of the energetic phenomena due to accretion disappear in the late stage, and Hα emission becomes weak. A young stellar object in this late T-Tauri stage is called a weak-line T-Tauri star or a naked T-Tauri star, which was identified by X-ray observations of its magnetosphere (e.g., Feigelson and Montmerle 1999).

A phenomenological classification of the evolutionary stages of low-mass protostellar and young stellar objects is achieved using the infrared spectral energy distribution (SED) of objects (e.g., Lada and Wilking 1984; Lada 1987; Andre et al. 1993). In general, young stellar objects are classified into three classes: Class I, Class II, and Class III. The typical SEDs of these classes are shown in Fig. 7.2. Class I corresponds to a protostar stage; Classes II and III correspond to the classical T-Tauri stage and the weak-line T-Tauri stage, respectively. A Class I source has an emission peak in the far infrared and shows weak emission in the near infrared. Near-infrared emission from the young stellar object becomes dominant in the Class II stage, and the stellar emission becomes dominant in the Class III stage. Later, a new category, Class 0, was added to the classification scheme to include a young protostar stage, in which the star mostly emits radiation in the far infrared. Classifications according to SEDs are sometimes ambiguous because of different inclination of disks and the multiplicity of objects. This ambiguity is particularly true for Class 0 and Class I objects. Hence, bolometric temperature is often employed for classification (e.g., Evans et al. 2009). Specifically, the source is Class 0 if its bolometric temperature is lower than 70 K. If the bolometric temperature is higher than 70 K, the object is presumed to be in Class I. The durations of Class 0 and I are reported to be 1.6×10^5 and 5.4×10^5 year, respectively, assuming a duration time for Class II of 2×10^6 year (Evans et al. 2009). In this classification scheme, a molecular outflow emerges in the Class 0 and Class I stages. Protostellar disks are possibly formed during evolution from Class 0 to Class I. These disks evolve into protoplanetary disks in the Class II (and Class III) stage. Planets will be formed in the Class II and Class III stages.

7.3 Formation of High-Mass Stars

The formation of high-mass stars is still controversial. Because the radiation from a high-mass protostar is much stronger than the radiation from a low-mass protostar, a high-mass protostar can suppress further gas accretion by radiation pressure. Hence, it is not trivial whether high-mass star formation is just a scaled-up version of low-mass star formation. Apparently, the problem lies in how mass is gathered from interstellar clouds.

There are three paradigms for high-mass star formation (Zinnecker and Yorke 2007). The first paradigm is the gravitational collapse of a turbulent isolated massive core (e.g., McLaughlin and Pudritz 1996; McKee and Tan 2003). This process is also called monolithic collapse. In this scenario, a high-mass starless core is first formed but has to be turbulent; otherwise it would have collapsed before gathering enough mass from its envelope. The high degree of turbulence results in a high accretion rate of gas onto the protostar, which fuels the rapid growth of the protostar. Such turbulent cores may be formed, for instance, during cloud–cloud collisions (e.g., Furukawa et al. 2009). Although the accretion is suppressed by the radiation pressure, it is thought to continue to some extent through a disk structure formed around the protostar (e.g., Hosokawa et al. 2010). The second paradigm is "competitive accretion" (Bonnell et al. 2001; Wang et al. 2010). In this scenario, a high-mass star is first born as a member of a low-mass protostar cluster in a protocluster cloud. If the low-mass protostar is in a central region of the cloud, its parent core is able to gather more gas from the cloud than the other cores because of its low gravitational potential. Hence, the core gathers more and more mass as it grows, and the protostar in the core grows more massive. The third paradigm is growth by merger of low-mass protostars. This mechanism may work in the central region of the cluster, where the density of protostars is high enough for merger.

Thus, high-mass star formation is significantly different from low-mass star formation. Although many observational and theoretical studies have been conducted on these subjects, a unified picture of star formation has not emerged. In particular, the initial conditions for high-mass star formation are poorly understood in comparison with the low-mass star formation case. This situation yields poor constraints not only on star formation models but also on the chemical processes after the onset of high-mass star formation.

Observationally, a disk-outflow system—generally found in low-mass star-forming regions—has been found in the high-mass protostar IRAS 20126+4104, whose protostellar mass is 7–10 $M_\odot$. A Keplerian disk is identified around the protostar by observations of $C^{34}S$ and CH_3CN (Cesaroni et al. 2005, 2014). In contrast, the Orion KL region is much more complex (e.g., Wright et al. 1996; Beuther et al. 2005). Many protostellar sources are found in this region, based on infrared observations (Sect. 7.5.1). Although a large-scale outflow can be seen along the northwest–southeast direction, it is difficult to identify the source (s) responsible for the outflow. A clump of hot and dense gas is known to exist in the Orion KL region, which is probably a parent core of the protostellar sources and is heated up by their protostellar activity, including radiation heating and outflow shocks. Such a hot core can generally be identified in young high-mass star-forming regions. As high-mass protostars evolve, they will ionize a part of their parent core to form an ultracompact H II region (UC H II). Then, as the UC H II becomes extended, it evolves into a compact H II region and finally to an extended H II region. These H II regions can be traced by free–free emission from the ionized gas in the centimeter regime, as well as by radio recombination lines of H and He.

7.4 Chemical Compositions of Low-Mass Star-Forming Regions

The chemical compositions of low-mass star-forming regions have been extensively studied for many sources. However, most observations only included spectral lines of fundamental molecules such as CO, HCO^+, HCN, H_2CO, CS, and their isotopic species. A more complete set of chemical compositions was obtained for a few representative sources by an unbiased spectral line survey. These sources include IRAS 16293-2422, L1527, and R CrA IRS7B, all of which are low-mass Class 0 protostars (Blake et al. 1994; van Dishoeck et al. 1995; Caux et al. 2011; Sakai and Yamamoto 2013; Watanabe et al. 2012). We summarize the observational results of these objects below.

7.4.1 *Hot Corino Chemistry*

IRAS 16293-2422 is a low-mass protostellar source in Ophiuchus at a distance of 120 pc. It is a multiple system consisting of sources A and B, whose projected separation is 5″ (600 au) (Fig. 7.3). For this reason, complex outflow features are observed in this source (e.g., Mizuno et al. 1990). The total bolometric luminosity is 15 $L_\odot$, assuming a distance of 120 pc (Chandler et al. 2005).

As mentioned in Sect. 7.1, the first spectral line survey toward this source was carried out by Blake et al. (1994) and van Dishoeck et al. (1995). In their observations, sources A and B were not spatially resolved. They detected spectral lines of SO_2, OCS, H_2S, and SiO, which are not common in starless cores. Indeed, these four molecules are not detected in TMC-1 CP, although SO_2, OCS, and H_2S are found in

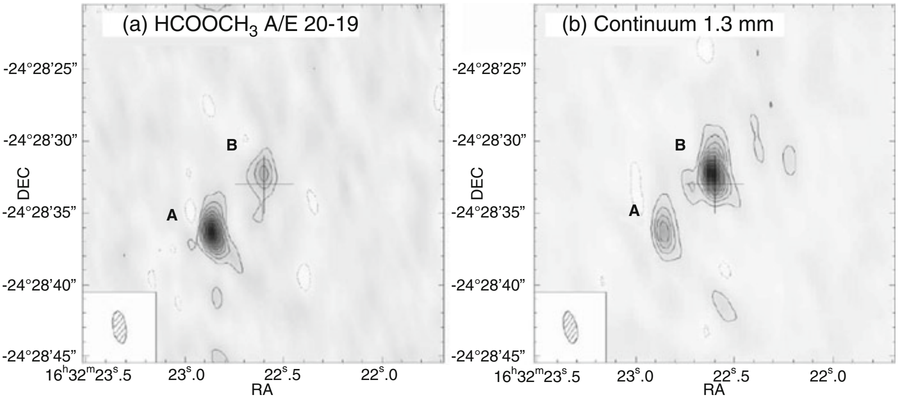

Fig. 7.3 Distributions of the $HCOOCH_3$ line (**a**) and the 1.3 mm dust continuum emission (**b**) from the low-mass protostar IRAS 16293-2422 observed with the PdBI. A synthesized beam is shown in the *bottom left* corner of each panel (Reprinted with permission from Bottinelli et al. (2004a, b). Copyright 2004 American Astronomical Society)

the other starless core L134 N (Swade 1989a, b; Minh et al. 1989; Dickens et al. 2000). The gas kinetic temperature and the H_2 density were found to be 70 to 80 K and (0.5–1.0) × 10^7 cm^{-3}, respectively. Hence, the above species should exist in a dense and hot region around protostars with a size of 500–1500 au. Moreover, CH_3OH and CH_3CN lines, which are not very bright in starless cores, were observed with a high intensity. These molecules also reside in dense and hot regions. Later, spectral lines of complex organic molecules such as $HCOOCH_3$, $(CH_3)_2O$, C_2H_5OH, and C_2H_5CN were found in this source (Cazaux et al. 2003). High spatial resolution observations of complex organic molecules with interferometers revealed that the emission from the molecules originates from dense and hot regions around protostars with sizes of a few 100 au or smaller (the hot corino) (Fig. 7.3). $HCOOCH_3$ and $(CH_3)_2O$ are associated with sources A and B; C_2H_5CN tends to be concentrated around source A. A cyclic isomer of C_3H_2 (c-C_3H_2) and H_2CCO can only be seen toward source B (Bottinelli et al. 2004a; Kuan et al. 2004; Jørgensen et al. 2011). Hence, systematic chemical differentiation is recognized between the two sources. Recent interferometric observations revealed that the $HCOOCH_3$ lines show a clear inverse P Cygni profile toward source B, indicating that $HCOOCH_3$ indeed exists in gas infalling onto the protostar of source B (Pineda et al. 2012).

In contrast, the CS, HCO^+, and H_2CO lines originate from the protostellar envelope, which has a gas kinetic temperature and H_2 density of 40 K and 10^6–10^7 cm^{-3}, respectively. The size of the protostellar envelope is approximately 2000 au. The CN, C_2H, and c-C_3H_2 molecules mainly reside in an outer envelope with a gas kinetic temperature of 10–20 K and an H_2 density of (0.3–2) × 10^5 cm^{-3}. That is, C_2H and c-C_3H_2 are deficient in the hot dense region around the protostar. The distributions of longer carbon-chain molecules are similar to those of CN, C_2H, and c-C_3H_2. The fractional abundances of molecules detected toward IRAS 16293-2422 are listed in Table 7.1.

Table 7.1 Fractional abundances of molecules in low-mass star-forming regions

	IRAS16293-2422[a]	L1527[b]	RCrA IRS7B[c]
$C^{18}O$	1.0×10^{-7}		
$C^{17}O$	3.8×10^{-8}		
CS	1.1×10^{-9}		1.6×10^{-9}
SO	3.9×10^{-9}		2.4×10^{-9}
SiO	1.0×10^{-10}		
HCS^+	2.0×10^{-11}		3.4×10^{-11}
OCS	7.1×10^{-9}		
H_2S	1.5×10^{-9}		
H_2CS	1.7×10^{-10}		2.2×10^{-10}
SO_2	1.5×10^{-9}		1.2×10^{-10}
HCO^+	1.8×10^{-9}		9.7×10^{-10}
HCN	1.9×10^{-9}	8.4×10^{-10}	9.3×10^{-10}
HNC	1.5×10^{-10}	6.0×10^{-9}	3.1×10^{-10}
CN	1.0×10^{-10}		1.6×10^{-9}
C_2H	2.5×10^{-10}	3.3×10^{-8}	5.3×10^{-9}
$c\text{-}C_3H_2$	3.5×10^{-11}		2.3×10^{-11}
H_2CO	7.0×10^{-10}	1.4×10^{-9}	1.4×10^{-9}
CH_3OH	4.4×10^{-9}	2.1×10^{-9}	1.0×10^{-9}
CH_3CN	1.5×10^{-10}		
CH_3CCH	6.5×10^{-10}	2.0×10^{-9}	
HC_3N	2.5×10^{-11}	9.0×10^{-10}	
HNCO	1.7×10^{-10}		
H_2CCO	1.8×10^{-10}		
CCD	4.5×10^{-11}		2.0×10^{-10}
DCN	2.5×10^{-11}	3.1×10^{-11}	8.1×10^{-12}
NO			2.3×10^{-9}
DCO^+	1.5×10^{-11}		2.5×10^{-12}
HDCO	1.1×10^{-10}		7.1×10^{-11}
$l\text{-}C_3H$		1.1×10^{-10}	
C_4H		6.3×10^{-9}	
C_4H_2		7.0×10^{-11}	
C_5H		3.0×10^{-11}	
C_6H		2.1×10^{-11}	
C_6H^-		1.9×10^{-12}	
HC_5N		2.3×10^{-10}	
HC_7N		5.0×10^{-11}	

[a] van Dishoeck et al. (1995) and Blake et al. (1994)
[b] Sakai and Yamamoto (2013)
[c] Watanabe et al. (2012)

Another characteristic feature of IRAS 16293-2422 is its high deuterium fractionation ratios despite its high-temperature conditions (van Dishoeck et al. 1995). Its $HDCO/H_2CO$ and CH_2DOH/CH_3OH ratios are 0.15 ± 0.07 and 0.9 ± 0.3 (Parise et al. 2002), which are significantly higher than the typical deuterium fractionation ratio found in starless cores. Moreover, doubly and triply deuterated species such as D_2CO, CHD_2OH, and CD_3OH are also detected (Ceccarelli et al. 1998; Parise et al. 2002, 2004). A similar trend can be seen for the CCD/CCH, NH_2D/NH_3, and HDS/H_2S ratios (van Dishoeck et al. 1995). In contrast, a low fractionation ratio is observed for DCO^+/HCO^+ (0.0086); a moderate fractionation ratio is seen for HCN and HNC (van Dishoeck et al. 1995).

Several protostellar cores that have similar chemical characteristics are known. These cores include NGC 1333 IRAS 4A, NGC 1333 IRAS 4B, NGC1333 IRAS 2A, Serpens SMM1, and Serpens SMM4, all of which are low-mass Class 0 protostellar sources (see Herbst and van Dishoeck 2009). In these sources, a hot dense region (the hot corino) is known to be associated with the protostar based on analysis of submillimeter-wave emission lines of H_2CO and CH_3OH. The abundances of these two species show an abrupt jump within a certain radius of the protostar. In these sources, several complex oxygen-bearing organic molecules such as $HCOOCH_3$ and $(CH_3)_2O$ are detected (e.g., Jørgensen et al. 2005; Bottinelli et al. 2004b; Oberg et al. 2011; Sakai et al. 2006a), and high deuterium fractionation ratios are observed for H_2CO and CH_3OH in NGC 1333 IRAS4A, IRAS4B, and IRAS2 (Parise et al. 2006). In NGC 1333 IRAS4A and its vicinity, ND_3 and D_2S are also found (van der Tak et al. 2002; Vastel et al. 2003), although these molecules are not detected in IRAS 16293-2422. However, emission from carbon-chain molecules is generally weak in these sources.

Here, it should be stressed that hot corino chemistry does not always occur in low-mass Class 0 sources. Despite extensive searches for complex organic molecules toward various low-mass Class 0 sources, only a few sources mentioned above are known to show such emission at present. This result may originate from the limited sensitivity of currently available radio telescopes, because the emission of complex organic molecules is generally faint. However, insufficient sensitivity is not the only possible reason for non-detection. Chemical compositions of low-mass protostellar cores are characterized by significant diversity, as discussed below.

7.4.2 Warm Carbon-Chain Chemistry Sources

L1527 is a protostellar core in Taurus at a distance of 140 pc that harbors the Class 0 protostar IRAS 04368+2557, whose luminosity is 2.75 $L_\odot$ (Tobin et al. 2013). The protostellar envelope has a disk-like structure with an almost edge-on configuration to the north and south; the outflow blows toward the east and west, almost parallel to a plane of the sky (e.g., Ohashi et al. 1997; Tobin et al. 2010) (Fig. 7.4). Because of its simple structure, this source has been targeted for detailed studies of the physical processes of low-mass star formation.

The chemical composition of this source is completely different from that found in hot corino sources (Sakai et al. 2008a). Despite very sensitive observations, the spectral lines of the complex organic molecule $HCOOCH_3$ were not detected

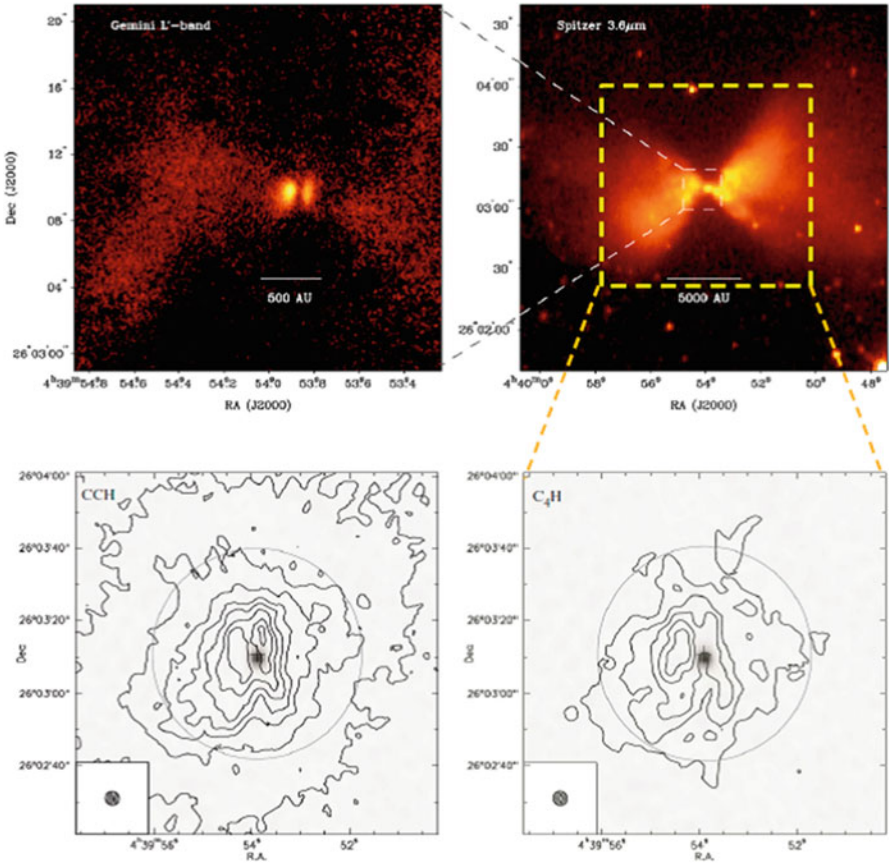

Fig. 7.4 (*Upper panels*) L' band image and Spitzer 3.5 μ m image of the low-mass protostar L1527 (Reprinted with permission from Tobin et al. (2010). Copyright 2010 American Astronomical Society) (*Lower panels*) Carbon-chain molecules such as CCH and C_4H toward this source are abundant in a warm and dense region near the protostar (Reprinted with permission from Sakai et al. (2010a, b). Copyright 2010 American Astronomical Society)

toward this source (Sakai et al. 2008c). The CH_3OH emission is not as bright as that in hot corino sources. Instead, bright emission of high excitation lines of various carbon-chain molecules such as c-C_3H_2, C_4H, and C_4H_2 is observed. Even long carbon-chain molecules such as HC_5N, HC_7N, C_6H, and C_6H_2, which are generally deficient in star-forming regions, are found to be moderately abundant. Furthermore, it is surprising that carbon-chain anions, including C_6H^- and C_4H^-, are detected in this source (Sakai et al. 2007a; 2008b; Agundez et al. 2008).

The rotation temperatures of C_4H_2 and CH_3CCH are 12.8 and 13.9 K, respectively. Although these numbers are beam-averaged values, they are significantly higher than the temperature of the ambient cloud (10 K). Moreover, the detections of high excitation lines with a critical density of about 10^6 cm^{-3} or higher mean that the emission from carbon-chain molecules comes from a warm and dense region around the protostar. In fact, high spatial resolution observations of CCH, c-C_3H_2, and C_4H with the Plateau du Bure Interferometer (PdBI) revealed that these carbon-chain molecules are indeed concentrated around the protostar with a radius of about 1000 au (Fig. 7.4). These features of carbon-chain molecules contradict the chemical evolutionary scenario presented in Chaps. 5 and 6. Because carbon-chain molecules are generally deficient in evolved starless cores, they should also be deficient in protostellar cores. Hence, a regeneration of carbon-chain molecules has to be invoked to explain the result. This mechanism is termed *warm carbon-chain chemistry* (WCCC). The details of this mechanism will be discussed in Sect. 7.8.

L1527 is not the only source showing WCCC. Another definitive WCCC source is found in the Lupus molecular cloud at a distance of 155 pc. This is the Class 0 protostar, IRAS 15398-3359, with a bolometric luminosity of 1.8 $L_\odot$ (Jørgensen et al. 2013). In this source, bright high excitation lines of carbon-chain molecules are observed, as found in L1527 (Sakai et al. 2009a). The intensity of the C_4H ($N = 10 - 9$) line is even brighter than the same line in L1527. The rotation temperature of CH_3CCH is 12.6 K, which is higher than the temperature of the ambient cloud. Furthermore, a distribution of the high excitation line of CCH is found to be concentrated around the protostar. Hence, carbon-chain molecules are abundant in a warm and dense region around a protostar, and IRAS 15398-3359 can be regarded as a WCCC source. A few other protostellar cores show moderately intense emission of C_4H. However, they cannot definitively be categorized as WCCC sources at the present time, because of a lack of high-resolution observations of the distributions of carbon-chain molecules.

An important chemical feature of WCCC sources is their low deuterium fractionation (Sakai et al. 2009b). In L1527, the deuterium fractionation ratios of various molecules, including carbon-chain molecules such as C_3D, C_4D, C_4HD, c-C_3HD, DC_3N, and DC_5N, were measured. These molecules show moderate fractionation ratios ranging from 0.02 to 0.07. The same is true for CH_2DOH. The upper limit on the deuterium fractionation ratio of CH_2DOH is 0.03. For HDCO, two measurements report quite different fractionation ratios: 0.06 ± 0.025 and $1.7^{+2.6}_{-1.1}$ (Roberts and Millar 2007; Parise et al. 2002, 2004, 2006). Except for one measurement for HDCO, the deuterium fractionation ratios are significantly lower than those found in hot corino sources (0.1 or higher).

The chemical compositions of hot corino sources and WCCC sources appear mutually exclusive. In hot corino sources, saturated complex organic molecules are abundant, and unsaturated organic molecules such as carbon-chain molecules are generally deficient. In contrast, carbon-chain molecules are abundant in WCCC sources, where saturated complex organic molecules are deficient. This exclusiveness is also seen in the deuterium fractionation ratios. Figure 7.5 shows a comparison of the spectra in the 3-mm band toward the hot corino source IRAS 16293-2422 (Caux et al. 2011) and the WCCC source L1527, demonstrating a striking difference in chemical composition based on different spectral patterns.

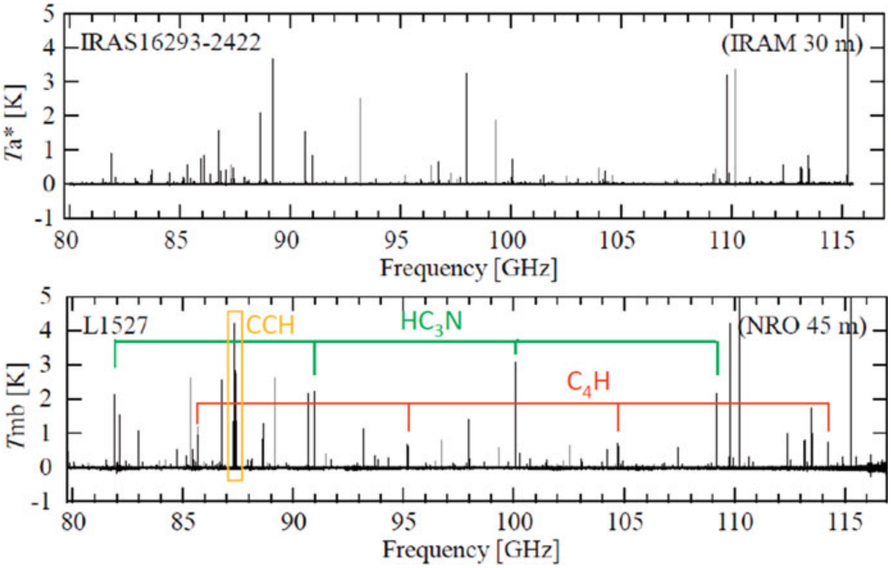

Fig. 7.5 Spectral line survey toward the hot corino IRAS 16293-2422 with the IRAM 30m telescope (Caux et al. 2011; *upper panel*) and the WCCC source L1527 with the Nobeyama 45m telescope (*lower panel*). Although these are both Class 0 protostars, their spectral patterns are significantly different; chemical diversity is evident

7.4.3 Chemical Diversity

So far, two distinct and exclusive chemical compositions have been recognized for low-mass protostellar sources, as described above. These two are hot corino chemistry and WCCC. At the same time, low-mass protostellar sources are not always categorized into one of these classes, which were partly revealed by a C_4H survey (Sakai et al. 2009a). Thus, chemical diversity of protostellar cores is evident.

An important example showing additional chemical diversity is the low-mass Class 0 protostar R CrA IRS7B. This source is located in the Corona Australis dark cloud at a distance of 170 pc. Its bolometric luminosity is 4.6 $L_\odot$. According to a spectral line survey in the 0.8-mm band toward this source (Watanabe et al. 2012; Lindberg et al. 2014), the abundances of CH_3OH and SO_2 are significantly lower than those in IRAS 16293-2422. Conversely, the abundances of CCH and CN are higher than those in IRAS 16393-2422. The deficiency of hot corino molecules (CH_3OH and SO_2) and the relatively high abundance of carbon-chain molecules (CCH) suggest a WCCC nature at first glance. However, no long carbon-chain molecules such as C_4H and HC_5N are found, and hence this source is not categorized as a WCCC source. Furthermore, it cannot be categorized as a hot corino source, because no complex organic molecules are found. It is suggested that this source is being strongly influenced by an external UV field from the nearby Herbig Ae star, R CrA (Watanabe et al. 2012; Lindberg et al. 2012). The chemical compositions of low-mass protostellar sources seem to be affected strongly by their environment.

7.5 Chemical Compositions of High-Mass Star-Forming Regions

In general, physical structures of high-mass star-forming regions are much more complex than those of low-mass star-forming regions, because high-mass stars are usually born as members of star clusters. The effects of nearby protostars in various evolutionary stages complicate the physical structures of star-forming regions, which also results in complex chemical structures. Nevertheless, the chemical compositions of high-mass star-forming regions can be characterized by a richness of saturated complex organic molecules, such as $HCOOCH_3$, $(CH_3)_2O$, C_2H_5OH, and C_2H_5CN, and sulfur-bearing molecules, such as SO, SO_2, and OCS, in hot cores around or near high-mass protostars (e.g., Blake et al. 1987). Conversely, carbon-chain molecules are generally deficient, except for a few simple molecules such as CCH and HC_3N. High-mass star-forming regions showing WCCC characteristics have not been found.

Because molecular emission from high-mass star-forming regions is much brighter than the emission from low-mass protostars owing to larger areas of high-temperature and high column density regions, the chemical compositions of high-mass star-forming regions have extensively been studied in some sources since the 1970s. A drawback to these studies is that such regions are mostly located far away (1 kpc or more) except for a few cases. Hence, high spatial resolution observations are required to resolve the complex physical and chemical structures of these regions. Observations with millimeter- and submillimeter-wave interferometers are often essential for a detailed understanding of the chemical processes in these regions. Here, we introduce a few observational results of high-mass star-forming regions.

7.5.1 Orion KL

Orion KL is the best studied high-mass star-forming region for astrochemistry. A number of bright infrared sources are associated with Orion KL (Fig. 7.6) (e.g., Dougados et al. 1993; Okumura et al. 2011; Sitarski 2013). Among them, at least three are high-mass stars: the Becklin–Neugebauer (BN) object (a B0 star), the radio continuum source I, and the infrared source n. Based on the proper motions of these three objects, they are moving away from an almost coincident point, where a close encounter or collision had occurred (e.g., Gomez et al. 2005). In Orion KL, source I is a young protostar and is responsible for the recent occurring energetic events. The SiO masers are associated with source I. Source I is on the edge of the

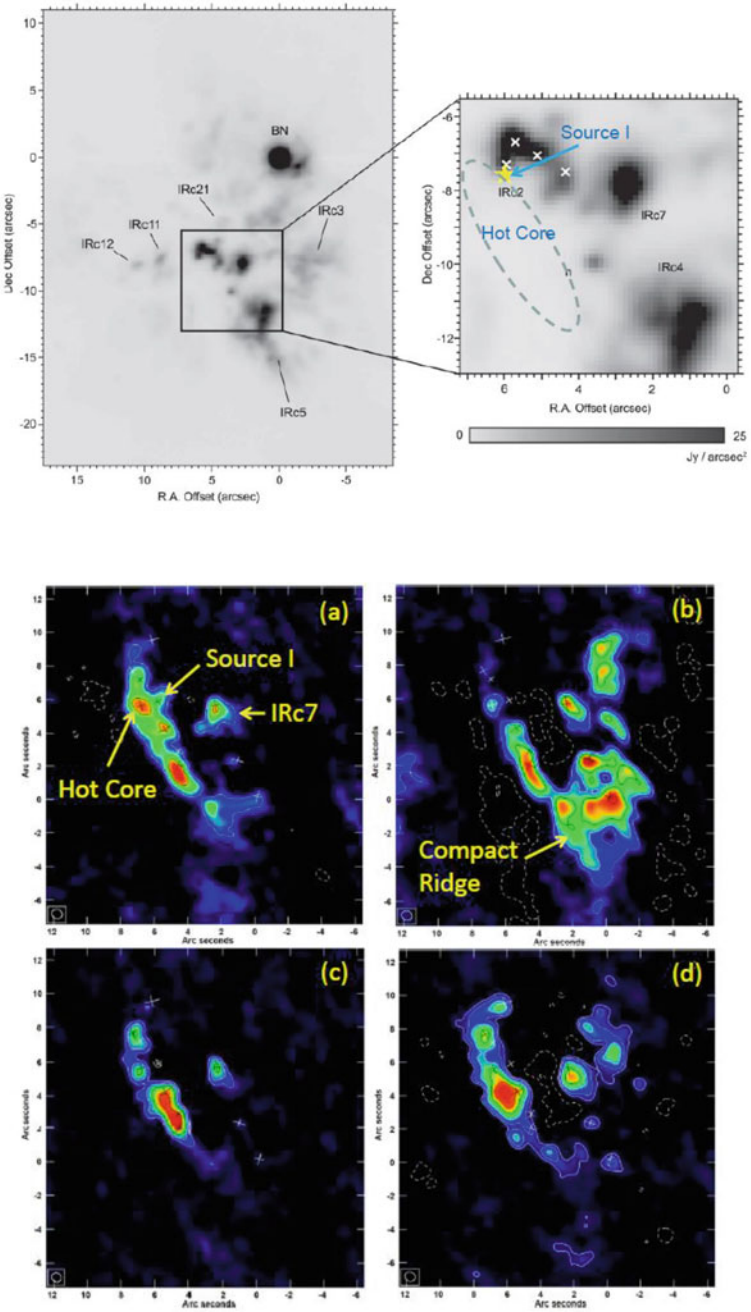

Fig. 7.6 (*Top panels*) 12.4 μ m image of the Orion KL region, indicating the complexity of this region (Reprinted with permission from Okumura et al. (2011)) (*Bottom panels*) Molecular distributions in the high-mass star-forming region Orion KL Source I consists of newly born high-mass protostars. Panels (**a**–**d**) represent the intensity distributions of the $H_2{}^{13}CO$, $HCOOCH_3$, NH_2CHO, and C_2H_5CN lines, respectively, observed in the 1.3-mm band with ALMA. A synthesized beam is shown in the *bottom left* corner of each panel. Cross marks represent the positions of the dust continuum peaks. (Hirota, T. private communication)

infrared source IRc2, which is thought to be illuminated by source I (Okumura et al. 2011). In contrast, the BN object and source n are more evolved.

Because of the complex physical structure of this region, the distributions of the various molecules differ, as determined by interferometric observations (Fig. 7.6). Although the distributions are complicated, we note here two prominent components. According to millimeter- and submillimeter-wave continuum observations, there exists a dense core just to the southeast of source I, called the Orion KL hot core. The hot core does not contain a self-luminous source and is thought to be heated externally by source I (Zapata et al. 2011). In Fig. 7.6, we show how the hot core can be seen in the emission of CH_3CN and NH_2CHO. It is known to be visible in other molecules such as CS, SO_2, H_2CO, CH_3OH, HCOOH, and H_2CS (Wright et al. 1996; Beuther et al. 2005). The second component is the compact ridge, which is located to the southwest of source I. In Fig. 7.6, the compact ridge can be seen in $HCOOCH_3$. It is known that this component can be traced by H_2CO, $(CH_3)_2O$, and C_2H_5OH emission (Wright et al. 1996; Beuther et al. 2005). In addition to these two components, the extended ridge, which is a part of the parent filamentary cloud, and the plateau component, which is thought to be a part of the outflowing (or expanding) gas, are known to exist from single-dish observations (e.g., Blake et al. 1987). Emission from the extended ridge can be seen, for instance, in HC_3N and N_2H^+, whereas broad emission from CO, HCO^+, and SiO is observed in the plateau. The extended ridge and plateau components are so broad that they are often resolved out in interferometric observations. The spectra toward the hot core and the compact ridge observed with the Submillimeter Array (SMA) are shown in Fig. 7.7 (Beuther et al. 2005). Spectral lines of oxygen-bearing complex organic molecules are strong in the compact ridge; lines of nitrogen-bearing complex organic molecules are strong in the hot core.

Despite the chemical complexity of this region, spectral line surveys with a single-dish telescope are useful for characterizing the chemical composition of the region. Because Orion KL is an outstanding source of strong molecular emission, spectral line surveys have extensively carried out in the millimeter- and submillimeter-wave regimes (e.g., Blake et al. 1987; Turner 1989; Schilke et al. 1997a; Comito et al. 2005; Tercero et al. 2010; Crockett et al. 2014). Chemical complexity can be resolved by careful analyses of spectral line profiles, because the line shapes ($v_{\rm lsr}$ and Δv) differ among the components discussed above. Table 7.2 lists the molecular abundances for each component derived in this way by Blake et al. (1987). Oxygen-bearing complex organic molecules are preferentially found in the compact ridge; nitrogen-bearing molecules mostly exist in the hot core. This result is consistent with findings from interferometric observations.

7.5.2 W3(OH) and W3(H_2O)

Another example of high-mass star-forming regions is the complex molecular cloud associated with the H II region W3 at a distance of 2.04 kpc (Hachisuka et al. 2006).

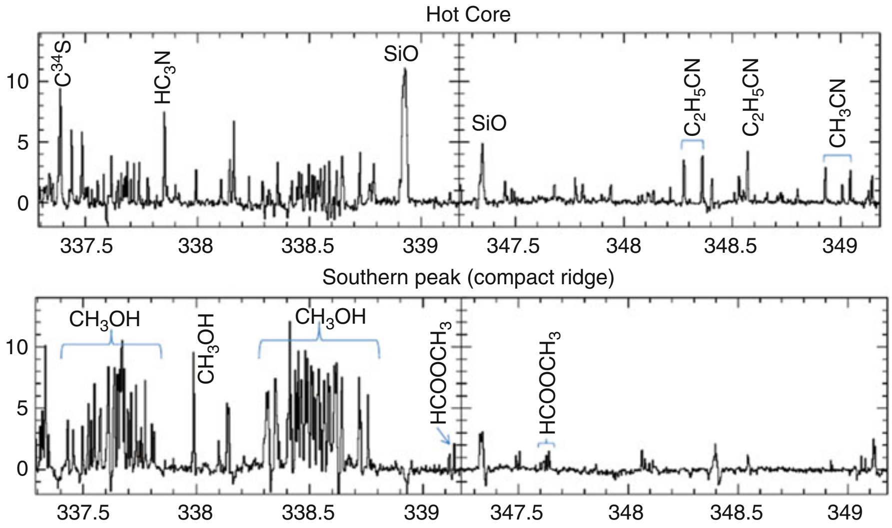

Fig. 7.7 Spatially resolved spectra of the Orion KL region observed with the SMA. The hot core (*upper panel*) and the compact ridge (*lower panel*) exhibit different chemical compositions (Reprinted with permission from Beuther et al. (2005). Copyright 2005 American Astronomical Society)

This region includes two high-mass star-forming regions, W3 Main and W3 (OH) (Tieftrunk et al. 1998; Sakai et al. 2006b). W3 Main is a large molecular cloud core embedded in an H II region. It harbors two bright infrared sources, IRS5 and IRS6, which are probably O stars. On the other hand, the W3(OH) region consists of the UC H II region, W3(OH), associated with OH masers and the hot core, W3(H_2O), associated with H_2O masers, which are separated only by 5″. Helmich and van Dishoeck (1994, 1997) conducted a spectral line survey toward W3(OH), IRS5, and IRS6. In their observations, W3(OH) and W3(H_2O) are not resolved, and the total abundances of the two sources are reported. The molecular abundances in W3(OH) are similar to those found in the hot core of Orion KL; the molecular abundances in IRS5 and IRS6 are generally lower than those found in W3(OH).

When W3(OH) and W3(H_2O) are resolved by interferometric observations, a clear chemical difference between the two sources can be seen (Wyrowski et al. 1999). The nitrogen-bearing complex organic molecule C_2H_5CN only resides in the hot core W3(H_2O); oxygen-bearing complex organic molecules exist both in W3 (H_2O) and W3(OH) (Fig. 7.8). This situation seems to be similar to the chemical difference between the hot core and the compact ridge seen in Orion KL. For this reason, the chemical differentiation of oxygen-bearing and nitrogen-bearing species is an interesting subject of astrochemistry (e.g., Fontani et al. 2007).

There is notably another massive clump in the W3 molecular cloud, AFGL 333, which is located 30′ south of W3(OH). This source does not show active high-mass star formation despite its high gas mass, although low-mass star formation

Table 7.2 Fractional abundances of molecules observed in characteristic components of Orion KL[a]

	Extended ridge	Compact ridge	Plateau	Hot core
CO	5.0×10^{-5}		1.2×10^{-4}	1.2×10^{-4}
CS	2.5×10^{-9}		2.2×10^{-8}	
CN	3.3×10^{-9}			
HNC	5.3×10^{-10}			
HCN	5.0×10^{-9}		2.8×10^{-7}	3.0×10^{-7}
C_2H	5.3×10^{-9}			
c-C_3H_2	8.7×10^{-11}			
HDCO	1.9×10^{-10}			
HCO^+	2.3×10^{-9}			
HCS^+	5.3×10^{-11}			
HC_3N	1.3×10^{-10}		3.3×10^{-8}	1.6×10^{-9}
DCN	1.7×10^{-11}			7.1×10^{-10}
CH_3CCH	3.3×10^{-9}			
OCS		3.3×10^{-9}	5.2×10^{-8}	
HDO		6.3×10^{-10}	1.7×10^{-8}	5.3×10^{-8}
H_2CO		1.7×10^{-8}	3.1×10^{-8}	2.6×10^{-8}
H_2CS		1.6×10^{-9}		
CH_3OH		1.2×10^{-7}		
HCOOH		5.0×10^{-10}		
H_2CCO		6.7×10^{-10}		
$(CH_3)_2O$		1.0×10^{-8}		
$HCOOCH_3$		8.7×10^{-9}		
SO	$<9.3 \times 10^{-10}$		5.2×10^{-7}	$<2.0 \times 10^{-8}$
SiO	$<3.3 \times 10^{-10}$		2.8×10^{-8}	
SO_2	$<3.3 \times 10^{-9}$		5.2×10^{-7}	$<2.4 \times 10^{-8}$
H_2S			9.8×10^{-8}	
HNCO	$<2.2 \times 10^{-9}$			5.8×10^{-9}
CH_3CN				7.8×10^{-9}
C_2H_3CN				1.8×10^{-9}
C_2H_5CN				9.8×10^{-9}

[a] Taken from Blake et al. (1987). Recent works are available for a part of the molecules (Tercero et al. 2010, 2011) and Esplugues et al. (2013)

activity has been identified. This source is rich in atomic carbon in comparison with W3 Main and W3(OH). The CCS emission, which is usually very faint in high-mass star-forming regions, is observed in this core. These results imply the chemical youth of this massive core (Sakai et al. 2007b).

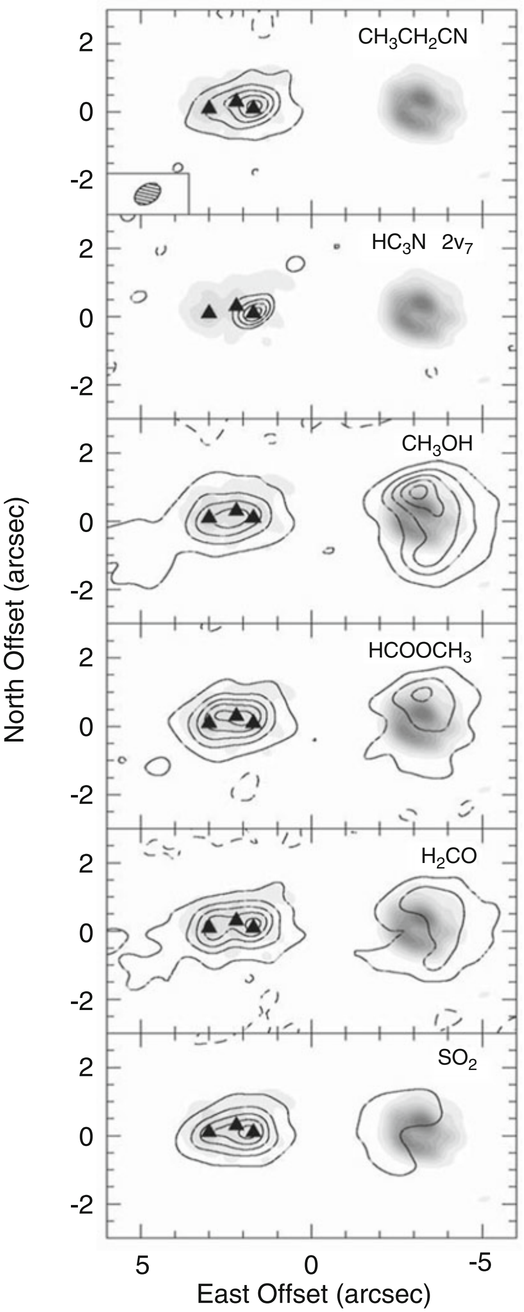

Fig. 7.8 Molecular distribution in the W3 star-forming region. There are two massive cores, W3 (OH) (*left*) and W3(H_2O) (*right*). CH_3CH_2CN is present only in W3(H_2O). Clear chemical differentiation is observed (Reprinted with permission from Wyrowski et al. (1999). Copyright 1999 American Astronomical Society)

7.5.3 Infrared Dark Clouds

Just as the chemical evolution of low-mass cores has been investigated using statistical analyses based on survey observations of many sources, the chemical evolution of high-mass prestellar and protostellar cores should be studied in a statistical way. The best set of samples is thought to be infrared dark clouds (IRDCs), which are dark patches seen against the diffuse galactic infrared background (e.g., Perault et al. 1996; Egan et al. 1998; Simon et al. 2006). High extinction in the mid-infrared means very a high column density of molecular gas; an extinction of 2 magnitudes at 8 μ m approximately corresponds to a visual extinction of 40 magnitudes (Chapman et al. 2009) and an H_2 column density of 4×10^{22} cm^{-2}. Dense massive clumps with masses higher than 100 $M_\odot$ are found in IRDCs. These clumps are thought to be formation sites of high-mass stars. With a sample of these dense clumps, statistical studies exploring the chemical evolution of high-mass star formation are now possible.

Such studies have been conducted by several groups on various molecules, including HCN, HCO^+, N_2H^+, CCH, SiO, CS, CCS, HC_3N, and CH_3OH (Sakai et al. 2010a, b; Vasyunina et al. 2011; Fontani et al. 2012). An interesting feature in the chemical compositions of massive clumps in IRDCs is the absence or weakness of CCS emission, even for sources without high-mass star formation. In contrast, CCS emission is brighter in younger sources in low-mass prestellar evolution (Chap. 5) and is used as an evolutionary tracer. Faint CCS emission in massive clumps in IRDCs means that the clumps are, in general, chemically evolved. Deuterium fractionation ratios have also been studied for massive clumps in IRDCs. For instance, the N_2D^+/ N_2H^+ ratio tends to be higher in high-mass starless core candidates than in high-mass protostellar cores, indicating that the N_2D^+/ N_2H^+ ratio can be used as an evolutionary indicator for IRDCs (Fontani et al. 2011).

7.6 General Features of Chemical Processes in Star-Forming Regions

Although the chemical structure of actual star-forming regions is very complicated, the most important driving source for chemical evolution in star-forming regions is the increase in temperature resulting from the birth of protostars. Here, we consider the temperature increase caused by radiation heating from protostars; the temperature increase caused by gas dynamics, including outflow shocks and accretion shocks, will be described in Sect. 7.9.

The timescales of formation and destruction of molecules are 9×10^5 year and 3×10^6 year, respectively, which are determined by the timescale of $H_3{}^+$ and He^+ reactions, respectively. These timescales are essentially the same as those for molecular clouds because they are independent of H_2 density (Sect. 5.10). If the major form of oxygen is H_2O adsorbed onto dust grains, the $H_3{}^+$ abundance will increase. In this case, the timescale of formation of molecules becomes shorter by a factor of 2. Hence, the timescale for chemical equilibrium is $(4-9) \times 10^5$ year. Conversely, the depletion timescale can be as short as 10^3 year for an H_2 density of 10^6 cm^{-3}. However, the depletion timescale is not very important, because the temperature generally increases as a function of time in star-forming regions. Instead of depletion, molecules are supplied from dust grains depending on the temperature. When new molecular species are liberated into the gas phase at a certain time, the gas-phase chemical composition will approach a new equilibrium state for all species, including the new species. The time necessary for this process is approximately the same as the timescale for chemical equilibrium.

The dynamical timescale of a star-forming core is rather short. The free-fall time of a core with an H_2 density of 10^6 cm^{-3} is 3.4×10^4 year. The timescale for the main accretion phase of a low-mass protostar (Class 0 and Class I) is about 10^5 year. The corresponding timescale for a high-mass protostar will be much shorter. These dynamical timescales are all shorter than the timescale for chemical equilibrium, and, hence, the chemical composition of star-forming regions is not in a steady state. Thus, time-dependent chemical models are essential for exploring chemical compositions of star-forming regions. Many chemical models of star-forming regions have been presented particularly for hot cores (e.g., Garrod and WidicusWeaver 2013; Garrod 2013; Nomura and Millar 2004; Charnley et al. 2001). Aikawa et al. conducted chemical model calculations tracing evolution from prestellar cores (starless cores) to protostellar cores by considering physical evolution (Aikawa 2013; Aikawa et al. 2008, 2012).

The most important effect of the increasing temperature is the desorption of molecules from dust grains. This process incurs substantial changes in the chemical compositions in the gas phase. The adsorption temperature varies from molecule to molecule. For instance, CO, CH_4, H_2CO, and H_2O have adsorption temperatures of 20, 25, 60, and 100 K, respectively. Desorption may occur only partly, even above the adsorption temperature. Because H_2O is a dominant constituent of grain mantles, CO, CH_4, H_2CO, CH_3OH, and other species are surrounded by cages of H_2O ice. If the above molecules are on the surfaces of grain mantles or are enclosed by the cages near the surface, they will be liberated into the gas phase above the adsorption temperature. However, they cannot escape from cages deep within grain mantles. This process of partial sublimation can be seen in the desorption spectra produced in the laboratory (e.g., Collings et al. 2004). When the temperature substantially becomes higher than the adsorption temperature of H_2O, all grain mantle species, including H_2O, are sublimated. Even if nonvolatile species are enclosed in the H_2O cages, they will also be liberated in the gas phase along with H_2O at least partially.

The sublimation of grain mantle species significantly affects the gas-phase composition. When most of H_2O molecules in grain mantle are sublimated above 100 K, a fractional abundance of H_2O in the gas phase is ~10^{-4}. In this condition, H_2O is the main contributor to the break-up of C^+:

$$C^+ + H_2O \rightarrow HCO^+ + H \tag{7.1}$$

HCO^+ is broken up by H_2O, because the proton affinity of H_2O is higher than that of CO:

$$HCO^+ + H_2O \rightarrow OH_3{}^+ + CO. \tag{7.2}$$

The electron recombination of $OH_3{}^+$ partly recovers H_2O, which means that H_2O breaks up C^+. Hence, carbon chemistry starting from C^+ is significantly suppressed.

Historically, the following reaction was considered to be important for producing oxygen-bearing complex organic molecules:

$$CH_3{}^+ + H_2O \rightarrow CH_3OH_2{}^+ + h\nu, \tag{7.3}$$

$$CH_3OH_2{}^+ + e \rightarrow CH_3OH + H, \tag{7.4}$$

$$CH_3{}^+ + CH_3OH \rightarrow (CH_3)_2OH^+ + h\nu, \tag{7.5}$$

$$(CH_3)_2OH^+ + e \rightarrow (CH_3)_2O + H, \tag{7.6}$$

$$CH_3OH_2{}^+ + H_2CO \rightarrow HCOOCH_4{}^+ + H_2, \tag{7.7}$$

$$HCOOCH_4{}^+ + e \rightarrow HCOOCH_3 + H. \tag{7.8}$$

However, it was pointed out that reaction (7.3) is not as fast as expected. Additionally, the recombination of protonated CH_3OH (reaction (7.4)) mostly causes cleavage of C–O bonds (Geppert et al. 2006). Hence, the gas-phase production of CH_3OH is not efficient. A similar problem for electron recombination is expected in reactions (7.6) and (7.8). Hence, these reactions are now thought to play a limited role in the production of complex organic molecules.

The increase in temperature also affects grain-surface reactions. If the temperature suddenly jumps from 10 K to 100 K, for instance, surface reactions are barely affected. In this case, molecules on dust grains are just sublimated. However, the situation differs significantly if the temperature gradually increases. Such a gradual increase in temperature is more realistic in star-forming regions, and its effect on chemical compositions was studied by Garrod and Herbst (2006). When the temperature increases, the evaporation timescale of H atoms rapidly becomes shorter than their accretion timescale. Hence, the surface abundance of H atoms becomes very low. That is, H atoms adsorbed onto dust grains are immediately desorbed before reacting with other species. This effect is significant even at 15 K. In this case, hydrogenation reactions, which are an important process in surface reactions, are suppressed by a lower surface abundance of H atoms. As a result, reaction intermediates, which are not fully hydrogenated, do remain in grain mantles without further hydrogenation. For instance, HCO and CH_3O, which are reaction intermediates in the formation of CH_3OH from CO, would escape from further hydrogenation.

The mobility of heavy atoms and molecules, which generally have a higher activation barrier for surface hopping than H and H_2, rapidly increases with increasing temperature. Hence, reactions between pairs of radicals, as well as those between radicals and molecules, can occur efficiently, producing complex molecules. Examples of this process include:

$$HCO + CH_3O \rightarrow HCOOCH_3, \tag{7.9}$$

$$CH_3 + CH_3O \rightarrow (CH_3)_2O, \tag{7.10}$$

$$OH + HCO \rightarrow HCOOH, \tag{7.11}$$

$$OH + H_2CO \rightarrow HCOOH + H, \tag{7.12}$$

where the first three reactions are radical–radical reactions without activation barriers, and the last reaction has an activation barrier. By these means, oxygen-bearing complex organic molecules form in the warm-up phase. Although these molecules would be to some extent formed in the cold phase through cosmic-ray-induced photodissociation of surface species, these processes are accelerated in the warm-up phase. The product molecules will be liberated into the gas phase when the temperature increases above the adsorption temperature of H_2O.

The formation processes of complex organic molecules can be testified by investigating how their abundances are correlated. Bisschop et al. (2007) conducted a survey observation of various complex organic molecules toward seven sources and investigated the correlation coefficients among their observed abundances. In Table 7.3, a correlation can be seen among the abundances of CH_3OH, $HCOOCH_3$, $(CH_3)_2O$, and C_2H_5OH. This result suggests that the formation pathways of these molecules are related to one another and supports the production mechanisms discussed above. Nevertheless, the abundances of these molecules are not correlated with those of CH_3CN, HNCO, and NH_2CHO. This result is similar to the chemical differentiation between nitrogen-bearing and oxygen-bearing complex organic molecules seen in Orion KL and W3(OH). Fontani et al. (2007) pointed out a correlation between the abundances of C_2H_5CN and C_2H_3CN. However, these authors also showed a correlation between C_2H_5CN and $(CH_3)_2O$. This contradiction most likely arises because the complex structure of the source is not resolved in their observations.

7.7 Chemical Differentiation Between Oxygen-Bearing and Nitrogen-Bearing Species

Chemical differentiation is clearly observed between oxygen-bearing complex organic molecules such as $HCOOCH_3$, $(CH_3)_2O$, and C_2H_5OH and nitrogen-bearing complex organic molecules such as C_2H_3CN and C_2H_5CN (Sect. 7.5). Chemical differentiation is seen not only in high-mass star-forming regions but also in low-mass star-forming regions such as IRAS 16293-2422 (Bottinelli et al. 2004a; Kuan et al. 2004). Because these molecules are difficult to form via

Table 7.3 Correlation coefficient between the abundances of molecules[a]

	H_2CO	CH_3OH	C_2H_5OH	HNCO	NH_2CHO	CH_3CN	$HCOOCH_3$	$(CH_3)_2O$
H_2CO	1.00	0.98	0.76	0.46	0.53	−0.07	0.88	0.75
CH_3OH	0.98	1.00	0.86	0.38	0.39	−0.07	0.92	0.86
C_2H_5OH	0.76	0.86	1.00	0.02	0.22	0.12	0.92	0.86
HNCO	0.46	0.38	0.02	1.00	0.38	0.81	0.16	−0.27
NH_2CHO	0.53	0.39	0.22	0.38	1.00	0.17	0.42	−0.02
CH_3CN	−0.07	−0.07	0.12	0.81	0.17	1.00	0.29	0.20
$HCOOCH_3$	0.88	0.92	0.92	0.16	0.42	0.29	1.00	0.90
$(CH_3)_2O$	0.75	0.86	0.95	−0.27	−0.02	0.20	0.90	1.00

[a] Based on Bisschop et al. (2007)

gas-phase reactions, they are thought to be produced on dust grains. Hence, chemical differentiation can be ascribed to the differences in the chemical compositions of grain mantles. How such different chemical compositions arise is a long-standing problem and has not yet been resolved completely, despite significant efforts. Our current understanding of this situation is still based on models by Caselli et al. (1993) and Charnley et al. (1992), as outlined below.

Here, we consider the sudden temperature jump at the birth of a protostar. Before the onset of star formation, molecules continuously accrete onto dust grains, and grain-surface chemistry proceeds. In the above two models, differences in the physical conditions of the molecular accretion phase result in large differences in grain mantle compositions.

If the temperature at this phase is, for instance, as high as 40 K, CO is not depleted onto dust grains. Furthermore, the surface abundance of H atoms is low because their evaporation time is short. Hence, the formation of CH_3OH is strongly suppressed because of the low abundances of CO and H. The formation of more complex species is subsequently suppressed. Instead, heavy atoms such as C, O, and N can migrate over the adsorption site, and reactions among them efficiently produce C_nN, which is a parent molecule of nitrogen-bearing complex organic molecules. For instance, sequential hydrogenations of C_3N makes C_2H_5CN, although hydrogenation is slow due to the low surface abundance of H. In this case, nitrogen-bearing complex organic molecules can be abundant in the gas phase, when they are liberated into the gas phase after the birth of protostars.

In contrast, if the temperature in the molecular accretion phase is lower than 20 K, CO can be depleted onto dust grains. In this condition, the surface H abundance is relatively high, and CO is efficiently hydrogenated. Hence, CH_3OH and even more complex oxygen-bearing molecules will be formed. The formation of C_n and C_nN will be suppressed because of the low diffusion rates and the efficient hydrogenation of C and N. As a result, the formation of C_2H_5CN will be suppressed. In this case, oxygen-bearing complex organic molecules can be abundant in the gas phase, when they are liberated into the gas phase after the birth of protostars.

7.8 Carbon Chemistry in Low-Mass Star-Forming Regions: Hot Corino Chemistry and WCCC

Significant chemical diversity is seen in low-mass star-forming regions. One distinct case is hot corino chemistry, which is characterized by the rich existence of saturated complex organic molecules (Cazaux et al. 2003). Another distinct case is WCCC, which is characterized by the rich existence of unsaturated organic molecules such as carbon-chain molecules (Sakai et al. 2008a, b, c; Sakai and Yamamoto 2013). In hot corinos, complex organic molecules such as $HCOOCH_3$, $(CH_3)_2O$, and C_2H_5CN are supplied from grain mantles to the gas phase in the hot and dense regions around low-mass protostars. These complex organic molecules are thought to be produced on dust grains during the cold starless phase and the warm-up phase. This process is almost equivalent to that considered for hot cores in high-mass star-forming regions.

In contrast, WCCC is thought to be triggered by the sublimation of CH_4 in the warm and dense regions around low-mass protostars. When CH_4 is abundantly liberated into the gas phase, it reacts with C^+ to form various carbon-chain molecules:

$$C^+ + CH_4 \rightarrow {C_2H_3}^+ + H, \tag{7.13}$$

$${C_2H_3}^+ + e \rightarrow C_2H_2 + H \tag{7.14}$$

$$\rightarrow C_2H_2 + H + H, \tag{7.15}$$

$$C^+ + C_2H_2 \rightarrow C_3H^+ + H, \tag{7.16}$$

$$C_3H^+ + \ H_2 \rightarrow {C_3H_2}^+ + H, \tag{7.17}$$

$$C_3H^+ + \ H_2 \rightarrow {C_3H_3}^+ + h\nu, \tag{7.18}$$

$${C_3H_2}^+ + e \rightarrow \text{c-}C_3H,\ \text{l-}C_3H + H, \tag{7.19}$$

$${C_3H_3}^+ + e \rightarrow \text{c-}C_3H_2,\ \text{l-}C_3H_2 + H. \tag{7.20}$$

Further reactions with C^+ produce C_4 species. This mechanism can explain the rich carbon-chain molecules in L1527 and IRAS 15398-3359 (Sakai et al. 2008a, b, c; 2009a, b). The sublimation temperature of CH_4 is 25 K, which is lower than that of H_2O. Hence, WCCC is expected to occur in a warm region (T>25 K), which is larger than the size of hot corinos. Indeed, interferometric observations of L1527 show that a sudden enhancement in the abundance of carbon-chain molecules occurs at a radius of 1000 au, which corresponds to the size of the 25-K region based on the protostellar envelope model (Sakai et al. 2010a, b). A high abundance of CH_4 in L1527 is supported by the tentative detection of CH_3D (Sakai et al. 2012). The basic chemical processes discussed above are confirmed by the chemical model calculations by Aikawa et al. (2008), Hassel et al. (2008), and Harada and Herbst (2008).

An important feature of hot corino chemistry and WCCC is their exclusiveness; carbon-chain molecules are deficient in hot corinos, and complex organic molecules are deficient in WCCC sources. Both hot corino chemistry and WCCC are triggered by the sublimation of molecules from dust grains, and hence the difference in grain mantle compositions is mainly responsible for the origin of the difference. Although it is still controversial, the following scenario has been proposed (Sakai and Yamamoto 2013).

We consider low-mass star formation in a dense core initially formed from a diffuse cloud. If the starless core phase after shutting off the interstellar UV radiation is much longer than the free-fall time due to supporting mechanisms against gravitational contraction (e.g., magnetic fields and/or turbulence), most of the carbon atoms are converted into CO via gas-phase reactions. As a result, the CO molecules are depleted onto dust grains. The CO molecules on dust grains are subject to efficient hydrogenation in low-temperature conditions (10 K) to form CH_3OH and even more complex molecules. Atomic carbon may be depleted onto dust grains in the early phase of a starless core producing to some extent CH_4 by hydrogenation. However, CH_4 will be buried under the overwhelming CO and CH_3OH layers. Hence, CH_4 does not sublimate efficiently, even when the temperature exceeds the sublimation temperature of CH_4. Finally, H_2O ice cages sublimate at 100 K, and all of the species, including complex organic molecules, are liberated into the gas phase. This process realizes hot corino chemistry. At the same time, CH_4 will also be liberated. However, the liberation of CH_4 does not cause WCCC, because H_2O is so abundant that C^+ reacts with H_2O before reacting with CH_4. Thus, the exclusive nature of these processes can be explained.

If the starless core phase is close to the free-fall time with the absence of supporting mechanisms against gravitational contraction, a substantial portion of atomic carbon is depleted onto dust grains thereby yielding an abundance of CH_4 on dust grains by hydrogenation. In this case, CH_4 is expected to be present even on the outermost layer of grain mantles. However, the formation of CH_3OH and more complex molecules is relatively inefficient. When the temperature approaches the sublimation temperature of CH_4, CH_4 efficiently comes out of the gas phase and triggers WCCC.

The above scenario ascribes the origin of the chemical difference to the different durations of the starless core phase after the UV shield. This picture is consistent with the fact that deuterium fractionation tends to be higher for hot corino sources than WCCC sources (Sect. 7.4.1), because higher deuterium fractionation is expected for longer duration time of the cold phase (Sect. 6.9). If this scenario is the case, the chemical diversity in low-mass star-forming regions can be regarded as an expression of the past history of the star formation processes stored in the grain mantle compositions.

Let us summarize a unified picture of the carbon chemistry of low-mass star-forming regions. For the initial chemical condition of a prestellar core just before the onset of star formation (the formation of the first core), we assume a core temperature of 10 K, with all molecules, except for H_2, H, He, H^+, H_2^+, H_3^+, He^+, and their deuterated species, depleted onto dust grains. This assumption is simplistic but would be satisfied largely in the central parts of low-mass prestellar cores. After the onset of star formation, the temperature gradually increases. There are three major processes that alter the chemical compositions:

1. Sublimation of CO at 20 K. At 20 K, CO is sublimated from grain mantles, which restarts the basic carbon chemistry via reactions with He^+:

$$\mathrm{CO} + \mathrm{He}^+ \rightarrow \mathrm{C}^+ + \mathrm{O}. \tag{7.21}$$

The C^+ ions react with H_2 to form CH_2^+, as for carbon chemistry in molecular clouds. However, the $C^+ + H_2$ reaction is a slow radiative association process, and hence the production efficiency of carbon-chain molecules is not very high.

2. Sublimation of CH_4 at 25 K. At this temperature, CH_4 is liberated into the gas phase at least partly and reacts with C^+ to form various carbon-chain molecules. This process represents WCCC. To ensure the efficiency of this process, the fractional abundance of CH_4 relative to H_2 should be higher than that of other potential reactants of C^+ such as OH. This condition is satisfied if the fractional abundance of CH_4 is well above 10^{-7}. Indeed, this condition is fulfilled in L1527, as confirmed by the tentative detection of CH_3D (Sakai et al. 2012). If the fractional abundance of CH_4 is much lower than 10^{-7}, the WCCC effect is not pronounced. We note that at this temperature, H_2O is still frozen and does not contribute to depleting C^+ in this stage.
3. Sublimation of H_2O at 100 K. At this temperature, H_2O is sublimated, and hence the H_2O ice cages are broken. Other caged complex organic molecules will also be liberated. If complex organic molecules were formed abundantly during the cold phase and the warm-up phase, hot corino chemistry appears.

7.9 Outflow Shocks

In the early stages of protostellar evolution (Class 0 and Class I stages for low-mass protostars), bipolar molecular outflows are launched from protostars (Bachiller 1996; McKee and Ostriker 2007). A typical image of the low-mass protostar L1157 is shown in Fig. 7.9 (Umemoto et al. 1992; Mikami et al. 1992; Bachiller et al. 1997). This phenomenon is thought to be caused by the interplay between the

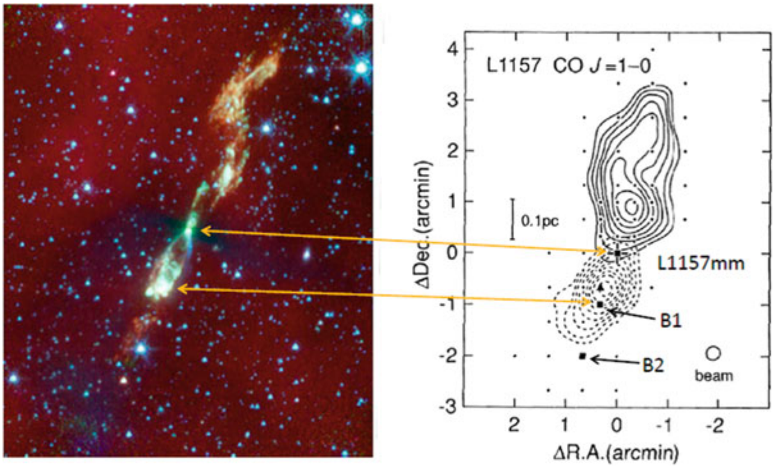

Fig. 7.9 (*Right panel*) Bipolar molecular outflow from the low-mass protostar (L1157 mm) (Reprinted with permission from Umemoto et al. (1992). Copyright 1992 American Astronomical Society). (*Left panel*) A *blue*-shifted lobe interacts with an ambient cloud and forms the shock regions, B1 and B2. The shock regions are visible in infrared observations (NASA home page: http://www.nasa.gov/mission_pages/spitzer/multimedia/spitzer20071129.html#backtoTop)

motion of accreting gas and a magnetic field and is responsible for transferring angular momentum from the accreting gas to outer space, allowing for further gravitational contraction. The outflow consists of two components. One component is an ionized jet that is strongly collimated and can be as fast as 100 km/s. This ionized jet can be seen in optical and infrared images. The other component is a molecular outflow, with a typical velocity of about a few tens of km/s. This molecular outflow can be traced by molecular emission at radio wavelengths. Outflows from protostars have been extensively investigated observationally and theoretically and shown to be the most characteristic phenomenon of star formation.

Outflows are supersonic flows of gas and hence cause strong shocks when they interact with ambient gas. The temperature of the shocked gas temporarily increases, and the gas is strongly compressed as the gas cools down. Hence, shocks significantly affect the chemical compositions of gas and grain mantles. In star-forming regions, shocks occur in various situations besides outflow impacts. Shock chemistry is therefore important for understanding the chemical compositions of star-forming regions. Moreover, shocks appear more often in interstellar clouds and are associated with cloud–cloud collisions, expansions of H II regions, and supernova expansions. Hence, the importance of shock chemistry is not restricted to star-forming regions.

We consider a collision of gas moving with a velocity, v, and a clump of gas at rest. If the velocity of the gas is lower than the speed of sound c_s, the density fluctuations caused by the collision simply propagate forward. However, if the velocity is higher than the speed of sound, a discontinuous change, called a shock, appears in physical conditions. The gas temperature suddenly increases at the discontinuity surface called the shock front, because the kinetic energy of the gas is converted into thermal energy. When the cooling of the gas is inefficient (an adiabatic shock), the maximum temperature attainable by the shock is given as:

$$T = \frac{5}{36 k_B} \mu v^2, \tag{7.22}$$

where μ is the mean mass of colliding particles (H_2 and He), v is the velocity of the colliding gas, and k_B is Boltzmann constant (Problem 3). We can rewrite this relation using representative values:

$$T = 3830 \left(\frac{v}{10 \mathrm{kms}^{-1}} \right)^2 \ \mathrm{K}. \tag{7.23}$$

Here, v can be regarded as the shock velocity. In this case, the maximum density ratio between the pre-shock gas and the post-shock gas is:

$$\frac{\rho_2}{\rho_1} = \frac{\gamma + 1}{\gamma - 1} = 6, \tag{7.24}$$

where ρ_1 and ρ_2 represent densities of the pre-shocked and post-shocked gas, and γ is the compression ratio, which is 7/5 for the diatomic gas. For the H_2 gas, the rotational energy levels are sparse, and, hence, the H_2 gas behaves as the atomic gas ($\gamma = 5/3$) at low temperature. In this case, the coefficient of Eq. (7.23) is 5160 K, and the ratio of Eq. (7.24) is 4. For the H atom gas, the coefficient of Eq. (7.23) is 2770 K.

The shocked layer will quickly be cooled by molecular and dust continuum emissions. As the shocked gas is cooled, the above density ratio increases. When the gas is cooled down to the original temperature of the pre-shocked gas, the density ratio becomes:

$$\frac{\rho_2}{\rho_1} = \left(\frac{v}{c_s}\right)^2 = M^2, \tag{7.25}$$

where M is called the Mach number, $M = v/c_s$. The shock structure is depicted schematically in Fig. 7.10.

Magnetic fields significantly reduce the shock effect. The shock structure is not discontinuous but is smoothed out. This phenomenon is due to the Alfven wave, which travels much faster than the speed of sound. This type of shock is called a C-shock; a conventional adiabatic shock is called a J-shock.

The temporal increase in the temperature and density will cause the following effects on chemical processes:

(1) Dissociation of molecules: When the temperature increases up to a few 1000 K at the shock front, some molecules are dissociated thermally. Dissociation of molecules is particularly significant in the J-shock.

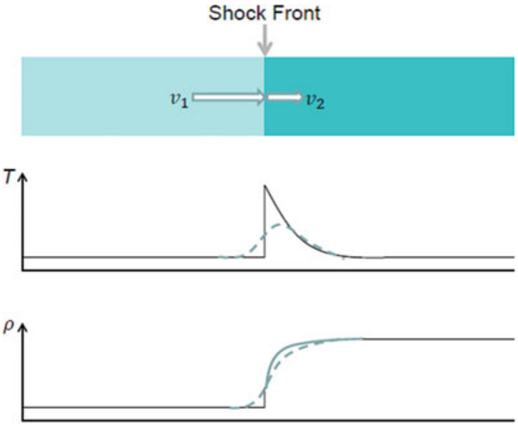

Fig. 7.10 Schematic of a one-dimensional shock front. *Solid lines* indicate the case without magnetic fields (J-shocks). The temperature suddenly increases at the shock front and gradually decreases in the post-shock region. The density increase is moderate at the shock front, while it increases in the post-shock region because of rapid cooling. The *dashed lines* represent the case with magnetic fields (C-shocks), where the Alfven wave mitigates the discontinuity

(2) Progress of endothermic reactions and reactions with activation barriers: In high-temperature conditions, these reactions can proceed efficiently. In particular, neutral–neutral reactions with activation barriers become important in shock regions. Good examples are the reactions forming H_2O:

$$O + H_2 \rightarrow OH + H \tag{7.26}$$

$$OH + H_2 \rightarrow H_2O + H. \tag{7.27}$$

(3) Desorption of molecules from dust grains: Grain mantle species are thermally sublimated and/or sputtered in the shock region. As a result, various complex species as well as nonvolatile molecules appear in the gas phase in shock regions. Furthermore, grain cores are also destroyed in strong shocks.

Shock chemistry has been invoked to explain the chemical compositions seen in high-mass star-forming regions. However, a detailed characterization of these compositions is difficult because of complex physical and chemical nature of these regions. A good target for investigating pure shock chemistry is the outflow shock found in the low-mass star-forming regions. An example is the shock region in L1157 (Fig. 7.9). In this region, outflows from the Class 0 protostar, IRAS 20386+6751, interact with ambient molecular gas clumps to form the shock regions (Umemoto et al. 1992). A strong shock can be confirmed from infrared H_2 emission (2 μ m) (e.g., Davis and Eisloffel 1995; Nisini et al. 2010). H_2 molecules are excited to the first vibrationally excited state by the shock, and subsequent quadrupole-allowed vibration–rotation transitions back to the ground state are observed in emission. The shock regions are well separated from the protostar, and hence their chemical composition can be studied without suffering from contamination from other star-forming activity. The shock region, L1157 B1, which is caused by an impact of the blue lobe of the outflow, is very rich in chemistry, as demonstrated by the spectral line survey shown in Fig. 7.11.

In L1157 B1, a strong line emission from SiO and CH_3OH is observed (Mikami et al. 1992; Bachiller et al. 1997). SiO is almost absent in molecular clouds, due most probably to the depletion onto dust grains. In shock regions, silicate grains are destroyed or sputtered, and SiO appears in the gas phase. Even if Si atoms are produced in break-up processes, Si atoms are efficiently converted to SiO through various reactions such as Si + OH (Herbst et al. 1989; Schilke et al. 1997b). In contrast, CH_3OH is an abundant in grain mantle, and it is sublimated or sputtered in shock regions. Indeed, the SiO and CH_3OH line emission is velocity shifted, which clearly indicates the interaction of the outflow with an ambient molecular cloud (Bachiller and Perez Gutierrez 1997; Mikami et al. 1992). The gas kinetic temperature is reported to be 200 K using high excitation lines of NH_3 (Umemoto et al. 1999), and the H_2 density was estimated to be 10^5 cm^{-3}. In this shock region, various molecules, including complex organic molecules such as CH_3CHO, $HCOOCH_3$, and C_2H_5OH, have been detected (Arce et al. 2008; Sugimura et al. 2011). These complex molecules are thought to be liberated from grain mantles.

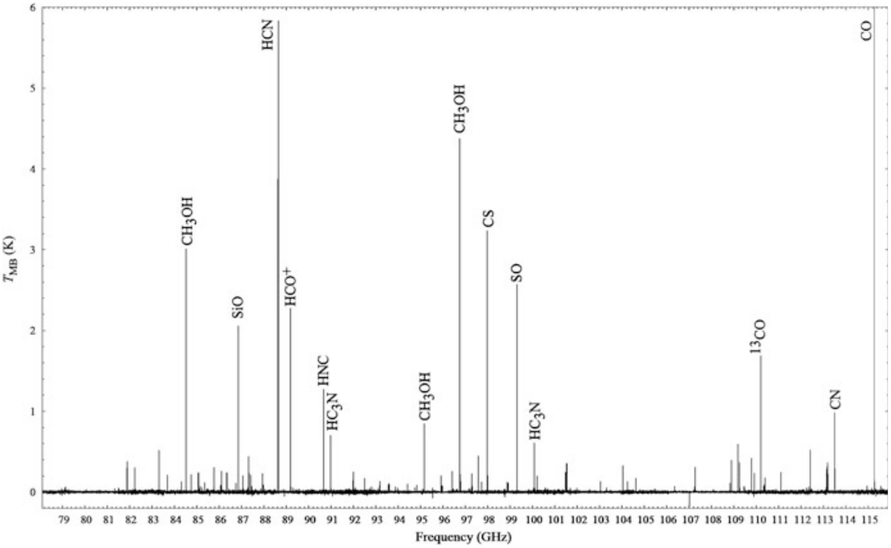

Fig. 7.11 Spectral line survey toward the shock region L1157 B1 with the Nobeyama 45m telescope (Reprinted with permission from Yamaguchi et al. (2012))

The upper limit on the duration time of the shock can be estimated by the dynamical timescale of the outflow. For L1157, the duration time is less than 10^4 year. For most molecules, it is difficult to produce complex organic molecules abundantly in the gas phase within this timescale. Hence, it is most likely that complex organic molecules come from dust grains.

As described above, an important role of shocks in astrochemistry is the desorption of grain mantle species. That is, the chemical compositions of grain mantles can be investigated through the chemical compositions of shock regions, although the gas-phase chemical processing may alter the chemical composition to some extent. Detections of $HCOOCH_3$ and C_2H_5OH in L1157 B1 mean that these molecules are already formed on the dust grains of an ambient cloud. It should be noted that C_2H_5CN and C_2H_3CN are not detected in L1157 B1. This fact may be related to the chemical differentiation occurring between oxygen-bearing and nitrogen-bearing complex organic molecules in star-forming regions. It has been proposed that the compact ridge of Orion KL, which is rich in oxygen-rich complex organic molecules, is a shocked region caused by outflows from high-mass protostars (Liu et al. 2002).

7.10 Phosphorous Chemistry in Star-Forming Regions

Only one phosphorous-bearing molecule, PN, is known in interstellar clouds, although some others, including CP, HCP, CCP, and PO, have been detected toward the envelopes of evolved stars (Guelin et al. 1990; Agundez et al. 2009; Halfen et al.

2008; Tenenbaum et al. 2007). PN has been detected in star-forming regions and in shock regions (e.g., Turner 1987; Ziurys 1987; Caux et al. 2011; Yamaguchi et al. 2012); it has not been seen in starless cores. If P atoms are in the gas phase, they will form PO through various reactions, and eventually PN (Millar 1991):

$$\mathrm{PO} + \mathrm{N} \rightarrow \mathrm{PN} + \mathrm{O}. \tag{7.28}$$

Hence, non-detection of PN in starless cores suggests that P atoms are contained in grain cores or depleted onto grain mantles.

In cold clouds, the P atoms on grain mantles are hydrogenated to form PH_3. Hence, grain mantles would contain PH_3 (Millar et al. 1991). In contrast, PH_3 is not formed in the gas phase from P atoms. When the temperature increases after the onset of star formation, PH_3 is sublimated along with H_2O. PH_3 will also be liberated into the gas phase by shocks. Then, PN is formed through reactions (Charnley and Millar 1994):

$$\mathrm{PH_3} + \mathrm{H} \rightarrow \mathrm{PH_2} + \mathrm{H_2}, \tag{7.29}$$

$$\mathrm{PH_2} + \mathrm{H} \rightarrow \mathrm{PH} + \mathrm{H_2}, \tag{7.30}$$

$$\mathrm{PH_2} + \mathrm{O} \rightarrow \mathrm{PH} + \mathrm{OH}, \tag{7.31}$$

$$\mathrm{PH_2} + \mathrm{O} \rightarrow \mathrm{HPO} + \mathrm{H}, \tag{7.32}$$

$$\mathrm{PH} + \mathrm{O} \rightarrow \mathrm{PO} + \mathrm{H}, \tag{7.33}$$

$$\mathrm{HPO} + \mathrm{O} \rightarrow \mathrm{PO} + \mathrm{OH}, \tag{7.34}$$

$$\mathrm{PH} + \mathrm{N} \rightarrow \mathrm{PN} + \mathrm{H}, \tag{7.35}$$

as well as reaction (7.28). Although the first two reactions (7.29 and 7.30) have activation barriers, they can proceed in the high-temperature conditions of star-forming regions and shock regions. PN is a stable molecule, and, hence, it is broken up by ionic dissociation or is depleted onto dust grains.

7.11 Photodissociation Regions

Molecular cloud surfaces that are illuminated by bright UV radiation from nearby stars show characteristic chemistry (Fig. 7.12, upper panel). This situation is often seen in both high-mass star-forming and cluster-forming regions, where stars born earlier illuminate parent clouds. The Orion Bar region is one example (Fig. 7.13). In molecular cloud surfaces, H atoms exist in a neutral form, in contrast with H II regions. Molecules are rapidly dissociated, and heavy atoms whose ionization potentials are lower than that of H atoms are ionized. The gas kinetic temperature can be as high as 100 K, because photoelectric heating is efficient. This situation is similar to diffuse clouds, although the density is typically higher than in diffuse clouds. Photodissociation and photoionization become inefficient with increasing

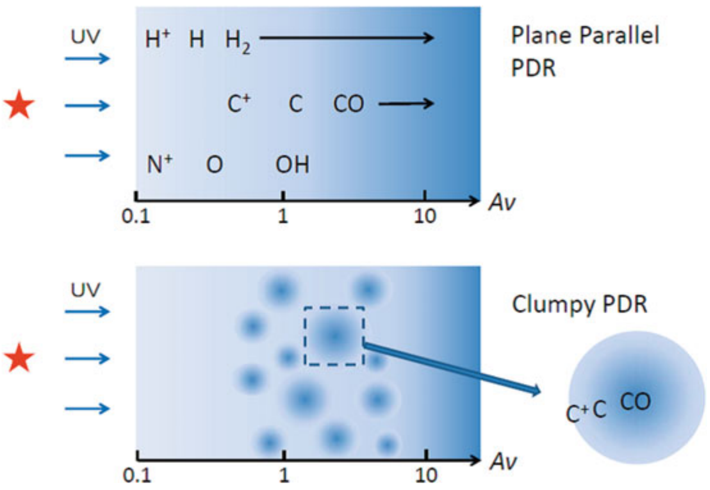

Fig. 7.12 Schematic of PDRs. *Upper panel*: Plane parallel (homogeneous) PDR. *Lower panel*: Clumpy (inhomogeneous) PDR

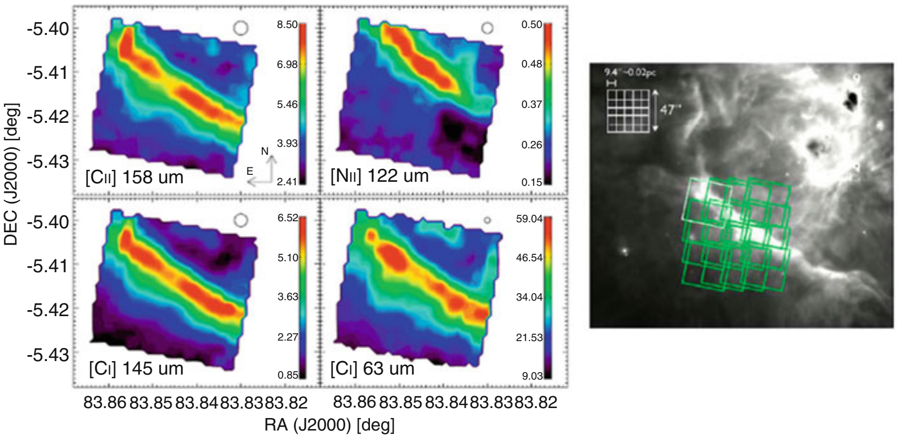

Fig. 7.13 (*Left*) *Herschel* PACS observation of the Orion Bar. The N II emission originates from the H II region; the C II and O I emission comes from the PDR. (*Right*) *Spitzer* view of the Orion Bar. The molecular cloud is illuminated by bright OB stars located at the *upper left* corner. The *green rectangles* are footprints of the PACS observations (Reprinted with permission from Bernard-Salas et al. (2012). Copyright 2012 European Southern Observatory)

depth from the surface, and the H/H_2 conversion occurs in a very thin layer in front of the molecular cloud, where the position of this layer depends on the strength of the UV radiation. Eventually, the physical and chemical conditions of a normal molecular cloud are realized when the UV radiation is well shielded. Such transition regions, where photon processes play an important role, are PDRs. The peripheries of molecular clouds, diffuse clouds, and translucent clouds are also regarded as PDRs in a general sense. In smaller scales, the cavity wall of a radiation-illuminated outflow from a protostar and the surface of a protoplanetary disk (Chap. 8) can also be a PDR.

If we assume a uniform steady-state cloud with, for simplicity, a plane-parallel configuration illuminated by UV radiation, carbon mostly exists as C^+ at the outermost surface. However, the major form of carbon is CO deep inside the molecular cloud. Neutral carbon atoms can exist in a thin layer between C^+ and CO. This picture is a simplified version of carbon chemistry in PDRs. Nonetheless, the most abundant oxygen-related species is O atoms, as long as the C/O ratio is less than unity. Hence, the fine structure lines of C^+, C, and O, as well as the rotational lines of CO, are good tracers of PDRs.

Physical and chemical models considering the thermal balance between heating and cooling processes, as well as chemical reaction networks (PDR models), have been extensively constructed under the assumption of steady-state conditions since the pioneering work of Tielens and Hollenbach (1985). PDR models are widely used for interpreting observational data, in particular for determining the strength of the UV field, H_2 density, and gas kinetic temperature (e.g., Kaufman et al. 1999; Le Petit et al. 2006).

However, the uniform plane-parallel model is thought to be too simplified. For instance, the distributions of C^+ and C have greater extent in the deep interiors of molecular clouds than is predicted by the steady-state uniform model. A clumpy cloud model has thus been proposed, where a molecular cloud is composed of dense clumps and a diffuse interclump medium (e.g., Stutzki et al. 1988; Meixner and Tielens 1993; Spaans 1996) (Fig. 7.12, lower panel). In this case, the external UV radiation can penetrate into the interior of the molecular cloud through the interclump medium (Fig. 7.14). Hence, the model has additional parameters such as the size of clumps, the H_2 density in clumps and interclump medium, the volume filling factor of the clumps, and the albedo of the clump surface.

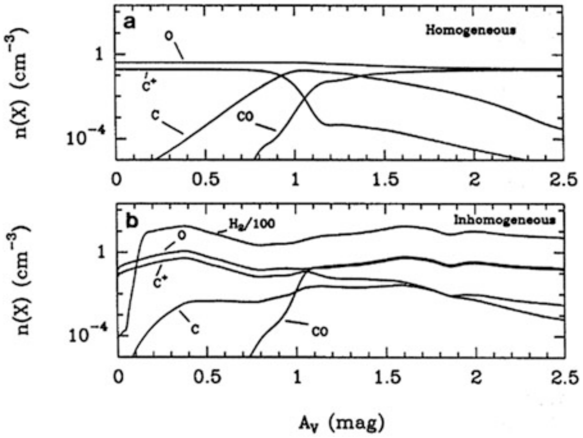

Fig. 7.14 Results from a PDR model for homogeneous (**a**) and inhomogeneous (**b**) clouds (Reprinted with permission from Spaans (1996). Copyright 1996 European Southern Observatory)

The timescale for chemical equilibrium in PDRs needs special attention. If the photoprocess is dominant, the dissociation timescale of molecules is determined by photodissociation (10^2–10^3 year). Because the formation timescale of molecules is usually as long as 10^5 year, the timescale for chemical equilibrium is determined by the photodissociation timescale and is approximately 10^2–10^3 year as in the case of diffuse clouds. This timescale is typically shorter than the dynamical timescale, and hence the steady-state approximation holds well. However, the effect of photodissociation becomes less significant inside of molecular clouds. Then, the primary destruction process is the ionic destruction, and its timescale becomes as long as 10^6 year. The timescale for chemical equilibrium is then as long as $10^5 - 10^6$ year, which is close to or even longer than the dynamical timescale of the cloud. Therefore, the steady-state condition is not fulfilled. These considerations indicate the importance of time-dependent chemistry in PDRs to ensure a complete understanding of chemical composition (e.g., Lee et al. 1996). The distribution of C^+ can be interpreted using the steady-state model, because C^+ mainly resides on the cloud surface. In contrast, the distribution of C should be considered using the time-dependent model, because C atoms can reside in the deep interiors of molecular clouds (Maezawa et al. 1999; Ikeda et al. 2001; Kamegai et al. 2003).

In some cases, PDRs harbor rich chemistry. The best example is the Horsehead Nebula in the Orion B molecular cloud. This PDR is illuminated by the nearby B star located on the western side of the Orion B molecular cloud. Various carbon-chain molecules such as C_2H, c-C_3H, l-C_3H, c-C_3H_2, l-C_3H_2, C_4H, and C_6H are detected in this cloud (e.g., Pety et al. 2005; Agundez et al. 2008). Detection of C_3H^+ was claimed by Pety et al. (2012), which was later verified by the laboratory spectroscopic study by Brunken et al. (2014). These molecules reside in a dense clump just behind the cloud edge. Rich carbon-chain molecules seem to be related to rich C^+ and C in PDRs. Because the steady-state PDR model cannot explain the abundances of these molecules, the possibility of photodestruction of PAHs has been argued (Pety et al. 2005).

7.12 Polycyclic Aromatic Hydrocarbons (PAHs) and PDRs

In PDRs, infrared emission bands of polycyclic aromatic hydrocarbons (PAHs) are observed. PAHs are carbonaceous dust particles consisting of two or more fused aromatic rings and are well known, for instance, as by-products of combustion processes of oil, charcoal, and woods. They are also recognized as important constituents of small dust grains in interstellar clouds, which are identified as the most probable carrier of the unidentified infrared (UIR) bands (e.g., Gillett et al. 1973; Russel et al. 1978). Figure 7.15 shows a schematic drawing of a PAH, as well as the two simple PAHs, anthracene and coronene. Usually, interstellar PAHs are thought to have about 50 or more carbon atoms each and are often aggregated with each other. Their origin is most likely from carbon-rich evolved stars, but their production from carbon-chain molecules in molecular clouds is also proposed.

Fig. 7.15 (**a**) A schematic example of a polycyclic aromatic hydrocarbon (PAH) consisting of fused aromatic (e.g., benzene) rings. (**b**) Anthracene as a simple PAH. (**c**) Coronene as another simple PAH

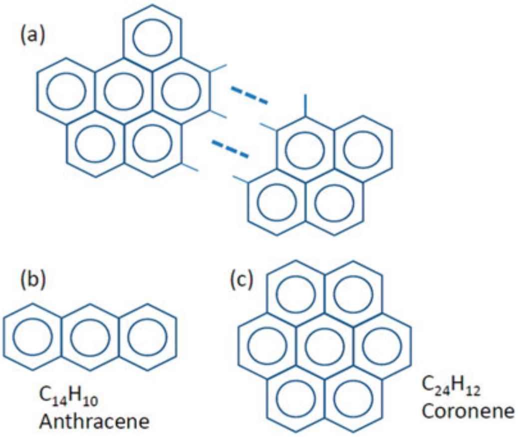

Fig. 7.16 Schematic illustration of the mechanism of the PAH emission in the infrared regime. First, a PAH is excited to the high electronic state by absorbing the UV photon, and then the energy is transferred to high vibrational states of lower electronic states including the ground electronic state. The infrared emission occurs during subsequent cascading of the vibrational states down to the ground state

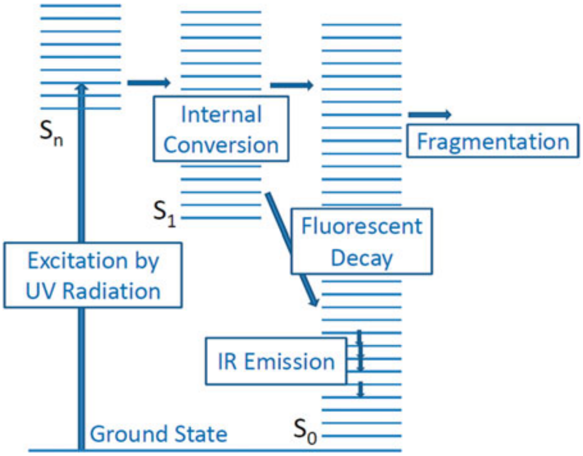

The infrared emission of PAHs is caused by UV excitation, as illustrated in Fig. 7.16. When PAHs are irradiated by UV radiation, they are excited to a high electronic state. Such electronic states of PAHs are usually dark, implying that they do not emit fluorescent light in relaxing to lower electronic states. Instead, the electronic energy is transferred to high vibrational states of lower (singlet) electronic states including the electronic ground state by internal conversion, because of the very high density of such vibrational states. The molecule then releases its energy as successive vibrational transitions in the infrared regime during the cascade process down to the ground state. The most prominent emission features appear at 3.3, 6.2, 7.7, 8.6, and 11.2 μ m (Fig. 7.17), although additional weak features are also known (Tielens 2008; Peters, 2014). Hence, these emissions of PAHs are widely observed in the region illuminated by UV radiation, including PDRs around star-forming regions, T-Tauri stars (Chap. 8), diffuse clouds (Chap. 4), planetary nebulae, and external galaxies (see papers in Joblin and Tielens 2011).

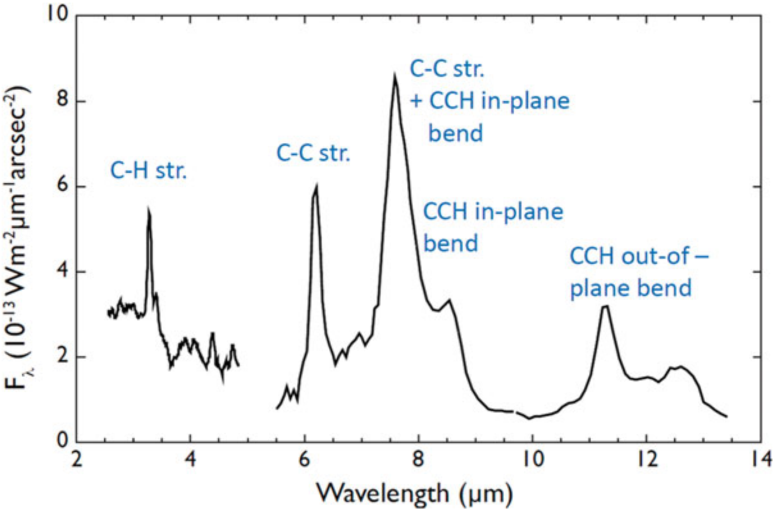

Fig. 7.17 An example of the spectrum of PAH observed toward the Galactic plane (ℓ =312° and $b = 0.5°$; averaged over the 5 × 40 arcsec^2 area) observed with *AKARI* (Onaka, T. and Sakon, I, private communication)

Because interstellar PAHs are a mixture of various PAHs, the observed emission feature (peak wavelength, intensity, and shape) changes from source to source. Moreover, interstellar PAHs are often ionized and/or subject to a partial loss of hydrogen atoms by UV radiation, which significantly affect the emission spectrum. Hence, assignments of the spectral features are not based on individual PAHs but on the characteristic wavelengths of vibrational modes. The 3.3, 6.2, 7.7, 8.6, and 11.2- μ m features are assigned to the C–H stretching mode, the C–C stretching mode, the combination mode of C–C stretching and C–H in-plane bending, the C–H in-plane bending mode, and the C–H out-of-plane bending mode, respectively. Although PAH emission features are different from source to source, it is known that the 3.3 and 11.2- μ m emission intensities are well correlated, because both bands are related to the C–H bond (e.g., Hony et al. 2001). Intensity ratios of the different bands are useful indicators for ionization state, the UV radiation strength, and dust temperature. These unique features of PAH emissions make them very useful tools in investigating distributions, physical conditions, and radiation fields of PDRs. The details of the PAH spectra are beyond the scope of this book. They are described in several good review articles (Tielens 2005, 2008; Joblin and Tielens 2011; Peeters 2011, 2014).

Problems

7.1 Evaporation of molecules from grain mantle affects the chemical composition. In particular, molecular ions are sensitive to the evaporation of particular species. In this regard, answer the following questions.

(a) In a starless core just before the birth of protostars, most molecules except for H_2 are depleted onto dust grains. Hence, N_2H^+ is mainly destroyed by electrons. Estimate the timescale for destruction of N_2H^+ by electrons.

Assume that the H_2 density and temperature are 10^6 cm^{-3} and 10 K, respectively. The recombination rate coefficient of N_2H^+ is $3 \times 10^{-7}(T/300\ K)^{-0.74}$ cm^3 s^{-1}.

(b) After the birth of protostars, the temperature increases, and CO frozen on dust grains is liberated into the gas phase. In this case, show that the main break-up process for N_2H^+ is the ion–molecule reactions with CO, by comparing the timescale of the ion–molecule reaction with that of the recombination reaction. Assume that the H_2 density and temperature are 10^6 cm^{-3} and 20 K, respectively. The reaction rate coefficient of $N_2H^+ + CO$ is assumed to be a typical Langevin rate coefficient (1×10^{-9} cm^3 s^{-1}).

(c) When the temperature is further increased to about 100 K, H_2O ice sublimates. Then, HCO^+ ions are broken up via reactions with H_2O. How much H_2O is necessary to ensure that the break-up rate of HCO^+ by H_2O exceeds that by electrons? The reaction rate coefficient of $HCO^+ + H_2O$ is assumed to be a typical Langevin rate coefficient (1×10^{-9} cm^3 s^{-1}). Assume that the H_2 density and temperature are 10^6 cm^{-3} and 100 K, respectively.

7.2 Heavy deuterium fractionation is often observed in star-forming regions. This fractionation is at odds with the lower deuterium fractionation expected for higher-temperature conditions. Hence, the deuterated molecules formed in the late starless core phase or liberated from dust grains should survive for a while after the birth of protostars.

(a) Estimate the lifetime of neutral deuterated molecules such as DCN and HDCO assuming an H_2 density of 10^6 cm^{-3} and a temperature of 60 K. Assume that neutral species are broken up through ionic dissociation with He^+.

(b) Show that the lifetime of deuterated molecular ions such as DCO^+ and DN_2^+ is much shorter than that of neutral species.

7.3 Consider the one-dimensional adiabatic shock shown in Fig. 7.10. The velocity, density, and temperature of the upper and lower streams are denoted by u_1, ρ_1, and T_1, and u_2, ρ_2, and T_2, respectively. Then, the following equations hold:

$$\rho_1 u_1 = \rho_2 u_2, \tag{7.36}$$

$$p_1 + \rho_1 u_1^2 = p_2 + \rho_2 u_2^2, \tag{7.37}$$

and

$$u_1\left(\frac{1}{2}\rho_1 u_1^2 + U_1\right) + u_1 p_1 = u_2\left(\frac{1}{2}\rho_2 u_2^2 + U_2\right) + u_2 p_2, \tag{7.38}$$

where p_1 and p_2 are the pressures in the upper and lower streams, respectively. The pressures are related to the internal energies U_1 and U_2:

$$U_i = \frac{p_i}{\gamma - 1} \quad (i = 1, 2). \tag{7.39}$$

Here, γ is the heat capacity ratio. Equations (7.36), (7.37), and (7.38) represent the conservation laws of mass, momentum, and energy, respectively.

(a) Substitute U_i of Eq. (7.38) by using Eq. (7.39) and combine the result with Eq. (7.36). Then, show that the following relation holds:

$$u_1^2 + \frac{2\gamma}{\gamma - 1} p_1 = u_2^2 + \frac{2\gamma}{\gamma - 1} p_2. \tag{7.40}$$

(b) Using Eqs. (7.37) and (7.40), omit p_2 and derive the following second-order equation:

$$(\gamma + 1)x^2 - 2\gamma\left(1 + \frac{1}{M^2}\right)x + \frac{2\gamma}{M^2} + \gamma - 1 = 0, \tag{7.41}$$

where $x = u_2/u_1$, $M = u_1/c_s$, and $c_s = \sqrt{p_1/\rho_1}$. Here, M is the Mach number.

(c) By solving Eq. (7.41), derive the ρ_2/ρ_1 ratio.

(d) Assume an ideal gas and the condition $p_1 \ll p_2$. Show that the temperature is increased at the shock front in accordance with:

$$T = \frac{2(\gamma - 1)}{k_B(\gamma + 1)^2} \mu u_1^2.$$

Here, μ is a particle mass and k_B Boltzmann's constant. For a diatomic molecule gas and an atomic gas, γ is 7/5 and 5/3, respectively.

(e) Calculate the coefficient of Eq. (7.23) for the H_2 gas. Also calculate it for the atomic H gas.

7.4 Consider C^+ in the one-dimensional PDR. For simplicity, C^+ is produced by the photoionization of C and is lost by radiative electron recombination, whose rate is given in Table 4.6. Other reactions are not considered. Hydrogen is assumed to be in molecular form.

(a) Calculate the C^+ abundance relative to H_2 as a function of A_v for illumination by normal interstellar UV radiation ($G_0 = 1$). Here, the H_2 density and the temperature are assumed to be 10^4 cm^{-3} and 100 K. A steady-state condition is assumed. Repeat it for illuminations by UV radiation higher than the normal UV radiation by factors of 100 and 10,000.

(b) The thickness of the C^+ layer in the PDR can roughly be defined as A_v at which the C^+ and C abundances are equal to each other. Show that the thickness depends on the ratio of the strength of the UV radiation (G_0) to the H_2 density in this simple picture.

References

M. Agundez, J. Cernicharo, M. Guelin, Astrophys. J. **662**, L29 (2007)

Y. Aikawa, V. Wakelam, R.T. Garrod, E. Herbst, Astrophys. J. **674**, 984 (2008)

Y. Aikawa, V. Wakelam, F. Hersant, R.T. Garrod, E. Herbst, Astrophys. J. **760**, 40 (2012)

Y. Aikawa, Chem. Rev. **113**, 8961 (2013)

M. Agundez, J. Cernicharo, M. Guelin, M. Gerin, M.C. McCarthy, P. Thaddeus, Astron. Astrophys. **478**, L19 (2008)

P. Andre, D. Ward-Thompson, B. Barsony, Astrophys. J. **406**, 122 (1993)

I. Appenzeller, R. Mundt, Astron. Astrophys. Rev. **1**, 291 (1989)

H. Arce, J. Santiago-Garcia, J.K. Jørgensen, M. Tafalla, R. Bachiller, Astrophys. J. **681**, L21 (2008)

R. Bachiller, Ann. Rev. Astron. Astrophys. **34**, 111 (1996)

R. Bachiller, M. Pirez Gutierrez, Astrophys. J. **487**, L93 (1997)

J. Bally, W.D. Langer, A.A. Stark, R. Wilson, Astrophys. J. **312**, L45 (1987)

P.J. Benson, P.C. Myers, Astrophys. J. Suppl. **71**, 89 (1989)

J. Bernard-Salas et al., Astron. Astrophys. **538**, A37 (2012)

H. Beuther, Q. Zhang, L.J. Greenhill, M.J. Reid, D. Wilner, E. Keto, H. Shinnaga, P.T.P. Ho, J.M. Moran, S.-Y. Liu, C.-M. Chang, Astrophys. J. **632**, 355 (2005)

S.E. Bisschop, J.K. Jørgensen, E.F. van Dishoeck, E.B.M. de Wachter, Astron. Astrophys. **465**, 913 (2007)

G.A. Blake, E.C. Sutton, C.R. Masson, T.G. Phillips, Astrophys. J. **315**, 612 (1987)

G.A. Blake, E.F. van Dishoeck, D.J. Jansen, T.D. Groesbeck, L.G. Mundy, Astrophys. J. **428**, 680 (1994)

I.A. Bonnell, C.J. Clarke, M.R. Bate, J.E. Pringle, Mon. Not. R. Astr. Soc. **324**, 573 (2001)

S. Bottinelli, C. Ceccarelli, B. Lefloch, J.P. Williams, A. Castets, E. Caux, S. Cazaux, S. Maret, B. Parise, A.G.G.M. Tielens, Astrophys. J. **615**, 354 (2004a)

S. Bottinelli, C. Ceccarelli, R. Neri, J.P. Williams, E. Caux, S. Cazaux, B. Lefloch, S. Maret, A.G.G.M. Tielens, Astrophys. J. **617**, L69 (2004b)

S. Brunken, L. Kluge, A. Stoffels, O. Asvany, S. Schlemmer, Astrophys. J. **783**, L4 (2014)

P. Caselli, T.I. Hasegawa, E. Herbst, Astrophys. J. **408**, 548 (1993)

E. Caux et al., Astron. Astrophys. **532**, 23 (2011)

S. Cazaux, A.G.G.M. Tielens, C. Ceccarelli, A. Castets, V. Wakelam, E. Caux, B. Parise, D. Teyssier, Astrophys. J. **593**, L51 (2003)

C. Ceccarelli, A. Castets, L. Loinard, E. Caux, A.G.G.M. Tielens, Astron. Astrophys. **338**, L43 (1998)

R. Cesaroni, R. Neri, L. Olmi, L. Testi, C.M. Walmsley, P. Hofner, Astron. Astrophys. **434**, 1039 (2005)

R. Cesaroni, D. Galli, R. Neri, C.M. Walmsley, Astron. Astrophys. **566**, A73 (2014)

C.J. Chandler, C.L. Brogan, Y.L. Shirley, L. Loinard, Astrophys. J. **632**, 371 (2005)

N. Chapman, L.G. Mundy, S.-P. Lai, N.J. Evans II, Astrophys. J. **690**, 496 (2009)

S.B. Charnley, A.G.G.M. Tielens, T.J. Millar, Astrophys. J. **399**, L71 (1992)

S.B. Charnley, T.J. Millar, Mon. Not. R. Astron. Soc. **270**, 570 (1994)

S.B. Charnley, S.D. Rogers, P. Ehrenfreund, Astron. Astrophys. **378**, 1024 (2001)

M.P. Collings, M.A. Anderson, R. Chen, J.W. Dever, S. Viti, D.A. Williams, M.R.S. McCoustra, Mon. Not. R. Astr. Soc. **354**, 1133 (2004)

C. Comito, P. Schilke, T.G. Phillips, D.C. Lis, F. Motte, D. Mehringer, Astrophys. J. Suppl. **156**, 127 (2005)

N.R. Crockett, E.A. Bergin, J.L. Neill, et al., Astrophys. J. **787**, 112 (2014)

C.J. Davis, J. Eisloffel, Astron. Astrophys. **300**, 851 (1995)

J.E. Dickens, W.M. Irvine, R.L. Snell, E.A. Bergin, F.P. Schloerb, P. Pratap, M.P. Miralles, Astrophys. J. **542**, 870 (2000)

C. Dougados, P. Lena, S.T. Ridgway, J.C. Christou, R.G. Probst, Astrophys. J. **406**, 112 (1993)

M.P. Egan, R.F. Shipman, S.D. Price, S.J. Carey, F.O. Clark, M. Cohen, Astrophys. J. **494**, L199 (1998)

G.B. Esplugues, B. Tercero, J. Cernicharo, J.R. Goicoechea, A. Palau, N. Marcelino, T.A. Bell, Astron. Astrophys. **556**, 143 (2013)

N.J. Evans II et al., Astrophys. J. Suppl. **181**, 321 (2009)

F. Fontani, I. Pascucci, P. Caselli, F. Wyrowski, R. Cesaroni, C.M. Walmsley, Astron. Astrophys. **470**, 639 (2007)

E.D. Feigelson, T. Montmerle, Ann. Rev. Astron. Astrophys. **37**, 363 (1999)

F. Fontani, P. Caselli, A. Crapsi, R. Cesaroni, S. Molinari, L. Testi, J. Brand, Astron. Astrophys. **460**, 709 (2011)

F. Fontani, A. Giannetti, M.T. Beltran, R. Dodson, M. Rioja, J. Brand, P. Caselli, R. Cesaroni, Mon. Not. R. Astron. Soc. **423**, 2342 (2012)

N. Furukawa, J.R. Dawson, A. Ohama, A. Kawamura, N. Mizuno, T. Onishi, Y. Fukui, Astrophys. J. **696**, L115 (2009)

R.T. Garrod, E. Herbst, Astron. Astrophys. **457**, 927 (2006)

R.T. Garrod, Astrophys. J. **778**, 158 (2013)

R.T. Garrod, S.L. Widicus Weaver, Chem. Rev. **113**, 8539 (2013)

W.D. Geppert et al., Fraday Discuss. **133**, 177 (2006)

R. Genzel, J. Stutzki, Ann. Rev. Astron. Astrophys. **27**, 41 (1989)

F.C. Gillett, W.J. Forrest, K.M. Merril, Astrophys. J. **183**, 87 (1973)

L. Gomez, L.F. Rodriguez, L. Loinard, S. Lizano, A. Poveda, C. Allen, Astrophys. J. **635**, 1166 (2005)

M. Guelin, J. Cernicharo, G. Paubert, B.E. Turner, Astron. Astrophys. **230**, L9 (1990)

K. Hachisuka, A. Brunthaler, K.M. Menten, M.J. Reid, H. Imai, Y. Hagiwara, M. Miyoshi, S. Horiuchi, T. Sasao, Astrophys. J. **645**, 337 (2006)

D.T. Halfen, D.J. Clouthier, L.M. Ziurys, Astrophys. J. **677**, L101 (2008)

N. Harada, E. Herbst, Astrophys. J. **685**, 272 (2008)

L. Hartmann, in *Protostellar Jet in Context*, eds. By K. Tsinganos, T. Ray, and M. Stute (Springer, Berlin, 2009), p. 23

G.E. Hassel, E. Herbst, R.T. Garrod, Astrophys. J. **681**, 1385 (2008)

C. Hayashi, PASJ. **13**, 450 (1961)

C. Hayashi, ARAZA **4**, 171 (1966)

E. Herbst, E.F. van Dishoeck, Ann. Rev. Astron. Astrophys. **47**, 427 (2009)

F.P. Helmich, D.J. Jansen, T. de Graauw, T.D. Groesbeck, E.F. van Dishoeck, Astron. Astrophys. **283**, 626 (1994)

F.P. Helmich, E.F. van Dishoeck, Astron. Astrophys. (Suppl.) **124**(205) (1997)

E. Herbst, T.J. Millar, S. Wlodek, D.K. Bohme, Astron. Astrophys. **222**, 205 (1989)

T. Hirota et al., Publ. Astron. Soc. Japan **59**, 897 (2007)

S. Hony, C. Van Kerckhoven, E. Peeters, A.G.G.M. Tielens, D.M. Hudgins, L.M. Allamandola, Astron. Astrophy. **370**, 1030 (2001)

T. Hosokawa, H.W. Yorke, K. Omukai, Astrophys. J. **721**, 478 (2010)

M. Ikeda, T. Oka, K. Tatematsu, Y. Sekimoto, S. Yamamoto, Astrophys. J. Suppl. **139**, 467 (2001)

C. Joblin, A. G. G. M. Tielens (eds.), ‘PAHs and the Universe: A Symposium to Celebrate the 25th Anniversary of the PAH Hypothesis’, EAS Publications Series, Vol. 46 (2011).

J.K. Jørgensen, T.L. Bourke, P.C. Myers, F.L. Schoier, E.F. van Dishoeck, D.J. Wilner, Astrophys. J. **632**, 973 (2005)

J.K. Jørgensen, T.L. Bourke, Q. Nyugen Lu’o’ng, S. Takakuwa, Astron. Astrophys. **534**, A100 (2011)

J.K. Jørgensen, R. Visser, N. Sakai, E.A. Bergin, C. Brinch, D. Harsono, J.E. Lindberg, E.F. van Dishoeck, S. Yamamoto, S.E. Bisschop, M.V. Persson, Astrophys. J. **779**, L22 (2013)

K. Kamegai et al., Astrophys. J. **589**, 378 (2003)

M.J. Kaufman, M.G. Wolfire, D.J. Hollenbach, M.L. Luhman, Astrophys. J. **527**, 795 (1999)

Y.-J. Kuan, H.-C. Huang, S.B. Charnley, N. Hirano, S. Takakuwa, D.J. Wilner, S.-Y. Liu, N. Ohashi, T.L. Bourke, C. Qi, Q. Zhang, Astrophys. J. **616**, L27 (2004)

C.J. Lada, B.A. Wilking, Astrophys. J. **287**, 610 (1984)

Lada, C.J., IAU Symp. 115, in *Star Forming Regions,* ed. By M. Peimbert, J. Jugaku, (Kluwer, Dordrecht, 1987, 1

R.B. Larson, Mon. Not. R. Astron. Soc. **145**, 271 (1969)

F. Le Petit, C. Nehme, J. Le Bourlot, E. Roueff, Astrophys. J. Suppl. **164**, 506 (2006)

H.H. Lee, E. Herbst, G. Pineau des Forets, E. Roueff, J. Le Bourlot, Astron. Astrophys. **311**, 690 (1996)

J.E. Lindberg, J.K. Jørgensen, Astron. Astrophys. **548**, A24 (2012)

J.E. Lindberg, J.K. Jørgensen, J.D. Green, G.J. Herczeg, O. Dionatos, N.J. Eans II, A. Karska, S.F. Wampfler, Astron. Astrophys. **565**, A29 (2014)

S.-Y. Liu, J.M. Girart, A. Remijan, L.E. Snyder, Astrophys. J. **576**, 255 (2002)

M.N. Machida, T. Hosokawa, Mon. Not. R. Astr. Soc. **431**, 1719 (2013)

H. Maezawa et al., Astrophys. J. **524**, L129 (1999)

H. Masunaga, S.M. Miyama, S. Inutsuka, Astrophys. J. **495**, 346 (1998)

C.F. McKee, J.C. Tan, Astrophys. J. **585**, 850 (2003)

C.F. McKee, E.C. Ostriker, Ann. Rev. Astron. Astrophys. **45**, 565 (2007)

D.E. McLaughlin, R.E. Pudritz, Astrophys. J. **476**, 750 (1996)

M. Meixner, A.G.G.M. Tielens, Astrophys. J. **405**, 216 (1993)

H. Mikami, T. Umemoto, S. Yamamoto, S. Saito, Astrophys. J. **392**, L87 (1992)

T.J. Millar, Astron. Astrophys. **242**, 241 (1991)

Y.C. Minh, W.M. Irvine, L.M. Ziurys, Astrophys. J. **345**, L63 (1989)

A. Mizuno, Y. Fukui, T. Iwata, S. Nozawa, T. Takano, Astrophys. J. **356**, 184 (1990)

B. Nisini, T. Giannini, D.A. Neufeld, Y. Yuan, S. Antoniucci, E.A. Bergin, Astrophys. J. **724**, 69 (2010)

H. Nomura, T.J. Millar, Astron. Astrophys. **414**, 409 (2004)

K.I. Oberg, N. van der Marel, L.E. Kristensen, E.F. van Dishoeck, Astrophys. J. **740**, 14 (2011)

N. Ohashi, M. Hayashi, P.T.P. Ho, M. Momose, Astrophys. J. **475**, 211 (1997)

S. Okumura, T. Yamashita, S. Sako, T. Miyata, M. Honda, H. Kataza, Y.K. Okamoto, Publ. Astron. Soc. Japan **63**, 823 (2011)

B. Parise, C. Ceccarelli, A.G.G.M. Tielens, E. Herbst, B. Lefloch, E. Caux, A. Castets, I. Mukhopadhyay, L. Pagani, L. Loinard, Astron. Astrophys. **393**, L49 (2002)

B. Parise, A. Castets, E. Herbst, E. Caux, C. Ceccarelli, I. Mukhopadhyay, A.G.G.M. Tielens, Astron. Astrophys. **416**, 159 (2004)

B. Parise, C. Ceccarelli, A.G.G.M. Tielens, A. Castets, E. Caux, B. Lefloch, S. Maret, Astron. Astrophys. **453**, 949 (2006)

E. Peeters, in *The Molecular Universe*, eds. By J. Cernicharo, R. Bachiller, Proceedings IAU Symposium No. 280, p. 149 (2011).

E. Peeters, in *The Diffuse Interstellar Bands*, eds. By J. Cami, N.L.J. Cox, Proceedings IAU Symposium No. 297, p. 187 (2014)

M. Perault et al., Astron. Astrophys. **315**, L165 (1996)

J.E. Pineda et al., Astron. Astrophys. **544**, L7 (2012)

J. Pety, D. Teyssier, D. Fosse, M. Gerin, E. Roueff, A. Abergel, E. Habart, J. Cernicharo, Astron. Astrophys. **435**, 885 (2005)

J. Pety et al., Astron. Astrophys. **548**, 68 (2012)

H. Roberts, T.J. Millar, Astron. Astrophys. **471**, 849 (2007)

R.W. Russell, B.T. Soifer, S.P. Willner, Astrophys. J. **220**, 568 (1978)

N. Sakai, T. Sakai, S. Yamamoto, PASJ **58**, L15 (2006a)

N. Sakai, T. Sakai, Y. Osamura, S. Yamamoto, Astrophys. J. **667**, L65 (2007a)

N. Sakai, T. Sakai, T. Hirota, S. Yamamoto, Astrophys. J. **672**, 371 (2008c)

N. Sakai, T. Sakai, S. Yamamoto, Astrophys. J. **673**, L71 (2008a)

N. Sakai, T. Sakai, S. Yamamoto, Astrophys. Space Sci. **313**, 153 (2008b)

N. Sakai, T. Sakai, T. Hirota, M. Burton, S. Yamamoto, Astrophys. J. **697**, 769 (2009a)

N. Sakai, T. Sakai, T. Hirota, S. Yamamoto, Astrophys. J. **702**, 1025 (2009b)

N. Sakai, T. Sakai, T. Hirota, S. Yamamoto, Astrophys. J. **722**, 1633 (2010a)

N. Sakai, Y.L. Shirley, T. Sakai, T. Hirota, Y. Watanabe, S. Yamamoto, Astrophys. J. **758**, L4 (2012)

N. Sakai, S. Yamamoto, Chem. Rev. **113**, 8981 (2013)

T. Sakai, T. Oka, S. Yamamoto, Astrophys. J. **649**, 268 (2006b)

T. Sakai, T. Oka, S. Yamamoto, Astrophys. J. **662**, 1043 (2007b)

T. Sakai, N. Sakai, T. Hirota, S. Yamamoto, Astrophys. J. **714**, 1658 (2010b)

P. Schilke, T.D. Groesbeck, G.A. Blake, T.G. Phillips, Astrophys. J. Suppl. **108**, 301 (1997a)

P. Schilke, C.M. Walmsley, G. Pineaudes Forets, D.R. Flower, Astron. Astrophys. **321**, 293 (1997b)

F.L. Schoier, J.K. Jørgensen, E.F. van Dishoeck, G.A. Blake, Astron. Astrophys. **390**, 1001 (2002)

R. Simon, J.M. Jackson, J.M. Rathborne, E.T. Chambers, Astrophys. J. **639**, 227 (2006)

B.N. Sitarski, M.R. Morris, J.R. Lu, G. Duchene, A. Stolte, E.E. Becklin, A.M. Ghez, H. Zinnecker, Astrophys. J. **770**, 134 (2013)

M. Spaans, Astron. Astrophys. **307**, 201 (1996)

M. Sugimura et al., Publ. Astron. Soc. Japan **63**, 459 (2011)

J. Stutzki, G.J. Stacey, R. Genzel, A.I. Harris, D.T. Jaffe, J.B. Lugten, Astrophys. J. **332**, 379 (1988)

F. Shu, J. Najita, E. Ostriker, F. Wilkin, S. Ruden, S. Lizano, Astrophys. J. **429**, 781 (1994a)

F. Shu, J. Najita, S. Ruden, S. Lizano, Astrophys. J. **429**, 797 (1994b)

H. Suzuki, S. Yamamoto, M. Ohishi, N. Kaifu, S. Ishikawa, Y. Hirahara, S. Takano, Astrophys. J. **392**, 551 (1992)

D.A. Swade, Astrophys. J. **345**, 828 (1989a)

D.A. Swade, Astrophys. J. Suppl. **71**, 219 (1989b)

E.D. Tenenbaum, N.J. Woolf, L.M. Ziurys, Astrophys. J. **666**, L29 (2007)

B. Tercero, J. Cernicharo, J.R. Pardo, J.R. Goicoechea, Astron. Astrophys. **517**, A96 (2010)

B. Tercero, L. Vincent, J. Cernicharo, S. Viti, N. Marcelino, Astron. Astrophys. **528**, 26 (2011)

A.R. Tieftrunk, S.T. Megeath, T.L. Wilson, J.T. Rayner, Astron. Astrophys. **336**, 991 (1998)

A.G.G.M. Tielens, D. Hollenbach, Astrophys. J. **291**, 722 (1985)

A.G.G.M. Tielens, Ann. Rev. Astron. Astrophys. **46**, 289 (2008)

A.G.G.M. Tielens, *The Physics and Chemistry of Interstellar Medium* (Cambridge Univ. Press, Cambridge, UK, 2005)

J.J. Tobin, L. Hartmann, L. Loinard, Astrophys. J. **722**, L12 (2010)

J.J. Tobin, L. Hartmann, H.-F. Chiang, D.J. Wilner, L.W. Looney, L. Loinard, N. Calvet, P. D'Alessio, Astrophys. J. **771**, 48 (2013)

K. Tomisaka, Astrophys. J. **575**, 306 (2002)

B.E. Turner, Astrophys. J. **321**, L75 (1987)

B.E. Turner, Astrophys. J. Suppl. **70**, 539 (1989)

T. Umemoto, T. Iwata, Y. Fukui, H. Mikami, S. Yamamot, O. Kameya, N. Hirano, Astrophys. J. **392**, L83 (1992)

T. Umemoto, H. Mikami, S. Yamamoto, N. Hirano, Astrophys. J. **525**, L105 (1999)

F.F.S. van der Tak, P. Schilke, H.S.P. Muller, D.C. Lis, T.G. Phillips, M. Gerin, E. Roueff, Astron. Astrophys. **388**, L53 (2002)

E.F. van Dishoeck, G.A. Blake, D.J. Jansen, T.D. Groesbeck, Astrophys. J. **447**, 760 (1995)

C. Vastel, T.G. Phillips, C. Ceccarelli, J. Pearson, Astrophys. J. **593**, L97 (2003)

T. Vasyunina, H. Linz, T. Henning, I. Zinchenko, H. Beuther, M. Voronkov, Astoron. Astrophys. **527**, 88 (2011)

P. Wang, Z.-Y. Li, T. Abel, F. Nakamura, Astrophys. J. **709**, 27 (2010)

Y. Watanabe, N. Sakai, J.E. Lindberg, J.K. Jørgensen, S.E. Bisschop, S. Yamamoto, Astrophys. J. **745**, 126 (2012)

M. Wright, G. Sandel, D.J. Wilner, R.L. Plambeck, Astrophys. J. **393**, 225 (1992)

M.C.H. Wright, R.L. Plambeck, D.J. Wilner, Astrophys. J. **469**, 216 (1996)

F. Wyrowski, P. Schilke, C.M. Walmsley, K.M. Menten, Astrophys. J. **514**, L43 (1999)

T. Yamaguchi et al., Publ. Astron. Soc. Japan **64**, 105 (2012)

L.A. Zapata, J. Schmid-Burgk, K.M. Menten, Astron. Astrophys. **529**, A24 (2011)

S. Zhou, Y. Wu, N.J. Evans, II, G.A. Fuller, P.C. Myers, Astrophys. J. 346, 168 (1989)

L.M. Ziurys, Astrophys. J. **321**, L81 (1987)

H. Zinnecker, H.W. Yorke, Ann. Rev. Astron. Astrophys. **45**, 481 (2007)

Chapter 8
Chemistry of Protoplanetary Disks

8.1 Introduction

Star-forming regions are also the formation sites of planetary systems particularly for low-mass star-forming regions. A flattened disk structure is formed just after the birth of a protostar and evolves into a protoplanetary disk and eventually into a planetary system. A protoplanetary disk has a typical size of a few 100 au and generally exhibits Keplerian rotation. When and how the disk structure is formed from the gas surrounding a protostar is still controversial. Disks are generally found in Class I sources and have also been reported for some Class 0 sources (e.g., Tobin et al. 2012; Yen et al. 2013). Hence, disk structure is thought to form in the early stages of protostellar evolution. Disks in Class 0 and I stages are called protostellar disks and will evolve into protoplanetary disks in the Class II and Class III stages.

The existence of disks around young stars was revealed by infrared observations (e.g., Rucinski 1985; Strom et al. 1989; Adams et al. 1990). The SEDs of Class II sources show an infrared excess in addition to stellar blackbody radiation (Sect. 7.2). The infrared excess originates from the thermal emission of dust around the star. The total amount of dust inferred from the infrared excess is very large. According to statistical studies, the median disk mass of Class II sources is 0.05 $M_{\odot}$, although the data show significant scatter (e.g., Williams and Cieza 2011). If the mass were distributed spherically within a radius of 200 au around the protostar, the average density would be about 1×10^8 cm^{-3}. The resultant column density from the surface to the star would be as high as 1×10^{23} cm^{-2}, which corresponds to a visual extinction (A_v) of 100 magnitudes. Hence, the stellar radiation would heavily be obscured in visible light. However, the stellar radiation is in fact observed, which implies that the dust must be distributed nonspherically, most probably in a disk structure around the star. As a result, the stellar radiation is not obscured in most directions, except for observations looking directly along the plane of the disk. In addition to the infrared excess, the SEDs of Class II sources often show a UV excess (e.g., Herbig and Goodrich 1986). This UV excess

S. Yamamoto, *Introduction to Astrochemistry*, Astronomy and Astrophysics
Library 7, DOI 10.1007/978-4-431-54171-4_8

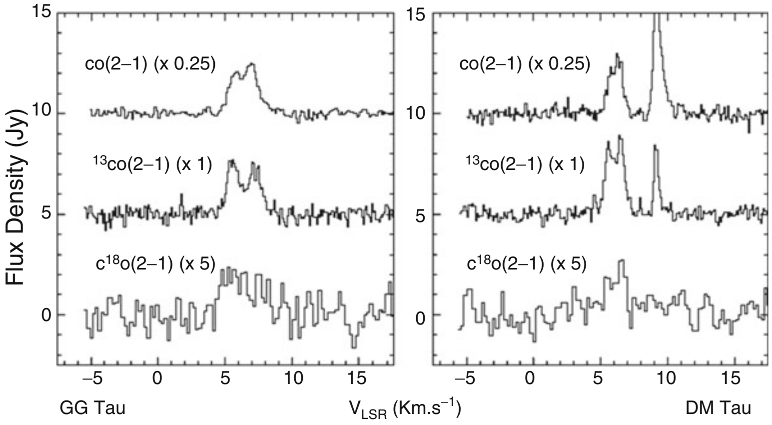

Fig. 8.1 Emission of CO and its isotopic species toward GG Tau and DM Tau. A double-peaked line profile can be seen for ^{13}CO. The 9 km s^{-1} component for DM Tau originates from an ambient cloud (Reprinted with permission from Dutrey et al. (1997). Copyright 1997 European Southern Observatory)

originates from interactions between the stellar atmosphere and the innermost part of the disk. Optical observations also reveal the existence of disks around young stars as a silhouette, where extinction by the disks is observed against a diffuse background light (e.g., Bally et al. 2000; Ricci et al. 2008).

In millimeter-wave observations, the thermal emission of dust from disks is observed toward many Class II sources (e.g., Beckwith et al. 1990; Andrews and Williams 2005; Mann and Williams 2010). Moreover, rotational spectral lines of CO and its isotopologues are also detected in disks (e.g., Strutskie et al. 1993; Dutrey et al. 1997), as shown in Fig. 8.1. Although the structure of the disk is not resolved with single-dish observations, the spectral lines show a double-peaked profile, reflecting the rotational motion of the disks. By millimeter and submillimeter interferometry, size and kinematics can be constrained for many Class II protoplanetary disks (e.g., Kawabe et al. 1993; Dutrey et al. 1994; Simon et al. 2001).

8.2 Basic Physical Structure of Protoplanetary Disks

The typical structure of a protoplanetary disk around a single star is illustrated in Fig. 8.2. The disk has a typical size of a few 100 au in radius and exhibits Keplerian rotation. The rotation velocity v_θ at radius of r is given by:

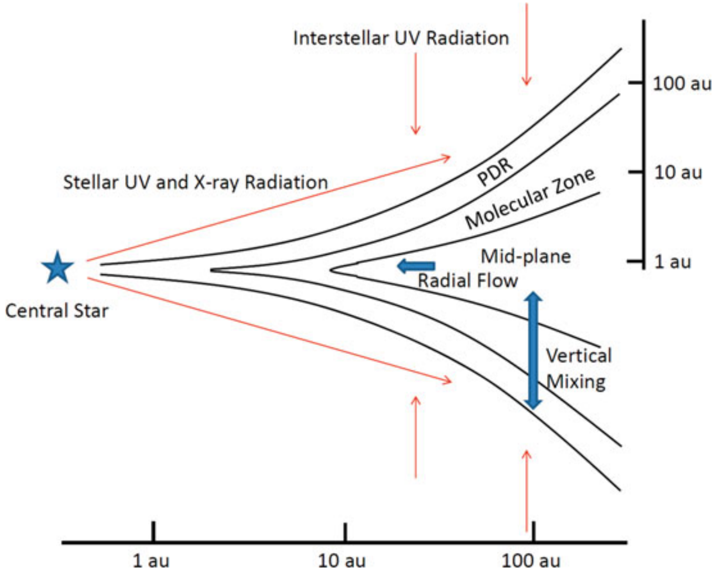

Fig. 8.2 Schematic of a cross section of a protoplanetary disk. The surface of the disk is illuminated by stellar UV and X-ray radiation, as well as interstellar UV radiation. Hence, the disk consists of a cold midplane, a molecular zone, and a photodissociation layer. Radial inflow and vertical mixing play important roles in disk chemistry

$$v_\theta = \sqrt{\frac{GM}{r}} = 30 \left(\frac{r}{1\ \text{au}}\right)^{-1/2} \left(\frac{M}{1\, M_\odot}\right)^{1/2} \text{km s}^{-1}, \tag{8.1}$$

where M is the stellar mass and G the gravitational constant. Here, the mass of the disk is assumed to be much smaller than the stellar mass, and the self-gravity of the disk is ignored.

The vertical scale of the disk is determined by hydrostatic equilibrium. Because the gravitational force along the vertical direction (z) balances the pressure gradient, one obtains:

$$\frac{1}{\rho}\frac{dP}{dz} = -\frac{GMz}{r^3}, \tag{8.2}$$

where ρ is mass density and P the gas pressure given in terms of the sound speed (c_s):

$$P = c_s^2 \rho. \tag{8.3}$$

By solving the differential equation for ρ assuming for simplicity constant c_s along z, the vertical density structure can be derived:

$$\rho = \frac{\Sigma}{\sqrt{\pi}H}\exp\left(-\frac{z^2}{H^2}\right). \tag{8.4}$$

Here, the scale height H is given as:

$$H = \sqrt{\frac{2}{GM}}c_s r^{\frac{3}{2}}. \tag{8.5}$$

In Eq. (8.4), the vertical column density (surface mass density Σ) constrains the coefficient in front of the exponential function. From Eq. (8.5), the scale height rapidly increases as a function of radius, and hence the disk is expected to be flared in the vertical direction. In reality, c_s depends on temperature:

$$c_s = \left(\frac{k_B T}{\mu m_H}\right)^{\frac{1}{2}}, \tag{8.6}$$

where μ is the average molecular weight in units of the mass of hydrogen atoms (m_H) and k_B the Boltzmann constant. Hence, c_s depends on z and r. Nevertheless, Eq. (8.5) captures the essential features of the vertical structure of the disk.

The gas in the disk is not simply rotating, but is slowly moving in the radial direction. Indeed, mass accretion is observationally inferred from the observed luminosity of T-Tauri stars. The mass accretion rate ($\dot{M}$) is typically 10^{-8} $M_\odot$ year^{-1}, which is significantly lower than the rate in the protostar stage (Class 0 and Class I). The turbulent motion of gas clumps induced by magnetorotational instability (MRI) in the disk plays an important role, because turbulent motion is responsible for the (large-scale) viscosity of the gas (Hartmann 2001). To deal with this mechanism, a so-called α disk model is often employed (Shakura and Sunyaev 1973). In this model, the viscosity (ν) is simply approximated by the effective parameter α as:

$$\nu = \alpha c_s H = \alpha\sqrt{\frac{2}{GM}}c_s^2 r^{3/2}. \tag{8.7}$$

Equation (8.7) can be regarded as analogous to molecular viscosity, which is proportional to the product of the mean-free path and the pressure divided by the molecular velocity. Here, a clump of gas moving approximately at the sound speed with a mean-free path on the order of the disk vertical height is regarded as a unit of macroscopic viscosity. For protoplanetary disks, α is typically around 0.01. By considering this effect in the equation of motion, the radial distribution of the surface mass density can be derived for a steady-state disk, in which the gas is always supplied from an outer envelope (Hartmann 2001):

$$\Sigma = \frac{\dot{M}}{3\pi\nu}\left(1 - \sqrt{\frac{r_{in}}{r}}\right), \tag{8.8}$$

where r_{in} is the inner radius of the disk from which the gas directly accretes onto the protostar, and $\dot{M}$ the mass accretion rate. Because H has a $r^{3/2}$ dependence, Σ is expected to have a $r^{-3/2}$ dependence for radii much larger than r_{in}. Then, the number density is expected to have an r^{-3} dependence. Although the condition for a steady-state disk is not always fulfilled for T-Tauri stars, it is employed in models for simplicity.

The temperature distribution in the disk is determined by heating and cooling processes. Two important heating sources are radiation from the protostar and turbulent mixing. The most important cooling process is thermal radiation of dust grains. When direct heating by the protostar radiation and the dust thermal radiation are balanced, the temperature of dust at a radius of r is given as:

$$T = \left(\frac{L}{16\pi r^2 \sigma}\right)^{\frac{1}{4}} \left(\frac{1-\eta}{\epsilon}\right)^{\frac{1}{4}}. \tag{8.9}$$

where L denotes the luminosity of the protostar, σ is the Stefan–Boltzmann constant, η the albedo of dust grains, and ϵ the emissivity of dust grains. Because the disk is opaque to infrared and optical photons, this heating is only effective in the disk surface. Additionally, a major heating mechanism in the midplane is the release of gravitational energy due to turbulent mixing. When the gravitational energy release at radius r and the dust thermal radiation are balanced, the following approximate relationship is obtained (Problem 3):

$$T \sim \left(\frac{GM\dot{M}}{2\pi\sigma r^3}\right)^{\frac{1}{4}}. \tag{8.10}$$

However, the actual temperature distribution is a complex function of the shape and density distribution of the disk and the SED of the protostar, as well as other minor contributions from interstellar UV radiation and cosmic-ray heating. Here, the effect of opacity must also be considered carefully. Furthermore, the temperature distribution affects the shape and density distribution of the disk, because the temperature affects the gas pressure. Hence, the temperature distribution is numerically calculated in a self-consistent manner in general (e.g., Nomura and Millar 2005; Walsh et al. 2010; Dutrey et al. 2014). Nevertheless, the above approximate relations are useful for rough understanding of the thermal structure of the disk.

Figure 8.3 shows an example of the numerical calculations. The temperature varies from 30 K in the midplane to 100 K or higher in the disk surface. The midplane density varies from 10^7 to 10^{11} cm^{-3} from 100 au to 10 au, which is apparently higher than the average density of molecular clouds and star-forming

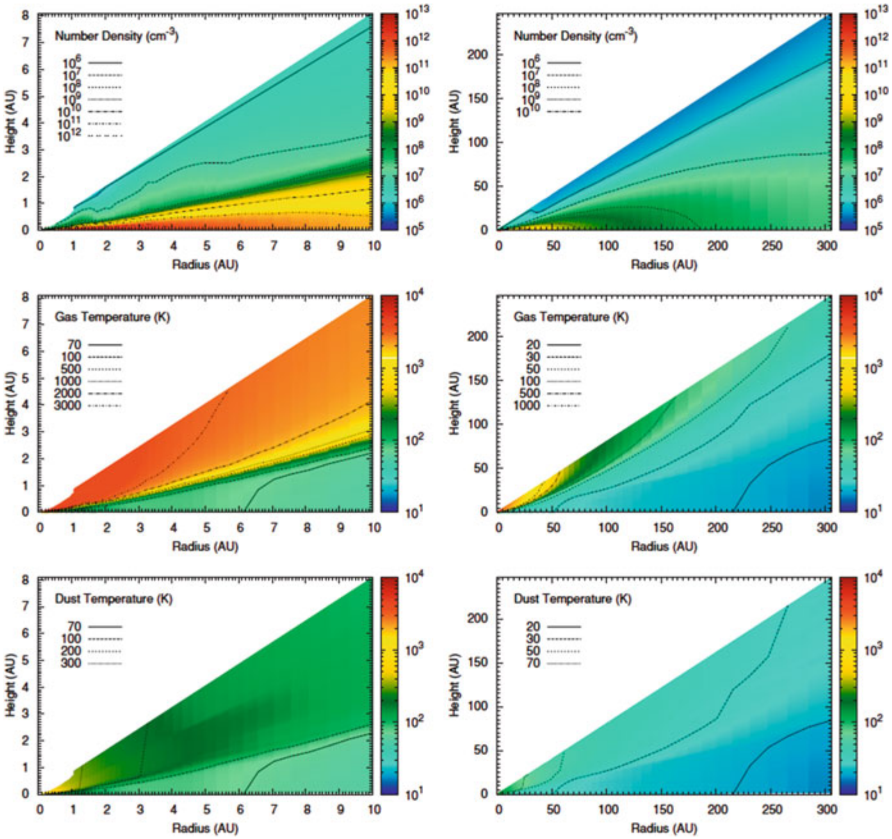

Fig. 8.3 Examples of numerical simulations of density and temperature profiles of a protoplanetary disk. The *left* panels are zoom-ins of inner regions of the *right* panels (Reprinted with permission from Walsh et al. (2010). "AU" means the astronomical unit, au. Copyright 2010 American Astronomical Society)

cores. The radial dependences of the density and the temperature in the midplane are almost consistent with the approximate relationships discussed above.

8.3 Molecules Detected in Protoplanetary Disks

So far, many molecules have been detected in protoplanetary disks, mostly with radio and infrared observations: H_2 (HD), CN, CO, CO_2, CS, CH^+, HCO^+ (DCO^+), HCN (DCN), HNC, CH_4, H_2CO, CCH, C_2H_2, HC_3N, CH_3OH, CH_3CN, c-C_3H_2, N_2H^+, OH, and H_2O (see Dutrey et al. 2014 for review). These detected molecules are all abundant molecules in interstellar clouds. Representative T-Tauri stars for molecular line observations include DM Tau, GG Tau, LkCa 15, and TW Hya. The former three sources are in the Taurus region at a distance of 140 pc; TW Hya is located at 56 pc. Additionally, a few Herbig Ae/Be stars such as MWC 480 and HD163296 have been observed for chemical studies. They are an intermediate-mass version of a T-Tauri star.

Molecular line emission from protoplanetary disks is generally faint, and, hence, radio observations require large-aperture single-dish telescopes and millimeter-wave interferometers with high sensitivity. With single-dish telescopes, it is often difficult to distinguish disk emission from the overwhelming contamination from remnant clouds and background/foreground clouds, unless the disk emission has different velocities from the contamination, as in the case of DM Tau (Fig. 8.1) (Dutrey et al. 1997; Handa et al. 1995). In contrast, interferometer observations have an advantage in this respect, because extended emission is resolved out. Hence, emission from protoplanetary disks can readily be extracted, and its distribution can be studied at a high spatial resolution.

Figure 8.4 shows an example of interferometric data of CO, HCN, HCO$^+$, and CN toward DM Tau, LkCa 15, and MWC 480 (Oberg et al. 2010). The spatial resolution is 2–3″. This resolution is comparable to or slightly smaller than the size of the disk of about 4″ (600 au). Hence, the distributions of these molecules are marginally resolved. Although the distributions are centrally concentrated, their spatial extent differs from molecule to molecule. For all three sources, CO and CN are more extended than HCO$^+$ and HCN. The color images represent the first-

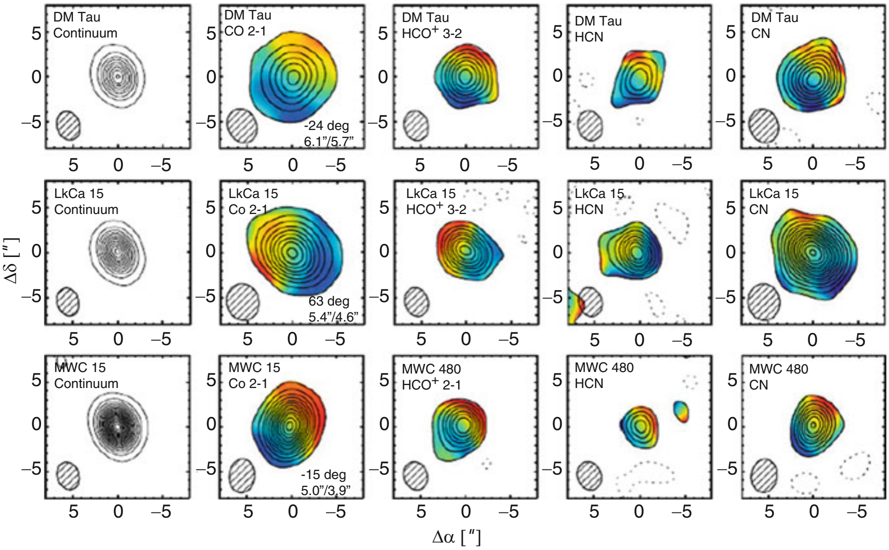

Fig. 8.4 Distribution of molecules in the protoplanetary disks of DM Tau, LkCa 15, and MWC 480 (Oberg et al. 2010). The color scale maps represent the velocity field map; contours represent the intensities. The resolution differs from molecule to molecule and from source to source and is indicated in the *bottom left* corner of each panel (Reprinted with permission from Oberg et al. (2010). Copyright 2010 American Astronomical Society)

moment maps (velocity centroid maps). A clear rotational signature can be seen in all of the maps. These results indicate that molecular emission observed in the radio wavelength comes from the disk, including its cold outer part.

In general, the molecular abundances of major components such as HCO^+, HCN, CS, and CCH in protoplanetary disks around T-Tauri stars are lower by an order of magnitude than those found in cold molecular clouds (Dutrey et al. 1997). The molecular abundances in protoplanetary disks around Herbig Ae/Be stars are reported to be lower than those in T-Tauri stars (Schreyer et al. 2008).

In addition to radio observations, several molecules have been detected toward protoplanetary disks with infrared observations. Vibration–rotation lines of H_2O, OH, CO, CO_2, HCN, C_2H_2, and CH_4 have been observed in absorption against infrared stellar radiation (e.g., Lahuis et al. 2006; Carr and Najita 2011; Pontoppidan et al. 2010; Mandell et al. 2012). Whereas CO had been observed for many years, the other molecules have only been detected quite recently using infrared observations from the *Spitzer Space Telescope* and with high-resolution spectrographs on large optical telescopes. We note that nonpolar molecules such as CO_2, C_2H_2, and CH_4 are only detected in infrared observations because their pure rotational transitions are forbidden. When the spectral resolution is sufficiently high to resolve individual rotational lines, the rotational temperature can be derived. In most cases, the rotational temperature derived in this way is as high as a few 100 K; this indicates that infrared observations trace the hot component near the central star. This situation arises because absorption against the central star originates from molecules near the central star. For nonpolar molecules, the rotational temperature approximately corresponds to the gas kinetic temperature in consequence of a lack of radiative transitions between rotational levels, although an infrared pumping effect may also affect the level populations. Thus, we can study the physical conditions, as well as the chemical compositions, of the innermost parts of protostellar disks.

The pure rotational transitions of H_2O and OH are observed in the far-infrared emission from various protoplanetary disks (e.g., Fedele et al. 2013; Howard et al. 2013; Hogerheijde et al. 2011). In contrast to infrared absorption spectra, this emission originates from the warm regions of the disk. Additionally, some atomic lines such as [O I] ($^3P_1$–$^3P_0$ 63 μm; $^3P_2$–$^3P_1$ 145 μm) and [C II] ($^2P_{3/2}$–$^2P_{1/2}$ 158 μm), which mainly originate from the PDR layer of the disk, have been observed. Because the disk has a flared structure, its surface is well illuminated by the central star (Fig. 8.2). Hence, the surface of the disk can be regarded as a PDR layer because of the UV radiation from the central star and the interstellar UV radiation. These far-infrared lines play an important role in cooling the disk surface. Additionally, the pure rotational spectral line of HD ($J = 1 - 0$) was detected in TW Hya with *Herschel* (Bergin et al. 2013). This line can be regarded as a good tracer of the total gas mass of the disk. In fact, the disk mass of TW Hya is reported to be higher than 0.05 $M_\odot$ or higher based on the observations of HD (Bergin et al. 2013).

8.4 Chemical Processes in Protoplanetary Disks

A protoplanetary disk has a fairly complex physical structure. To consider chemical processes in the disk, the disk is divided into the following three characteristic components for convenience, as shown in Fig. 8.2: the midplane, the molecular zone, and the PDR layer. Additionally, an inner disk is also considered. For the former three parts, we employ a radius of 100 au from the central star as the representative radius. We choose a radius of a few to 10 au as the representative one for the inner disk. These components have quite different physical conditions that affect chemical processes.

Here, we consider an axisymmetric disk around a central star, where the stellar mass is 1 $M_\odot$. We assume a steadily accreting disk with a mass accretion rate $\dot{M}$ of 10^{-8} $M_\odot$ year^{-1}. The α parameter for the viscosity is assumed to be 0.01. Using Eqs. (8.7 and 8.8), we calculate the surface density at the radius of 100 au to be 2×10^{23} cm^{-2}, where a temperature of 30 K is assumed for calculating c_s by referring to Fig. 8.3. This surface density corresponds to a visual extinction of 200 magnitudes, and hence the midplane is well shielded from external UV radiation. The H_2 density in the midplane is 1×10^9 cm^{-3} at a radius of 100 au found by dividing the surface density by $2H$. Similarly, the H_2 density at a radius of 10 au is calculated to be 3×10^{11} cm^{-3}. Here, the scale height of the disk H is 15 and 0.5 au at radii of 100 and 10 au, respectively. Table 8.1 summarizes the assumed physical conditions employed in the following subsections. Although these values are representative, readers should note that they are not based on actual observational results for a particular source.

8.4.1 Disk Midplane

The visual extinction toward the disk surface can be as high as 100 magnitudes, if the grain properties are the same as those in molecular clouds. Hence, the interstellar UV radiation is well shielded. Moreover, the UV and X-ray radiation from the central star is also negligible because of the high column density. Hence, the major heating source is gravitational energy release due to the accreting motion, as discussed above. Cosmic-ray heating provides an additional contribution. For this reason, the gas kinetic temperature in the midplane can be as low as 20 K.

Table 8.1 Typical physical conditions at representative disk positions

	Midplane	Molecular layer	Surface	Inner disk
R/au	100	100	100	10
z/au	0	15	37.5	0
H_2 density/cm^{-3}	10^9	10^8	10^7	10^{12}
T/K	20	50	100	100

The ionization sources are cosmic rays and the decay of radioactive nuclei, although the latter contribution is minor. Therefore, Eq. (5.11) can be used to evaluate the degree of ionization, but it assumes that the major carrier of positive charge is HCO^+ and $OH_3{}^+$. If CO and H_2O are completely depleted onto dust grains, $H_3{}^+$ becomes the major positive charge carrier. Therefore, its abundance should be balanced with the electron abundance. Even with this proviso, Eq. (5.11) still holds. For a H_2 density of 10^9 cm^{-3}, the degree of ionization is 10^{-11}.

Because of the high H_2 density of 10^9 cm^{-3}, the adsorption temperatures of molecules become slightly higher. For instance, the adsorption temperature of CO is 25 K at 10^9 cm^{-3}; it is 20 K at 10^4 cm^{-3}. Most of the heavy molecules except for CO are depleted onto dust grains, even at 30 K. The timescale for depletion is as short as 1 year. Under this condition, we evaluate the abundance of $H_3{}^+$, which is an important parent molecule in the ion–molecule reaction scheme. When CO is assumed to be depleted completely, $H_3{}^+$ is mainly destroyed by free electrons. Hence, the abundance of $H_3{}^+$ relative to H_2 is given by Eq. (4.58). Using the electron recombination rate at 20 K, the abundance is calculated to be 10^{-11}, unless the cosmic ray is significantly attenuated in the midplane. This abundance is the same as the degree of ionization, because a major carrier of positive charge is $H_3{}^+$, under the assumed conditions. Then, the timescale for $H_3{}^+$ chemistry starting from the neutral species X is evaluated to be 500 year using relation:

$$\tau = \frac{1}{k_L\left[H_3^+\right]}, \tag{8.11}$$

where k_L is the Langevin rate coefficient. Therefore, the neutral species X tends to be depleted onto dust grains before it reacts with $H_3{}^+$. For this reason, the gas-phase ion–molecule chemistry is not very active in the midplane of the disk. This situation is also true for neutral–neutral reactions. For reactions with atomic oxygen with a reaction rate of 10^{-10} cm^3 s^{-1}, the reaction timescale is longer than 1 year for the fractional abundances of atomic oxygen less than 10^{-7}.

The deuterium fractionation reaction presents an exception:

$$H_3{}^+ + HD \rightarrow H_2D^+ + H_2 + 230K. \tag{8.12}$$

Because CO is depleted onto dust grains, the main reaction breaking up H_2D^+ at 20 K is the backward reaction of reaction (8.12) and the reaction with HD. Using Eq. (6.75), we show that:

$$\frac{[H_2D^+]}{[H_3^+]} \sim \frac{k_f[HD]}{k_b[H_2] + k_2[HD]} \sim 0.75. \tag{8.13}$$

If the temperature is higher, the $[H_2D^+]/[H_3{}^+]$ ratio becomes lower. Hence, the ratio is a good indicator of the temperature of the midplane.

In contrast to the poor chemistry in the gas phase, the grain-surface reactions are still active. At 20 K, the timescale over which hydrogen atoms scan the entire grain surface is roughly estimated to be 2.3×10^{-2} s, which is longer than the evaporation timescale of 1.8×10^{-3} s. Hence, hydrogenation reactions are relatively suppressed in comparison with the reactions at 10 K. The scanning timescales for O, C, and CO are 4.3×10^{2}, 3.7×10^{5}, and 3.0×10^{6} s, which are significantly faster than those at 10 K and are comparable to or faster than their respective evaporation timescales (2.1×10^{5}, 1.8×10^{5}, and 9.2×10^{12} s). As a result, the diffusive reactions of heavy atom species efficiently occur on dust grains. For instance, CO_2 is formed through the following reactions (e.g. Minissale et al. 2013; Oba et al. 2010):

$$\mathrm{CO} + \mathrm{O} \rightarrow \mathrm{CO_2}, \tag{8.14}$$

$$\mathrm{CO} + \mathrm{OH} \rightarrow \mathrm{CO_2} + \mathrm{H}. \tag{8.15}$$

More complex organic molecules will be formed in the midplane. When CO is converted to larger molecules, they are not readily liberated from dust grains due to their high adsorption temperatures. The CO molecule has the lowest adsorption temperature among carbon-bearing molecules, and hence, these grain-surface reactions will reduce the abundance of carbon potentially used in the gas-phase reactions. This behaves as a carbon sink (Aikawa et al. 1997).

Even in the midplane, the temperature decreases with increasing distance to the central star. Hence, CO is depleted beyond a certain radius, called the CO snow line. Because of CO depletion, N_2H^+ is enhanced significantly, because its major breakup process is the proton transfer reaction with CO. A doughnut-like distribution for N_2H^+ was recently identified in interferometric observations toward TW Hya (Qi et al. 2013) (Fig. 8.5). This is interpreted as the destruction of N_2H^+ by CO inward of the CO snow line. Similarly, the H_2O snow line can be traced by a hole in the HCO^+ distribution, although the hole should be very small.

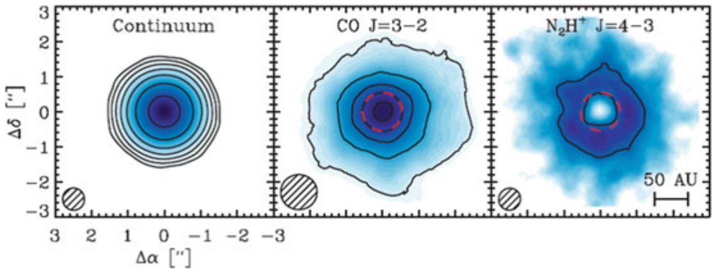

Fig. 8.5 Interferometric observations of TW Hya. The N_2H^+ distribution has a hole that is caused by the sublimation of CO from dust grains. Hence, the CO *snow line* (*red dashed circle*) is clearly identified from the N_2H^+ distribution, although it is difficult to identify in the CO distribution in consequence of contributions from the disk surface (Reprinted with permission from Qi et al. 2013)

8.4.2 Disk Surface

If the vertical density distribution is given by Eq. (8.4), the column density toward the out-of-plane direction is given as:

$$N(z) = \frac{\Sigma}{\sqrt{\pi} H} \int_z^{\infty} \exp\left(-\frac{z'^2}{H^2}\right) dz'. \tag{8.16}$$

Here, the $z = 2.5H$ position at a radius of 100 au is considered the representative position of the disk surface, where the H_2 density at this position is 10^7 cm^{-3}. The above column density can be evaluated as:

$$N(2.5\mathrm{H}) = 0.0062\Sigma = 1.2 \times 10^{21} \ \mathrm{cm}^{-2}, \tag{8.17}$$

where a surface density of 2×10^{23} cm^{-2} is employed. This column density, $N(2.5H)$, corresponds to a visual extinction of 1.2 magnitudes for interstellar UV radiation. Additionally, the surface area of the disk is also illuminated by the UV and X-ray radiation from the central star (e.g., Glassgold et al. 1997). Because the stellar radiation from T-Tauri stars typically contains a UV excess and X-ray component—due to gas accreting onto the central star—in addition to the stellar blackbody radiation, the UV radiation from the central star contributes significantly to the thermal balance in the surface region. The effective UV radiation strength has to be calculated numerically by considering the stellar properties and density structure of the disk. Here, we simply adopt a UV radiation strength 100 times larger than the interstellar UV radiation level ($G_0 = 100$). However, the X-ray radiation makes a minor contribution to the thermal balance.

Hence, the disk surface is a typical PDR with a high H_2 density (10^7 cm^{-3}). Molecules are photodissociated by the UV radiation, and some of them are ionized. In particular, CO is photodissociated, and carbon atoms are ionized as C^+. Indeed, the emission of [C II] and [O I] lines is observed toward protoplanetary disks (e.g., Dent et al. 2013). These line emissions as well as thermal emission of dust grains are associated with an important cooling mechanism. Additionally, photoelectric heating is a major heating source. Given a balance of heating and cooling rates, the typical temperature of the disk surface is 50–100 K, which is significantly higher than the temperature in the midplane. In this condition ($\sim$100 K), molecules adsorbed on dust grains, including CO, H_2O, and organic molecules, are liberated into the gas phase.

On the disk surface, the typical chemistry of PDRs described in Sect. 7.11 takes place. The degree of ionization is determined by the photoionization of C atoms to be 10^{-4}, unless carbon is locked in the sink. Although X-rays do not significantly contribute to the degree of ionization, these photons can ionize H, He, and N and affect chemical compositions. The timescale for photodissociation is as short as 1 year or less for the adopted UV radiation strength ($G_0 = 100$), which determines the timescale for chemical equilibrium. Hence, steady-state chemistry is realized locally. Chemical species characteristic of the disk surface include CN and CCH, which are typical products in PDRs.

8.4.3 Molecular Zone

An intermediate region between the midplane and the disk surface shows a rich chemical composition and is called the "molecular zone." Here, the position of $z = H$ at a radius of 100 au is arbitrarily chosen as the representative location of this region. The H_2 density and the temperature are typically 10^8 cm^{-3} and 50 K. The temperature is higher than that in the midplane because of the contribution of UV heating. The degree of ionization is also intermediate between that of the midplane and the surface. Cosmic-ray ionization makes a basic contribution. Additionally, the contribution of X-rays becomes more important for higher z (the out-of-plane distance), because the column density toward the central star decreases rapidly due to the flared structure of the disk. The UV radiation from the central star and the interstellar UV radiation also contribute to the degree of ionization close to the disk surface. In chemical model calculations, all of these contributions are taken into account by numerical calculations at each position of the disk (e.g., Walsh et al. 2012). In this section, the cosmic-ray and X-ray ionization rates are set to 10^{-15} s^{-1} for simplicity, resulting in the ionization fraction of 10^{-10} according to Eq. (5.11).

In the molecular zone, CO and some volatile species can mainly exist in the gas phase. Ionization by cosmic rays and X-rays triggers gas-phase chemistry. The H_3^+ abundance is 1.8×10^{-4} cm^{-3}, and hence the timescale of reactions with H_3^+ for a neutral molecule is 6×10^{12} s (2×10^5 years). Moreover, the timescale of depletion onto dust grains can be as short as 10 year. Hence, depletion is faster than the gas-phase reactions if adsorption temperature is well above 50 K. As a result, the gas-phase production of larger molecules having higher adsorption temperatures is not very efficient. In contrast to the gas-phase processes, active grain-surface chemistry is expected because heavy atoms and molecules can more rapidly move over the surface at 50 K than at lower temperatures, which leads to the formation of complex molecules. Molecules on dust grains will partly be released into the gas phase via nonthermal desorption mechanisms such as photodesorption by cosmic ray-induced UV radiation and desorption by excess reaction energy. Most molecules detected in protoplanetary disks by radio astronomical observations would mainly exist in this molecular zone.

8.4.4 Vertical and Radial Mixing

Although we have discussed separately the chemistry in three regions of disks at different out-of-plane distances, these three regions are actually related through vertical mixing. Vertical mixing is caused by turbulent motions induced by MRI (Hartmann 2001). Because the diffusion constant can be given as:

$$D = \alpha c_s H, \tag{8.18}$$

the timescale for vertical mixing is:

$$\tau = \frac{H^2}{D} = \frac{H}{\alpha c_s} \quad . \tag{8.19}$$

For $\alpha = 0.01$, the timescale is evaluated to be 2×10^4 year for H_2. This timescale is much shorter than the lifetime of the disk (10^6–10^7 year). Diffusion is generally slower for more massive molecules, and the timescale will be longer than the value cited above. Nevertheless, molecules and dust grains can vertically move among the three regions. For instance, molecules formed in the PDR of the surface region will be delivered to the molecular zone for further chemical processing. Grain mantle species on dust grains will be released into the gas phase at least in part, if they can move from the midplane to the molecular zone. These effects are actually considered in current chemical models.

Vertical mixing is generally more important than radial mixing at a radius of 100 au. The timescale for the radial motion by l is similarly given as:

$$\tau = \frac{l^2}{D} \quad . \tag{8.20}$$

Hence, the diffusion timescale for the same distance is the same between for vertical and radial motions. At a radius of 100 au, the physical conditions do not rapidly change in the radial direction. As a result, chemical processes are only weakly affected by accretion. It should be noted that radial motion is very important in the inner part of the disk, because the physical conditions rapidly change with decreasing radius.

Above, we assumed that the properties of dust grains are the same as those in molecular clouds. However, grain size gradually increases in the high-density state of disks through grain–grain collisions. In general, grain growth decreases the visual extinction, which allows UV radiation from the central star or the interstellar space to penetrate deeper into disks. This process effectively extends the PDR layer and activates the gas-phase production of molecules. Larger grains generally have smaller surface areas per unit weight of dust grains, and hence grain growth also affects the surface reactions on dust grains. Another important phenomenon is grain settling into the midplane. During the lifetime of disks (10^6–10^7 year), heavy dust grains are settled by gravity. Such grain settling also affects the shielding of UV radiation, as well as grain-surface reactions (e.g., Fogel et al. 2011).

8.4.5 *Inner Disk*

At a radius of 10 au, the temperature is higher than 100 K because of substantial UV heating from the central star and gravitational heating, even in the midplane. The H_2 density can be as high as 10^{12} cm^{-3}, assuming a steady accretion model. Such high-temperature and high-density conditions are very peculiar in astrochemistry. For an H_2 density of 10^{12} cm^{-3}, the evaporation temperature of H_2O is about 150 K. Hence, the ice mantle will have evaporated in the inner disk out to the snow line. It is typically located around 5 au. Because of the high-temperature conditions, gas-phase chemical reactions are significantly different from those proceeding in cold molecular clouds. Reactions with activation barriers and endothermic reactions can proceed, which make substantial contributions to molecular formation. For instance, H_2O is formed from atomic oxygen by the following reactions with H_2:

$$\mathrm{O} + \mathrm{H_2} \rightarrow \mathrm{OH} + \mathrm{H}, \tag{8.21}$$

$$\mathrm{OH} + \mathrm{H_2} \rightarrow \mathrm{H_2O} + \mathrm{H}. \tag{8.22}$$

These reactions are endothermic by 3150 and 1736 K, respectively. However, they are important pathways for forming H_2O from atomic oxygen. The importance of high-temperature reactions is also invoked to account for the chemical compositions of active galactic nuclei (AGNs) (Harada et al. 2010). Moreover, three-body reactions may become significant in some cases.

8.5 Chemical Models

Since the pioneering work of Aikawa et al. (1997), various chemical models of protoplanetary disks have been reported (see review by Henning and Semenov (2013)). Most current models adopt the physical structure and dynamics of disks using a steadily accreting disk model, where the radial and vertical mixings are taken into account. Photodissociation and photoionization rates are typically evaluated from point to point in a disk by considering the extinction of radiation from the central star and from interstellar space. Ionization by X-rays from the central star is also taken into account in a similar way. The temperature distribution is calculated by balancing the heating and cooling at each point. Under these conditions, molecular abundances are calculated by solving a large set of reaction rate equations. Because the depletion timescale is short, gas–grain interactions play an essential role in chemical processes in the disk.

Although different chemical models highlight different physical and chemical effects, a three-layered chemical structure is a universal result. Here, we introduce an example. Figures 8.3 and 8.6 show chemical model calculations by Walsh et al. (2010). This model presumes a mass of the central star of 0.5 $M_{\odot}$ and a surface

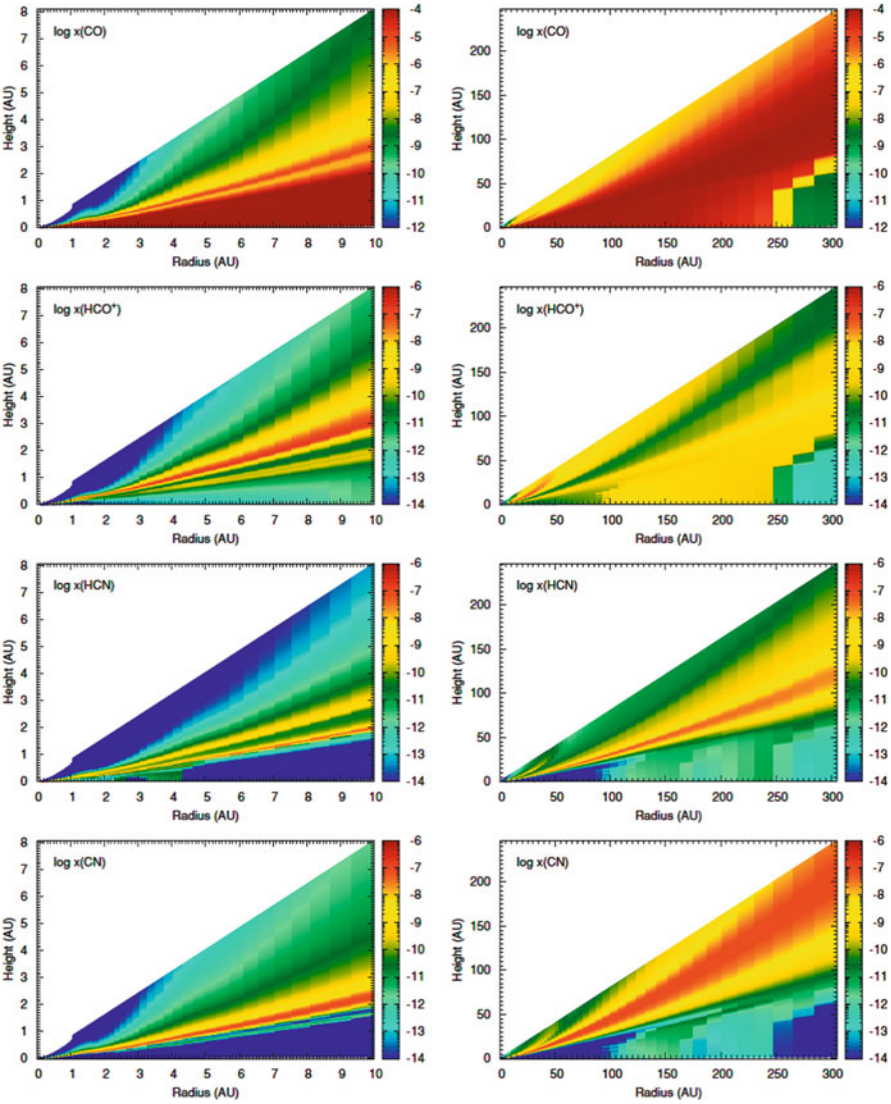

Fig. 8.6 Examples of chemical model simulations of a protoplanetary disk (Walsh et al. 2010). The distributions differ from molecule to molecule. The *left* panels are zoom-ins of inner regions of the *right* panels. "AU" means the astronomical unit, au (Reprinted with permission from Walsh et al. (2010). Copyright 2010 American Astronomical Society)

temperature of 4000 K. Furthermore, the model assumes a constant mass accretion rate of 10^{-8} $M_{\odot}$year^{-1} and an α parameter of 0.01. In the midplane, even CO is frozen out onto dust grains beyond 250 au. HCO^+ almost traces the distribution of CO. Additionally, HCN preferentially exists in the molecular zone and is heavily depleted onto dust grains in the midplane. CN is a photodissociation product of

HCN, and hence is enhanced in both the PDR layer and the molecular zone. In the inner region, photodissociation effects are significant over the surface, and molecules are mostly concentrated in the midplane. The qualitative chemical trends described in the previous sections are indeed seen in numerical simulations.

8.6 Molecules in Comets

Molecules formed in the disk will be delivered to planets and planetary systems in both the gas and solid phases. Although these chemical processes are complex, various efforts have been conducted to identify a possible relation between molecules in the disk and materials found in solar systems. The most important information about this link can be obtained from observations of comets, as is briefly described below.

Molecular compositions of comets have been observed at UV/visible, infrared, and radio wavelengths. So far, 30 or more species have been found in comets: CN, CO, OCS, CO_2, CS, HCN(DCN), HNC, HCO^+, HNCO, H_2CO, HCOOH, NH_2CHO, CH_4, CH_3OH, C_2, C_2H_2, CH_3CN, CH_3CHO, $HCOOCH_3$, C_2H_6, $(CH_2OH)_2$, C_3, HC_3N, NH, OH, NH_2, H_2O(HDO), H_2S, NH_3, SO, SO_2, and S_2. In the UV/visible regime, simple free radicals such as CN, C_2, C_3, and OH, as well as CO, have been detected. Fundamental (nonpolar) species such as CO_2, CH_4, C_2H_2, and C_2H_6 have been observed in the infrared regime. Radio observations play an important role in the identification of more complex molecules, which are of particular interest in chemical evolution. All of the detected molecules have also been detected in the interstellar medium. That is, no molecules specific to comets have been detected. Example spectra taken toward comet Hale–Bopp are shown in Fig. 8.7. The molecular abundances relative to H_2O for three comets are listed in Table 8.2. It is noteworthy that fairly complex organic molecules such as $HCOOCH_3$ and $(CH_2OH)_2$ are found in some comets. Because these complex organic molecules are also found in star-forming regions, some of these molecules will remain on ice mantles and may have been delivered to solar nebulae.

The molecular compositions of comets exhibit a pronounced diversity, likely reflecting their past history. Comets can be roughly categorized into two groups: Oort comets and Jupiter family comets (Mumma and Charnley 2011). Most long-period comets belong to the group of Oort comets. Their origin is the Oort Cloud, which surrounds the Solar System at a size scale of 1000 au. Because the Oort Cloud is a remnant of the parent cloud from which the Solar System was born, Oort comets are rich in materials with a pre-solar origin. Indeed, various molecules have been detected in this type of comets, including the comets Hale–Bopp and Lemmon. On the other hand, Jupiter family comets have mostly short periods and originate from the Kuiper belt just outside the orbit of Neptune. The Kuiper belt is an annulus of debris, which is also found around other nearby stars (Holland et al. 1998; Matthews et al. 2014). Material on dust grains is significantly processed

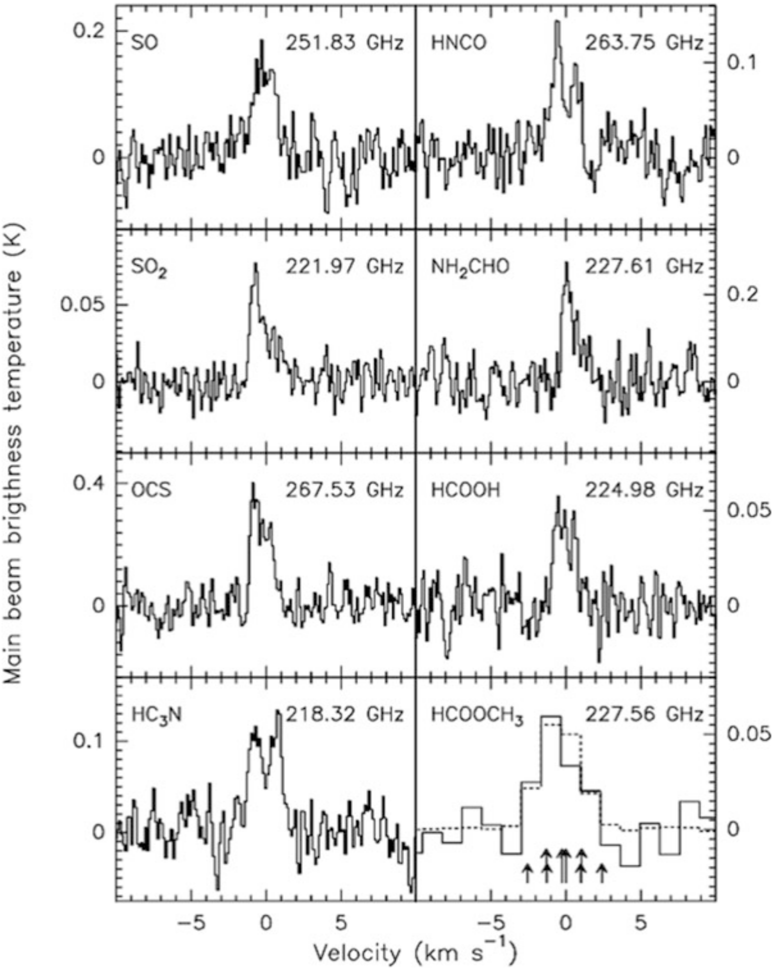

Fig. 8.7 Spectra observed toward comet C/1995 (O1) (Hale–Bopp) (Reprinted with permission from Bockelee-Morvan et al. (2000). Copyright 2000 European Southern Observatory)

during disk formation and evolution. As a result, Jupiter family comets do not show rich molecules in general.

Comets consist of a nucleus, a coma, and a tail. The nucleus is the solid body of comets and consists of a mixture of dust and ice. The coma is the bright envelope surrounding the nucleus, where most of the gaseous molecules are present. The tail is the diffuse and faint stream of gas and dust ejected by radiation pressure from the Sun. As a comet approaches the Sun, ice from the nucleus evaporates, and various molecules contained in the nucleus are liberated into the gas phase to form a coma. Parent species such as H_2O, HCN, H_2CO, and CH_3OH are evaporated from the coma and are subject to photodissociation by the UV radiation from the Sun. Some molecules such as OH, CN, and CCH are the photodissociation products of H_2O, HCN, and C_2H_2, respectively.

Table 8.2 Molecular abundances relative to H_2O in comets[a]

Molecule	C/1995 O1 (Hale–Bopp)	C/2012 F6 (Lemmon)	C/2013 R1 (Lovejoy)
HCN	0.25	0.14	0.16
CO	23	4.0	7.2
H_2CO	1.1	0.7	0.7
CH_3OH	2.4	1.6	2.6
HCOOH	0.09	<0.07	0.12
$(CH_2OH)_2$	0.25	0.24	0.35
HNCO	0.10	0.025	0.021
NH_2CHO	0.02	0.016	0.021
$HCOOCH_3$	0.08	<0.16	<0.20
CH_3CHO	0.025	<0.07	0.10

[a] Biver et al. (2014)

For additional details about comets and their chemistry, we refer the interested reader to a review article by Mumma and Charnley (2011).

Problems

8.1 The effective evaporation temperature depends on H_2 density. Calculate the evaporation temperatures of CO, H_2CO, and H_2O at H_2 densities of 10^9 cm^{-3} and 10^{12} cm^{-3}.

8.2 Consider the following three-body reaction:

$$C + H_2 + M \rightarrow CH_2 + M.$$

This reaction has a rate coefficient of 1.51×10^{-31} cm^6 s^{-1}. Evaluate the timescales of this reaction for H_2 densities of 10^9 cm^{-3} and 10^{12} cm^{-3}.

8.3 Let us consider the temperature in the midplane of protoplanetary disks. The energy released by the turbulent mixing (δE) in an infinitesimal range from $r + \Delta r$ to r is represented as:

$$\delta E = \frac{GM\dot{M}}{r^2}\Delta r.$$

Considering that δE is balanced to the radiation cooling, derive Eq. (8.10). Note that the cooling only from the disk surface is effective.

References

F.C. Adams, J.P. Emerson, G.A. Fuller, Astrophys. J. **357**, 606 (1990)
Y. Aikawa, T. Umebayashi, T. Nakano, S.M. Miyama, Astrophys. J. **486**, L51 (1997)
S.M. Andrews, J.P. Williams, Astrophys. J. **631**, 1134 (2005)

J. Bally, C.R. O'Dell, M.J. McCaughrean, Astron. J. **119**, 2919 (2000)

S.V.W. Beckwith, A.I. Sargent, R.S. Chini, R. Gusten, Astron. J. **99**, 924 (1990)

E.A. Bergin, L. Ilsedore Cleeves, U. Gorti, K. Zhang, G.A. Blake, J.D. Green, S.M. Andrews, N.J. Evans II, T. Henning, K. Oberg, K. Pontoppidan, C. Qi, C. Salyk, E.F. van Dishoeck, Nature **493**, 644 (2013)

N. Biver et al., Astron. Astrophys. **566**, L5 (2014)

D. Bockelee-Morvan et al., Astron. Astrophys. **353**, 1101 (2000)

J.S. Carr, J.R. Najita, Astrophys. J. **733**, 102 (2011)

W.R.F. Dent et al., Publ. Astron. Soc. Pac. **125**, 477 (2013)

A. Dutrey, S. Guilloteau, M. Simon, Astron. Astrophys. **286**, 149 (1994)

A. Dutrey, S. Guilloteau, M. Guelin, Astron. Astrophys. **317**, L55 (1997)

A. Dutrey, D. Semenov, E. Chapillon, U. Gorti, S. Guilloteau, F. Hersant, M. Hogerheijde, M. Hughes, G. Meeus, H. Nomura, V. Pietu, C. Qi, V. Wakelam, in *Protostars and Planets VI*, ed. by H. Beuther, R.S. Klessen, C.P. Dullemond, T. Henning (University of Arizona Press, Tuscon, 2014) p. 317

D. Fedele et al., Astron. Astrophys. **559**, A77 (2013)

J.K.J. Fogel, T.J. Bethell, E.A. Bergin, N. Calvet, D. Semenov, Astrophys. J. **726**, 29 (2011)

A.E. Glassgold, J. Najita, J. Igea, Astrophys. J. **480**, 344 (1997); Errata 485, 920 (1997)

T. Handa et al., Astrophys. J. **449**, 894 (1995)

N. Harada, E. Herbst, V. Waklam, Astrophys. J. **721**, 1570 (2010)

L. Hartmann, *Accretion Processes in Star Formation*, 2nd edn. (Cambridge University Press, Cambridge, 2001)

T. Henning, D. Semenov, Chem. Rev. **113**, 9016 (2013)

G.H. Herbig, R.W. Goodrich, Astrophys. J. **309**, 294 (1986)

M.R. Hogerheijde et al., Science **334**, 338 (2011)

W.S. Holland et al., Nature **392**, 788 (1998)

C.D. Howard et al., Astrophys. J. **776**, 21 (2013)

R. Kawabe, M. Ishiguro, T. Omodaka, Y. Kitamura, S.M. Miyama, Astrophys. J. **404**, L63 (1993)

F. Lahuis et al., Astrophys. J. **636**, L145 (2006)

A.M. Mandell, J. Bast, E.F. van Dishoeck, G.A. Blake, C. Salyk, M.J. Mumma, G. Villanueva, Astrophys. J. **747**, 92 (2012)

R.K. Mann, J.P. Williams, Astrophys. J. **725**, 430 (2010)

B. Matthews, G. Kennedy, B. Sibthorpe, M. Booth, M. Wyatt, H. Broekhoven-Fiene, B. Macintosh, C. Marois, Astrophys. J. **780**, 97 (2014)

M. Minissale, E. Congiu, G. Manico, V. Pirronello, F. Dulieu, Astron. Astrophys. **559**, A49 (2013)

M.J. Mumma, S.B. Charnley, Annu. Rev. Astron. Astrophys. **49**, 471 (2011)

H. Nomura, T.J. Millar, Astron. Astrophys. **438**, 923 (2005)

Y. Oba, N. Watababe, A. Kouchi, T. Hama, V. Pirronello, Astrophys. J. **712**, L174 (2010)

K. Oberg, C. Qi, J.K.J. Fogel, E.A. Bergin, S.M. Andrews, C. Espaillat, T.A. van Kempen, D.J. Wilner, I. Pascucci, Astrophys. J. **720**, 480 (2010)

K.M. Pontoppidan, C. Salyk, G.A. Blake, R. Meijerink, J.S. Carr, J. Najita, Astrophys. J. **720**, 887 (2010)

C. Qi, K.I. Oberg, D.J. Wilner, P. D'Alessio, E. Bergin, S.M. Andrews, G.A. Blake, M.R. Hogerheijde, E.F. van Dishoeck, Science **341**, 630 (2013)

L. Ricci, M. Robberto, D.R. Soderblom, Astron. J. **136**, 2136 (2008)

S.M. Rucinski, Astron. J. **90**, 2321 (1985)

K. Schreyer et al., Astron. Astrophys. **491**, 821 (2008)

N.I. Shakura, R.A. Sunyaev, Astron. Astrophys. **24**, 337 (1973)

M. Simon, A. Dutrey, S. Guilloteau, Astrophys. J. **545**, 1034 (2001)

K.M. Strom, S.E. Strom, S. Edwards, S. Cabrit, M.F. Skrutskie, Astron. J. **97**, 1451 (1989)

M.F. Strutskie, R.L. Snell, K.M. Strom, S.E. Strom, S. Edwards, Y. Fukui, A. Mizuno, M. Hayashi, N. Ohashi, Astrophys. J. **409**, 422 (1993)

J.J. Tobin, L. Hartmann, H.-F. Chiang, D.J. Wilner, L.W. Looney, L. Loinard, N. Calvet, P. D'Alessio, Nature **492**, 83 (2012)
C. Walsh, T.J. Millar, H. Nomura, Astrophys. J. **722**, 1607 (2010)
C. Walsh, H. Nomura, T.J. Millar, Y. Aikawa, Astrophys. J. **747**, 114 (2012)
J.P. Williams, L.A. Cieza, Annu. Rev. Astron. Astrophys. **49**, 67 (2011)
H.-W. Yen, S. Takakuwa, N. Ohashi, P.T.P. Ho, Astrophys. J. **772**, 22 (2013)

Chapter 9
Chemical Evolution from Interstellar Clouds to Star- and Planet- Forming Regions

In Chaps. 4, 5, 6, 7, and 8, we discussed the chemistry of diffuse clouds, molecular clouds, star-forming regions, and protoplanetary disks individually. However, the chemistry of each is not always independent of the others, but instead related. Here, the basic picture of chemical evolution from interstellar clouds to star-forming regions is presented by unifying the information presented in Chaps. 4, 5, 6, 7, and 8. We focus on the formation of solar-type (low-mass) stars, because the physical process of this type of star formation is better understood than that of high-mass stars.

As noted in Chap. 1, astronomers have identified roughly 170 molecular species as interstellar molecules. We now know that these molecules are neither distributed uniformly nor randomly in interstellar clouds. Chemical compositions systematically change as interstellar clouds physically evolve toward star and planet formation. The scheme of these changes is known as chemical evolution. When we consider star formation from interstellar clouds, as depicted in Fig. 9.1, there are three main drivers of chemical evolution: C to CO conversion, the depletion of molecules onto dust grains, and the evaporation of grain mantles after the birth of protostars.

In diffuse clouds, interstellar UV radiation can penetrate deeply. As a result, molecules are photodissociated, and carbon atoms are mostly ionized. Hence, the dominant form of gas-phase carbon is C^+ (Chap. 4). In this stage, molecular formation is limited because of fast photodissociation, and only simple molecules are produced. Chemical composition quickly reaches a steady-state condition for a given physical condition. This stage of a diffuse cloud can be regarded as the starting point of chemical evolution.

Although a diffuse cloud is in pressure equilibrium, it starts to collapse when triggered by some perturbation, such as a cloud–cloud collision and/or gravitational instability. As the density increases, the interstellar UV radiation is gradually shielded in the interior of the cloud. The C^+ ions then recombine with electrons to form C atoms. These C atoms react with oxygen-containing species to form CO molecules. This conversion of C to CO is slow in molecular cloud conditions and

S. Yamamoto, *Introduction to Astrochemistry*, Astronomy and Astrophysics Library 7, DOI 10.1007/978-4-431-54171-4_9

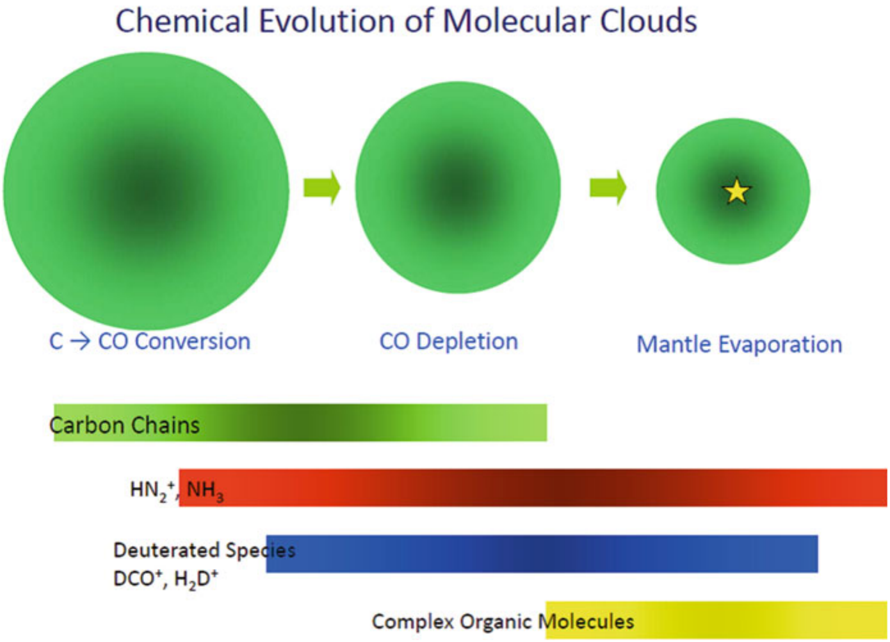

Fig. 9.1 Schematic of chemical evolution from diffuse clouds to low-mass star formation. The chemical composition systematically changes as the cloud evolves toward forming stars

typically takes several time, 10^5 year (Chap. 5). Because CO is a very stable molecule, it no longer reacts further in the gas phase. During the early stages before C atoms are completely converted to CO molecules, various organic molecules are produced by gas-phase reactions. As described in Chap. 5, gas-phase chemistry preferentially produces unsaturated organic molecules as opposed to saturated organic molecules. This is because reactions of organic molecules with H atoms is prohibited in the gas phase, and ion–molecule reactions with H_2 molecules are terminated because of the presence of very stable unsaturated hydrocarbon ions. As a result, various kinds of carbon-chain molecules are efficiently produced in the early stages of cloud evolution. In contrast, simple nitrogen-containing species such as NH_3 and N_2H^+ are gradually produced toward the later stages. The late production of these molecules is also related to the slow neutral–neutral reactions producing the parent molecule, N_2. Thus, C to CO conversion causes systematic chemical differentiation between carbon-chain molecules and NH_3/N_2H^+. This systematic chemical differentiation is indeed visible in observations of molecular cloud cores, because the conversion timescale is comparable to the dynamical timescale of the cloud (the free-fall time is 3.4×10^5 year for an H_2 density of 10^4 cm^{-3}).

As the cloud becomes denser in later stages of cloud evolution, the depletion of molecules onto dust grains becomes significant (Chap. 6). In particular, the depletion of CO onto dust grains affects the gas-phase chemical composition. For instance, the depletion of CO enhances the abundance of N_2H^+. Because CO is the main contributor in breaking up N_2H^+, the removal of CO from the gas phase extends the lifetime of N_2H^+. Similarly, deuterium fractionation is accelerated. In cold clouds, H_2D^+ ions, whose abundance is enhanced by the exothermic reaction of $H_3^+ + HD$, play an important role in deuterium fractionation. The depletion of CO extends the lifetime of H_3^+ and H_2D^+, resulting in heavy deuterium fractionation. Hence, the deuterium fractionation ratio is sensitive to the extent of depletion, and thus to the evolutionary state of the cloud (Chap. 6).

Molecules depleted onto dust grains do undergo change. They are subject to grain-surface reactions, as described in Chap. 6. In contrast to the gas-phase reactions, hydrogenation reactions by H atoms play a major role in grain-surface reactions. As a result, various kinds of saturated organic molecules are formed on dust grains. For instance, CO is hydrogenated by H atoms and successively forms HCO, H_2CO, CH_3O, and CH_3OH. Similarly, hydrogenation of C atoms produces CH, CH_2, CH_3, and CH_4 successively. Even more complex molecules are thought to be formed by the condensation reactions of heavy atoms and molecules, although these reactions are relatively slow in cold conditions. However, these molecules rarely emerge from dust grains into the gas phase in low-temperature conditions before the birth of protostars. Nevertheless, a small fraction of these molecules are now known to be liberated into the gas phase by nonthermal processes such as photodesorption by cosmic ray-induced UV radiation and desorption by excess reaction energy. This occurs even in cold starless cores, but the majority of molecules are delivered to protostellar cores in the solid phase.

After the birth of protostars, the temperature of the protostellar core gradually increases as protostellar evolution proceeds. Outflow shocks and accretion shocks associated with star-formation activities also contribute to the liberation of molecules. Molecules on dust grains sublimate roughly at the adsorption temperature. First, CO is liberated into the gas phase at 20 K and then CH_4 and H_2CO follow. Above 100 K, H_2O ice, which is the major constituent of grain mantles, sublimates. At this time, most complex organic molecules such as $HCOOCH_3$ and C_2H_5CN are also released into the gas phase. Most notably, molecular evolution still continues on dust grains during the temperature rise. In warm conditions (a few 10 K), hydrogenation is generally inefficient because H atoms are not adsorbed effectively. Instead, heavy atoms and molecules (radicals) can move from adsorption site to adsorption site to find reaction partners. This process enhances the production rate of complex organic molecules.

Because molecules are liberated from grain mantles in protostars, gas-phase chemical compositions around protostars strongly depend on the chemical compositions of grain mantles (Chap. 7). If saturated complex organic molecules are dominant, so-called hot corino chemistry appears; if CH_4 is sufficiently abundant, WCCC appears. Further chemical diversity will result from environmental effects such as illumination of the parent cloud by nearby luminous stars. Hence, the chemical compositions of protostellar cores depend not only on the present physical conditions but also on the history and environmental effects of the parent core in its starless core phase. That is, the chemical history contained within grain mantles appears in protostellar cores.

The chemical evolution of protostellar cores to protoplanetary disks is a current frontier of study in astrochemistry (Chap. 8). This evolution is related to how disk structures form around protostars, which is also a current area of research in star-formation studies. Thus, it is very interesting to study how the chemical diversity found in protostellar cores is passed on to protoplanetary disks, and eventually to planets. Such studies have long been difficult because of the limited sensitivity and resolution of radio observations. Although fundamental species such as CO, HCO^+, HCN, and H_2CO have been observed toward various Class I protostars, observing minor species such as saturated complex organic molecules, carbon-chain molecules, and deuterated species for tracing chemical evolution is necessary. Similarly, our understanding of the chemical composition of protoplanetary disks is also limited to simple molecules. Although chemical models of protoplanetary disks successfully explain the observations, the chemical diversity of protoplanetary disks has thus far not been investigated in detail. We reiterate that observations of minor molecular species are essential. The Atacama Large Millimeter/submillimeter Array (ALMA) is now in operation, and the chemical evolution that proceeds after the formation of protostellar cores can now be understood in detail. The astrochemical results from ALMA will be essential not only for a complete understanding of chemical evolution but also for star formation studies related to when and how protoplanetary disks are formed.

This book dealt mainly with the basics of astrochemistry, with a particular emphasis placed on the formation of low-mass (solar-type) protostars. Hence, many important topics that have been studied in recent years and many specialized topics that necessitate a more advanced understanding of astrochemistry have been omitted from this text. Furthermore, many topics were introduced only briefly in a simplified way. There are many good review articles that address the topics not included in this book; several of these reviews are listed below, and we refer the interested reader to these studies.

Further Readings

E.A. Bergin, M. Tafalla, Cold dark clouds: The initial conditions for star formation. Annu. Rev. Astron. Astrophys. **45**, 339 (2007)

P. Caselli, C. Ceccarelli, Our astrochemical heritage. Astron. Astrophys. Rev. **20**, 56 (2012)

A. Dutrey, D. Semenov, E. Chapillon, U. Gorti, S. Guilloteau, F. Hersant, M. Hogerheijde, M. Hughes, G. Meeus, H. Nomura, V. Pietu, C. Qi, V. Wakelam, in *Protostars and Planets VI*, ed. by H. Beuther, R.S. Klessen, C.P. Dullemond, T. Henning (University of Arizona Press, Tuscon, 2014) p. 317

T. Hama, N. Watanabe, Surface processes on interstellar amorphous solid water: Adsorption, diffusion, tunneling reactions, and nuclear-spin conversion. Chem. Rev. **113**, 8783 (2013)

T. Henning, D. Semenov, Chemistry in protoplanetary disks. Chem. Rev. **113**, 9016 (2013)

E. Herbst, Chemistry in the interstellar medium. Annu. Rev. Astron. Astrophys. **46**, 27 (1995)

E. Herbst, E.F. van Dishoeck, Complex organic interstellar molecules. Annu. Rev. Astron. Astrophys. **47**, 427 (2009)

M.J. Mumma, S.B. Charnley, The chemical composition of comets – emerging taxonomies and natal heritage. Annu. Rev. Astron. Astrophys. **49**, 471 (2011)

T. Oka, Interstellar H_3^+. Chem. Rev. **113**, 8738 (2013)

N. Sakai, S. Yamamoto, Warm carbon-chain chemistry. Chem. Rev. **113**, 8981 (2013)

A.G.G.M. Tielens, The molecular universe. Rev. Mod. Phys. **85**, 1021 (2013)

E.F. van Dishoeck, G.A. Blake, Annu. Rev. Astron. Astrophys. **36**, 317 (1998)

E.F. van Dishoeck, E. Herbst, D.A. Neufeld, Interstellar water chemistry: From laboratory to observations. Chem. Rev. **113**, 9043 (2013)

J.P. Williams, L.A. Cieza, Protoplanetary disks and their evolution. Annu. Rev. Astron. Astrophys. **49**, 67 (2011)

Chapter 10
Appendix 1: Rotational Spectra of Molecules

In radio observations, rotational spectral lines of interstellar molecules are typically observed. Here, we briefly summarize the fundamentals of the rotational spectra of molecules. For further details, we refer the reader to textbooks discussing spectroscopy (Townes and Schawlow 1975; Gordy and Cook 1984; Hirota 2011).

10.1 Rigid Rotor

We regard a molecule as a rigid body specified by atomic positions expressed in Cartesian coordinates (x, y, z) with origin defined as the center of mass of the molecule. The classical energy of rotation for the molecule can then be represented using the moment of inertia tensor:

$$E_{\mathrm{rot}} = \frac{1}{2}\left(\omega_x, \omega_y, \omega_z\right)\begin{pmatrix} I_{xx} & I_{xy} & I_{xz} \\ I_{yx} & I_{yy} & I_{yz} \\ I_{zx} & I_{zy} & I_{zz} \end{pmatrix}\begin{pmatrix} \omega_x \\ \omega_y \\ \omega_y \end{pmatrix}, \tag{10.1}$$

where ω_i is the angular velocity around the ith axis. The diagonal elements of the tensor represent the moments of inertia around the x, y, and z axes. The off-diagonal elements are products of inertia defined, for instance, as

$$I_{xy} = -\sum_{j=1}^{N} m_j x_j y_j, \tag{10.2}$$

where m_j is the mass of the jth atom and N is the total number of atoms in the molecule. If the x, y, and z axes are appropriately chosen, the products of inertia become zero. Such axes can be found by diagonalizing the moment of inertia tensor. These axes are the principal axes and denoted a axis, b axis, and c axis in

S. Yamamoto, *Introduction to Astrochemistry*, Astronomy and Astrophysics Library 7, DOI 10.1007/978-4-431-54171-4_10

order of increasing moment of inertia about the axis. When the angular momenta around the principal axes, P_a, P_b, and P_c, are defined ($P_i = \omega_i I_{ii}\,;\, i = a\,,b\,,c$), the rotational energy can be represented as:

$$E_{\mathrm{rot}} = \frac{P_a^2}{2I_{aa}} + \frac{P_b^2}{2I_{bb}} + \frac{P_c^2}{2I_{cc}}. \tag{10.3}$$

10.2 Rotational Spectra of Diatomic and Linear Molecules

In the case of diatomic and linear molecules, there is no rotation around the a axis. Hence, the end-over-end rotation axis is always perpendicular to the molecular axis (the axis along the chemical bonds). Because $I_{bb} = I_{cc} = I$, the rotation energy can thus be written as:

$$E_{\mathrm{rot}} = \frac{1}{2I}\left(P_b^2 + P_c^2\right) = \frac{P^2}{2I}, \tag{10.4}$$

where P represents the total angular momentum. According to quantum theory, the eigenvalue of P^2 is given by $\hbar^2 J(J+1)$, where J is the rotational quantum number and $\hbar(= h/2\pi)$ is the Planck constant. Converting the rotational energy to frequency units, we have:

$$\frac{E_{\mathrm{rot}}}{h} = \frac{h}{8\pi^2 I} J(J+1) = BJ(J+1), \tag{10.5}$$

where B is called the rotational constant. Each rotational level is degenerate for a magnetic quantum number M_J by a factor of $(2J+1)$. The rotational energy levels of a diatomic/linear molecule are shown in Fig. 10.1. The wave function is represented by spherical harmonics.

If a molecule has an electric dipole moment, transitions between rotational levels are allowed. The transition moment can be represented as:

$$\mu \int \psi_f^* \cos\theta \psi_i d\tau, \tag{10.6}$$

where ψ_i and ψ_f are the wave functions of the initial and final levels of the transition, and θ is the angle between the dipole moment μ and the electric field of radiation. From this equation, the selection rule for a transition in a diatomic/linear molecule can be obtained: $\Delta J = \pm 1$. Hence, the transition frequency ν of the transition $J+1 \rightarrow J$ is given by:

$$\nu = 2B(J+1). \tag{10.7}$$

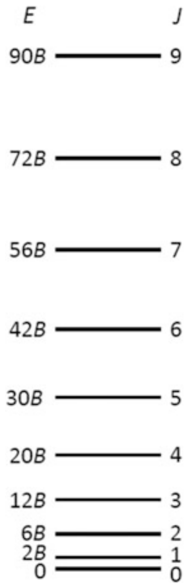

Fig. 10.1 Rotational levels of a diatomic or linear molecule B is the rotational constant

The rotational transitions appear at frequencies with a constant spacing of $2B$. Because B is specific to a molecular species, the rotational transition frequencies are specific to a particular molecule as well. Conversely, molecular species can be identified unambiguously from the rotational transitions.

In the above derivation, molecules are assumed to be rigid rotors. In reality, the molecular structure is slightly distorted by the centrifugal force of the rotation—called the centrifugal distortion effect. In quantum mechanics, this effect is regarded as a vibrational–rotational interaction, which can be treated by a second-order perturbation. The rotational energy and the transition frequency are modified as:

$$\frac{E_{\mathrm{rot}}}{h} = BJ(J+1) - DJ^2(J+1)^2 \tag{10.8}$$

and

$$\nu = 2B(J+1) - 4D(J+1)^3, \tag{10.9}$$

respectively, where D is the centrifugal distortion constant. For a diatomic molecule, the centrifugal distortion constant has the form:

$$D = \frac{4B^3}{\omega_{vib}{}^2}, \tag{10.10}$$

where ω_{vib} is the vibrational frequency. Since ω_{vib} is much larger than B, the contribution of the centrifugal distortion is very small. When the vibration–rotation interaction is considered, the rotational constant and the centrifugal distortion constants are averaged values for a particular vibrational state (e.g., the ground vibrational state). These constants therefore depend on the vibrational states.

10.3 Rotational Spectra of Symmetric-Top Molecules

If two out of the three moments of inertia of a nonlinear molecule are identical by symmetry, the molecule is referred to as a symmetric top. That is, a molecule having threefold or higher rotational symmetry is a symmetric top. If $I_{bb} = I_{cc}$, the molecule is called a prolate symmetric top; examples include CH_3CN and CH_3CCH. If $I_{aa} = I_{bb}$, however, the molecule is called an oblate symmetric top; examples include NH_3 and H_3^+. The rotation axis of a symmetric top is not always perpendicular to the symmetry axis, unlike a diatomic/linear molecule, because the molecule can rotate about its symmetry axis. Rotation about the symmetry axis becomes a constant of the motion for a symmetric top. Hence, the total angular momentum quantum number (J) and its projection onto the symmetry axis (k: $k = -J, -J+1, \cdots, J$) are good quantum numbers. For a prolate symmetric top, the eigenvalue for P_a is $\hbar k$, and hence, the rotation energy is given as

$$\frac{E_{\mathrm{rot}}}{h} = BJ(J+1) + (A-B)k^2 - D_J J^2(J+1)^2 - D_{JK} J(J+1)k^2 - D_K k^4, \tag{10.11}$$

where A and B are the rotational constants about the a axis and b axis, respectively:

$$A = \frac{h}{8\pi^2 I_{aa}} \tag{10.12}$$

and

$$B = \frac{h}{8\pi^2 I_{bb}}. \tag{10.13}$$

D_J, D_{JK}, and D_K denote the centrifugal distortion constants. Because the rotational levels of ±k are degenerate, we define the quantum number K as $K = |k|$. We then rewrite Eq. (10.12) as

$$\frac{E_{\mathrm{rot}}}{h} = BJ(J+1) + (A-B)K^2 - D_J J^2(J+1)^2 - D_{JK} J(J+1)K^2 - D_K K^4. \tag{10.14}$$

The wave function (ψ_{Jk}) is represented by a rotation matrix. For an oblate symmetric top, the symmetry axis is the c axis, and the rotational energy is represented as:

$$\frac{E_{\mathrm{rot}}}{h} = BJ(J+1) + (C-B)K^2 - D_J J^2 (J+1)^2 - D_{JK} J(J+1)K^2 - D_K K^4, \tag{10.15}$$

where C is the rotational constant about the c axis:

$$C = \frac{h}{8\pi^2 I_{cc}}, \tag{10.16}$$

and K ($=|k|$) represents the quantum number projected onto the c axis. The schematic energy-level diagrams for prolate and oblate symmetric tops are shown in Fig. 10.2.

Each rotational level is degenerate for a magnetic quantum number by a factor of $(2J+1)$. Furthermore, $\pm k$ degeneracy exists for all of the levels, except for the $K=0$ levels. The majority of symmetric-top molecules found in interstellar clouds contain three identical hydrogen nuclei around their symmetry axis. In this case, the nuclear spin degeneracies for the $k=3n$ and $k=3n\pm1$ levels are 4 and 2, respectively, because of Fermi statistics.

The selection rule for rotational transitions of symmetric-top molecules is $\Delta J = \pm 1$ and $\Delta K = 0$. Because the permanent dipole moment of a symmetric-top molecule is always oriented along the symmetric axis, rotation about the symmetric axis does not enable the molecule to interact with an electromagnetic field. Hence, the K-changing transition is forbidden. Then, the transition frequency ν of the transition $J+1 \rightarrow J$ for a symmetric-top molecule is given as:

$$\nu = 2B(J+1) - 4D_J(J+1)^3 - 2D_{JK}(J+1)K^2. \tag{10.17}$$

Although spectral lines with different K appear at almost the same frequency, they are slightly separated by the contribution of the D_{JK} term. The group of the

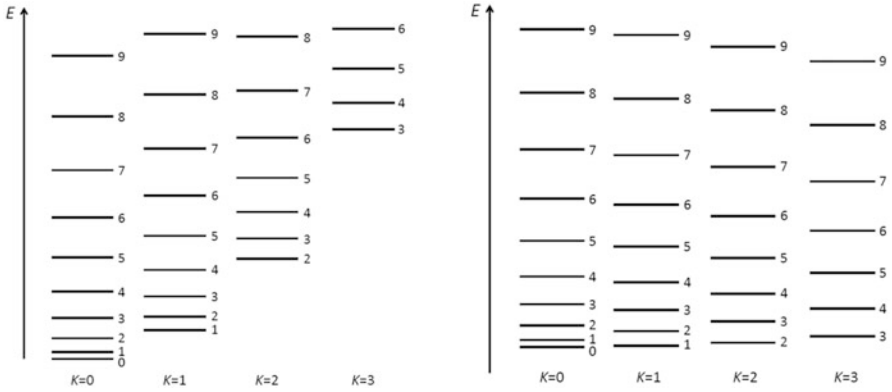

Fig. 10.2 Rotational levels for prolate (*left*) and oblate (*right*) symmetric-top molecules. The number to the right of each level is the corresponding total angular momentum quantum number, J

$J + 1 \rightarrow J$ transitions with different K values is called a K structure. The transition between different K levels is forbidden for a symmetric-top molecule, and hence, the population between them tends to be thermalized to the gas kinetic temperature of H_2 molecules in interstellar clouds. Because spectral lines with different K have significantly different upper state energies, an observation of the K structure is useful to determine the gas kinetic temperature.

10.4 Rotational Spectra of Asymmetric-Top Molecules

A molecule whose three principal moments of inertia are different from one another is referred to as an asymmetric top. Most nonlinear molecules found in interstellar clouds belong to this class. The Hamiltonian of the rotational motion of an asymmetric top takes the form

$$\frac{H}{h} = \frac{AP_a^2 + BP_b^2 + CP_c^2}{\hbar^2}, \tag{10.18}$$

where the centrifugal distortion terms are ignored for simplicity.

Here, we consider a molecule that is nearly a prolate symmetric top. Because A is much larger than B and C in this case, we modify Eq. (10.18):

$$\frac{H}{h} = \left(\frac{B+C}{2}\right)\frac{P_a^2 + P_b^2 + P_c^2}{\hbar^2} + \left(A - \frac{B+C}{2}\right)\frac{P_a^2}{\hbar^2} + \left(\frac{B-C}{2}\right)\frac{P_b^2 - P_c^2}{\hbar^2}. \tag{10.19}$$

The Hamiltonian matrix is constructed for each J state using the wave functions of a prolate symmetric top (ψ_{Jk_a}) as a basis set. Because the total angular momentum, $P^2 = P_a^2 + P_b^2 + P_c^2$, and its projection on the (hypothetical) symmetric axis (the a axis in this case), P_a, have eigenvalues of $\hbar^2 J(J+1)$ and $\hbar k_a$, respectively, the diagonal matrix elements of the Hamiltonian matrix are given as:

$$\left\langle \psi_{Jk_a}, \left|\frac{H}{h}\right|, \psi_{Jk_a} \right\rangle = \frac{B+C}{2} J(J+1) + \left(A - \frac{B+C}{2}\right) k_a^2. \tag{10.20}$$

In addition, the third term on the right-hand side of Eq. (10.19) can be expressed in terms of ladder operators P_+ and P_-:

$$\left(\frac{B-C}{2}\right)\frac{P_b^2 - P_c^2}{\hbar^2} = \left(\frac{B-C}{4}\right)\frac{P_+^2 + P_-^2}{\hbar^2}, \tag{10.21}$$

where

$$P_\pm = P_b \pm iP_c. \tag{10.22}$$

Table 10.1 Selection rules for asymmetric-top molecules[a]

Transition dipole moment	(K_a', K_c')-(K_a, K_c)	$(K_a', K_c') - (K_a, K_c)$.
μ_a	(even, even)−(even, odd)	(odd, even)−(odd, odd)
μ_b	(even, even)−(odd, odd)	(odd, even)−(even, odd)
μ_c	(even, even)−(odd, even)	(odd, odd)−(even, odd)

[a] The selection rule for J is $\Delta J = 0, \pm 1$. Note that the $J = 0$ to $J = 0$ transition is always forbidden

This term gives the off-diagonal elements in the Hamiltonian matrix between the levels whose k_a values differ by 2:

$$\left\langle \psi_{J,k_a} \left| \frac{H}{h} \right| \psi_{J,k_a \pm 2} \right\rangle = \left(\frac{B - C}{4} \right) \sqrt{J(J+1) - k_a(k_a \pm 1)} \times \sqrt{J(J+1) - (k_a \pm 1)(k_a \pm 2)}. \tag{10.23}$$

This term removes the degeneracy of the $\pm k_a$ levels. For each J, a Hamiltonian matrix of dimension $(2J + 1)$ is created and is numerically diagonalized to obtain the energy levels. In practice, the matrix can be factored into the four smaller matrices by symmetry. A molecule similar to an oblate symmetric top can be treated in a similar way using the projected quantum number of k_c.

The rotational energy levels of an asymmetric-top molecule are labeled $J_{K_a K_c}$, where K_a is the absolute value of the projection quantum number, k_a, when the molecule is regarded as a prolate symmetric top. Alternatively, K_c is the absolute value of the projection quantum number, k_c, when the molecule is regarded as an oblate symmetric top. If a molecule is similar to a prolate symmetric top, K_a is a good quantum number. If a molecule is, however, close to an oblate symmetric top, K_c is a good quantum number. For prolate tops, removing the $\pm k_a$ degeneracy is represented by K_c, because these two levels correlate with the rotational levels of an oblate symmetric top with different K_c, and vice versa for the oblate case. The selection rules depend on the direction of the dipole moment responsible for the transition, as summarized in Table 10.1. Transitions involving the a, b, and c components of the dipole moment are called a-type, b-type, and c-type transitions, respectively. In all cases, the total angular momentum quantum numbers have to be

$$\Delta J = 0, \pm 1. \tag{10.24}$$

A complex spectral pattern is usually observed for an asymmetric-top molecule. As an example, Fig. 10.3 shows the energy levels of c-C_3H_2.

10.5 Fine Structure in Rotational Transitions

If a molecule possesses unpaired electrons and/or a non-zero orbital angular momentum of its electrons, the angular momenta of the electron spin and orbital motion can couple with the angular momentum of the end-over-end rotation of the

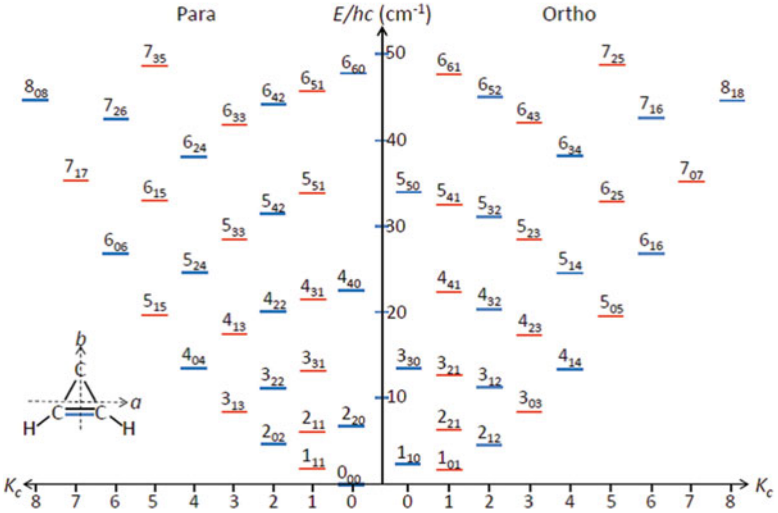

Fig. 10.3 Rotational energy levels of the asymmetric-top molecule cyclic C_3H_2. Because of the presence of identical hydrogen nuclei, the rotational energy levels are classified into ortho-species with (K_a,K_c) = (*even, even*) or (*odd, odd*) levels and para-species with (K_a,K_c) = (*even, odd*) or (*odd, even*) levels. Within each species, transitions between *red* levels and *blue* levels with $\Delta J = 0, \pm 1$ are allowed

molecule. This process results in the splitting of each rotational level and referred to as the fine structure. Physical mechanisms responsible for the fine structure include spin–rotation interaction, spin–spin interaction, and spin–orbit interaction. Here, we do not go into the details of these processes, but we instead briefly describe a few examples.

The electronic state of a diatomic/linear molecule is classified by the projection of its orbital angular momentum onto the molecular axis, Λ, and the total electron spin of S. The $\Lambda = 0$, 1, and 2 states are denoted Σ, Π, and Δ, respectively, and the electron spin multiplicity $(2S + 1)$ is appended as a left superscript to Σ, Π, and Δ. In case of the Σ state, the $\pm$ symmetry of the electronic wave function with respect to a plane involving the molecular axis is right superscripted. For instance, the $^2\Sigma^+$ state means that $\Lambda = 0$, $S = 1/2$, and the plane symmetry is positive. Examples of interstellar molecules having this electronic state include CN, CCH, and C_4H. The $^3\Sigma^-$ state means that $\Lambda = 0$, $S = 1$, and the plane symmetry is negative, where two unpaired electrons occupy different π orbitals. Representative interstellar molecules having this electronic state include NH, OH^+, SO, and CCS. The $^2\Pi$ state means that $\Lambda = 1$ and $S = 1/2$. Examples of interstellar molecules having such electronic states include CH, OH, NO, C_3H, C_5H, and C_6H.

In $^2\Pi$ molecules, the orbital motion of an unpaired electron around the molecular axis produces a magnetic field along it, and the electron spin couples to the molecular axis, either parallel or antiparallel to the magnetic field. This coupling is the spin–orbit interaction. If the projection of the electron spin is denoted by Σ

(note that this usage of Σ does not indicate the Σ state), the total projected angular momentum (Ω) can be written as:

$$\Omega = \Lambda + \Sigma. \tag{10.25}$$

The $^2\Pi$ state has two fine-structure levels with $|\Omega|=3/2$ and 1/2, depending on the orientation of the spin ($\Sigma = \pm 1/2$). These two states are well separated by the spin–orbit interaction as

$$E_{\mathrm{SO}} = A_{\mathrm{SO}} \Lambda \Sigma, \tag{10.26}$$

where A_{SO} is the spin–orbit interaction constant. If A_{SO} is positive, the $|\Omega|=1/2$ state has a lower energy than the $|\Omega|=3/2$ state. If A_{SO} is negative, the $|\Omega|=3/2$ state has a lower energy than the $\Omega=1/2$ state. Couplings of such angular momenta are called Hund's coupling case (a), where the total angular momentum and its projection onto the molecular axis are good quantum numbers (Fig. 10.4). Because the total angular momentum is the vector sum of the angular momentum of the end-over-end rotation, the orbital angular momentum of an unpaired electron, and the electron spin, it takes on half-integer values. The rotational energies for the $|\Omega|=1/2$ and 3/2 states are obtained from the crude approximation:

$$\frac{E_{\mathrm{rot}}}{h} = \left(B \pm \frac{B^2}{A_{\mathrm{SO}}}\right) J(J+1) = B^{\pm}_{\mathrm{eff}} J(J+1), \tag{10.27}$$

where the negative and positive signs correspond to the $|\Omega|=1/2$ and 3/2 states, respectively. Because the selection rule is $\Delta J = 0, \pm 1$, the lowest transitions for the $|\Omega|=1/2$ and 3/2 states appear at $3B^{-}_{eff}\left(J = \frac{3}{2} - \frac{1}{2}\right)$ and $5B^{+}_{eff}\left(J = \frac{5}{2} - \frac{3}{2}\right)$, respectively. All of the rotational levels are degenerate by a factor of 2 through

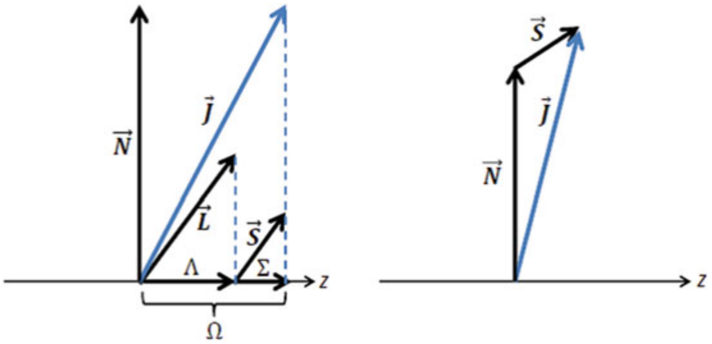

Hund's case (a) Hund's case (b)

Fig. 10.4 Coupling schemes of angular momenta for a molecule with orbital and spin angular momenta of electrons. The z axis is the molecular axis parity (i.e., the plane symmetry in this case), and this degeneracy is lifted by perturbation from the $^2\Sigma^{\pm}$ electronic excited states. This process is called Λ-type doubling. Hence, each rotational transition is split into two fine-structure levels (Λ-type doubling levels). In general, separation via Λ-type doubling is larger for the $|\Omega|=1/2$ state than for the $|\Omega|=3/2$ state. The Λ-type doubling of the $|\Omega|=3/2$ state is sometimes too small to be resolved. Furthermore, the splitting is larger for higher J states. The intensities of the two Λ-type doubling transitions are essentially the same. The energy-level structure of OH is shown in Fig. 10.5 as an example for a $^2\Pi$ molecule.

Because $\Delta J = 0$ is allowed, a transition between the Λ-type doubling levels with the same J is observed. This transition is called an Λ-type doubling transition. Although the separation of Λ-type doubling levels is on the order of 1–100 MHz for most cases, it becomes on the order of GHz or higher for light molecules. Such transitions are actually observed for OH and CH in the centimeter-wave regime.

In $^2\Sigma$ molecules, the coupling of the electron spin to the molecular axis is weak because of the absence of orbital angular momentum. The electron spin instead couples to the end-over-end rotation to form the total angular momentum (Hund's case (b) coupling: Fig. 10.4). This coupling is caused by a spin–rotation

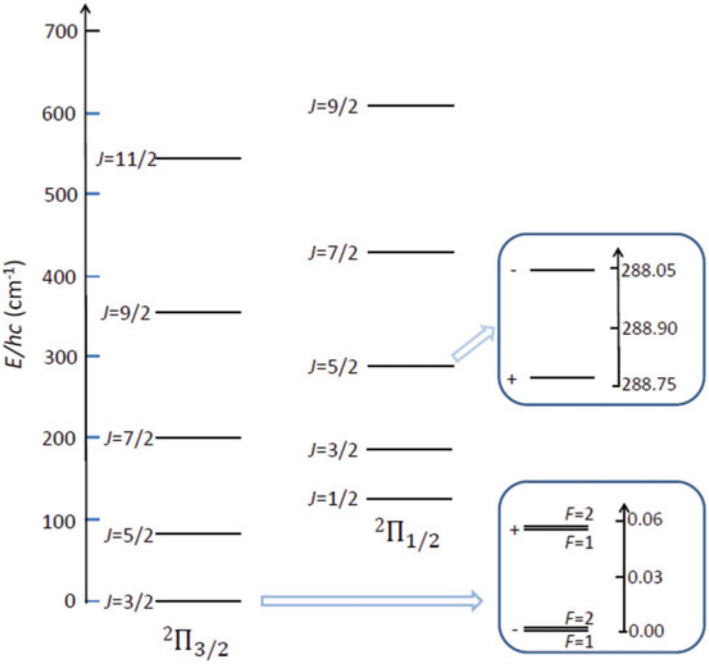

Fig. 10.5 Rotational energy levels of OH in the $^2\Pi$ ground electronic state. The coupling scheme of angular momenta is close to Hund's case (**a**), and hence there are two ladders of rotational levels, $^2\Pi_{1/2}$ and $^2\Pi_{3/2}$, which are well separated. For OH, the $^2\Pi_{3/2}$ state is lower than the $^2\Pi_{1/2}$ state because the spin–orbit interaction constant is negative. Each rotational level is split into two levels (+ and −) by Λ-type doubling, each of which is further split into two levels by hyperfine interactions due to the nuclear spin ($I=1/2$) of the hydrogen nucleus, depicted in the insets

interaction. Although this interaction is classically thought of as a coupling to the weak magnetic field caused by the rotational motion of molecule, it mainly arises from perturbations of the $^2\Pi$ electronic excited states. Because of the weak coupling of the electron spin, the angular momentum of the end-over-end rotation is still a good quantum number, in addition to the total angular momentum. The total angular momentum J is the vector sum of the rotational angular momentum N and the electron spin, and hence J can be $N+1/2$ and $N+1/2$ for each N. The energies for these states are obtained from

$$\frac{E_{\mathrm{rot}}(J=N+1/2)}{h}=BN(N+1)+\frac{\gamma N}{2}, \tag{10.28}$$

and

$$\frac{E_{\mathrm{rot}}(J=N-1/2)}{h}=BN(N+1)-\frac{\gamma(N+1)}{2}, \tag{10.29}$$

where γ is the spin–rotation interaction constant. This constant is much smaller than the rotational constant. The selection rule is $\Delta J=0, \pm 1$ and $\Delta N=\pm 1$, and the transition frequencies for the $(J+1, N+1)-(J, N)$ transition are given as:

$$\nu=2B(N+1)\pm\frac{\gamma}{2}, \tag{10.30}$$

where the plus and minus terms correspond to the $J=N+1/2$ and $J=N-1/2$ states, respectively. The $\Delta J=0$ transitions are typically very weak, except for low-N lines. The transitions approximately appear every $2B$ in frequency, as in the case of a diatomic/linear molecule without an electron spin. However, each transition is split into two components separated by γ. Because the two components have different total angular momenta, their intensities are different.

In the $^3\Sigma^-$ state, the coupling scheme is sometimes close to Hund's case (b) and sometimes to Hund's case (a). In the former, the rotation angular momentum is a good quantum number, and hence the energy-level structure is essentially the same as that for a diatomic/linear molecule, except that each rotational level is split into three fine-structure levels (one for $N=0$) due to spin–rotation and spin–spin interactions. The total angular momentum can be $J=N+1$, $J=N$, or $J=N-1$. The spectral pattern is similar to that of a diatomic/linear molecule, but each rotational transition is split into three main components. Among the three components, the $J=N$ state lines follow exactly the transition frequencies without being influenced by electron spin effects. Examples of such molecules include NH and OH^+.

In contrast, SO and CCS behave differently. The spin–spin interaction is essentially a second-order perturbation effect of the spin–orbit interaction, and hence the large spin–orbit interaction of the S atom enhances the spin–spin interactions of these molecules. For this reason, the electron spin tends to couple to the molecular axis rather than the rotational angular momentum, resulting in Hund's case (a). In this case, the total angular momentum and its projection are good quantum numbers. Because the projection quantum number Ω is 0 or ± 1, the energy levels are approximately separated by $|\Omega|$. The separation is 2λ, where λ is the spin–spin interaction constant. As the total angular momentum increases, the coupling between the spin and the rotation becomes important. Hence, the coupling changes from Hund's case (a) to Hund's case (b). The energy-level diagram for CCS is shown in Fig. 10.6. The complex nature of the energy-level structure of CCS prevented scientists from identifying this molecule in space and in the laboratory. Once the spectrum was fully characterized in the laboratory, many unidentified interstellar lines were assigned to this molecule.

For nonlinear molecules, Hund's case (b) can typically be applied, except for symmetric-top molecules in a degenerate electronic state. Hence, each rotational level is split into 2 or 3 for $S=1/2$ and 1, respectively. Although beyond the scope of this book, additional details of this process are in various textbooks on spectroscopy (Hirota 2011), as well as the original paper (Bowater et al. 1973).

10.6 Hyperfine Structure of Rotational Transitions

If a molecule has one or more nuclei with non-zero nuclear spins, the nuclear spins cause a further splitting in the energy levels and additional lines in the rotational spectra that result in the hyperfine structure. The hyperfine interaction is classified into two categories based on the physical mechanisms responsible for the interaction: one is magnetic in origin and the other stems from the nuclear quadrupole moment.

The magnetic hyperfine interaction includes (a) the nuclear spin–orbit interaction, (b) the nuclear spin–electron spin interaction (spin–dipolar interaction), (c) the Fermi contact term, (d) the nuclear spin–rotation interaction, and (e) the nuclear spin–nuclear spin interaction. The first three interactions are specific to free radicals (paramagnetic molecules), which have unpaired electrons and/or electron orbital angular momenta. Because the electron spin has a large magnetic moment, the interaction energy is typically larger than a few tens of MHz, depending on the nucleus and the electronic state. In contrast, the last two interactions are manifest in all molecules, including diamagnetic molecules. The nuclear spin–rotation interaction is usually less than 100 kHz, while the nuclear spin–nuclear spin interaction is much smaller (~kHz or less). Hence, the magnetic hyperfine interaction in diamagnetic molecules is nearly negligible, unless very high-resolution observations are conducted toward a quiescent cloud with a very narrow-line width. Nevertheless, a large hyperfine splitting of the rotational levels is often observed for free radicals.

If a nucleus has a nuclear spin of one or larger, it has an electric quadrupole moment. The electric quadrupole moment interacts with the electric field gradient around the nucleus and therefore with the end-over-end rotation of a molecule. This

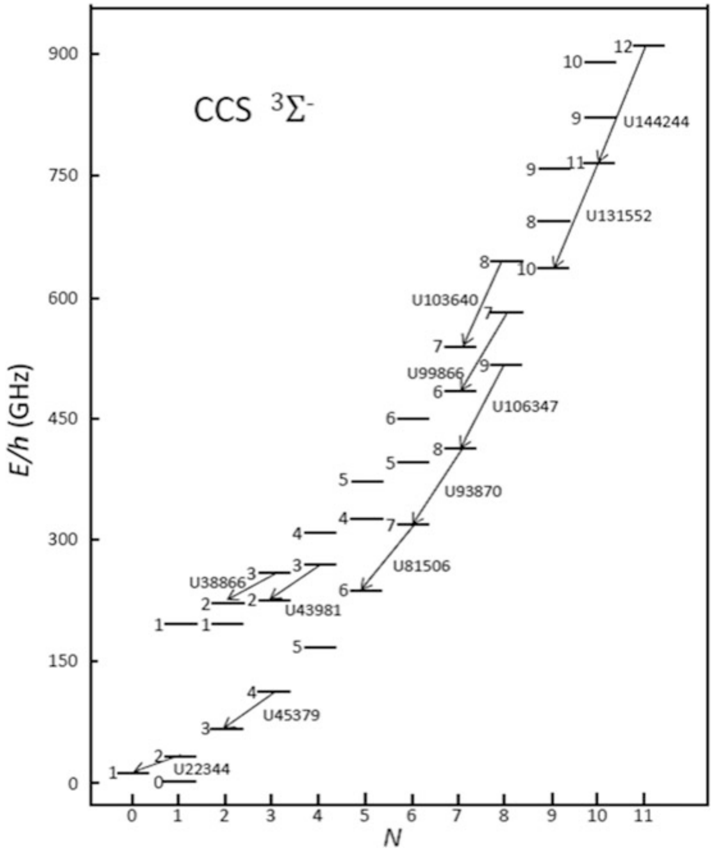

Fig. 10.6 Energy level diagram of CCS in the $^3\Sigma^-$ electric ground state. The numbers to the left of the levels are the quantum numbers for total angular momentum. Each rotational level is split into three fine-structure levels because of spin–spin interactions (Hund's case (**b**)). For low-*N* states, the energy-level structure obeys closely Hund's case (**a**), where each rotational level is split into two groups with a relatively large separation. Many unidentified lines indicated by the arrows are assigned to this molecule based on laboratory spectroscopic data

type of interaction is called the nuclear quadrupole interaction. The magnitude of this kind of interaction is typically a few MHz, depending on the nucleus. The ^{14}N nucleus, which has a nuclear spin of one, is important in radio astronomy. The hyperfine splitting due to the nuclear quadrupole interaction of the ^{14}N nucleus is observed in the low-*J* transitions of HC^{14}N and ^{14}NH$_3$. In contrast, HC^{15}N and ^{15}NH$_3$ exhibit no nuclear quadrupole interaction because ^{15}N has a nuclear spin of 1/2. The nuclear spin–rotation interactions of ^{14}N, ^{15}N, and H are much smaller, but they are sometimes recognizable as a broadening of the line width.

To specify the hyperfine levels, the following coupling scheme of the angular momenta is typically adopted. The rotational angular momentum (plus the electron spin and orbital angular momenta) is denoted as $\vec{J}$ in units of $\hbar$. The nuclear spin $\vec{I}$ then couples to $\vec{J}$ to form a total angular momentum $\vec{F}$:

$$\vec{F} = \vec{J} + \vec{I} \ . \tag{10.31}$$

F and J are typically good quantum numbers, and hence the hyperfine levels are represented by these numbers. When two nonequivalent nuclear spins are coupled, the following scheme is employed:

$$\vec{F}_1 = \vec{J} + \vec{I}_1 \tag{10.32}$$

and

$$\vec{F} = \vec{F}_1 + \vec{I}_2 \tag{10.33}$$

for the two-nuclear spin case. In this case, F, F_1, and J are used to specify the hyperfine levels. The selection rules of the rotational transitions are $\Delta F_1 = 0, \pm 1$ and $\Delta F = 0, \pm 1$. It is worth noting that the transitions with $\Delta F = \Delta F_1 = \Delta J$ are typically intense, except for low-J transitions. The calculations of hyperfine energy levels are beyond the scope of this book, and we refer the reader interested in the spectroscopy to Townes and Schawlow (1975), Gordy and Cook (1984), and Hirota (2011). An example of the fine- and hyperfine-level structures and the resultant spectral pattern for CCH is shown in Figs. 10.7, 10.8, and 10.9.

10.7 Internal Rotation and Inversion

Molecules consisting of N atoms have vibrational modes of $3N-6$ ($3N-5$ for linear molecules). Vibrational motions have much higher energies than rotational motions, and hence the effect of vibrational motions on rotational motions can be treated using perturbation theory. However, molecules often have slow internal motions, such as internal rotation and inversion. The energies of these internal motions are typically close to rotational energies. In this case, the rotational motion couples strongly to the slow internal motions, which makes the rotational spectrum complicated.

The internal rotation of the methyl group (CH_3) is a good example. Let us consider molecules having methyl group ($-CH_3$), such as CH_3OH, CH_3CHO, and CH_3NH_2. In these molecules, the methyl group can rotate around the C–O, C–C, and C–N single bonds (internal rotation). It is not a free rotation, but has the following effective potential as a function of the rotation angle of the methyl group (θ). Considering that the methyl group has threefold symmetry, the potential function can be approximated as

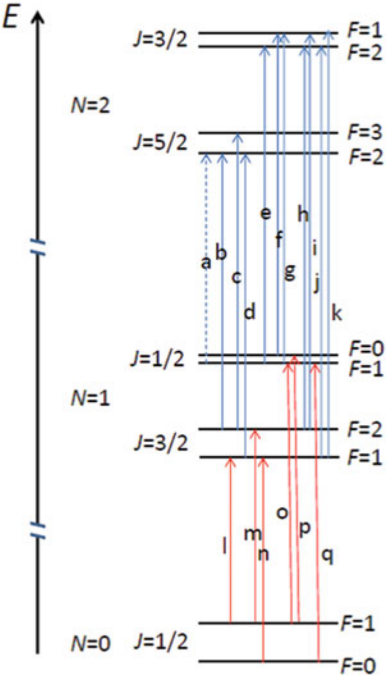

Fig. 10.7 Fine and hyperfine energy-level structure for the lowest three rotational states of CCH. Because this molecule has an unpaired electron, each rotational level except for the $N=0$ level is split into the two fine-structure levels labeled J. Because of the nuclear spin of the hydrogen nuclei, each fine-structure level is further split into the two hyperfine-structure levels labeled F. The allowed transitions are indicated by solid arrows, where each line is labeled with a letter corresponding to that in Figs. 10.6 and 10.7. The dashed arrow indicates a forbidden transition, the initial and final states are allowed by wave function mixing among the hyperfine levels

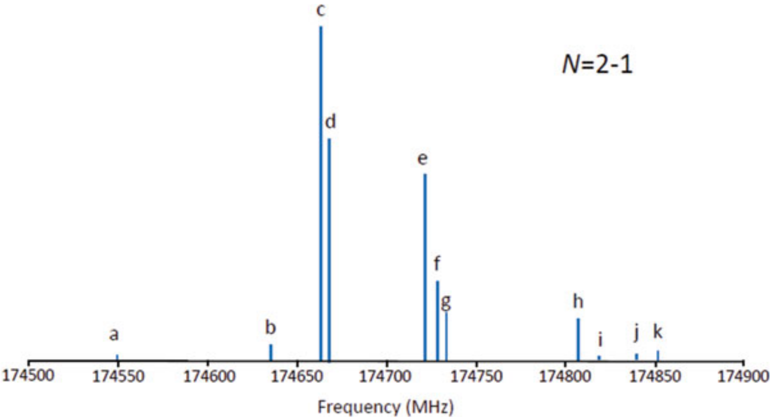

Fig. 10.8 Fine and hyperfine spectral pattern of the $N=2$–1 transition of CCH. The letters correspond to those in the energy-level diagram of Fig. 10.7

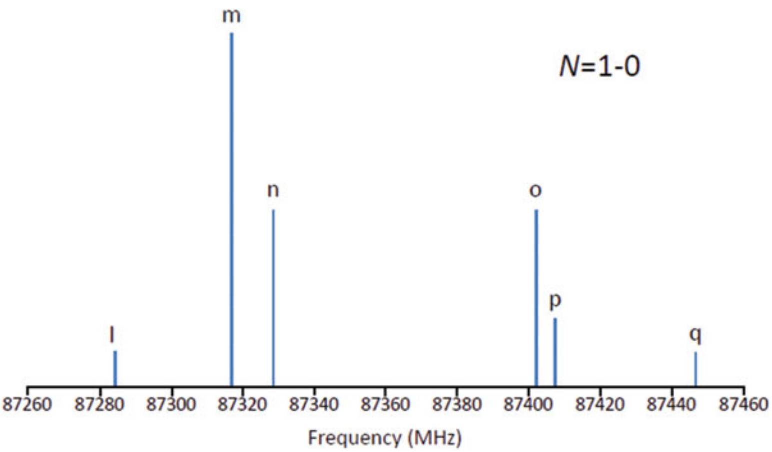

Fig. 10.9 Fine and hyperfine spectral pattern of the $N=1$–0 transition of CCH. The letters correspond to those in the energy-level diagram of Fig. 10.7

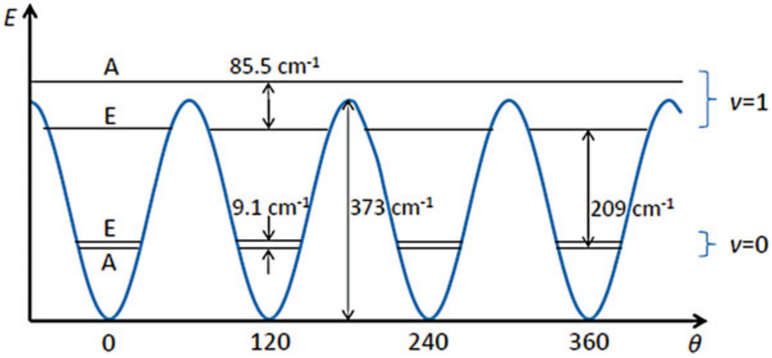

Fig. 10.10 Potential energy for the internal rotation of the CH_3 group of CH_3OH. The barrier to the internal rotation V_3 is 373 cm^{-1}. Above the barrier, the internal rotation is almost free

$$V = \frac{V_3}{2}(\cos 3\theta - 1) + (\text{higher order}), \tag{10.34}$$

where V_3 represents the barrier to the rotation. If V_3 is sufficiently high, the internal rotation can be regarded simply as the (small-amplitude) torsional motion localized around the three minimums of the potential. That is, the three eigenvalues of the three states are degenerate. Nonetheless, tunneling is possible for the low-V_3 case, and the wave functions of the three states are mixed. As a result, the degeneracy of the three states is lifted, and one non-degenerate state (the A state) and two doubly degenerate states (the E states) appear (Fig. 10.10). The overall wave function can be expanded using the wave functions of the localized states (ϕ_1, ϕ_2, and ϕ_3) as follows:

$$\psi(A) = \frac{1}{\sqrt{3}}(\phi_1 + \phi_2 + \phi_3), \tag{10.35a}$$

$$\psi(E) = \frac{1}{\sqrt{3}}\left(\phi_1 + e^{-\frac{2}{3}i\pi}\phi_2 + e^{-\frac{4}{3}i\pi}\phi_3\right), \tag{10.35b}$$

and

$$\psi(E) = \frac{1}{\sqrt{3}}\left(\phi_1 + e^{\frac{2}{3}i\pi}\phi_2 + e^{\frac{4}{3}i\pi}\phi_3\right), \tag{10.35c}$$

In detail, the CH_3 group is not rotating in the A state (ground state), whereas it is rotating either clockwise or counterclockwise in the E states. For this reason, the rotational energy-level structure is different between the A and E states (Fig. 10.11). The energy separation between the A and E states depends on the height of the barrier. We observe rotational spectral lines in the A and E states. When the energy separation between the A and E states is small, the frequency difference between the spectral lines of the A and E states is also typically small. Again, we note that calculations of the energy levels are beyond the scope of this book (e.g., see Gordy and Cook 1984).

NH_3 is characterized by many transitions in the centimeter-wave regime. However, these transitions are not pure rotational lines. Instead, they are inversion lines, which are a kind of vibration–rotation transition. Although the equilibrium structure of NH_3 is non-planar, the barrier to planar structure is relatively small (1770 cm^{-1}). Hence, the inversion motion occurs via quantum tunneling. The two equivalent non-planar states thus form mixed states, and the degeneracy of the two states is lifted. The wave functions are given as follows:

$$\psi(s) = \frac{1}{\sqrt{2}}(\phi_1 + \phi_2) \tag{10.36a}$$

$$\psi(a) = \frac{1}{\sqrt{2}}(\phi_1 - \phi_2), \tag{10.36b}$$

where ϕ_1 and ϕ_2 are the wave functions of the localized states. The s-state is more stable than the a-state; their energy separation, arising from the inversion motion, is about 0.8 cm^{-1}, and transitions between them are observed (inversion transitions). Note that inversion splitting does not appear in the $K = 0$ state, because the s- and a-states are not allowed for J =even and odd, respectively, because of the nuclear spin statistics of the three equivalent hydrogen nuclei (Townes and Schawlow 1975).

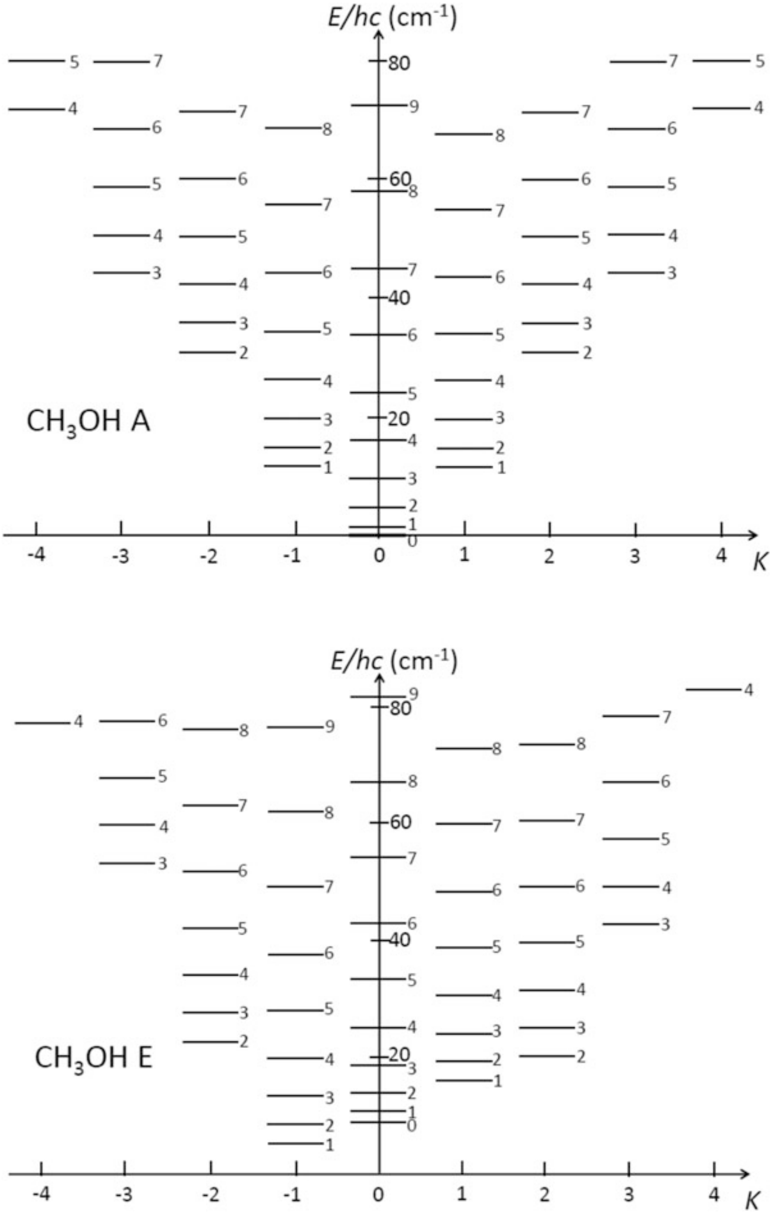

Fig. 10.11 Rotational energy-level diagrams for the A and E state of CH_3OH. Because of the internal rotation of the CH_3 group, the rotational energy levels in the E state are asymmetric with respect to the plus and minus signs of the quantum number *K*

References

I.C. Bowater, J.M. Brown, A. Carrington, Proc Roy Soc London A **333**, 265 (1973)
W. Gordy, R.L. Cook, *Microwave Molecular Spectra* (John Wiley & Sons, New York, 1984)
E. Hirota, *High-Resolution Spectroscopy of Transient Molecules* (Springer, Berlin, 2011)
C.H. Townes, A.L. Schawlow, *Microwave Spectroscopy* (Dover, 1975)

Chapter 11
Appendix 2: Observational Techniques

Radio observations are the most important way of observing interstellar molecules. Here, we briefly summarize the fundamentals of radio observation techniques and calibration methods of radio astronomy. Additional details can be found in the book written by Wilson et al. (2013).

11.1 Atmospheric Transmittance

Observations with ground-based telescopes are affected by absorption by water molecules (water vapor) and oxygen molecules in the atmosphere. In the millimeter-wave range, frequencies around 60 and 118 GHz are very opaque because of absorption by oxygen molecules, and the frequency around 180 GHz is opaque because of absorption by water vapor. The submillimeter-wave band is significantly more affected by the strong absorption by water vapor, as indicated in Fig. 11.1 (Matsushita et al. 1999). Submillimeter-wave observations are only possible in certain frequency bands, called "atmospheric windows." Hence, ground-based submillimeter-wave observations require a high-altitude and dry site. Atmospheric windows above 1000 GHz (1 THz) are very limited, and their transmittance is only 10–20 % under the best conditions from 5000 m sites in the Atacama Desert in Chile. Because water vapor is typically localized within a few km above the ground, the atmospheric transparency is significantly enhanced above altitudes of 10 km. Hence, observation from aircraft, balloons, and satellites are essential for observing frequencies higher than 1000 GHz.

Atmospheric molecules not only absorb signals from space but also add thermal noise. Here, the optical depth of the atmosphere at a certain frequency toward a certain line of sight is denoted as τ. The intensity observed through the atmosphere can then be represented as:

S. Yamamoto, *Introduction to Astrochemistry*, Astronomy and Astrophysics
Library 7, DOI 10.1007/978-4-431-54171-4_11

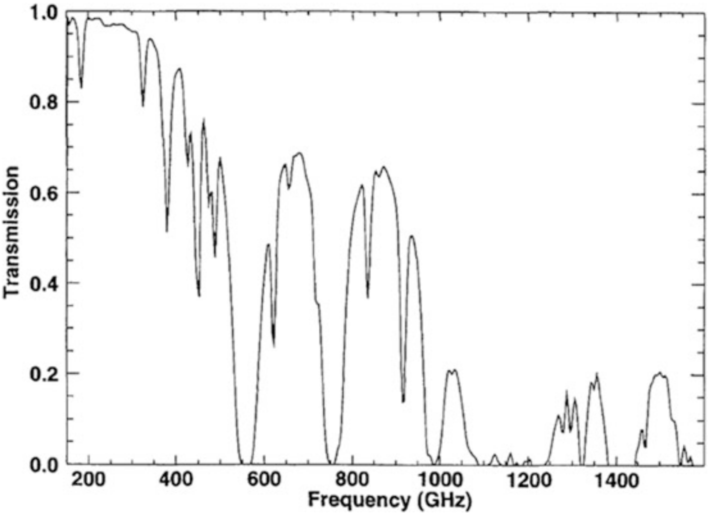

Fig. 11.1 Atmospheric transmission from Pampa la Bola in northern Chile (alt. 4800 m) observed with a Fourier transform spectrometer (Reprinted with permission from Matsushita et al. 1999)

$$T = T_0 \exp(-\tau) + T_{\mathrm{ATM}}\{1 - \exp(-\tau)\} + T_{\mathrm{RX}}, \tag{11.1}$$

where T_0 is the intensity outside the atmosphere, T_{ATM} the atmospheric temperature, and T_{RX} the noise temperature produced by the telescope system. The first term on the right-hand side represents the attenuation of the signal from space; the second and third terms are the noise added by the thermal emission of the atmosphere and the telescope noise, respectively. The equivalent noise temperature in observations outside the atmosphere is defined as:

$$T_{\mathrm{sys}} = T_{\mathrm{ATM}}\{\exp(\tau) - 1\} + T_{\mathrm{RX}} \exp(\tau), \tag{11.2}$$

where T_{sys} is called the system noise temperature. T_{sys} rapidly increases with increasing τ.

The optical depth of the atmosphere can be measured by observations of the noise temperature as a function of the zenith angle of the telescope. When we define the optical depth of the atmosphere toward the zenith as τ_0, the optical depth at a zenith angle of θ is:

$$\tau = \tau_0 \sec\theta, \tag{11.3}$$

assuming that the atmosphere is plane parallel. When we look at a direction without a celestial source emission, the intensity can be written as:

$$T = T_{\mathrm{ATM}}\{1 - \exp(-\tau_0 \sec\theta)\} + T_{\mathrm{RX}}. \tag{11.4}$$

The output power of a receiver P is typically measured instead of the absolute intensity:

$$P = f\{T_{\mathrm{ATM}}\{1 - \exp(-\tau_0 \sec\theta)\} + T_{\mathrm{RX}}\}, \tag{11.5}$$

where f is the proportionality constant specific to the telescope system. When we put an absorber (blackbody) at a temperature of T_{ABS} in front of the receiving system, the output power becomes:

$$P_{\mathrm{ABS}} = f\{T_{\mathrm{ABS}} + T_{\mathrm{RX}}\}. \tag{11.6}$$

When the absorber temperature T_{ABS} is assumed to be the atmospheric temperature T_{ATM}, we obtain:

$$P_{\mathrm{ABS}} - P = fT_{\mathrm{ATM}} \exp(-\tau_0 \sec\theta), \tag{11.7}$$

which can be re-expressed as:

$$\ln(P_{\mathrm{ABS}} - P) = \ln(fT_{\mathrm{ATM}}) - \tau_0 \sec\theta. \tag{11.8}$$

Hence, the zenith optical depth can be obtained by measuring the noise temperature as a function of the zenith angle.

Although this method is convenient, an apparent limitation is the assumption that the absorber temperature is the same as the atmospheric temperature. To overcome this limitation, the response to another absorber with a different temperature is measured. The output power for the second absorber is:

$$P'_{\mathrm{ABS}} = f\{T'_{\mathrm{ABS2}} + T_{\mathrm{RX}}\}. \tag{11.9}$$

Using Eqs. (11.6 and 11.9), f and T_{RX} can be determined; the optical depth of the atmosphere can then be evaluated using Eq. (11.5).

11.2 Antennas

For radio telescopes, a parabolic reflector with directivity is usually used to collect faint radio signals from space. The angular resolution of the telescope (θ) is determined by the diameter of the main reflector (D) and the wavelength (λ) of the observations:

$$\theta = \frac{k\lambda}{D}. \tag{11.10}$$

This θ value is also called as the beam size. Here, k is a constant determined by the illumination pattern on the main reflector. If all of the signals on the reflector are sent to the receiver with equal weights, k equals 1.02. In this case, θ becomes the minimum value (highest angular resolution). This resolution corresponds to that for Fraunhofer diffraction. However, diffraction at edges of the reflector becomes significant in this case, and the beam pattern of the telescope has undesirable side lobe levels. To reduce the side lobes, the illumination is usually reduced for the edge of the main reflector, resulting in k values varying from 1.2 to 1.5. Then, the angular resolution of a 10 m telescope at a wavelength of 3 mm is $80''$, if k equals 1.3.

To collect efficiently the plane waves from space at the focus of the main reflector, the deviation of the reflector surface from a parabolic shape has to be much less than the observational wavelength (λ). Typically, the standard deviation should be less than $\lambda/20$. For instance, the tolerance of the reflector surface of a telescope observing at a wavelength at 3 mm has to be better than 0.15 mm. Moreover, it should be maintained for a wide range of meteorological conditions (temperature change, wind, and sunshine) and for all ranges of elevation angle against gravitational deformation.

The surface accuracy and aperture illumination pattern of the main reflector mainly affect the collection efficiencies of the signal. The aperture efficiency η_A is defined as the fraction of the aperture area effectively used to detect plane waves relative to the geometrical surface area. The aperture efficiency is measured by observing point-like sources with known intensities such as quasars and planets. On the other hand, the main beam efficiency η_{MB} is defined as the fraction of power observed by the main beam of the telescope relative to the total power corrected by the telescope. This efficiency is important for observations of extended sources. The main beam efficiency can be determined by observing appropriate sources with known intensities whose spatial extents are comparable to the beam size. A low main beam efficiency implies a substantial contribution from the side lobes and hence is not suitable for observations of extended sources. Both the aperture efficiency and the main beam efficiency degrade as the surface accuracy degrades. For given surface accuracy, uniform illumination gives the highest aperture efficiency and the lowest main beam efficiency.

Pointing of the telescope has to be as accurate as 10–20 % of the telescope beam size at least. To ensure that this requirement is satisfied, calibration observations of point-like sources in pointing the telescope are usually conducted for a certain time interval (1–2 hours). The continuum emission of planets and quasars and the maser emission from late-type stars and star-forming regions are often used for calibration observations.

11.3 Receivers

11.3.1 Receiver Configuration

Radio waves collected by the telescope are fed into a receiver. Because the input power can be as small as 10^{-19}–10^{-21} W, it has to be amplified for detection and

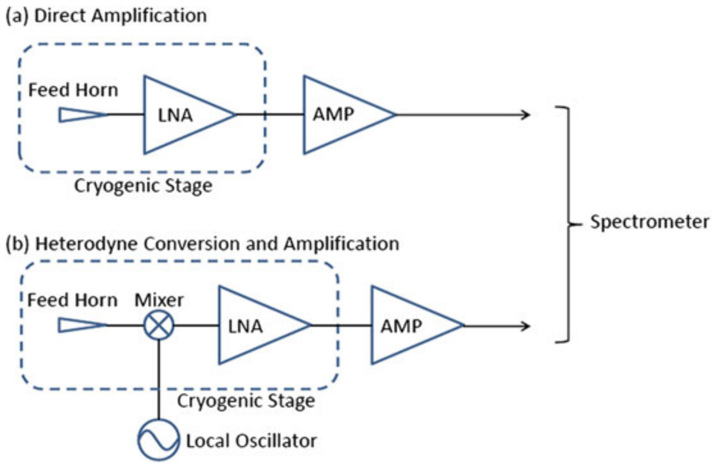

Fig. 11.2 Block diagram of a receiver. LNA is the low-noise amplifier, and AMP is the room temperature amplifier. Below 100 GHz, direct amplification is feasible; above 100 GHz, the heterodyne mixing technique is employed. Superconducting devices such as SIS mixers and HEB mixers are commonly used in heterodyne mixing

spectroscopic analyses. Below 100 GHz, the input signal can be amplified by low-noise high-electron mobility transistor amplifiers (Fig. 11.2a). The input equivalent noise of the receiver system is determined by the noise of the first-stage amplifier:

$$T_{\mathrm{RX}} = T_1 + \frac{1}{G_1}T_2 + \frac{1}{G_1 G_2}T_3 + \ldots, \tag{11.11}$$

where T_i and G_i represent the noise temperature and the gain of the i-th-stage amplifier, respectively. Hence, the first-stage amplifier is usually cooled down to 20 K or lower to reduce noise.

At frequencies above 70 GHz, low-noise direct amplification becomes more and more difficult. Low-noise amplifiers usable in such high frequencies are still in the developmental stages. Hence, the heterodyne technique is usually employed, in which the incoming signal (ν) is coherently converted to a lower-frequency signal (intermediate-frequency (IF) signal: ν_{IF}) by mixing it with the local oscillator signal (ν_{LO}) using nonlinear devices (Fig. 11.2b). Because the relation

$$\nu_{\mathrm{IF}} = |\nu - \nu_{\mathrm{LO}}| \tag{11.12}$$

holds, the receiver is sensitive to the input frequencies of $\nu = \nu_{\mathrm{LO}} \pm \nu_{\mathrm{IF}}$ for a given ν_{IF} and ν_{LO}. The higher frequency is called the upper side band (USB), and the lower frequency is called the lower side band (LSB) (Fig. 11.3). If the receiver is sensitive to the sum of the USB and LSB, it is called a double-side-band receiver. If the receiver is sensitive to only one of these frequencies by using an input filter or a

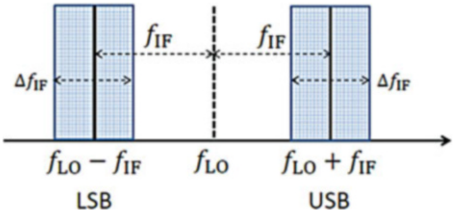

Fig. 11.3 Heterodyne receivers can be sensitive to two frequencies for a given intermediate frequency (f_{IF}). The higher (lower) frequency is called the USB (LSB)

sophisticated mixing technique using two mixers, it is called a single-side-band (SSB) receiver. If the receiver observes the USB and LSB separately at the same time, it is called a side-band-separating receiver. Regardless, the receiver noise temperature can be expressed by Eq. (11.11). In a heterodyne receiver, the mixer is regarded as the first-stage "amplifier" with a gain G_1 of less than unity. The conversion gain, which is the inverse of the conversion loss, is typically on the order of 0.1, and hence the noise of the second stage (the first IF amplifier) can significantly contribute to the receiver noise.

For nonlinear devices (mixers), GaAs Schottky barrier diodes, superconductor–insulator–superconductor (SIS) mixers, and superconducting hot electron bolometer (HEB) mixers are used. The Schottky barrier diode mixer is an older device, and nowadays SIS mixers are typically used in the millimeter- and submillimeter-wave regime below 1 THz; HEB mixers are employed for higher frequencies.

11.3.2 SIS Mixers

A classical interpretation of the operation principle of an SIS mixer is briefly outlined here. A SIS mixer uses the Josephson junction of a superconductor, where a very thin insulator layer is sandwiched between two superconductive films. When a DC voltage is applied to the junction, a tunneling current appears if the applied voltage is higher than twice the superconducting gap energy. However, the tunneling current is observed even below the above threshold voltage, if the local oscillator signal is applied. In this case, the photon energy of the local oscillator signal assists the tunneling, which is referred to as photon-assisted tunneling (PAT) (see Fig. 11.4). When the input signal from the antenna is applied to the SIS mixer in a PAT state, the total power fed into the mixer varies at an intermediate frequency of $|\nu - \nu_{LO}|$. Hence, the tunneling current by PAT follows this variation, and the intermediate-frequency signal can be extracted by filtering the input and local oscillator signals. A quantum theory of the SIS mixer is presented in Tucker and Feldman (1985).

Most SIS mixers for millimeter- and submillimeter-wave regimes employ Nb as the superconducting material. The Nb/AlOx/Nb Josephson junction shows a very good noise temperature performance. The receiver noise temperature is sometimes as low as a few times the quantum noise (e.g., Kojima et al. 2009). The SSB mixer

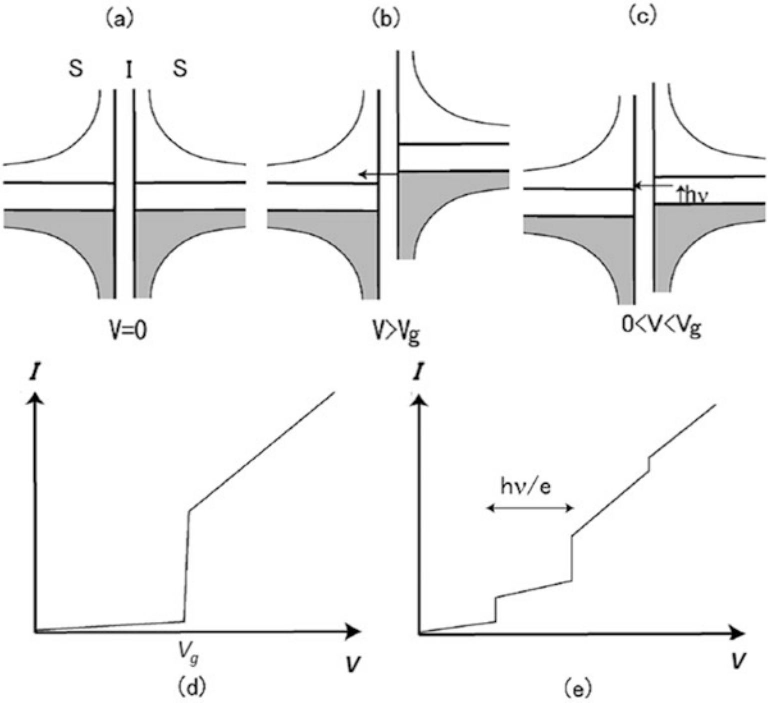

Fig. 11.4 Operation of an SIS mixer. The upper panels show a semiconductor model of the density of state of the SIS junction. If the bias voltage exceeds the gap energy, a tunneling current flows (**a**, **b**). Even for a bias voltage lower than the gap energy, the tunneling current appears assisted by energy from photons (**c**). The current (I)–voltage (V) curve of the SIS junction without the local oscillator signal is shown in (**d**), whereas that with the local oscillator signal with frequency of ν is shown in (**e**)

and the side-band-separating mixer can also be realized using two SIS mixes. In this case, the input signal (or the local oscillator signal) is divided into the two mixers with a phase shift of 90°, and the two intermediate-frequency outputs are merged with phase shifts of ±180° to extract the USB and LSB signal separately (e.g., Nakajima et al. 2008).

11.3.3 HEB Mixers

Unfortunately, SIS mixers generally do not perform well above twice the superconducting gap frequency because the input photons are directly absorbed by the gap. For Nb, twice the gap frequency is 700 GHz. Hence, superconducting materials with a larger gap frequency, e.g., NbN and NbTiN, have to be used for

Fig. 11.5 Schematic of the HEB mixer device. A superconducting microbridge structure with a typical size of 0.1–1 μm is connected to gold electrodes. The bottom left panel shows the *I*–*V* curve. When the local oscillator signal is fed into the HEB mixer, the *I*–*V* curve changes (*solid line* of *bottom right* panel). When the local oscillator power is increased further, the dashed line *I*–*V* curve is observed

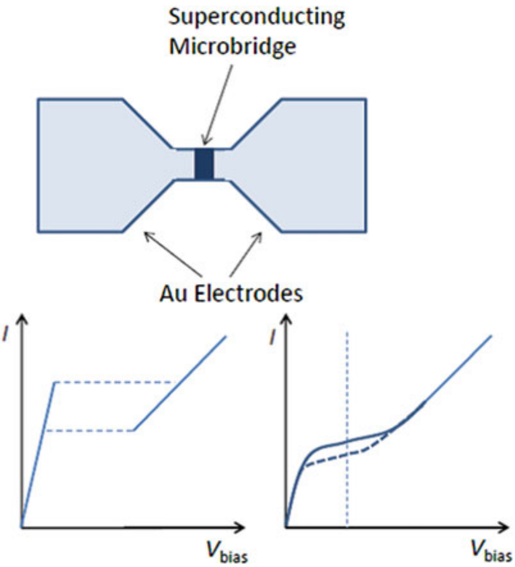

higher frequencies. Even in these cases, the upper limit to the frequency is still around 1.2 THz.

For higher-frequency regimes (THz), HEB mixers are mainly used as low-noise mixer devices. In contrast to SIS mixers, HEB mixers use the absorption of the input signal by a small superconducting microbridge (Fig. 11.5). When the input signal and the local oscillator signal are fed into a HEB mixer, the size of a hot spot where the superconducting state is broken varies at the intermediate frequency. The resistance of the microbridge thus varies at the intermediate frequency, and hence the intermediate-frequency signal is extracted as the biasing current. For this mechanism to work, hot electrons generated in the microbridge by absorption of the THz signals have to be cooled much faster than the period of the intermediate frequency. The cooling mechanism depends on which superconducting materials are used. For NbN or NbTiN, the hot electrons are usually cooled by interactions with phonon, and the phonon energy is finally transferred to the substrate. In contrast, the hot electrons directly escape to the electrodes for Nb and Al mixers. Phonon-cooling HEB mixers using NbN and NbTiN exhibit very good performance in the THz regime, although their intermediate-frequency range is not as wide as SIS mixers (e.g., Semenov et al. 2009; Tretyakov et al. 2011; Meledin et al. 2009; Shiino et al. 2015).

11.3.4 Measurements of Receiver Noise Temperature

The receiver noise temperature T_{RX} can be evaluated as follows. Two blackbodies with different temperatures, T_{H} and T_{L}, are alternately put in front of the receiver, producing receiver output powers of V_{H} and V_{L}, respectively. Using Eqs. (11.6 and 11.9), we obtain:

$$T_{\mathrm{RX}} = \frac{T_{\mathrm{H}} - YT_{\mathrm{L}}}{Y - 1}, \tag{11.13}$$

where $Y = V_{\mathrm{H}}/V_{\mathrm{L}}$. This method is called the Y-factor method. A room temperature absorber is typically used for T_{H}; the absorber cooled by liquid N_2 is used for T_{L}.

11.4 Radio Spectrometers

The output of the receiver (IF signals) conserves the spectroscopic information within the intermediate-frequency range. After sufficient amplification, the IF signals undergo spectroscopic analysis. This situation differs significantly from spectroscopic observations at other wavelengths, e.g., infrared, optical, and X-rays, where the spectroscopic devices such as gratings, prisms, and interferometers are always set in front of the detector devices.

The IF range of a SIS receiver can be from 4 to 12 GHz for each side band. Hence, part or all of the 8 GHz range is divided into many spectral channels, for which the frequency widths are a few kHz to a few MHz. The required resolution depends on the purposes of the observations (and target sources). In the early years of radio astronomy, a filter-bank spectrometer, consisting of a number of narrowband filters, was often used. Nowadays, two types of radio spectrometers are mainly employed.

1. Acousto-optical radio spectrometer (AOS): The intermediate-frequency signal is converted to an ultrasonic wave traveling through a crystal. Because an ultrasonic wave is a compressional wave, it produces a tentative diffraction grating in the crystal. The diffraction of the laser beam of this crystal is observed by a CCD array. The diffraction angle and intensity depend on the frequency and the intensity of the incoming signal, respectively. We then can directly observe the spectrum of the input signal. The AOS is a compact and reliable spectrometer that was used even in space missions. However, the spectral resolution and the bandwidth cannot be changed.
2. Autocorrelation spectrometer: The autocorrelation function can be obtained by taking the correlation between the input signal and the corresponding signal delayed by a time t. By Fourier transforming the autocorrelation function, we can obtain the power spectrum. The sampling interval of the delay determines the bandwidth; the longest delay determines the spectral resolution. These values can easily be changed following an observation request. Owing to the rapid development of digital technologies, this type of spectrometer has become standard for large-scale spectrometers.

11.5 Aperture Synthesis

At a wavelength of 3 mm, the spatial resolution of a 100 m radio telescope is about 7″. To achieve a higher spatial resolution, a radio telescope with a larger aperture is necessary. However, it is in practice difficult to realize such a large single-dish telescope with a good surface accuracy for millimeter- and submillimeter-wave observations. Instead, many small antennas can be distributed over a few hundreds of meters to a few tens of kilometers and used to observe the same object. By taking the interference of the signals detected with different antennas, a source image can be synthesized with a high spatial resolution that almost corresponds to the resolution obtained from a single-dish telescope with an aperture size of the extent of the maximum antenna separation. This method is called aperture synthesis, and such a telescope system is called an interferometer.

First, recall the famous interference experiment by Thomas Young (e.g. Born and Wolf 1974) (Fig. 11.6). The first slit defines the source size and position. The second pair of slits corresponds to two antennas with which the source is observed. The interference of the signals observed by the two antennas is recorded on a screen. For a radio interferometer, this last step can be completed using electric circuits. If the source is point-like, a clear interference fringe is observed on the screen. If, however, the source is slightly extended, the interference fringe is less visible, inferring that the amplitude of the interference fringe possesses information about the source size. If the position of the point source is slightly shifted from the center of the two slits (antennas), the interference fringe on the screen shifts in the opposite direction to the spatial shift, inferring the phase of the interference fringe possesses information about the source position. Hence, the interference fringe contains information about the source structure.

The relation between the visibility of the interference fringe and the source distribution is given by the van Cittert–Zernike theorem (e.g., Born and Wolf 1974). Consider the intensity distribution of the source as $I(\theta, \varphi)$, where $\theta = \xi/R$ and $\varphi = \eta/R$ (Fig. 11.7). When the radio waves detected at P_1 and P_2 are represented as $E_1(t)$ and $E_2(t)$, respectively, the mutual intensity $\langle E_1{}^*(t)\, E_2(t)\rangle$, which is related to the visibility of the interference fringe, can be written in terms of $I(\theta, \varphi)$ as:

$$J(u,v) = \left\langle E_1{}^*(t)\, E_2(t)\right\rangle = \int_S^{\nu} I(\theta,\varphi)\exp[-2\pi i(u\theta + v\varphi)]d\theta d\varphi, \tag{11.14}$$

where

$$u = \frac{x_1 - x_2}{\lambda}, \tag{11.15}$$

and

$$v = \frac{y_1 - y_2}{\lambda}. \tag{11.16}$$

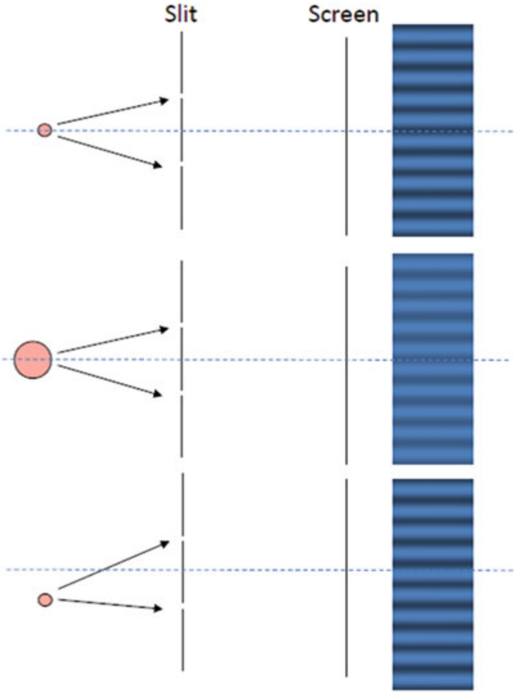

Fig. 11.6 A schematic illustration of Young's experiment. In radio astronomy, two slits correspond to two antennas, and the interference is taken by using electric circuits. (*Top*) Monochromatic point source is placed on a perpendicular bisector line of the two slits. (*Middle*) Monochromatic extended source is placed instead of a point source. In this case, visibility of the interference fringe on a screen is reduced. (*Bottom*) Monochromatic point source is placed on a position slightly offset from a perpendicular bisector line of the two slits. In this case, phase of the interference fringe on a screen changes. Hence, the visibility of the interference fringes possesses information on a source structure

In addition, $\langle X \rangle$ represents the time average. From $J(u, v)$ measured for various $(u,\ v)$, the source distribution $I(\theta, \varphi)$ can be obtained by the inverse Fourier transformation. To obtain a good-quality image of the source distribution, the $(u,\ v)$ coverage should be as complete as possible. Sparse (u, v) coverage will significantly reduce the quality due to an imperfect Fourier transformation. In this sense, a larger number of antennas provide a better image. In regard to ALMA, situated in the Atacama Desert in northern Chile, 50 12 m antennas are used simultaneously for observations.

In aperture synthesis observations, the spatial resolution of the image is determined by the distance of the longest baseline; the field of view is determined by the beam size of the element antennas. For instance, ALMA realizes a spatial resolution of $0.1''$ at 350 GHz with a baseline of 1 km, and the field of view at this frequency is $14''$. The detection sensitivity toward a point source is proportional to the total collecting area of all the antennas. In this sense, the sensitivity is higher for a larger

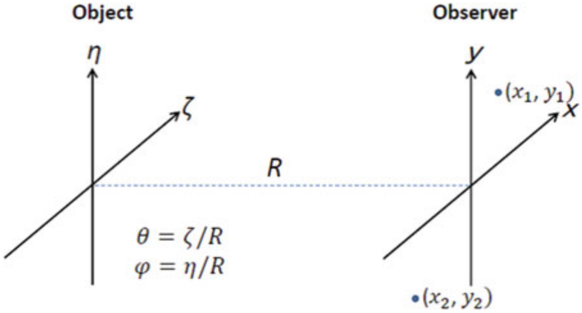

Fig. 11.7 Coordinate system for the van Cittert–Zernike theorem

number of antennas. It should be noted that the interferometer is not sensitive to extended components with sizes larger than that determined by the shortest baseline. This fact can readily be understood by the observation that no interference fringe appears when the first slit of Young's experiment is removed. Therefore, the interpretation of the aperture synthesis data requires focusing on this point. To overcome this difficulty, short baseline data and single-dish data ($(u, v) = (0, 0)$) have to be combined with interferometric data before Fourier transforming.

11.6 Intensity Calibrations

A source is continuously tracked during observations, and frequency corrections are applied for the Doppler motion due to the Earth's rotation, its orbital motion, and the motion toward the solar apex. The observed intensity is affected by the atmospheric attenuation. When the telescope points toward a source, the output power of the receiver can be written as:

$$V_{\mathrm{on}} = f[T_0 \exp(-\tau) + T_{\mathrm{ATM}}\{1 - \exp(-\tau)\} + T_{\mathrm{RX}}], \tag{11.17}$$

where the intensity from the source measured outside the atmosphere is represented by T_0, and the optical depth of the atmosphere at the measuring frequency is denoted by τ. On the other hand, the output voltage of the receiver toward an off-source position is given as:

$$V_{\mathrm{off}} = f[T_{\mathrm{ATM}}\{1 - \exp(-\tau)\} + T_{\mathrm{RX}}]. \tag{11.18}$$

For the intensity calibrations, the absorber is inserted in front of the receiver. In this case, the output voltage becomes:

$$V_{\mathrm{ABS}} = f[T_{\mathrm{ATM}} + T_{\mathrm{RX}}], \tag{11.19}$$

where the absorber temperature is assumed to be the same as the atmospheric temperature. In this approximation, we can derive the intensity as:

$$T_0 = \frac{V_{\mathrm{on}} - V_{\mathrm{off}}}{V_{\mathrm{ABS}} - V_{\mathrm{off}}} \times T_{\mathrm{ATM}} \equiv T_A^*. \tag{11.20}$$

This method is called the chopper wheel method. T_A^* is the antenna temperature corrected for atmospheric attenuation. To derive the main beam temperature, T_A^* should be divided by the main beam efficiency, η_{MB}. For even more accurate measurements, the two temperature calibrations discussed in Sect. A2.1 can be used to determine the T_{RX} and τ values directly for corrections. For aperture synthesis, point sources with known intensities such as quasars and satellites of Solar System planets can be observed for intensity and phase calibrations.

The input equivalent system noise temperature including the atmospheric attenuation is defined by Eq. (11.2) and can be measured as:

$$T_{\mathrm{sys}} = \frac{V_{\mathrm{off}}}{V_{\mathrm{abs}} - V_{\mathrm{off}}} \times T_{\mathrm{ATM}}, \tag{11.21}$$

where again the absorber temperature is assumed to be the same as the atmospheric temperature. The system noise temperature rapidly increases as the optical depth of the atmosphere increases. The rms noise of the spectrum depends on the system noise temperature, the resolution bandwidth of the back end, and the on-source integration time t. In position-switching observations, the rms noise can be represented as:

$$\delta T = \frac{\sqrt{2} T_{\mathrm{sys}}}{\sqrt{Bt}}. \tag{11.22}$$

As is evident from this relation, the integration time necessary to obtain a certain noise level is reduced by a factor of 4 if the system temperature can be decreased by a factor of 2. Note that the total telescope time has to include the integration time for the off-position and the overhead time for telescope movements in position-switching observations. Hence, the total telescope time is approximately 2.5–3 times the on-source integration time. Moreover, the observational conditions (atmospheric conditions) should be as stable as possible during the on-source and off-source observations, otherwise, baseline distortion appears, and the intensity calibration is not as accurate as would be expected. In this regard, the switching time should carefully be chosen, depending on the atmospheric conditions. This caution is particularly important for submillimeter-wave observations.

To save the off-position time, the frequency-switching method is often employed for spectroscopic observations of narrow-line sources. In this case, the frequency is shifted by a few MHz to a few tens of MHz while tracking the source, and the data are used for the off-position. Because the line for the “off-position” appears in different spectrometer channels, it can be used to improve the signal-to-noise ratio. In this case, the rms noise can be written as:

$$\delta T = \frac{T_{\text{sys}}}{\sqrt{Bt}}. \tag{11.23}$$

Except when tracking the source, moving the telescope is not necessary for the frequency-switching technique, and hence observations are more efficient than when position switching is used. A drawback of the frequency-switching technique is its baseline distortion, which is sometimes too strong to be subtracted.

References

M. Born, E. Wolf, *Principles of Optics* (Pargamon Press, Oxford, 1974)

T. Kojima, M. Kroug, M. Takeda, Y. Uzawa, W. Shan, Y. Fujii, Z. Wang, H. Ogawa, Appl. Phys. Express **2**, 102201 (2009)

S. Matsushita, H. Matsuo, J.R. Pardo, S.J.E. Radford, Publ. Astron. Soc. Jpn. **51**, 603 (1999)

D. Meledin, A. Pavolotsky, V. Desmaris, I. Lapkin, C. Risacher, V. Perez, D. Henke, O. Nystrom, E. Sundin, D. Dochev, M. Pantaleev, M. Fredrixon, M. Strandberg, B. Voronov, G. Gol'tsman, V. Belitsky, IEEE Trans. Microwave Theory Tech. **57**, 89 (2009)

T. Nakajima, M. Kawamura, K. Kimura, Y. Yonekura, H. Ogawa, T. Sakai, N. Kuno, M. Tsuboi, S. Asayama, T. Noguchi, Publ. Astron. Soc. Jpn. **60**, 435 (2008)

A. Semenov, B. Gunther, U. Bottger, H.W. Hubers, H. Bartolf, A. Engel, A. Schilling, K. Ilin, M. Siegel, R. Schneider, D. Gerthsen, N.A. Gippius, Phys. Rev. B **80**, 054510 (2009)

T. Shiino, R. Furuya, T. Soma, Y. Watanabe, T. Sakai, L. Jiang, H. Maezawa, T. Yamakura, N. Sakai, S. Yamamoto, J. Japanese, Appl. Phys. **54**, 033101 (2015)

I. Tretyakov, S. Ryabchun, M. Finkel, A. Maslennikova, N. Kaurova, A. Lobastova, B. Voronov, G. Gol'tsman, Appl. Phys. Lett. **98**, 033507 (2011)

J.R. Tucker, M.J. Feldman, Rev. Mod. Phys. **57**, 1055 (1985)

T.L. Wilson, K. Rohlfs, S. Huttemeister, *Tools of Radio Astronomy* (Springer Science & Business Media, Berlin, 2013)

Chapter 12
Solution to Problems

Chapter 2

2.1

The energy flowing through regions dS_1 and dS_2 are given as

$$dE_1 = I_{\nu 1} dS_1 dt d\nu d\Omega_1$$

and

$$dE_2 = I_{\nu 2} dS_2 dt d\nu d\Omega_2.$$

If all rays passing through dS_1 also pass through dS_2, we obtain the following relations:

$$d\Omega_1 = \frac{dS_2}{R^2}, d\Omega_2 = \frac{dS_1}{R^2}$$

and

$$dE_1 = dE_2.$$

Therefore,

$$I_{\nu 1} = I_{\nu 2.}$$

2.2

The partial differential of the Planck function with respect to T gives

S. Yamamoto, *Introduction to Astrochemistry*, Astronomy and Astrophysics Library 7, DOI 10.1007/978-4-431-54171-4_12

$$\frac{\partial B_\nu(T)}{\partial T} = \frac{2h^2\nu^4}{c^2kT^2}\frac{\exp(h\nu/kT)}{[\exp(h\nu/kT)-1]^2} > 0.$$

Hence, the Planck function, $B_\nu(T)$, monotonically increases as increasing T.

2.3

Using Eq. (2.40), we obtain an equation for the optical depth of the ^{13}CO line:

$$\frac{\exp(-\tau_{13})}{1-\exp(-0.1054\tau_{13})} = 3.$$

Solving this equation numerically yields a value for τ_{13} of 3.73. The excitation temperature is thus determined to be 6.14 K.

2.4

By combining Eqs. (2.29), (2.33), and (2.34), we obtain an expression for τ_{ul} in terms of the Gaussian line shape function $\phi(\nu)$:

$$\tau_{ul} = \frac{8\pi^3 S_{ul}\mu^2}{3hU(T)}\frac{\nu_{ul}}{c}\phi(\nu)\left\{\exp\left(\frac{h\nu_{ul}}{k_BT}\right)-1\right\}\exp\left(-\frac{E_u}{k_BT}\right)N,$$

where

$$\phi(\nu) = \frac{2\sqrt{\ln 2}}{\sqrt{\pi}\Delta\nu}\exp\left(-\frac{4\ln 2(\nu-\nu_{ul})^2}{\Delta\nu^2}\right).$$

Here, $\Delta\nu$ is the full line width at half maximum. Assuming the optically thin condition with $T > T_b$, the peak temperature of the Gaussian profile at $\nu = \nu_{ul}$ can be obtained as:

$$T_{\mathrm{G}} = \frac{8\pi^3 S_{ul}\mu^2\nu_{ul}}{3U(T)k_{\mathrm{B}}\Delta\nu}\sqrt{\frac{4\ln 2}{\pi}}\exp\left(-\frac{E_u}{k_{\mathrm{B}}T}\right)N.$$

Hence,

$$T_{\mathrm{G}}\Delta\nu\sqrt{\frac{\pi}{4\ln 2}} = \frac{8\pi^3 S_{ul}\mu^2\nu_{ul}}{3U(T)k_{\mathrm{B}}}\exp\left(-\frac{E_u}{k_{\mathrm{B}}T}\right)N,$$

where

$$\sqrt{\frac{\pi}{4\ln 2}} = 1.064.$$

2.5

Using Eq. (2.30), the A coefficient is calculated to be $3.45 \times 10^{-3}\ \mathrm{s}^{-1}$, and the critical density is found to be $7.2 \times 10^{7}\ \mathrm{cm}^{-3}$ using Eq. (2.50).

2.6

By combining Eqs. (2.27) and (2.28), we obtain:

$$\alpha_{ul} = \frac{c^2 n_u}{8\pi^2 \nu_{ul}^2 \Delta\nu}\left(\frac{n_l g_u}{n_u g_l} - 1\right) A_{ul}.$$

For a population inversion,

$$\frac{n_u g_\ell}{n_\ell g_u} > 1,$$

and hence $\alpha_{ul} < 0$ and $\tau_{ul} < 0$. This population corresponds to the Boltzmann distribution with a negative excitation temperature.

2.7

(a) $U(T) = \sum_{J=0}^{\infty} (2J+1)\exp\left\{-\frac{hBJ(J+1)}{k_{\mathrm{B}}T_{\mathrm{ex}}}\right\}$

(b) $U(T) \approx \int_0^{\infty} (2x+1)\exp\left\{-\frac{hBx(x+1)}{k_{\mathrm{B}}T_{\mathrm{ex}}}\right\}dx = \frac{k_{\mathrm{B}}T}{hB}$

(c) To evaluate the difference between the sum and the integral, the Euler–Maclaurin summation formula is employed:

$$\sum_{k=m+1}^{n} f(k) = \int_m^n f(x)dx + \sum_{k=1} \frac{B_k}{k!}\left[\left\{f^{(k-1)}(n) - f^{(k-1)}(m)\right\}\right] + \cdots.$$

Here B_k is the Bernoulli number. We define $f(k)$ as

$$f(k) = (2k+1)\exp\Big(-\alpha k(k+1)\Big),$$

where $\alpha = hB/(k_B T)$. Then,

$$U(T) = f(0) + \int_0^{\infty} (x)dx - B_1 f(0) - \frac{B_2}{2!}f'(0) - \frac{B_4}{4!}f'''(0) - \cdots,$$

where $B_1 = \frac{1}{2}, B_2 = \frac{1}{6}, B_3 = 0,$ and $B_4 = -\frac{1}{30}$. We then obtain $U(T)$ as a function of α:

$$U(\mathrm{T}) = \frac{1}{\alpha}\left(1 + \frac{\alpha}{3} + \frac{\alpha^2}{15} - \cdots\right).$$

If $\alpha \ll 1$, the result obtained in (a) is a good approximation.

2.8

(a) The deuterium nucleus has a nuclear spin of I. The nuclear spin state of D_2CO is represented by the integer pair $(m_{\mathrm{I}1}, m_{\mathrm{I}2})$, where $m_{\mathrm{I}i} = -1, 0, 1$ $(i = 1, 2)$. Hence, nine spin states are available, and they can be classified into the following two groups by the symmetry with respect to the interchange of the two deuterium nuclei $(i = 1, 2)$.

Symmetric spin states (six states):

$$(-1,-1), (0,0), (1,1)$$
$$\{(-1,0) + (0,-1)\}/\sqrt{2}$$
$$\{(0,1) + (1,0)\}/\sqrt{2}$$
$$\{(-1,1) + (1,-1)\}/\sqrt{2}$$

Antisymmetric spin states (three states):

$$\{(-1,0) - (0,-1)\}/\sqrt{2}$$
$$\{(0,1) - (1,0)\}/\sqrt{2}$$
$$\{(-1,1) - (1,-1)\}/\sqrt{2}$$

These are the states that transform as irreducible representations of spin and are eigenfunctions of the spin part of the Hamiltonian.

(b) The deuterium nucleus is a boson, and hence, the total wave function (the product of the rotational wave function and the spin wave function) has to be symmetric with respect to the interchange of the identical bosons. For the $K_a = even$ state, the rotational wave function is symmetric with respect to the interchange of the two deuterium nuclei. In contrast, for $K_a = odd$, the state is antisymmetric. Hence, the symmetric spin functions must be coupled with the $K_a = even$ states, while the antisymmetric spin functions must be coupled with the $K_a = odd$ states. Then, $K_a = even$ and $K_a = odd$ states are ortho and para, respectively, because the $K_a = even$ states have higher spin degeneracy. This situation is contrary to that for H_2CO. The statistical ortho/para ratio is 2 for D_2CO.

Chapter 3

3.1

The dispersion force can be represented as:

$$F = -\frac{dV}{dr} = -\frac{9I\alpha^2}{2r^7},$$

where I and α are the ionization potential and the polarizability of H_2. At r=10 nm (10^{-6} cm), its value is 6.9×10^{-16} dyn.

3.2

The effective interaction potential including the centrifugal potential is given as:

$$V_{\text{eff}} = -\frac{\beta}{r^n} + \frac{b^2}{r^2}\frac{\mu v^2}{2},$$

where b is the impact parameter, and $n \geq 3$. The radius of the peak of the potential hump is determined by differentiating V_{eff} yielding:

$$r_{\text{barrier}} = \left(\frac{n\beta}{b^2\mu v^2}\right)^{\frac{1}{n-2}}.$$

The barrier height is represented as:

$$V_{\text{barrier}} = \left(\frac{1}{2} - \frac{1}{n}\right)(n\beta)^{-\frac{2}{n-2}}(b^2\mu v^2)^{\frac{n}{n-2}}.$$

The collision occurs when

$$V_{\text{barrier}} < \frac{\mu v^2}{2}.$$

From this relation, the cross section is given as

$$\sigma = \pi\left(\frac{1}{2\gamma}\right)^{\frac{n-2}{n}}\left(\mu v^2\right)^{-\frac{2}{n}},$$

where

$$\gamma = \left(\frac{1}{2} - \frac{1}{n}\right)(n\beta)^{-\frac{2}{n-2}}.$$

As $<v> \propto T^{1/2}$, the cross section has the following temperature dependence:

$$\sigma \propto T^{-\frac{2}{n}}.$$

The rate coefficient thus has a dependency of

$$k \propto T^{-\frac{2}{n}+\frac{1}{2}}.$$

Note: For a full derivation of the rate coefficient, the integral of Eq. (3.8) has to be calculated. In this case, the gamma function appears in the integral:

$$\Gamma(x) = \int_0^{\infty} e^{-t} t^{x-1} dt.$$

An example is shown in Eq. (3.50).

3.3

Photons with energy ranging from 11 eV (1127 Å) to 13.6 eV (912 Å) contribute to the ionization. Using Eq. (3.67), the photoionization rate is calculated to be 2.2×10^{-9} s^{-1}.

3.4

The Maxwell–Boltzmann distributions for species A and B are given respectively as:

$$f(\vec{v}_A, T) d\vec{v}_A = \left(\frac{m_A}{2\pi k_\mathrm{B} T}\right)^{\frac{3}{2}} \exp\left(-\frac{m_A \vec{v}_A^2}{2k_\mathrm{B} T}\right) d\vec{v}_\mathrm{A}$$

and

$$f(\vec{v}_B, T) d\vec{v}_B = \left(\frac{m_B}{2\pi k_\mathrm{B} T}\right)^{\frac{3}{2}} \exp\left(-\frac{m_B \vec{v}_B^2}{2k_\mathrm{B} T}\right) d\vec{v}_B.$$

In terms of the relative velocity ($\vec{v}$) and the velocity of the center of mass ($\vec{v}_G$), the total distribution becomes:

$$\vec{v} = \vec{v}_A - \vec{v}_B$$

$$\vec{v}_G = \frac{m_A \vec{v}_A + m_B \vec{v}_B}{m_A + m_B}.$$

$$f(\vec{v}, \vec{v}_G, T) d\vec{v} d\vec{v}_G = f(\vec{v}_A, T) f(\vec{v}_B, T) d\vec{v}_A d\vec{v}_B$$

$$= \left(\frac{m_A}{2\pi k_\mathrm{B} T}\right)^{\frac{3}{2}} \left(\frac{m_B}{2\pi k_\mathrm{B} T}\right)^{\frac{3}{2}} \exp\left(-\frac{(m_A + m_B)\vec{v}_G^2}{2k_\mathrm{B} T}\right) \exp\left(-\frac{\mu \vec{v}^2}{2k_\mathrm{B} T}\right) d\vec{v} d\vec{v}_G.$$

By integrating over $\vec{v}_G$, we obtain:

$$f(\vec{v},T)d\vec{v} = \left(\frac{\mu}{2\pi k_\mathrm{B}T}\right)^{\frac{3}{2}} \exp\left(-\frac{\mu\vec{v}^2}{2k_\mathrm{B}T}\right)d\vec{v}.$$

In this derivation, note that $d\vec{v}_G = 4\pi v_G^2$. Hence, we obtain the distribution of the relative speed, as shown in Eq. (3.6) using the relation $d\vec{v} = 4\pi v^2 dv$.

3.5

The H_2–H_2 collision can be analyzed using the interaction potential for the dispersion interaction given in Eqs. (3.47 and 3.48). The coefficient β of Eq. (3.48) is:

$$\beta = \frac{3I\alpha^2}{4},$$

where I and α are the ionization potential and the polarizability of H_2. Substituting their values, β is calculated to be 1.16×10^{-59} erg cm^6. From Eq. (3.50), the collision rate coefficient is calculated to be 5.0×10^{-10} cm^3 s^{-1} at 10 K. The mean free time for the H_2 density of 10^4 cm^{-3} at 10 K is calculated as:

$$t_\mathrm{free} = \frac{1}{k[\mathrm{H_2}]} = 2 \times 10^5 \mathrm{s}.$$

The mean relative velocity of H_2 molecule at 10 K is calculated to be 4.6×10^4 cm s^{-1}, and hence, the mean free path is 9.2×10^9 cm (9.2×10^4 km).

Note: The geometrical cross section significantly underestimates the collision rate.

3.6

The Langevin rate coefficient is calculated to be 1.1×10^{-9} cm^3 s^{-1} using Eq. (3.31). The rate coefficient under the locked-dipole approximation is calculated to be 2.3×10^{-8} cm^3 s^{-1} at 27 K. The experimental value is just between these two approximations.

Chapter 4

4.1

Exothermicity is calculated as

$$H_f(\mathrm{CH^+}) + H_f(\mathrm{H}) - H_f(\mathrm{C^+}) = 1619 + 216 - 1798 = 37\mathrm{kJmol^{-1}}.$$

This corresponds to 0.38 eV.

4.2

The rate equations for CF^+ and HF are as follows:

$$\frac{d[\mathrm{CF^+}]}{dt} = k_2[\mathrm{HF}][\mathrm{C^+}] - k_3[\mathrm{CF^+}][\mathrm{e}]$$

$$\frac{d[\mathrm{HF}]}{dt} = k_1[\mathrm{F}][\mathrm{H_2}] - k_3[\mathrm{C^+}][\mathrm{HF}] - k_4[\mathrm{HF}].$$

Furthermore, the total number of the F atom, α, has to be conserved:

$$[\mathrm{F}] + [\mathrm{HF}] + [\mathrm{CF^+}] = \alpha.$$

In the steady state, the abundance of HF, F, and CF^+ are represented as:

$$[\mathrm{HF}] = \frac{k_1 k_3 [\mathrm{H_2}]\alpha}{k_1(k_2 + k_3)[\mathrm{H_2}] + k_3(k_2[\mathrm{e}] + k_4)}$$

$$[\mathrm{F}] = \frac{k_3(k_2[\mathrm{e}] + k_4)\alpha}{k_1(k_2 + k_3)[\mathrm{H_2}] + k_3(k_2[\mathrm{e}] + k_4)}$$

$$[\mathrm{CF^+}] = \frac{k_1 k_2 [\mathrm{H_2}]\alpha}{k_1(k_2 + k_3)[\mathrm{H_2}] + k_3(k_2[\mathrm{e}] + k_4)},$$

where we assume that $[C^+] \approx [e]$. For A_v of magnitude 1, the abundance of HF, F, and CF^+ are calculated to be $1.93 \times 10^{-6,}$, $1.48 \times 10^{-6,}$, and $1.92 \times 10^{-7,}$ cm^{-3}, respectively, at 100 K and the H_2 density of 10^4 cm^{-3}.

4.3

(b) Formation and destruction rates are as follows: $CH_2{}^+$ formation rate:

$C^+ + H_2$: 9.2×10^{-16} cm^{-3} s^{-1}

$CH^+ + H_2$: $1.3 \times 10^{-16} \mathrm{cm}^{-3} \mathrm{s}^{-1}$

Total formation rate: 1.0×10^{-15} cm^{-3} s^{-1}

$CH_2{}^+$ destruction rate: $CH_2{}^+ + H_2$: 9.4×10^{-16} cm^{-3} s^{-1}

$CH_2{}^+ + e$: $1.0 \times 10^{-16} \mathrm{cm}^{-3} \mathrm{s}^{-1}$

Total destruction rate: 1.0×10^{-15} cm^{-3} s^{-1}

Chapter 5

5.1

We consider the hypothetical reaction as:

$$\mathrm{CH} + \mathrm{H} + \mathrm{CH_2}^+ + \Delta E_1,$$

where ΔE_1 corresponds to the proton affinity of CH by definition. Similarly, we consider the hypothetical reaction for the corresponding neutrals as:

$$\mathrm{CH} + \mathrm{HCH_2} + \Delta E_2,$$

where ΔE_2 is the bond dissociation energy of CH_2. Using ΔE_2 and the ionization potentials of H and CH_2, the proton affinity of CH, ΔE_1, can be derived. The proton affinities of CH_2 and CH_3 can also be evaluated. The results are given in Table 5.2.

5.2

The ionization fraction $[\mathrm{e}]/[\mathrm{H_2}]$ is given by Eq. (5.13). When the cosmic-ray ionization rate is enhanced by a factor of 100, the ionization fraction is increased by a factor of 10. Hence, $[\mathrm{e}]/[\mathrm{H_2}]$ is 2×10^{-7}. With this electron abundance, the destruction of H_3^+ is dominated by the proton transfer to CO and O, and hence Eq. (5.15) can be applied to evaluate the H_3^+ abundance. Then $[\mathrm{H_3^+}]$ is evaluated to be 1.8×10^{-3} cm^{-3}. The He^+ abundance can be calculated using Eq. (5.33). If the cosmic ionization rate of He is higher by a factor of 100 than the nominal value as that of H_2, $[\mathrm{He^+}]$ is calculated to be 5.8×10^{-4} cm^{-3}. Hence, using Eq. (5.34), the destruction time is found to be 9.3×10^{11} s (3×10^4 year), and the formation timescale is then 2.8×10^{11} s (9×10^3 year) obtained from Eq. (5.155). From these results, the steady-state timescale is 9×10^3 year. A higher cosmic-ray ionization rate results in a chemical equilibrium timescale.

5.3

The ionization fraction $[\mathrm{e}]/[\mathrm{H_2}]$ is given by Eq. (5.13). This does not change significantly if metallicity is low. The H_3^+ abundance can be calculated from Eq. (5.15) because the major destruction processes of H_3^+ are still the reactions with CO and O. If the CO and O abundances are lower by a factor of 10 than the nominal value, the H_3^+ abundance is enhanced by a factor of 10. Then, $[\mathrm{H_3^+}] = 1.8\times10^{-4}$ cm^{-3}. Similarly, the He^+ abundance is enhanced by a factor of 10 and is 5.8×10^{-5} cm^{-3}. Hence, the destruction timescale by He^+ and the timescale for formation of molecules are evaluated to be 3×10^5 year and 9×10^4 year, respectively. Hence, the steady-state timescale is 9×10^4 year. The low-metallicity condition tends to make the chemical equilibrium timescale shorter.

5.4

The reaction rate coefficient for $\mathrm{CO} + \mathrm{He^+} \rightarrow \mathrm{C^+} + \mathrm{O} + \mathrm{He}$ is denoted by k_1, and that for $^{12}\mathrm{C^+} + \mathrm{H_2} \rightarrow {}^{12}\mathrm{CH_2^+} + h\nu$ by k_2. Here, the rate coefficients are independent of isotope species. Denoting the reaction rate coefficient for $^{13}\mathrm{C^+} + {}^{12}\mathrm{CO} \rightarrow {}^{12}\mathrm{C^+} + {}^{13}\mathrm{CO}$ by k_3, then, that for the inverse reaction $k_4$is given by $k_3 \exp(-35/T)$. The rate equation for $^{12}\mathrm{C^+}$ and $^{13}\mathrm{C^+}$ are written as follows:

$$\frac{d[^{12}\mathrm{C}^+]}{dt} = k_1[^{12}\mathrm{CO}][\mathrm{He}^+] - k_2[^{12}\mathrm{C}^+][\mathrm{H}_2] + k_3[^{13}\mathrm{C}^+][^{12}\mathrm{CO}] - k_4[^{12}\mathrm{C}^+][^{13}\mathrm{CO}],$$

and

$$\frac{d[^{13}\mathrm{C}^+]}{dt} = k_1[^{13}\mathrm{CO}][\mathrm{He}^+] - k_2[^{13}\mathrm{C}^+][\mathrm{H}_2] - k_3[^{13}\mathrm{C}^+][^{12}\mathrm{CO}] + k_4[^{12}\mathrm{C}^+][^{13}\mathrm{CO}].$$

In the steady-state condition, we obtain:

$$\frac{[^{12}\mathrm{C}^+]}{[^{13}\mathrm{C}^+]} = \frac{k_2[\mathrm{H}_2] + k_3([^{12}\mathrm{CO}] + [^{13}\mathrm{CO}])}{k_2[\mathrm{H}_2] + k_3([^{12}\mathrm{CO}] + [^{13}\mathrm{CO}])\exp(-35/T)} \frac{[^{12}\mathrm{CO}]}{[^{13}\mathrm{CO}]}.$$

As $k_2[\mathrm{H}_2]$ is much smaller than $k_3([^{12}\mathrm{CO}] + [^{13}\mathrm{CO}])$,we obtain the approximate relation:

$$\frac{[^{12}\mathrm{C}^+]}{[^{13}\mathrm{C}^+]} = \exp\left(\frac{35}{T}\right)\frac{[^{12}\mathrm{CO}]}{[^{13}\mathrm{CO}]}.$$

5.5

The reaction rate coefficient for $\mathrm{C_nH} + \mathrm{e} \rightarrow \mathrm{C_nH^-} + h\nu$ is denoted by k_{ra}, and that of the dissociative electron-attachment reaction, $\mathrm{C_nH_2}$ (cumulene type) + e → $\mathrm{C_nH^-}$ + H, is denoted by k_{da}. With the rate coefficients for the following three destruction reactions for anions,

$$\mathrm{C_nH^-} + \mathrm{HC_nH_2}\ (\text{cumulene type}) + \mathrm{e},$$

$$\mathrm{C_nH^-} + \mathrm{Oproducts} + \mathrm{e},$$

and

$$\mathrm{C_nH^-} + \mathrm{M^+products}$$

denoted by k_{H}, k_{O}, and k_{M}, respectively, the rate equation for $\mathrm{C_nH^-}$ is then given as

$$\frac{d[\mathrm{C_nH^-}]}{dt} = k_{\mathrm{ra}}[\mathrm{C_nH}][\mathrm{e}] + k_{\mathrm{da}}[\mathrm{C_nH_2}][\mathrm{e}] - k_{\mathrm{H}}[\mathrm{C_nH^-}][\mathrm{H}] - k_{\mathrm{O}}[\mathrm{C_nH^-}][\mathrm{O}] - k_{\mathrm{M}}[\mathrm{C_nH^-}][\mathrm{M^+}].$$

In the steady-state condition, we obtain

$$\frac{[\mathrm{C_nH^-}]}{[\mathrm{C_nH}]}=\frac{\left(k_{\mathrm{ra}}+\frac{[\mathrm{C_nH_2}]}{[\mathrm{C_nH}]}k_{\mathrm{da}}\right)}{k_{\mathrm{H}}[\mathrm{H}]+k_{\mathrm{O}}[\mathrm{O}]+k_{\mathrm{M}}[\mathrm{M^+}]}.$$

In TMC-1, $\frac{[\mathrm{C_6H_2}]}{[\mathrm{C_6H}]}$ is 0.06 (Table 5.1), and hence, $\frac{[\mathrm{C_6H_2}]}{[\mathrm{C_6H}]}k_{\mathrm{da}}$ is estimated to be 1.8×10^{-7}. This is almost comparable to k_{ra}.

Chapter 6

6.1

(a) The dust surface area can be calculated using the dust size distribution $n(a)da$:

$$S=\int_{a_{\min}}^{a_{\max}}4\pi a^2 n(a)da=8\pi A\left(\frac{1}{\sqrt{a_{\min}}}-\frac{1}{\sqrt{a_{\max}}}\right),$$

for the MRN distribution, where $a_{\min}$ and $a_{\max}$ are the minimum and maximum sizes of dust grains. We arbitrarily set $a_{\min}$ and $a_{\max}$ to be 5 nm and 300 nm, respectively. Apparently, $a_{\min}$ gives a dominant contribution to S. Using the A values given in this problem, we obtain a dust surface area of 2.41×10^{-21} cm^2/(H atom). Similarly, the cross section σ is found to be:

$$\sigma=\int_{\mathrm{a_{min}}}^{\mathrm{a_{max}}}\pi a^2 n(a)da=6.03\times10^{-22}\mathrm{cm}^2/(\mathrm{H\ atom}).$$

(b) For CO, the mean velocity is calculated from Eq. (3.10) to be 86.9 m s^{-1}. Hence the collision rate of a molecule to dust grains is evaluated as:

$$R=\sigma\langle v\rangle=5.24\times10^{-18}n_{\mathrm{H}}(\mathrm{s}^{-1}).$$

Hence, the depletion timescale of a molecule is

$$\tau=R^{-1}=6.1\times10^9/n_{\mathrm{H}}(\mathrm{cm}^{-3})(\mathrm{year})=3.0\times10^9/n_{\mathrm{H_2}}(\mathrm{cm}^{-3})(\mathrm{year}),$$

where the sticking probability is assumed to be unity.

6.2

The condition that Eq. (6.7) is unity gives the approximate desorption temperature of 36 K for H_2CO at the H_2 density of 10^4 cm^{-3}. Note that the desorption temperature depends weakly on the H_2 density. The desorption timescale for each H_2CO molecule is given by

$$\tau_{\mathrm{des}} = \left(\frac{R_{\mathrm{des}}}{N_{\mathrm{s}}(\mathrm{H_2CO})}\right)^{-1} = \frac{1}{\nu_0 \exp\left(-\frac{E_{\mathrm{d}}}{k_{\mathrm{B}}T}\right)}.$$

The result is 8.2×10^{76} s and 2.5×10^{32} s at 10 K and 20 K, respectively. The diffusion timescale is calculated from Eqs. (6.16 and 6.17) to be 2.5×10^{38} s and 1.4×10^{16} s at 10 K and 20 K, respectively. At these temperatures, H_2CO stays on dust grains for a long time.

6.3

In dense molecular clouds, one cosmic-ray hit to H_2 molecule produces two H atoms. Then the formation rate of the H atoms is given as $2\zeta[\mathrm{H_2}]$. In the steady state, this has to be balanced with the formation rate of H_2 from H. Using Eq. (6.38), we obtain:

$$2\zeta[\mathrm{H_2}] = 4.4 \times 10^{-18}\sqrt{T} \times 2[\mathrm{H_2}][\mathrm{H}].$$

Then, the number density of the H atoms is calculated to be 0.7 $\mathrm{cm^{-3}}$, regardless of the H_2 density. This value is close to the nominal H density of 1 $\mathrm{cm^{-3}}$.

6.4

(a) The probability of the tunneling reaction between H and CO (or H_2CO) can be evaluated from Eq. (6.25). When we assume a barrier width of 1 Å and an activation barrier of 2000 K, the probability is estimated to be 1.3×10^{-8}.

(b) The rate equation for HCO(s) can be written as:

$$\frac{d[\mathrm{HCO(s)}]}{dt} = K_{\mathrm{CO}}[\mathrm{CO(s)}][\mathrm{H(s)}] - K_{\mathrm{HCO}}[\mathrm{HCO(s)}][\mathrm{H(s)}].$$

In the steady-state condition, we obtain

$$\frac{[\mathrm{HCO(s)}]}{[\mathrm{CO(s)}]} = \frac{K_{\mathrm{CO}}}{K_{\mathrm{HCO}}} = 1.3 \times 10^{-8}.$$

(c) From Eq. (6.32), we have the following relation in the steady-state condition:

$$k_{\mathrm{ad,H}}[\mathrm{H(g)}] = k_{des,\mathrm{H}}[\mathrm{H(s)}] + 2k_{\mathrm{HH}}[\mathrm{H(s)}]^2.$$

Here, we evaluate $k_{ad,\mathrm{H}}$, $k_{des,\mathrm{H}}$, and k_{HH} to be $2.9 \times 10^{-13}\ \mathrm{s^{-1}}$, $9.7 \times 10^{-8}\ \mathrm{s^{-1}}$, and $5.7 \times 10^{4}\ \mathrm{cm^{-3}\ s^{-1}}$, respectively, using Eqs. (6.33, 6.34, and 6.35). Then the number density of the H atoms on dust grains is $1.6 \times 10^{-9}\ \mathrm{cm^{-3}}$. The reaction rate coefficient for CO + H → HCO, K_{CO}, is calculated using Eq. (6.22) to be $3.7 \times 10^{-4}\ \mathrm{cm^3\ s^{-1}}$. Hence, the timescale of the CO + H reaction is given as

$$\tau = \frac{1}{K_{\mathrm{CO}}[\mathrm{H(s)}]} = 1.7 \times 10^{12}(\mathrm{s}) = 5.4 \times 10^{4}(\mathrm{year}).$$

To produce CH_3OH, another hydrogenation reaction with the reaction barrier, $H_2CO + H$, is necessary. Assuming the same barrier width and height, the timescale is the same as that for the $CO + H$ reaction. For the other reactions, $HCO + H$ and $H_3CO + H$ are rapid, and hence, the total production timescale from CO to CH_3OH is estimated to be 10^5 year.

Note: The above evaluation is based on the rate equation method. In reality, the stochastic approach mentioned in the text is preferable.

6.5

(a) For the H_2 density of 10^6 cm^{-3}, the number density of HD is 30 cm^{-3}, and that of the electrons is 2×10^{-3} cm^{-3}. Hence, the timescale for the reaction with HD is 9.5×10^7 s, where the rate coefficient for reaction (6.65) is used. On the other hand, the timescale for the reaction with electrons is evaluated to be 1.3×10^9 s. Here, the rate coefficient of the electron recombination reaction is:

$$k_{\mathrm{r}} = 6.7 \times 10^{-8} \left(\frac{T}{300}\right)^{-0.52} \mathrm{cm}^3\mathrm{s}^{-1}.$$

Hence, the most important destruction process of H_3^+, H_2D^+, and HD_2^+ is the reaction with HD at this H_2 density, if CO is completely frozen out onto dust grains.

(b) The rate coefficient of the ion–molecule reaction of $H_2D^+ + HD$ and $HD_2^+ + HD$ is denoted by k. Then, the rate equation for HD_2^+ and D_3^+ can be written as

$$\frac{d[\mathrm{HD_2}^+]}{dt} = k[\mathrm{H_2D}^+][\mathrm{HD}] - k[\mathrm{HD_2}^+][\mathrm{HD}] - k_{\mathrm{r}}[\mathrm{HD_2}^+][\mathrm{e}]$$

and

$$\frac{d[\mathrm{D_3}^+]}{dt} = k[\mathrm{HD_2}^+][\mathrm{HD}] - k_{\mathrm{r}}[\mathrm{D_3}^+][\mathrm{e}].$$

In the steady-state condition, we obtain the following results:

$$\frac{[\mathrm{HD_2}^+]}{[\mathrm{H_2D}^+]} = \frac{k[\mathrm{HD}]}{k[\mathrm{HD}] + k_{\mathrm{r}}[\mathrm{e}]}$$

and

$$\frac{[\mathrm{D_3}^+]}{[\mathrm{HD_2}^+]} = \frac{k[\mathrm{HD}]}{k_\mathrm{r}[\mathrm{e}]}.$$

Chapter 7

7.1

(a) For the H_2 density of 10^6 cm^{-3}, the number density of the electrons is 2×10^{-3} cm^{-3}. The electron recombination rate of N_2H^+ at 10 K is calculated to be 3.7×10^{-6} cm^3 s^{-1}. Hence, the timescale of the electron recombination is 1.4×10^8 s (4.4 year).

(b) The electron recombination rate of N_2H^+ at 20 K is calculated to be 2.2×10^{-6} cm^3 s^{-1}. Hence, the timescale of the electron recombination is 2.3×10^8 s (7.3 year). As CO is evaporated from dust grains, its number density is 10^2 cm^{-3}. The timescale for the reaction of N_2H^+ with CO is 10^7 s, where the rate coefficient is assumed to be 1×10^{-9} cm^3 s^{-1}. Thus, N_2H^+ is mainly lost in its reaction with CO at 20 K.

(c) The electron recombination rate of HCO^+ at 100 K is 5.1×10^{-7} cm^3 s^{-1} (Table 5.3). Hence, the timescale of the electron recombination is 9.8×10^8 s (31 year). For the timescale of the reaction of HCO^+ with H_2O to be shorter than this, the number density of H_2O has to be higher than 1 cm^{-3}, which corresponds to a fractional abundance for H_2O higher than 10^{-6}.

7.2

(a) The timescale for the destruction of neutral molecules by He^+ is roughly 3×10^6 year (Eq. 5.34).

Note: For some deuterated neutral species, the destruction by protonated ions such as H_3^+, HCO^+, and H_3O^+ would also contribute to their loss, depending on their proton affinities (proton affinities of the neutral species have to be higher than that of the above three protonated ions). The abundance of HCO^+ is estimated to be 2×10^{-9}, and hence, the destruction timescale by the HCO^+ reaction is 1.6×10^4 year.

(b) The electron recombination rate coefficients for HN_2^+ and HCO^+ are 9.9×10^{-7} cm^3 s^{-1} and 7.3×10^{-7} cm^3 s^{-1}, respectively. Given a number density of electrons of 2×10^{-3} cm^{-3} at the H_2 density of 10^6 cm^{-3}, the timescale for the loss of deuterated ionic species through electron recombination is as short as 20 year.

7.3

Follow the derivation given in the problem.

7.4

(a) The rate equation for C^+ for the simplified situation given in the problem is

$$\frac{d[C^+]}{dt} = G_0 k_{pd}[C] - k_{rr}[C^+][e],$$

where k_{pd} and k_{rr} are the photodissociation rate coefficient of C and the radiative recombination rate of C^+, respectively, both of which are tabulated in Tables 4.6. Considering the charge balance, $[C^+] \approx [e]$, and the conservation of the total number of the carbon atoms, $[C^+] + [C] = \alpha$ (constant), we have the following second-order equation for $[C^+]$ in the steady-state condition:

$$k_{rr}[C^+]^2 + G_0 k_{pd}[C^+] - G_0 k_{pd}\alpha = 0.$$

Here, k_{pd} is given as a function of the visual extinction, A_v:

$$k_{pd} = k_0 \exp(-\gamma A_v),$$

where $k_0 = 2.2 \times 10^{-10}$ s^{-1} and $\gamma = 2.96$ for C. Hence, $[C^+]$ can be calculated as a function of A_v under constant density and constant temperature for a given G_0.

(b) Here, we can consider the visual extinction satisfying $[C^+] = [C] = \alpha/2$. This visual extinction, denoted as $A_{v,1/2}$, can be regarded as the effective thickness of the C^+ layer in the PDR. It is given as:

$$A_{v,1/2} = \frac{1}{\gamma} \ln \frac{2G_0 k_0}{k_{rr}\alpha}.$$

Note that the thickness of the C^+ layer depends on the log of the ratio G_0/α.

Chapter 8

8.1

The timescale is calculated in the same way as done in solving Problem 6.2. For the H_2 density of 10^9 cm^{-3}, the desorption temperature is approximately 27, 45, and 130 K, respectively. For a H_2 density of 10^{12} cm^{-3}, the desorption temperature is approximately 31, 55, and 150 K, respectively. For a higher H_2 density, the evaporation temperature tends to be higher.

8.2

The timescale for the three-body reaction of C^+ with H_2 is given as

$$\tau = \frac{1}{k[H_2][M]}.$$

The third particle that mostly contributes to this reaction is apparently H_2, and hence the timescale can be calculated as 6.6×10^{12} s (2.1×10^5 year), and 6.6×10^6 s (0.21 year) for H_2 densities of 10^9 cm^{-3} and 10^{12} cm^{-3}, respectively. Therefore, the three-body reactions cannot be ignored particularly for the densest part of protoplanetary disks.

8.3

The energy released under radial contraction from $r + \Delta r$ to r is assumed to be balanced by the radiation cooling from dust emission in the perpendicular direction to the disk:

$$\frac{GM\dot{M}}{r^2}\Delta r = 2 \times (2\pi r \Delta r)\sigma T^4.$$

Here, the factor of 2 on the right-hand side means that the emission can go out from the upper and lower surfaces of the disk. Furthermore, the dust emission is assumed to be optically thick. For the mid-plane direction, the radiative energy flow can be ignored because of a small temperature gradient. From this relation, we obtain Eq. (8.10).

Index

S. Yamamoto, *Introduction to Astrochemistry*, Astronomy and Astrophysics Library 7, DOI 10.1007/978-4-431-54171-4